Tests of the Planck Cosmology at High and Low Redshifts

UNIVERSITY OF
CAMBRIDGE

Pablo Lemos Portela

Selwyn College

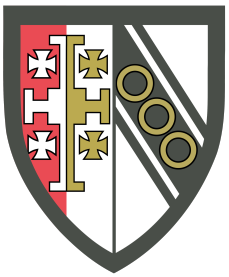

2018 September

A dissertation submitted for the degree of Doctor of Philosophy

To Stine. The Universe was made for you and me.

Summary

The inflationary ΛCDM cosmology currently provides an accurate description of the Universe. It has been tested using several observational techniques over a wide redshift range, and it provides a good fit to most of them. In addition, it is a surprisingly economical model, requiring only six parameters to characterize the background cosmology and its fluctuations. In this model, the Universe is dominated by a cosmological constant Λ driving an accelerated expansion, and by cold dark matter. The strongest constraints on parameters to date come from observations of the temperature and polarization anisotropies of the cosmic microwave background measured by the *Planck* satellite. There are, however, indications of features in the *Planck* power spectra, possible differences with high redshift ground-based CMB experiments, and 'tensions' between *Planck* and low redshift measurements of the Hubble constant and weak gravitational lensing.

In this thesis, we review possible tensions and extensions to the *Planck* cosmology, at both high and low redshifts. We begin with the high redshift analysis, using the *Planck* data to test models which introduce oscillatory features in the primordial power spectrum. We also study possible departures from slow roll inflation using the generalized slow-roll formalism, which allows for order unity deviations. Although we find models which give marginal improvements on the temperature or polarization power spectra, the combination of temperature and polarization is found to be consistent with a featureless power-law primordial spectrum. We then focus on measurements of the polarized CMB sky by the South Pole Telescope collaboration, who report tension between their measurements and the ΛCDM cosmology and with the cosmological parameters determined by *Planck*. We find evidence of a high χ^2 in the SPTpol spectra which is unlikely to be cosmological. We report consistency between the *Planck* and SPTpol polarization spectra over the multipoles accessible to *Planck* ($\ell \lesssim 1500$).

We then investigate tension at low redshifts. We begin with weak gravitational lensing in which a number of surveys have suggested that the amplitude of the fluctuation spectra is lower than the *Planck* value. We review the small-angle approximations commonly used in galaxy weak lensing analyses and their effect on cosmological parameters. We find that these approximations are perfectly adequate for present and near future experiments. We find internal

inconsistencies in the recent KiDS-450 analysis involving photometric redshifts and the KiDS covariance matrix at large scales. Finally, we investigate the difference between measurements of the present day expansion rate of the Universe. We apply a novel parameterization of the inverse distance ladder to determine the present date value of the Hubble parameter H_0, which assumes General Relativity but makes no further assumptions about systematic errors or the nature of dark energy. Our analysis uses baryon acoustic oscillation data and Type Ia Supernovae to constrain the expansion history assuming a value of the sound horizon determined from the CMB. Our results are in tension with recent direct determinations of H_0. We conclude that this tension, if real, cannot be solved by modifications of the ΛCDM model at late times. Instead, we would require a modification of the theory at early times which reduces the sound horizon.

We conclude that at this time there is no compelling evidence that conflicts with the ΛCDM cosmology either at low or at high redshifts.

Contents

Declaration

This dissertation is the result of my own work and includes nothing which is the outcome of work done in collaboration except as declared in the Preface and specified in the text. The use of 'we' instead of 'I' throughout this thesis merely reflects a stylistic choice. All chapters are intended to be self-contained. The following parts of this thesis have been published or submitted for publication, or will be submitted in the following days:

- **Chapters 2 and 3** will soon be submitted for publication.
- The results from **Chapter 4** appeared in [1]
- **Chapter 5** was published as [2]
- **Chapter 6** was published as [3].
- The results from **Appendix B** were used in [4].
- **Chapter 7** has been submitted for publication as [5]

This thesis is not substantially the same as any that I have submitted, or, is being concurrently submitted for a degree or diploma or other qualification at the University of Cambridge or any other University or similar institution. I further state that no substantial part of my dissertation has already been submitted, or, is being concurrently submitted for any such degree, diploma or other qualification at the University of Cambridge or any other University or similar institution.

The length of this thesis does not exceed the stated limit of the Degree Committee of Physics and Chemistry of 60,000 words.

Pablo Lemos
Cambridge, September 26, 2018.

Acknowledgements

While my name is the only one in the title, this PhD would not have been possible without the help of a large number of people. I know this is an unusually long acknowledgements section, and despite that, I am sure there are others I am not mentioning, for which I apologise.

First of all, I would like to thank the Institute of Astronomy and the Kavli Institute for Cosmology, for giving me the opportunity to work in such an outstanding environment, and funding my PhD. I have worked and will continue working to live up to the chance that you gave me when you accepted my application. Special thanks to Debbie Peterson and Sandra Berner, for always being willing to help with a smile.

I would also like to thank Selwyn College for their support, and in particular to my tutor Garvin Jarvis, who not only helped me fund trips for conferences but also stepped up to help me when I needed him the most. I am also grateful to the admissions officer Samantha Carr, and to the porters of Selwyn, for making my college feel like home for the last three years. Special mention to John Morley of Lucy Cavendish, for the bike fixes. I have had a sense of belonging to Selwyn college from day one, and that has been mostly thanks to the tireless work of the MCR committee. I want to thank everyone who has spent part of their own time over the last three years to make Selwyn more fun and welcoming, and I am incredibly grateful to the graduate students of the college for giving me the opportunity to contribute myself. As much as I complained, it was a real pleasure.

I would have probably lost my mind during these three years of intense work had it not been for the fun moments that allowed me to disconnect from science now and then. To thank for this, I have not only my friends from home who have always been there (Pereira, Joni, Viru, Alfonso, Alejandra, etc.) but also some of the fantastic people I have met in Cambridge, who I hope will stay in my life. Marcos, thank you for your eternal optimism, that is often contagious. Harvey, thanks for being a friend in good and bad times. Andrew, who has shared some of the miseries of PhD life with me, but showed me that those go away if you drink enough wine. Cameron, I am still your friend despite your constant distractions and how annoyingly intelligent you are all the time, I think that says a lot about how much I appreciate you. And of course, James. At Christmas, people sing 'And a night in with Pabs and Massey' for a reason. I could not have

found a better friend.

My life's passion (apart from cosmology, of course) has always been football. I want to thank Selwyn College Association Football Club, and Cambridge University Association Football Club, for the opportunity to represent my college and my University and create some unforgettable memories. One of the things I will miss the most from Cambridge is the football, and the people I met there.

On the academic side: Antonio Benito, thank you for showing me the beauty of mathematics in high school, you are the only reason I chose this path. Gabriel Alvarez Galindo, by far the best professor I had during my undergraduate degree, who went above and beyond, to help me start a career as a researcher. To Scott Dodelson, for giving me an opportunity, showing me how research is done, and helping me find a PhD position, I will never be able to thank you enough. I am also grateful to Robert Wald, David Kutasov and Andrey Kravtsov for their advice to a confused Masters student.

During my PhD, I have had to ask for help more times than I can remember. I want to thank all my officemates for their patience and support and in particular Bjoern. I would have been disappointed by your decision to quit cosmology if you had not chosen to save the world instead. Good luck with that by the way! I want to thank Antony Lewis, Stuart Rankin, Will Handley, and all the IT staff at the IoA. I would still be stuck in the CosmoMC tutorial if not for all your help. I want to thank Steven Gratton; you might not have been my official supervisor but it always felt like you were. I am very grateful to my secondary supervisor Anthony Challinor, whose door has always been open for me.

And of course, there is George. I remember the day I met you when you made a joke about what a cruel and horrible supervisor you are, how much I would end up hating you, and about how relieved I would feel when I got out of here. You have made those jokes regularly during my degree. I am not going to deny that you can be blunter than most people and that you are very clear when you think something is not good enough. But, at least for me, every time you have said that, I have learned and improved. The truth is, I cannot believe to this day that someone as wise and brilliant has spent such a significant amount of time helping and teaching me. You have taught me not only cosmology, but also the way scientific research should be done, always looking for the truth instead of the publications. There are no words I can write in this piece of paper to tell you how grateful I am, and how much I have learned and enjoyed being your student.

I remember, now and always, my late grandparents Sara, Joaquin, Nela and Pepe. Not only did you love me unconditionally, but also taught me the value of hard work. I wish you could be here to see me. I also want to thank all my extended family for their love and support.

More importantly, I want to thank the three people who have always been at the centre of my

life: my father, Tito. Not only have you ever been the ideal parent, but you are also the person who makes me feel capable of anything. I admire your courage and determination. Every time I doubt myself you tell me that you are betting on my success. That always makes me want to prove you right. I also want to thank my mother, Rous, for smiling and making me smile all twenty-seven years I have been in this world. You know me better than anyone, and you always know what to say to make me feel better. I also want to thank my little brother, Tatas. I have always felt like I had to protect you, but now you are not only as tall as I am, but also a lot more brilliant. Soon you will do the protecting. I am very proud of you.

There are three more people I want to thank: Maddy and Julia, thank you for letting me live in your house this last year. You started the year as my girlfriend's friends, but you feel like my friends now. A lot of this thesis was written in your kitchen. And that leads me to Stine, the last person I want to thank since I have been saving best for last. What can I say that I have not told you already? You have changed everything. From the moment you appeared in my life, the way I see things has changed completely. Every day you have been with me, I have felt happy, whatever happened, because I knew at the end of the day I would see you, and everything else would become irrelevant. Thanks to you, I am one of the few people who will remember the days of thesis writing as extremely happy days. Now that Cambridge is over, we start a new chapter of our lives together. The first of many, and they will all be good as long as you are with me. The Universe was made for you and me.

Part I

Introduction

Chapter 1

Introduction

1.1 Mathematics of an Expanding Universe

The inflationary ΛCDM model of cosmology is considered the best model to describe the Universe. It fits most of the available observations using only six parameters to explain the evolution of both the background Universe and its fluctuations. The present chapter establishes the foundations of the ΛCDM model (numerous textbooks present detailed accounts of the ΛCDM model, e.g. [6; 7; 8; 9; 10]). Additionally, some of the tensions between different observations that motivate the search for extensions to the ΛCDM cosmology are reviewed. A detailed discussion of a number of such extensions will be the topic of this thesis.

This section introduces the basic concepts, mathematical tools, and notation commonly used in cosmology, which will be used throughout this thesis. Sec. 1.1.1 establishes a number of key concepts in General Relativity, which are applied to a homogeneous, isotropic, expanding Universe in Sec. 1.1.2. The different components of the Universe are presented in Sec. 1.1.3. The results from the two previous subsections are combined in Sec. 1.1.4 to obtain the Friedmann equations describing the evolution of the Universe as a function of its constituents. Finally, definitions of times and distances that will reappear throughout this thesis are presented in Sec. 1.1.5.

1.1.1 General Relativity

General Relativity is established as the theory of gravitational interactions in modern physics. It is an extensive topic and the subject of ongoing research. Therefore, this section presents

a condensed and simplified overview of the fundamental concepts required to describe an expanding Universe. The interested reader can find a detailed introduction to General Relativity in any of the numerous textbooks on the topic such as [11; 12; 13; 14].

- **Metric**: The metric[a] $g_{\mu\nu}$ is a rank two symmetric tensor which encodes information about the geometry. Given a coordinate system $\{x^\mu\}$, the metric relates infinitesimal coordinate displacements dx^μ to line segments in the corresponding geometry ds^2 through the expression[b]:

$$ds^2 = g_{\mu\nu} dx^\mu dx^\nu. \tag{1.1.1}$$

  This line displacement, or *interval*, is an invariant quantity (independent of the choice of coordinates). In Einstein's special relativity, the geometry is described by the Minkowski metric[c]:

$$ds^2 = -c^2 dt^2 + dx^2 + dy^2 + dz^2. \tag{1.1.2}$$

  with c the speed of light in vacuum $c \approx 2.998 \times 10^8$ m/s. The interval ds defines the *causal structure* of spacetime. In particular, the sign of the interval has the following interpretation:

  * $ds^2 < 0$ (*timelike interval*): There exists a coordinate system such that $ds^2 = -c^2 dt^2$. Proper time can then be defined as:

$$d\tau = \frac{1}{c}\sqrt{-ds^2} = \frac{1}{c}\sqrt{-g_{\mu\nu} dx^\mu dx^\nu}. \tag{1.1.3}$$

    Proper time gives the time measured by a clock that is moving along a timelike path. Massive particles move along timelike trajectories.
  * $ds^2 > 0$ (*spacelike interval*): There exists a coordinate system such that $dt = 0$.
  * $ds^2 = 0$ (*null interval*). Massless particles move along null trajectories at the speed of light.

  The metric plays a fundamental role in General Relativity since the geometry of spacetime encodes information about matter and energy. Mass distributions curve the spacetime, and free bodies follow *geodesics* (paths of minimum length) in this geometry.

[a] Greek letters μ, ν, σ... denote spacetime indices (0,1,2,3), and roman letters i, j, k... denote space indices (1,2,3).

[b] Repeated upper and lower indices are summed over, following Einstein's summation convention [15].

[c] We adopt the signature $(-+++)$.

- **Geodesics**: Paths of minimum length in a given geometry obey the equation:

$$\frac{\mathrm{d}^2 x^\mu}{\mathrm{d}r^2} = -\Gamma^\mu_{\nu\sigma}\frac{\mathrm{d}x^\nu}{\mathrm{d}r}\frac{\mathrm{d}x^\sigma}{\mathrm{d}r}, \tag{1.1.4}$$

  where r as in affine parameterization[a]. For timelike trajectories it is common to use the proper time as an affine parameter. $\Gamma^\mu_{\nu\sigma}$ are the Christoffel symbols, defined as:

$$\Gamma^\mu_{\nu\sigma} = \frac{1}{2}g^{\mu\eta}\left(\frac{\partial g_{\eta\sigma}}{\partial x^\nu} + \frac{\partial g_{\nu\eta}}{\partial x^\sigma} - \frac{\partial g_{\sigma\nu}}{\partial x^\eta}\right). \tag{1.1.5}$$

- **Curvature**: Intrinsic curvature[b] is defined in a coordinate independent way through the *Riemann* or *curvature tensor*:

$$R^\delta_{\mu\nu\sigma} \equiv \partial_\nu\Gamma^\delta_{\mu\sigma} - \partial_\sigma\Gamma^\delta_{\mu\nu} + \Gamma^\eta_{\mu\sigma}\Gamma^\delta_{\eta\nu} - \Gamma^\eta_{\mu\nu}\Gamma^\delta_{\eta\sigma}. \tag{1.1.6}$$

  The *Ricci tensor* and *Ricci scalar* are defined through contractions[c] of the Riemann tensor:

$$R_{\mu\nu} \equiv R^\sigma_{\mu\sigma\nu}, \qquad R \equiv R^\mu_\mu. \tag{1.1.8}$$

- **Einstein's field equations**: The *Einstein tensor* $G_{\mu\nu}$ is defined as a function of the Ricci tensor and scalar. *Einstein's field equations* provide a linear relation between the Einstein tensor and the stress-energy tensor $T_{\mu\nu}$ which describes matter and energy distributions:

$$G_{\mu\nu} \equiv R_{\mu\nu} - \frac{1}{2}g_{\mu\nu}R = \frac{8\pi G}{c^4}T_{\mu\nu}. \tag{1.1.9}$$

  where G is the universal gravitational constant $G \approx 6.67408 \times 10^{-11}$ $\mathrm{m^3 kg^{-1} s^{-2}}$. Secs. 1.1.2 and 1.1.3 will focus respectively on the left and right-hand sides of Einstein's equations (1.1.9) for a homogeneous, isotropic, expanding Universe.

1.1.2 The Friedmann-Lemaître-Robertson-Walker Metric

- **Fundamental observers**: The cosmological principle states that:

  The Universe is homogeneous and isotropic on large scales.

[a] An affine parameterization of a curve is defined as a parameterization for which the length of the tangent vector remains constant along the curve.

[b] Intrinsic curvature refers to curvature that is a property of the geometry itself, as opposed to curvature that depends on how a surface is embedded in a space of higher dimensions. In General Relativity, matter only creates intrinsic curvature.

[c] The contraction of two indices μ, ν of a tensor $T_{\mu\nu}$ is defined as:

$$T^\mu_\mu \equiv g^{\mu\nu}T_{\mu\nu}. \tag{1.1.7}$$

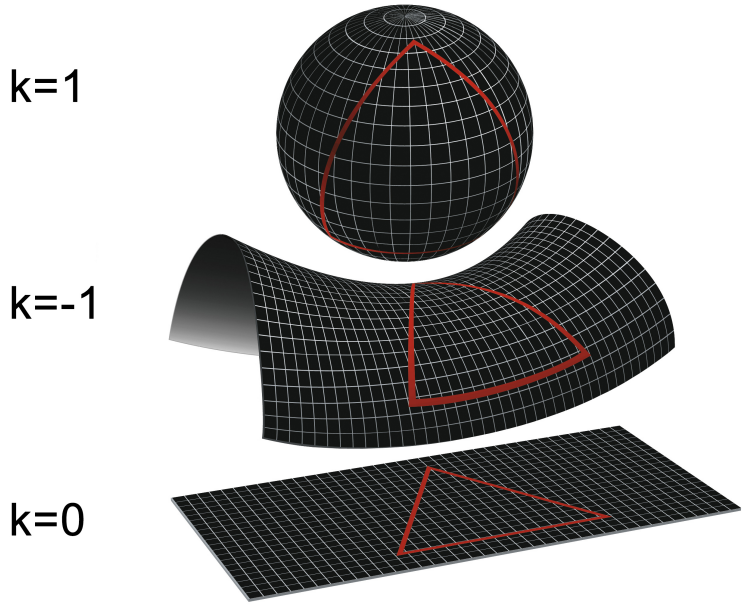

Figure 1.1: Illustration of the spatial shape of the Universe for all three possible values of k. Image credit: NASA / WMAP Science Team.

The cosmological principle only applies to certain observers: *Fundamental observers* are defined as observers at rest with respect to the *cosmological fluid*.

- **FLRW metric**: Isotropy and homogeneity allow the metric to be expressed as:

$$ds^2 = -c^2dt^2 + a^2(t)\left[\frac{dr^2}{1-Kr^2} + r^2\left(d\theta^2 + \sin^2\theta d\phi^2\right)\right], \tag{1.1.10}$$

where spherical coordinates have been adopted. This is called the *Friedmann-Lemaître-Robertson-Walker metric*, henceforth also referred to as FLRW metric. The spatial coordinates in this metric are *comoving coordinates* related to the physical coordinates by $x^i_{\rm ph} = a(t)x^i_{\rm com}$ where the function $a(t)$ is known as the scale factor. The parameter K is called the curvature parameter, since it is proportional to the Ricci scalar for the spatial part of this metric (${}^{(3)}R = 6K/a^2$). Therefore, its sign $k \equiv |K|/K$ defines the sign of the spatial curvature (Fig.1.1):

  - $k = 1$ (positive curvature) corresponds to a spherical or closed Universe.
  - $k = -1$ (negative curvature) corresponds to a hyperbolic Universe.
  - $k = 0$ (no curvature) corresponds to a spatially flat Universe.

The metric (1.1.10) can be written in a different, more compact way, that will be used throughout the rest of this introduction:

$$ds^2 = -c^2dt^2 + a^2(t)\left[d\chi^2 + S^2(\chi)\left(d\theta^2 + \sin^2\theta d\phi^2\right)\right], \tag{1.1.11}$$

where χ is the *comoving radial distance*, and $S(\chi)$ is given by:

$$S(\chi) = \begin{cases} K^{-1/2} \sin\left(K^{1/2}\chi\right) & : \ k = 1, \\ \chi & : \ k = 0, \\ |K|^{-1/2} \sinh\left(|K|^{1/2}\,\chi\right) & : \ k = -1. \end{cases} \tag{1.1.12}$$

- **Low redshift expansion** A Taylor series expansion of the scale factor for a time t close to the present time t_0[a] yields:

$$\begin{aligned} a(t) &= a(t_0) + \dot{a}(t_0)(t-t_0) + \frac{\ddot{a}(t_0)}{2}(t-t_0)^2 + \frac{\dddot{a}(t_0)}{6}(t-t_0)^3 + O(t-t_0)^4, \\ &\equiv a_0 \left[1 + H_0(t-t_0) - \frac{q_0 H_0^2}{2}(t-t_0)^2 + \frac{j_0 H_0^3}{6}(t-t_0)^3 + O(t-t_0)^4\right], \end{aligned} \tag{1.1.13}$$

where $a_0 \equiv a(t_0)$ and $\dot{a} \equiv da/dt$. The Hubble, deceleration[b] and jerk parameters are defined as:

$$H(t) \equiv \frac{\dot{a}(t)}{a(t)}, \tag{1.1.14a}$$

$$q(t) \equiv -\frac{\ddot{a}(t)a(t)}{\dot{a}^2(t)}, \tag{1.1.14b}$$

$$j(t) \equiv \frac{\dddot{a}(t)a^2(t)}{\dot{a}^3(t)}. \tag{1.1.14c}$$

Note that, while in Eq. (1.1.13) these parameters have been defined for the present time, their definitions have been generalized to an arbitrary time in Eqs. (1.1.14a) to (1.1.14c).

- **Cosmological redshift**: The frequency of a photon emitted at a time t_e and received at the present time, decreases as it propagates through an expanding Universe as:

$$\frac{\nu(t_e)}{\nu(t_0)} = \frac{a(t_0)}{a(t_e)} \equiv 1 + z. \tag{1.1.15}$$

where z is called the redshift. The scale factor is commonly normalized as $a_0 = 1$, which means redshift and scale factor are related by:

$$a = \frac{1}{1+z}. \tag{1.1.16}$$

As a consequence, redshift can be used as an alternative parameterization of the scale factor, and therefore time, for open and flat universes.

[a] The subindex 0 will be used to refer to the present time throughout the rest of this work.

[b] The name deceleration parameter is misleading: It was established when the Universe was thought to be decelerating, a notion that changed with the discovery of the accelerated expansion of the Universe [16; 17].

1.1.3 Components of the Universe

The FLRW metric that describes an expanding, homogeneous and isotropic Universe can be used to calculate the left-hand side of Einstein's equations (1.1.9). We now introduce the different components of the Universe that determine the right-hand side of Eq. (1.1.9).

- **Stress-energy tensor**: The stress-energy or energy-momentum tensor is a rank two symmetric tensor that describes the distributions of mass, energy and momentum of a fluid. For a perfect fluid in a homogeneous and isotropic Universe, the stress-energy tensor takes the form:

$$T^{\mu\nu} = (\rho + \frac{p}{c^2})u^\mu u^\nu + pg^{\mu\nu}, \tag{1.1.17}$$

  where ρ is the mass density, and p the pressure. It is frequently convenient to work on a reference frame comoving with the fluid at every point $\mathbf{u} = (c, 0, 0, 0)$, such as that of a fundamental observer, in which case the energy-momentum tensor takes the form:

$$T^\mu_\nu = \begin{pmatrix} -\rho c^2 & 0 & 0 & 0 \\ 0 & p & 0 & 0 \\ 0 & 0 & p & 0 \\ 0 & 0 & 0 & p \end{pmatrix}. \tag{1.1.18}$$

- **Conservation equation:** An important property of the energy-momentum tensor is that it satisfies the following conservation equation:

$$\nabla_\mu T^{\mu\nu} = \partial_\mu T^{\mu\nu} + \Gamma^\mu_{\mu\sigma} T^{\sigma\nu} + \Gamma^\nu_{\mu\sigma} T^{\mu\sigma} = 0, \tag{1.1.19}$$

  where ∇ is the *covariant derivative*. This conservation equation for an FLRW metric leads to:

$$\dot{\rho} + 3H(\rho + \frac{p}{c^2}) = 0. \tag{1.1.20}$$

  The equation of state of a given component is defined as the relation between its density and pressure:

$$p = w\rho c^2, \tag{1.1.21}$$

  where w is called equation of state parameter. Assuming a constant equation of state ($\dot{w} = 0$), Eq. (1.1.21) in combination with Eq. (1.1.20) provides an expression for the time evolution of the mass density of a given component as a function of the scale factor that depends only on its equation of state parameter:

$$\rho \propto a^{-3(1+w)}. \tag{1.1.22}$$

- **Components of the Universe**: The different components can be defined by their equation of state (1.1.21):
  - **Matter**: The term matter includes all pressureless components ($w = 0$), which include dark matter and baryonic matter, consisting of baryons and leptons whose rest mass energy is well above the thermal energy of the cosmological fluid, which will be described in the following section.
  - **Relativistic Species**: Frequently called radiation, consist of photons and particles of rest mass energy well below the thermal energy of the cosmological fluid. Their equation of state is $w = 1/3$.
  - **Dark Energy**: A cosmological constant, also called vacuum energy ($w = -1$), or some form of *dark energy* ($w \approx -1$), is required to explain the observed accelerated expansion of the Universe. Note that a cosmological constant in the stress-energy tensor is equivalent to a term $\Lambda g_{\mu\nu}$ on the left-hand side of Einstein's equations (1.1.9), with Λ a constant.

1.1.4 The Friedmann Equations

- **Friedmann equations**: Using the metric (1.1.11) and the stress-energy tensor (1.1.18), Einstein's equations (1.1.9) yield the cosmological field equations, or Friedmann equations:

$$\frac{\ddot{a}}{a} = -\frac{4\pi G}{3}\left(\rho + \frac{3p}{c^2}\right), \tag{1.1.23a}$$

$$H^2 = \frac{8\pi G}{3}\rho - \frac{Kc^2}{a^2}. \tag{1.1.23b}$$

- **Density parameters**: Eq. (1.1.23b) can be expressed in a more compact way. The critical density is defined as:

$$\rho_{\text{crit}} = \frac{3H^2}{8\pi G}. \tag{1.1.24}$$

The dimensionless density parameters are formed as the ratio between the mass density and the critical density of a given component:

$$\Omega_I \equiv \frac{\rho_I}{\rho_{\text{crit}}}, \tag{1.1.25}$$

Model	Dominant component	Scale factor
Einstein-de Sitter Universe	Ω_m	$a(t) = \left(\frac{3}{2}H_0 t\right)^{2/3}$
Radiation-only Friedmann Universe	Ω_r	$a(t) = (2H_0 t)^{1/2}$
Milne Universe	Ω_k	$a(t) = H_0 t$
de Sitter Universe	Ω_Λ	$a(t) = e^{H_0 t}$

Table 1.1: Scale factor dependence of the Universe when it is dominated by a single component (Ω_I is unity for the dominant component, and zero for the rest).

where the subindex I refers to matter m, radiation r or a cosmological constant Λ. Similarly, the curvature density parameter is defined as:

$$\Omega_k \equiv -\frac{Kc^2}{a^2H^2}. \tag{1.1.26}$$

Using these definitions Eq. (1.1.23b) can be restructured as:

$$1 = \Omega_m + \Omega_r + \Omega_\Lambda + \Omega_k. \tag{1.1.27}$$

Or, equivalently, using the time dependence of the density for each component (Eq. 1.1.22):

$$H(z)^2 = H_0^2\left[\Omega_{m,0}(1+z)^3 + \Omega_{r,0}(1+z)^4 + \Omega_{\Lambda,0} + \Omega_{k,0}(1+z)^2\right]. \tag{1.1.28}$$

This equation relates the time evolution of the scale factor $a(t)$ to the present day density parameters of the Universe. Note that the expansion history $H(z)$ depends only on four independent parameters through the constraint (1.1.27). The scale factor dependence of a universe dominated by a single component is summarized in table 1.1.

- **Age of the Universe**: The age of the Universe can be determined once the values of four parameters H_0, $\Omega_{m,0}$, $\Omega_{k,0}$ and $\Omega_{r,0}$ are specified. The estimation of the values of these parameters using different observations is a central aim of this thesis. However, for the purpose of this introduction, approximate values that are not far from any of the measurements will be used:

$$H_0 = 70\ \text{km s}^{-1}\text{Mpc}^{-1}, \qquad \Omega_{m,0} = 0.3, \qquad \Omega_{k,0} = 0, \qquad \Omega_{r,0} = 10^{-4}. \tag{1.1.29}$$

Note that these values imply that the Universe is flat, which we know to be true to a very high precision through observations. The age of the Universe can be estimated from these parameters:

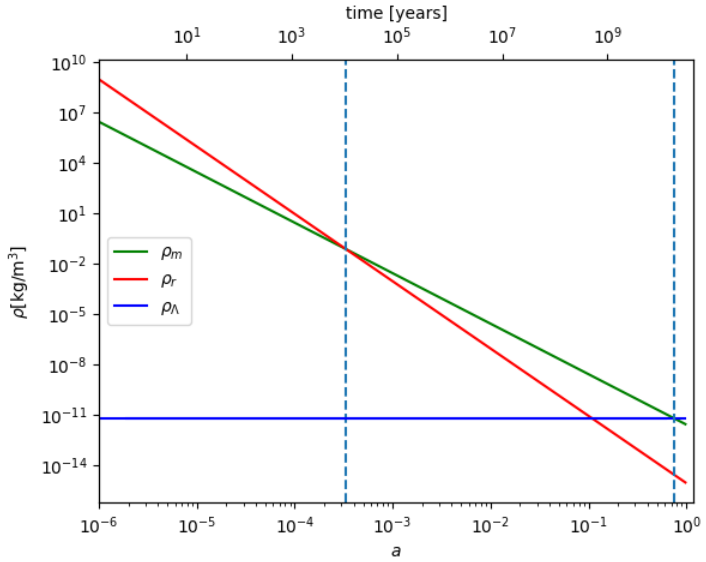

Figure 1.2: Time evolution of the density of matter, radiation and vacuum energy using the values (1.1.29). Vertical lines represent matter-radiation equality (left) and dark energy-matter equality (right). This figure illustrates the coincidence problem: dark energy becomes the dominant component at very recent times.

$$t_0 = \int_0^{t_0} \mathrm{d}t = \int_0^1 \frac{\mathrm{d}a}{aH(a)} \approx 13.5 \times 10^9 \text{years}. \tag{1.1.30}$$

The observed age and present-day components of the Universe raise two issues that have not been solved to date. One of the possible explanations for these issues is resorting to *anthropic* arguments (see [18]), but it is also possible that they are a consequence of problems with the ΛCDM model.

- *Coincidence problem*: Dark energy becomes the dominant component at very recent times ($z = (\Omega_{\Lambda,0}/\Omega_{m,0})^{1/3} - 1 \approx 0.33, t \approx 9.8 \times 10^9$years), as illustrated in Fig. 1.2.
- *Synchronicity problem*: The dimensionless age of the Universe defined as $t_0 H_0$ is extremely close to one:

  $$t_0 H_0 \approx 0.96. \tag{1.1.31}$$

  There is no reason for this number to be so close to unity. In fact, that has not been the case through the evolution of the Universe [19].

1.1.5 Times and Distances in Cosmology

- **Conformal time**: A transformation $\mathrm{d}\eta \equiv \mathrm{d}t/a(t)$, where η is called conformal time, reshapes the FLRW metric (Eq. 1.1.11) into:

$$ds^2 = a^2(t)\left[-c^2 d\eta^2 + d\chi^2 + S^2(\chi)\left(d\theta^2 + \sin^2\theta d\phi^2\right)\right]. \tag{1.1.32}$$

- **Hubble radius**: It is defined as:

$$r_H = \frac{c}{H(t)}. \tag{1.1.33}$$

The Hubble radius of Eq. (1.1.33) is a physical quantity. A comoving radius can be defined as $r_{H,\mathrm{com}} = r_H/a(t)$. The comoving Hubble radius decreases with time for an accelerated expansion, which is the case during inflation and in the present, and increases with time for a decelerated expansion, such as a matter or a radiation dominated Universe. A region of comoving size R is inside or outside the Hubble radius if the ratio $R/r_{H,\mathrm{com}}$ is smaller or larger than unity respectively.

- **Particle horizon**: It is defined as the distance light could have travelled since the beginning of the Universe up to a given time t:

$$r_{\mathrm{ph}} \equiv \int_0^t \frac{c\,\mathrm{d}t'}{a(t')} = c\eta(t) - c\eta(0). \tag{1.1.34}$$

Particles separated by a distance larger than the particle horizon at a given time are not in causal contact, i.e. they cannot have exchanged information.

- **Event horizon**: Similarly to the particle horizon, the event horizon describes the distance light will be able to travel in the future from a given time:

$$r_{\mathrm{eh}} \equiv \int_t^\infty \frac{c\,\mathrm{d}t'}{a(t')} = c\eta(\infty) - c\eta(t). \tag{1.1.35}$$

The event horizon provides a measure of causally connected distances: If a particle crosses our event horizon, it goes out of causal contact with us.

- **Luminosity distance**: The luminosity distance is useful for sources whose luminosity L is known. Such objects are known as *standard candles*. In Euclidean geometry, flux and luminosity for a source at a distance d are related by $F = L/(4\pi d^2)$. In a FLRW metric, the equivalent expression is:

$$F = \frac{L}{4\pi S(\chi)^2(1+z)^2}. \tag{1.1.36}$$

Therefore, analogously to the Euclidean case, The luminosity distance is defined as:

$$d_L \equiv S(\chi)(1+z). \tag{1.1.37}$$

Observing the flux of a standard candle constrains the luminosity distance of such a source, which depends on cosmological parameters.

- **Angular diameter distance**: While the luminosity distance is useful for objects of known luminosity, the angular diameter distance is useful for objects of known physical size, known as *standard rulers*. In Euclidean space, the angle subtended by an object of size L at a distance d is $\Delta\theta = L/d$. Similarly, the angular diameter distance is defined as:

$$d_A \equiv \frac{L}{\Delta\theta}. \tag{1.1.38}$$

For an object at redshift z in a FLRW metric, the angular diameter distance can be related to the comoving radial distance through:

$$d_A = \frac{S(\chi)}{1+z}. \tag{1.1.39}$$

1.2 History of the Universe

This section applies the concepts introduced in the previous section to study the thermal history of the Universe and the evolution of perturbations to the homogeneous background. The discussion follows a chronological order: It starts with an introduction to inflation, which is a theory of the Universe before the Big Bang (i.e. before the matter and radiation that we observe today were created). After summarizing the essential elements of the theory in Sec. 1.2.1, Sec. 1.2.2 discusses the formation of perturbations that evolve from quantum fluctuations. Subsequently, the analysis focuses on the Big Bang Universe: Sec. 1.2.3 explains the different stages of the thermal history of the Universe, while Sec. 1.2.4 presents an overview of the evolution of perturbations to the homogeneous background. Particular emphasis is placed on the theory of inflation since it will be one of the central topics of this thesis.

Detailed discussions about the concepts reviewed in this subsection can found in the literature. In particular, [9] presents a detailed discussion of inflation, the thermal history of the Universe is explained in [7; 8], and for a clear discussion of cosmological perturbation theory, [6] and [10] are recommended.

1.2.1 The Theory of Inflation

The theory of inflation relies on near-exponential expansion in the early Universe. Inflation is widely accepted as the theory of the early Universe since it solves three inconsistencies based on observations: The problems of the horizon, flatness, and relics. More importantly, it predicts the formation of structure in the Universe that agrees to excellent accuracy with observations.

- **The three problems**: The problem of horizons, originates from the Cosmic Microwave Background radiation (CMB), the afterglow from the Big Bang, emitted at $z \approx 1100$ that will be reviewed later in this introduction. From Eq. (1.1.34), the physical particle horizon at the time the CMB radiation was emitted is $r_{\rm ph} \approx 0.24$ Mpc, which corresponds to an observed angle $\theta \approx 1^{\rm o}$. This raises the question of why the Universe is homogeneous and isotropic on large scales (Fig. 1.3). The problem of flatness is a problem of fine tuning. From observations of the CMB and Baryon Acoustic Oscillations (BAO, a characteristic distance scale in the observed distribution of galaxies that will be detailed in the following section) the Universe is observed to be very nearly spatially flat ($|\Omega_{k,0}| < 0.005$) [21]. The curvature density parameter (Eq. 1.1.26) $\Omega_k \propto (aH)^{-2}$ increases with time for matter and radiation dominated universes. Therefore, our Universe requires $|\Omega_k| < O(10^{-60})$ at the Planck time ($t \approx 10^{-44}$ s). This value can only be obtained through an extremely fine tuning (or perhaps again using anthropic arguments). Finally, the problem of relics is a consequence of the formation of magnetic monopoles predicted by Grand Unified

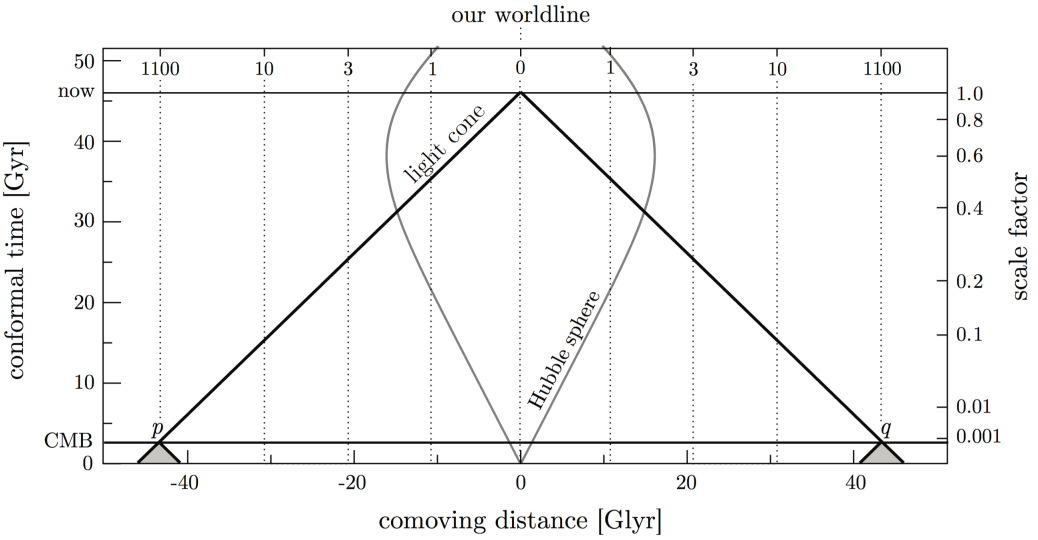

Figure 1.3: Illustration of the problem of horizons. Image credit: [20]

Theories (GUT): If the Universe experienced a GUT phase transition, one monopole would have formed inside each particle horizon. Without inflation, and for a GUT transition taking place at around 10^{15} GeV, this would correspond to an abundance of approximately one magnetic monopole per nucleon today. Since this is not the case (magnetic monopoles have not been observed at all), a mechanism that explains the lack of monopoles is required if the formation of Standard Model particles through symmetry breaking in a GUT is assumed.

- **Definition of inflation**: The simplest definition of inflation is as a phase of accelerated expansion:

$$\ddot{a} > 0. \tag{1.2.1}$$

Therefore, the comoving Hubble radius[a] $(aH)^{-1}$ decreases with time, and comoving scales become bigger than the horizon ('leave' the horizon) during inflation. As a consequence inflation solves the problem of horizons: The light cones of different points in the CMB intersected before the 'Big Bang'. In the context of inflation, the Big Bang is not understood as the beginning of the Universe, but as the point of transition between an inflationary universe, and the Universe of increasing comoving Hubble radius (Fig. 1.4). The condition (1.2.1) is equivalent to:

[a] In order to simplify the notation, the rest of this chapter uses units such that $c = \hbar = k_B = 1$ where $\hbar$ is the *Planck* constant and k_B is the Boltzmann constant.

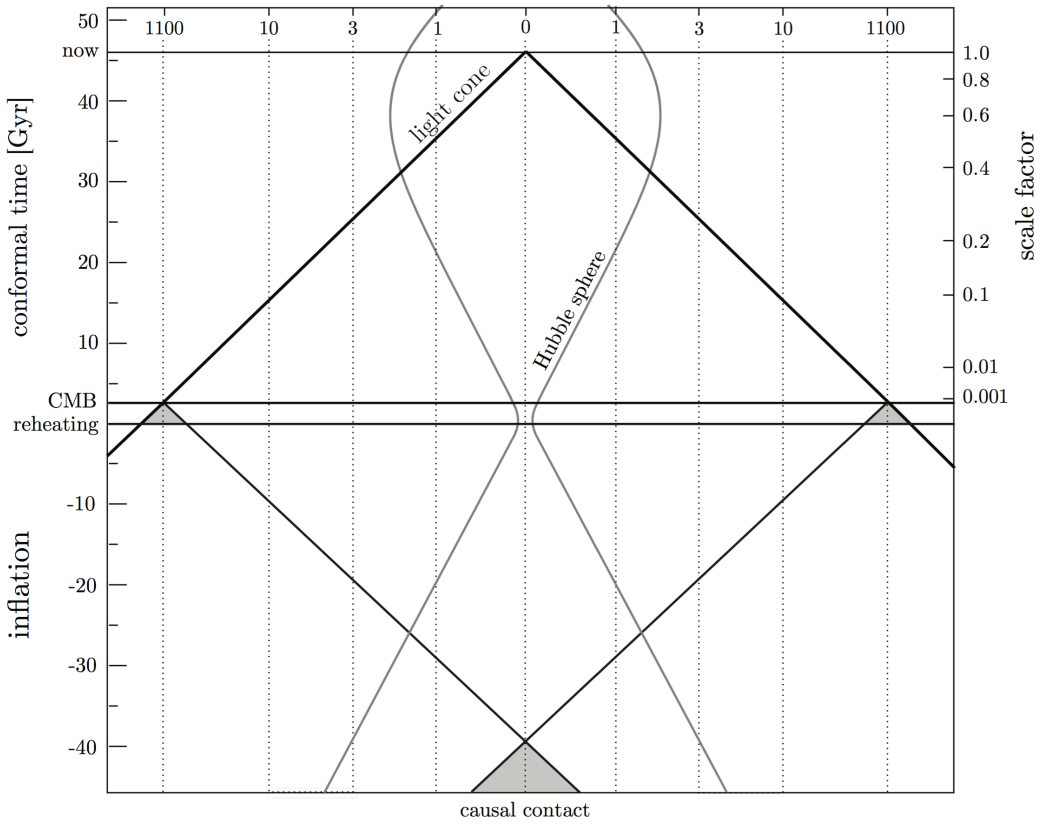

Figure 1.4: How inflation solves the horizons problem. Image credit: [20]

$$-\frac{\dot{H}}{H^2} < 1, \tag{1.2.2}$$

which, in the limiting case, indicates that $|\dot{H}| << H^2$ and the expansion is nearly exponential $a \propto e^{Ht}$. Assuming that during this period the Universe is dominated by a component with a constant equation of state, the Friedmann equation (1.1.23a) and the condition (1.2.2) can be combined to obtain:

$$\rho + 3p < 0. \tag{1.2.3}$$

Since the energy density is assumed to be positive, inflationary expansion requires negative pressure (i.e. a violation of the strong energy condition). Note how this solves the problem of flatness: During inflation $\Omega_k \propto (aH)^{-2}$ decreases with time. Therefore, an order unity initial value of $|\Omega_k|$ can be brought down to negligible values. Inflation solves the problem of relics such as magnetic monopoles since their density can be diluted away during inflation.

- **Mechanisms driving inflation**: Most models of inflation assume that the inflationary Universe is dominated by one or more scalar fields. Furthermore, it is usually assumed that these fields are spatially homogeneous, under the assumption that any inhomogeneities are quickly smoothed out by the rapid increase of the scale factor. The most general Lorentz invariant Lagrangian satisfying physical requirements (to be more concrete, that have a particle interpretation after quantization) for N fields with a standard kinetic term can be written as:

$$\mathcal{L} = -\sum_{m,n}^{N} \partial^{\mu}\phi_m \partial_{\mu}\phi_n - V(\phi_1, ..., \phi_N). \tag{1.2.4}$$

For a single, homogeneous field ($N = 1$) on a Friedmann-Lemaître-Robertson-Walker (FLRW) spacetime, this leads to:

$$\ddot{\phi} + 3H\dot{\phi} + \frac{\mathrm{d}V}{\mathrm{d}\phi} = 0. \tag{1.2.5}$$

From the Lagrangian (1.2.4), using its invariance under space-time translation, the energy-momentum tensor can be obtained through Noether's theorem [22];

$$T_{\mu\nu} = -2\frac{\partial \mathcal{L}}{\partial g^{\mu\nu}} + g_{\mu\nu}\mathcal{L} = -\sum_{n} \partial_{\nu}\phi_n \partial_{\mu}\phi_n + g_{\mu\nu}\left[\frac{1}{2}\sum_{n} \partial^{\alpha}\phi_n \partial_{\alpha}\phi_n + V(\phi_1, ..., \phi_N)\right]. \tag{1.2.6}$$

Thus, the energy density and pressure for a canonically normalized homogeneous field are:

$$\rho = \frac{1}{2}\sum_{n} \dot{\phi}_n^2 + V\,, \qquad p = \frac{1}{2}\sum_{n} \dot{\phi}_n^2 - V\,. \tag{1.2.7}$$

- **Slow-roll inflation**: Eq. (1.2.7) indicates that negative pressure can be achieved with a sufficiently slowly varying scalar field[a]. This can be realized by an inflaton field that dominates the energy content of the Universe during this epoch and slowly 'rolls down' a hill in the potential (Fig. 1.5). For a single scalar field, slow-roll inflation requires the limiting case of the condition (1.2.2) (exponential inflation, $|\dot{H}| << H^2$). Using the Friedmann equation (1.1.23a), combined with the energy density and pressure of a homogeneous canonical scalar field (1.2.7) and its evolution equation (1.2.5), this condition can be expressed in terms of the field and its potential:

$$3H\dot{\phi} \approx -\frac{\mathrm{d}V}{\mathrm{d}\phi} \Leftrightarrow |\ddot{\phi}| << 3H|\dot{\phi}|. \tag{1.2.8}$$

[a]For simplicity, single field inflation is assumed throughout the rest of the present chapter.

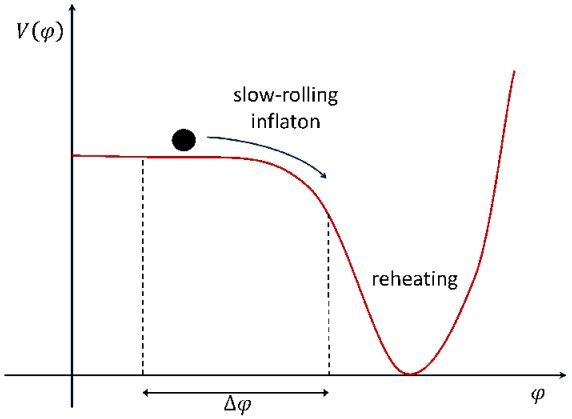

Figure 1.5: Toy example of a slow-roll potential. Inflation takes place in the flat region of the potential. Once the slope becomes steep enough, slow-roll regime breaks and inflation ends. The inflaton then oscillates around the minimum of the potential, starting the process of reheating. Image credit: [23].

These are called flatness conditions, and they can be formulated in a more compact form defining the *potential slow roll parameters*:

$$\epsilon_V \equiv \frac{M_P^2}{2}\left(\frac{1}{V}\frac{\mathrm{d}V}{\mathrm{d}\phi}\right)^2, \qquad \eta_V \equiv \frac{M_P^2}{V}\left|\frac{\mathrm{d}^2V}{\mathrm{d}\phi^2}\right|, \tag{1.2.9}$$

where M_P is the reduced Planck mass[a]. The flatness conditions are then equivalent to requiring $\epsilon_V << 1$ and $\eta_V << 1$. Equivalently, *Hubble slow-roll parameters* are defined as:

$$\epsilon_H \equiv \frac{\dot{\phi}^2}{2M_P^2H^2}, \qquad \eta_H \equiv -\frac{\dot{\epsilon_H}}{H\epsilon_H}. \tag{1.2.10}$$

- **Duration of inflation** While inflation could last for an arbitrarily long time, it is necessary to ensure inflation lasts enough to allow the scale corresponding to the observable Universe today H_0^{-1} to leave the Hubble horizon. The number of e-folds of inflation after the scale[b] k^{-1} has left the horizon is defined as:

$$N(k) = \log\frac{a_{\mathrm{end}}}{a_k}, \tag{1.2.11}$$

where a_k and a_{end} are the values of the scale factor when the scale k^{-1} leaves the horizon and when inflation ends respectively. Since the scale k leaves the horizon when $k^{-1} = (aH)^{-1}$, for nearly constant H the number of e-folds between two scales is:

[a]The reduced Planck mass is $M_P \equiv \sqrt{\hbar c/(8\pi G)}$, which for our choice of units is simplified to $M_P \equiv (8\pi G)^{-1/2}$.
[b]Throughout this section, scales of size L are often defined by their size in Fourier space $k = 1/L$.

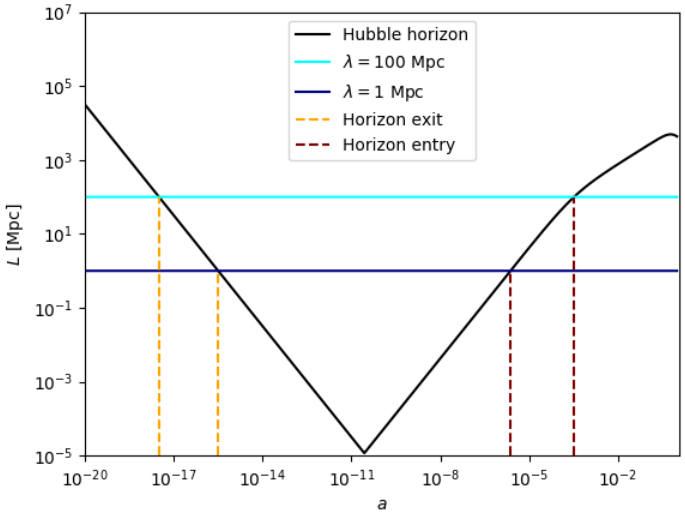

Figure 1.6: Evolution of the comoving Hubble horizon. The Hubble horizon (black) decreases during inflation and then starts increasing after inflation. Comoving scales (blue) exit the horizon during inflation, becoming superhorizon scales, and later reenter. When dark energy becomes the dominant component, the horizon starts decreasing again.

$$N(k_2) - N(k_1) = \log \frac{a_{k_1}}{a_{k_2}} = \log \frac{k_1}{k_2}. \tag{1.2.12}$$

The number of e-folds required to ensure that the scale H_0^{-1} corresponding to the observable Universe today was inside the Hubble radius during inflation depends on the choice of models of both inflation and reheating (a process that will be discussed later in this section). Assuming instantaneous transition between inflation and reheating, the minimum number of e-folds required is [24]:

$$N = 56 - \frac{2}{3} \log \left(\frac{10^{16}\ \text{GeV}}{\rho_*^{1/4}} \right) - \frac{1}{3} \log \left(\frac{10^9\ \text{GeV}}{T_{\text{rh}}} \right), \tag{1.2.13}$$

where ρ_* is the energy density at the end of inflation, and T_{rh} is the reheat temperature that will be defined in more detail in the following subsection. Under these conditions, the minimum number of e-folds of inflation required is $N \sim 60$. Instead of using the scale H_0^{-1}, it is common to use a pivot scale k_0 to define the amount of inflation required.

1.2.2 The Primordial Curvature Perturbation

The prediction of fluctuations that can eventually evolve into the large-scale structure we observe today is the most important consequence of the theory of inflation. During inflation, the initial

conditions for the study of cosmological fluctuations and the formation of structure in the Universe are set. The previous subsection introduced the concept of horizon exit: During inflation, the horizon is decreasing, and comoving scales leave the horizon. After inflation, these scales reenter the horizon as it increases with time (Fig.1.6). Superhorizon scales cannot undergo gravitational collapse, so their evolution is straightforward. Only after entering the horizon can gravitational collapse occur.

- **Perturbations to the FLRW metric**: The most general perturbation to the FLRW metric in conformal time (1.1.32) can be expressed as:

$$ds^2 = a^2(\eta)\left\{-(1+2A)d\eta^2 - 2B_i d\eta dx^i + \left[(1+2D)\delta_{ij} + 2E_{ij}\right] dx^i dx^j\right\}. \quad (1.2.14)$$

  In this equation, A and D are scalar fluctuations, B_i is a vector fluctuation, and E_{ij} is a tensor fluctuation. These fluctuations can be decomposed in an SVT decomposition consisting of scalar, divergenceless vector, and traceless tensor components [25]. The SVT decomposition is particularly useful in cosmology, since at linear, order scalar, vector and tensor modes evolve independently. Throughout the rest of this introduction, we focus on scalar perturbations, since vector perturbations decay with the expansion of the Universe [6], and primordial tensor perturbations have not been detected at the moment of writing this thesis. Tensor perturbations will briefly be discussed at the end of this section. The symmetries of the Universe allow us to fix two of the four scalar degrees of freedom through the choice of a coordinate system, often referred to as a choice of *gauge*. In the *Newtonian gauge*, the scalar parts of the vector and tensor perturbations B and E are set to zero. Redefining $\Psi \equiv A$ and $\Phi \equiv -D$ as the gravitational potentials, the metric is:

$$ds^2 = a^2(\eta)\left[-(1+2\Psi)d\eta^2 + (1-2\Phi)\delta_{ij}dx^i dx^j\right]. \quad (1.2.15)$$

  The difference between Ψ and Φ is anisotropic stress which will not be considered throughout this thesis ($\Psi = \Phi$).
- **The primordial curvature fluctuation**: The *primordial curvature fluctuation* ζ is a gauge invariant quantity [26] defined as:

$$\zeta = \Psi - \mathcal{H}\frac{\delta\rho}{\rho'}, \quad (1.2.16)$$

  where $x' \equiv \mathrm{d}x/\mathrm{d}\eta$ and $\mathcal{H} \equiv a'/a$. ζ parameterizes quantum fluctuations created during inflation and it is conserved on superhorizon scales. Thus, its value at horizon crossing $k = aH$ is conserved until scales reenter the horizon after inflation.

- **Quantum fluctuations** Primordial perturbations from inflation originate as the fluctuations of a quantum field. This subsection uses a different gauge called the *spatially-flat gauge*, which significantly simplifies the calculations. In this gauge $D = E = 0$ in Eq. (1.2.14), and as a consequence assuming single field inflation dominated by a scalar field ϕ:

$$\zeta = -\frac{\mathcal{H}}{\phi'}\delta\phi. \tag{1.2.17}$$

This field can be expanded as a homogeneous background field $\bar{\phi}$ and a perturbation $\delta\phi$:

$$\phi(t, \mathbf{x}) = \bar{\phi}(t) + \delta\phi(t, \mathbf{x}). \tag{1.2.18}$$

Note that ϕ is a classical field while $\delta\phi$ is treated as a quantum field and therefore promoted to an operator $\hat{\delta\phi}$. This expansion is only possible because the energy scale of inflation is much smaller than the Planck energy[a], therefore a quantum theory of gravity is not needed to describe ϕ, and it can instead be described by a quantum field $\hat{\delta\phi}$ imposed on a classical background $\bar{\phi}$. Perturbations to the metric in the spatially-flat gauge are suppressed relative to the perturbations to the inflaton field. It is convenient to redefine the fluctuation as $\hat{f} = a\hat{\delta\phi}$, so:

$$\phi(t, \mathbf{x}) = \bar{\phi}(t) + \frac{\hat{f}(t, \mathbf{x})}{a(t)}. \tag{1.2.19}$$

This expansion can be used in the Lagrangian (1.2.4). Minimization of the action to second order in the fluctuations leads to:

$$\hat{f}'' - \nabla^2\hat{f} - \frac{a''}{a}\hat{f} = 0, \tag{1.2.20}$$

where $\nabla^2 f \equiv \sum_i \partial_i^2 f$ is the spatial gradient of f. This is called the *Mukhanov-Sasaki equation* [27; 28; 29], and it describes the quantum fluctuations to the inflaton field. It is convenient to write this equation in Fourier space[b] and a de-Sitter cosmology:

$$\hat{f}_{\mathrm{k}}'' + \left(k^2 - \frac{2}{\eta^2}\right)\hat{f}_{\mathrm{k}} = 0. \tag{1.2.22}$$

After selecting the appropriate initial conditions, the solution to this equation is:

[a] The Planck energy is given by $E_p = \sqrt{\hbar c^5/G}$, which given our choice of units is simplified to $E_p = G^{-1/2}$.

[b] The convention used in this thesis for Fourier transforms is

$$f(\mathbf{x}) = \int \frac{\mathrm{d}^3 k}{(2\pi)^3} e^{-i\mathbf{k}\cdot\mathbf{x}} f_{\mathbf{k}}, \qquad f_{\mathbf{k}} = \int \mathrm{d}^3 x e^{i\mathbf{k}\cdot\mathbf{x}} f(\mathbf{x}). \tag{1.2.21}$$

$$\hat{f}_k(t) = \frac{e^{-ik\eta}}{\sqrt{2k}}\left(1 - \frac{i}{k\eta}\right). \tag{1.2.23}$$

- **Power spectrum**: The quantum operator $\hat{f}$ has zero expectation value $\langle\hat{f}\rangle = 0$ and variance:

$$\langle|\hat{f}|^2\rangle = \int \mathrm{d}\,(\log k)\,\frac{k^3}{2\pi^2}|f_k(t)|^2. \tag{1.2.24}$$

The *dimensionless power spectrum* is defined as:

$$\Delta^2_f(k,t) \equiv \frac{k^3}{2\pi^2}|f_k(t)|^2. \tag{1.2.25}$$

The dimensionless power spectrum of the primordial fluctuations can be obtained from Eq. (1.2.23):

$$\Delta^2_{\delta\phi}(k,t) = \left(\frac{H}{2\pi}\right)^2\left[1 + \left(\frac{k}{aH}\right)^2\right]. \tag{1.2.26}$$

On superhorizon scales, this is reduced to:

$$\Delta^2_{\delta\phi}(k,t) \xrightarrow[k<<aH]{} \left(\frac{H}{2\pi}\right)^2. \tag{1.2.27}$$

- **Primordial power spectrum**: The power spectrum of the primordial curvature perturbations is obtained from the power spectrum of primordial fluctuations on superhorizon scales (1.2.27) combined with Eq. (1.2.17), and evaluated at horizon crossing $k = aH$:

$$\Delta^2_\zeta = \frac{H^2}{\dot{\phi}^2}\Delta^2_{\delta\phi}\bigg|_{k=aH} = \frac{H^4}{4\pi^2\dot{\phi}^2}\bigg|_{k=aH}. \tag{1.2.28}$$

In the slow-roll regime, Δ^2_ζ can be expressed in terms of the Hubble slow-roll parameters (1.2.10):

$$\Delta^2_\zeta = \frac{1}{8\pi^2 M_P^2}\frac{H^2}{\epsilon_H}\bigg|_{k=aH}. \tag{1.2.29}$$

This quantity is called the *primordial power spectrum*. Because the right hand of Eq. (1.2.29) is evaluated at $k = aH$, it depends only on the wave number k, and both H and ϵ_H are slowly varying functions of time, the power spectrum is close to constant. Therefore, the primordial power spectrum can be parameterized as:

$$\Delta^2_\zeta = A_s\left(\frac{k}{k_0}\right)^{n_s-1}, \tag{1.2.30}$$

The parameter n_s, that quantifies deviations from a scale-invariant power spectrum (independent of k), is called the *spectral index*. The spectral index can be approximated to first order in the Hubble slow-roll parameters as:

$$n_s - 1 = -2\epsilon_H - \eta_H. \tag{1.2.31}$$

A similar expression can be found for the running of the spectral index, defined as the departure from a power-law spectrum $n_{\rm run} \equiv \mathrm{d}n_s/\mathrm{d}(\log k)$. The latest constraints from *Planck* are consistent with a vanishing value of the running of the spectral index [30].

- **Primordial gravitational waves**: The derivation of the primordial power spectrum for scalar perturbations can be repeated for tensor perturbations introduced at the beginning of this section, which are sourced by gravitational waves. The primordial spectrum of gravitational waves can be expressed as:

$$\Delta_t^2 = A_t \left(\frac{k}{k_0}\right)^{n_t - 1}. \tag{1.2.32}$$

The ratio of tensor to scalar fluctuations is defined as:

$$r = \frac{A_t}{A_s}. \tag{1.2.33}$$

This ratio can be related to the Hubble slow-roll parameters through $r = 16\epsilon_H$ [10]. Observations to date have not detected primordial tensor perturbations.

- **Reheating**: Reheating is a poorly understood process and the subject of ongoing research beyond the scope of this introduction (for a review, see [31]). This section presents a 'sketch' of the main processes that are accepted by most theories of reheating, but the details are highly model dependent and poorly understood: During inflation, all the energy in the Universe is contained in the scalar field driving inflation. When the inflaton potential becomes too steep for the slow-roll conditions to be satisfied, inflation ends. The inflaton then starts to oscillate around the minimum of the potential $V(\phi)$, losing its energy density via couplings to other particles. This leads to the inflaton decaying into particles. Because these particles are not in thermal equilibrium, they interact until reaching thermal equilibrium at a reheat temperature $T_{\rm rh}$ (mentioned in the previous section). Once this temperature is reached, the Universe is dominated by radiation in thermal equilibrium at a very high temperature ($T \gg 100$ GeV), starting the *Hot Big Bang*.

1.2.3 The Hot Big Bang

This section focuses on the main processes of the Big Bang Theory. We start this thermal history of the Universe with a 'primordial plasma' or 'thermal bath' of particles in thermal equilibrium at $T \gg 100$ GeV, since at those temperatures all Standard Model particles are relativistic, i.e. their typical energies are much greater than their masses $T \gg m$. Particles remain in thermal equilibrium with the primordial plasma while their interaction rate Γ is much bigger than the expansion rate H, where:

$$\Gamma = n\sigma v, \tag{1.2.34}$$

with n the number density of particles, σ the cross-section for the interaction, and v the average velocity of the particles. When $\Gamma \sim H$, those components are said to *decouple* from the primordial plasma. Particles in thermal equilibrium follow *Fermi-Dirac* and *Bose-Einstein* distributions[a] , which for non-relativistic particles leads to an exponential suppression of the number density, energy density and pressure with respect to relativistic particles. Therefore, the number density of the primordial plasma is dominated by relativistic species, and its temperature provides an alternative measurement of time, since in order to maintain a thermal distribution, the temperature of relativistic species must follow:

$$T \propto \frac{1}{a}. \tag{1.2.36}$$

We now study the main processes that take place through the thermal history of the Universe. Starting with a Universe formed by a primordial plasma at $T \gg 100$ GeV:

- **Baryogenesis**: An asymmetry between the amount of matter and anti-matter is produced. Such asymmetry is known to exist, but the mechanism causing it is not yet known [32; 33].
- **Electroweak Phase Transition** ($T \sim 100$ GeV): Particles receive mass through the Higgs mechanism.
- **QCD Phase transition** ($T \sim 150$ MeV): Quarks and gluons combine to form *baryons* and *mesons*. The latter are unstable and eventually decay, leaving only neutrons and protons.

At a temperature $T \sim 1$ MeV, the Universe is formed of radiation consisting of photons, neutrinos, electrons and positrons; and non-relativistic baryons. Three important events take place around this time:

[a] The distribution function for Fermi-Dirac and Bose-Einstein distributions is given by:

$$f(p) = \frac{1}{e^{\frac{E-\mu}{T}} \pm 1}, \tag{1.2.35}$$

where μ is the chemical potential, the + sign corresponds to fermions, and the − sign to bosons.

- **Neutrino decoupling**: The strength of weak interactions starts to decrease below $T \sim 100$ GeV since electroweak symmetry breaking leads to the gauge bosons $W^{\pm}$ and Z that mediate weak interactions receiving masses. At $T \sim 1$ MeV, the rate of weak interactions falls below the expansion rate. As a consequence, neutrinos, which only interact weakly with the cosmic fluid, decouple. Because neutrinos decouple while they are still relativistic, they maintain a Fermi-Dirac distribution with temperature $T_\nu \propto 1/a$. Weakly interactive massive particles with masses of typically $m \sim 10$ GeV, the main candidate for dark matter, could also freeze out when $T \sim 1$ MeV, thus their total number na^3 freezes, which can be derived from their Boltzmann equation.
- **Electron-positron annihilation** ($T \sim 0.5$ MeV): The temperature of the photons falls below the mass of the electron. Electron-positron pairs can no longer be formed from photon-photon collisions, so they start annihilating, and continue to do so until only a number of electrons equal to the number of protons is left. This process has the effect of boosting the temperature of the photons by a factor of $(11/4)^{1/3}$ relative to the neutrino temperature because of entropy conservation.
- **Big Bang nucleosynthesis**: It starts when the reaction rate for the reactions:

$$\mathrm{n} \leftrightarrow \mathrm{p} + \mathrm{e} + \bar{\nu}_\mathrm{e}, \tag{1.2.37a}$$

$$\mathrm{n} + \nu_\mathrm{e} \leftrightarrow \mathrm{p} + \mathrm{e}, \tag{1.2.37b}$$

  falls below the expansion rate. The neutron to proton ratio is then frozen at a value that is set by the temperature of freeze-out, with the exception of the decay of free neutrons, which continues until the temperature of the primordial plasma drops below $T \approx 1$ MeV, when deuterium production becomes important. After this, through a series of reactions, nearly every neutron left ends up locked into helium-4.

After these processes, photons and electrons are tightly coupled via Thomson scattering and electrons and protons are tightly coupled via Coulomb interactions. The net effect is that the primordial plasma consists of photons, electrons and protons, until recombination.

- **Recombination**[a] ($z \approx 1100, T \approx 0.25$ eV): At $T \gtrsim 1$ eV, equilibrium between baryons and photons is maintained below the ionization potential of hydrogen ($B_H = 13.6$ eV) by the low baryon-to-photon ratio[b] $\eta = 5.5 \times 10^{-10}(\Omega_b h^2/0.20)$. However, as the temperature drops, dissociation of hydrogen atoms becomes less frequent, and the number density of free electrons drops very sharply. This is described very approximately by the Saha ionization equation [35; 36; 37]:

[a] The term *recombination* is misleading since this is the first time nuclei and electrons combine.
[b] We have defined $h \equiv H_0/100$ as the reduced Hubble constant.

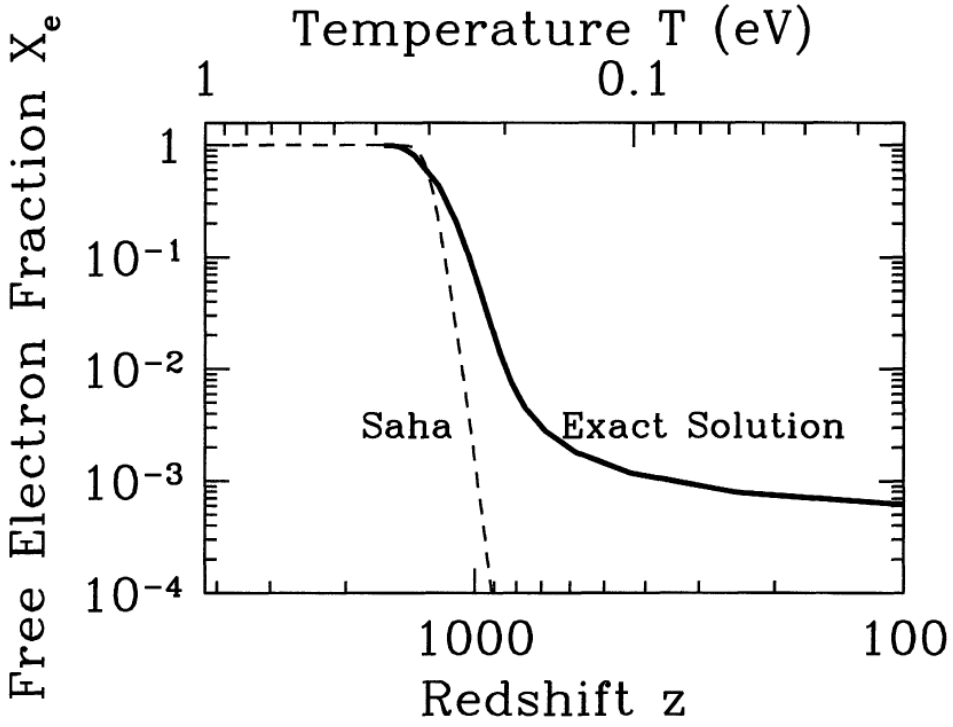

Figure 1.7: Evolution of the free electron fraction, defined as $X_e \equiv n_e/n_b$. The curves show the solution predicted by the Saha equation, and by a numerical solution of the Boltzmann equation. Note how the Saha equation is only valid while equilibrium is maintained, and clearly shows the drop in the number density of free electrons at recombination. Image credit: [34].

$$\left(\frac{1-X_e}{X_e^2}\right)_{\rm eq} = \frac{2\zeta(3)}{\pi^2}\eta\left(\frac{2\pi T}{m_e}\right)^{3/2} e^{B_H/T}, \tag{1.2.38}$$

where $X_e \equiv n_e/n_b$ is the free electron fraction, n_e and n_b are the number density of electrons and baryons respectively and m_e is the electron mass. The dashed line in Fig. 1.7 shows the evolution of the free electron fraction predicted by the Saha equation. As illustrated by the figure, the Saha approximation breaks down as the electron fraction decreases, since the decrease in the density of free electrons leads to a decrease in their interaction rate, and therefore to the breaking of thermal equilibrium. To track the free electron abundance, it is therefore necessary to solve a Boltzmann equation, which as shown by the continuous line in Fig. 1.7, leads to the freeze-out of a small number of free electrons.

- **Photon decoupling**: As mentioned above, before recombination, electrons are strongly coupled to the baryons through Thomson scattering with free electrons. After recombination, the number density of free electrons drops very quickly, and as a consequence,

the Thomson interaction rate falls below the expansion rate. The photons then decouple from the baryons and free stream through the Universe. These photons form the *cosmic microwave background* (CMB).

After these two processes, the Universe is neutral, formed mostly of hydrogen atoms and both the CMB radiation and the neutrinos free streaming. This time is known as the *Dark Ages*. The Universe is mostly ionized today; thus there must be a stage in which the Universe is *reionized*:

- **Reionization**: The dark ages extend from recombination ($z \approx 1100$) until $z \sim 10$ when matter starts to collapse around overdensities (which will be described in the following section) until the first stars and galaxies are born. The radiation from these stars and galaxies is energetic enough to ionize the neutral hydrogen. Reionization is a field of ongoing research, because of its importance not only for cosmology but also for star and galaxy formation. There is, therefore, a vast range of scenarios of reionization that are beyond the scope of this introduction. For cosmological purposes, nearly instantaneous reionization taking place at a redshift $z_{\rm re}$ is commonly assumed.

1.2.4 Cosmological Perturbation Theory

Having introduced the thermal history of the Universe, it is possible to study the evolution of different perturbation modes after they reenter the horizon. The study of perturbations in cosmology is an extremely complex topic, so a detailed study is beyond the scope of this introduction. A particularly comprehensible and detailed analysis of perturbations in Cosmology can be found in [6].

The evolution of each component of the cosmic fluid is dictated by the difference between gravity, which tries to increase the overdensities, and random motions that tend to reduce them. The distributions of different components are related through different interactions, leading to a large number of coupled equations describing the evolution of all components. The total density and pressure of the Universe can be separated into a homogeneous background and a perturbation:

$$\rho = \bar{\rho} + \delta\rho, \qquad p = \bar{p} + \delta p. \tag{1.2.39}$$

This section focuses only on scalar perturbations in the Newtonian gauge (1.2.15), assumes no anisotropic pressure, so $\Psi = \Phi$, and uses conformal time η. The Einstein equations (1.1.9) for

the perturbations yield [10]:

$$\nabla^2\Phi - 3\mathcal{H}(\Phi' + \mathcal{H}\Phi) = 4\pi G a^2 \delta\rho, \tag{1.2.40a}$$

$$\Phi' + \mathcal{H}\Phi = -4\pi G a^2(\bar{\rho} + \bar{p})v, \tag{1.2.40b}$$

$$\Phi'' + 3\mathcal{H}\Phi' + (2\mathcal{H}' + \mathcal{H}^2)\Phi = 4\pi G a^2 \delta p. \tag{1.2.40c}$$

where, again, $x' \equiv \mathrm{d}x/\mathrm{d}\eta$ and $\mathcal{H} \equiv a'/a$, and v is the 3-velocity, which is zero in the absence of perturbations. In addition, from conservation of the perturbed stress energy tensor $\nabla_\mu T^{\mu\nu}$, the continuity and Euler equations are:

$$\delta' + \left(1 + \frac{\bar{p}}{\bar{\rho}}\right)(\nabla \cdot \mathbf{v} - 3\Phi') + 3\mathcal{H}\left(\frac{\delta p}{\delta\rho} - \frac{\bar{p}}{\bar{\rho}}\right)\delta = 0, \tag{1.2.40d}$$

$$\mathbf{v}' + \mathcal{H}\mathbf{v} - 3\mathcal{H}c_s^2\mathbf{v} = -\frac{\nabla\delta p}{\bar{\rho} + \bar{p}} - \nabla\Phi, \tag{1.2.40e}$$

where $\delta \equiv \delta\rho/\bar{\rho}$ is the fractional overdensity, and the expression for the sound speed $c_s^2 \equiv \bar{p}'/\bar{\rho}'$ valid for adiabatic fluctuations[a] is used. The last equation required is the curvature perturbation ζ expressed in Newtonian gauge:

$$\zeta = -\Phi - \frac{2}{3(1+w)}\left(\frac{\Phi'}{\mathcal{H}} + \Phi\right) \tag{1.2.40f}$$

These equations cannot be solved analytically and require numerical methods. The present section describes the qualitative behaviour for each component:

- **Gravitational Potential**
  - On superhorizon scales, the curvature potential remains constant. However, while the curvature perturbation remains constant through the transition from radiation to matter domination, the gravitational potential decreases by a factor of 9/10 ($\Phi_{\mathrm{MD}} = 9/10\Phi_{\mathrm{RD}}$).
  - In a matter dominated Universe, the the gravitational potential on subhorizon scales also remains constant.
  - During radiation domination, the gravitational potential on subhorizon modes oscillates with decaying amplitude as:

$$\Phi_{\mathbf{k}}(\eta) \propto \frac{\cos\left(\frac{1}{\sqrt{3}}k\eta\right)}{(k\eta)^2} \tag{1.2.41}$$

[a] Adiabatic perturbations are generated by a single inflaton field, and as a consequence all the components of the Universe are coupled and evolve under the same equation of state during inflation. Adiabatic perturbations will be assumed throughout this thesis.

- **Radiation**
  - On superhorizon scales, fluctuations in the radiation density in the Newtonian gauge also remain constant, and are related to the superhorizon gravitational potential in the radiation dominated era by $\delta_r \approx -2\Phi_{\rm RD}$, where $\delta_I \equiv \delta\rho_I/\bar{\rho}_I$ is the fractional overdensity for a given species.
  - Subhorizon fluctuations oscillate with constant amplitude, around $\delta_r = 0$ during radiation domination, and around $-4\Phi_{\rm MD}(k)$ during matter domination. These oscillations are called *acoustic oscillations*, and they will be discussed in the following section.
- **Dark Matter**
  - Matter fluctuations also remain constant on superhorizon scales, and they are related to radiation fluctuations by $\delta_m = (3/4)\delta_r$ assuming adiabaticity.
  - Subhorizon fluctuations grow logarithmically during radiation domination $\delta_m \propto \log a$, and linearly during matter domination $\delta_m \propto a$. For a dark energy dominated Universe, matter fluctuations remain constant.
  - For matter fluctuations, the *transfer function* $T(k, z)$ relates matter perturbations to the primordial curvature perturbation

$$\Delta_m(\mathbf{k}, z) = T(k, z)\zeta_{\mathbf{k}}, \tag{1.2.42}$$

    where $\Delta_m \equiv \nabla^2\Phi/(4\pi G a^2\bar{\rho})$ is the comoving gauge density contrast. The *matter power spectrum* is defined as:

$$P_\delta(k, z) \equiv |\Delta_m(\mathbf{k}, z)|^2 = T^2(k, z)\,|\zeta_{\mathbf{k}}|^2\,. \tag{1.2.43}$$

    For scale-invariant initial conditions $|\zeta_{\mathbf{k}}|^2 \propto k^{-3}$, the matter power spectrum grows linearly $P_\delta \propto k$ for $k < k_{\rm eq}$, and decays as k^{-3} for $k > k_{\rm eq}$. In linear theory, the time dependence of the power spectrum can be factored out introducing the growth factor $D(z)$:

$$\delta(k, z) = \frac{D(z)}{D(z=0)}\delta(k, z=0). \tag{1.2.44}$$

- **Baryons**
  - Before photon decoupling, baryons are tightly coupled to photons, with $\mathrm{v}_\gamma = \mathrm{v}_b$ and $\delta_\gamma = (4/3)\delta_b$. The baryons therefore undergo acoustic oscillations.
  - Because dark matter perturbations grow during radiation and matter equality, right after decoupling $|\delta_c| \gg |\delta_b|$ on scales much smaller than the Hubble radius. Then the baryons fall into the dark matter potential wells, so $\delta_b \to \delta_c$.

– These acoustic oscillations followed by gravitational collapse after photon decoupling leave an imprint in the large scale structure that will be discussed in the following section.

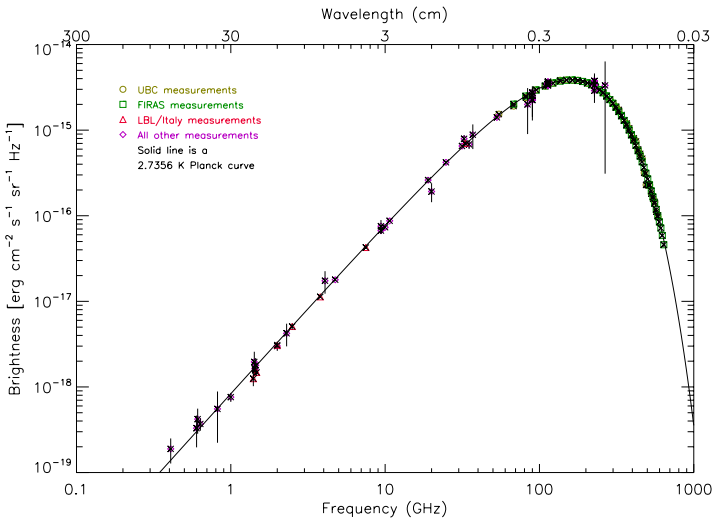

Figure 1.8: The CMB brightness as a function of frequency. The solid black line is the best fit blackbody spectrum. Image credit: [38]

1.3 Methods to Observe the Universe

The previous two sections have presented an overview of the ΛCDM model, which describes the background Universe and its fluctuations. The present section focuses on the different techniques to observe the Universe and their results. Cosmological observations are highly challenging, and only in the last decades have the various methods started to provide precise constraints on cosmological parameters, starting what is called the *era of precision cosmology*. Higher accuracy in cosmological observations has also shown tensions in parameters estimated using different techniques. Such discrepancies can be caused by systematic effects, experimental or statistical errors, or by problems with the theoretical model, in this case, ΛCDM. This thesis presents a detailed study of the significance and possible causes of some of these discrepancies.

The discussion in this section will focus on the observational techniques that feature in the remaining chapters of this thesis: CMB temperature and polarization anisotropies (Sec. 1.3.1), weak galaxy lensing (Sec. 1.3.2), baryon acoustic oscillations (Sec. 1.3.3) and type Ia supernovae (Sec. 1.3.4). Other observational methods that are not so relevant to this thesis are also briefly introduced: CMB lensing in Sec. 1.3.5, redshift-space distortions is Sec. 1.3.6, and standard sirens in Sec. 1.3.7.

1.3.1 Cosmic Microwave Background Anisotropies

- **Detection**: The concepts of recombination and photon decoupling were introduced in

the previous section: After electrons and protons combine to form hydrogen, the rate of Thomson scattering drops very rapidly, and photons free stream through the Universe. These photons constitute the Cosmic Microwave Background (CMB). The existence of the CMB was predicted in the midst of the argument between those favoured a *steady state Universe* that maintains a constant mass density [39] and those who favoured an evolving Universe whose light elements had formed via primordial nucleosynthesis during an early hot dense phase [40; 41; 42]. The latter group forecasted the existence of a CMB if their model of the Universe was correct [43]. The first detection of the CMB, which confirmed the Big Bang Theory, took place accidentally by a group trying to detect radio waves bounced off Echo balloon satellites [44].

The CMB follows a nearly perfect blackbody shape (Fig. 1.8), and it is highly isotropic over the entire sky, which as mentioned in the previous section is the origin of the problem of horizons. However, we now know that the temperature of the CMB is not entirely uniform over the sky. The CMB has small temperature anisotropies that originate from the fluctuations described in the previous section. These small anisotropies ($\Delta T/T_{\rm CMB} \sim 10^{-5}$) were first detected by the Cosmic Background Explorer (COBE [45]), and further measured with higher accuracy by the Wilkinson Microwave Anisotropy Probe (WMAP) and *Planck* teams [1; 21; 46; 47], as well as ground based experiments [48]. The effect of the fluctuations can also be detected through the polarization of the CMB radiation, which was first discovered by the Degree Angular Scale Interferometer (DASI) [49] and has been measured to high precision by *Planck*, the South Pole Telescope (SPT) [50] and the Atacama Cosmology Telescope (ACT) [51].

- **Temperature anisotropies**: Anisotropies in the CMB temperature $\Theta(\hat{\mathbf{n}}) \equiv \Delta T(\hat{\mathbf{n}})/T_{\rm CMB}$ can be expanded in a basis of spherical harmonics[a] Y_ℓ^m:

$$\Theta(\hat{\mathbf{n}}) = \sum_{\ell=0}^{\infty} \sum_{m=-\ell}^{\ell} \Theta_{\ell m} Y_\ell^m(\hat{\mathbf{n}}). \tag{1.3.3}$$

The coefficients of this expansion $\Theta_{\ell m}$ have zero mean, but non-zero variance. The CMB *power spectrum* C_ℓ is defined as:

[a]Spherical harmonics are defined as:

$$Y_\ell^m \equiv \sqrt{\frac{2\ell+1}{4\pi}\frac{(\ell-m)!}{(\ell+m)!}} P_\ell^m(\cos\theta) e^{im\phi}, \tag{1.3.1}$$

where θ and ϕ are the polar and azimuthal coordinates respectively, and $P_\ell^m(x)$ are the associated Legendre polynomials:

$$P_\ell^m(x) \equiv (-1)^m (1-x^2)^{m/2} \frac{\mathrm{d}^m}{\mathrm{d}x^m} P_\ell(x). \tag{1.3.2}$$

$$\langle \Theta^{\star}_{\ell m} \Theta_{\ell' m'} \rangle = \delta_{\ell\ell'} \delta_{mm'} C_{\ell}^{\Theta\Theta}, \tag{1.3.4}$$

where $\langle\rangle$ denotes the ensemble average. Equivalently, the spectrum $C_{\ell}^{TT} = T^2_{\rm CMB} C_{\ell}^{\Theta\Theta}$ is frequently used. If the temperature anisotropies are Gaussian[a], all their statistical information is contained in their power spectrum. Slow-roll single field inflation does not lead to detectable non-Gaussianity [52; 53], therefore a detection of primordial non-Gaussianity in the CMB would be indicative of inflation with multiple fields [54; 55; 56; 57; 58; 59; 60] or a departure from ordinary single-field slow roll inflation [61; 62; 63; 64; 65; 66; 67; 68; 69]. However, *Planck* has placed very tight-constraints on non-Gaussianity, and obtained consistency with a Gaussian primordial perturbation [30; 70].

- **Main features of the CMB temperature spectrum**: Fig. 1.9 shows the temperature power spectrum measured by *Planck*. There are three main features in the CMB temperature spectrum:
  - The *large-scale plateau* consists of scales that cross the Hubble radius after recombination ($\ell \lesssim 100$). These scales are not affected by pre-recombination physics and therefore reflect the primordial curvature perturbation, through the parameters A_s and n_s. For a nearly scale-invariant primordial power spectrum, $C_\ell \propto [\ell(\ell+1)]^{-1}$ in this regime.
  - *Acoustic oscillations* form the most prominent features in the CMB power spectrum. The mechanism that causes these oscillations was introduced in the previous section: The baryon-photon fluid oscillates before recombination due to the opposing effects of gravity and radiation pressure. At photon decoupling, the maxima and minima of these oscillations are imprinted in the CMB radiation. The position of the peaks provides a measurement of the extrema of these oscillations at last scattering, and in particular of the *sound horizon at radiation drag* r_d, which measures the distance sounds waves can travel before recombination [71]:

$$r_d = \int_{z_d}^{\infty} \frac{c_s(z)}{H(z)} \mathrm{d}z, \tag{1.3.6}$$

where z_d is the redshift at photon decoupling and $c_s(z)$ is the sound speed in the photon-baryon fluid [72]:

[a] Gaussian random fields are random fields that follow a Gaussian probability distribution

$$P(\mathbf{x}) = \frac{1}{\sqrt{(2\pi)^N |\mathbf{C}|}} e^{-\frac{1}{2}\mathbf{x}^T \cdot \mathbf{C}^{-1} \cdot \mathbf{x}}, \tag{1.3.5}$$

where N is the number of dimensions, $\mathbf{C}$ is the covariance matrix and $|\mathbf{C}|$ is its determinant.

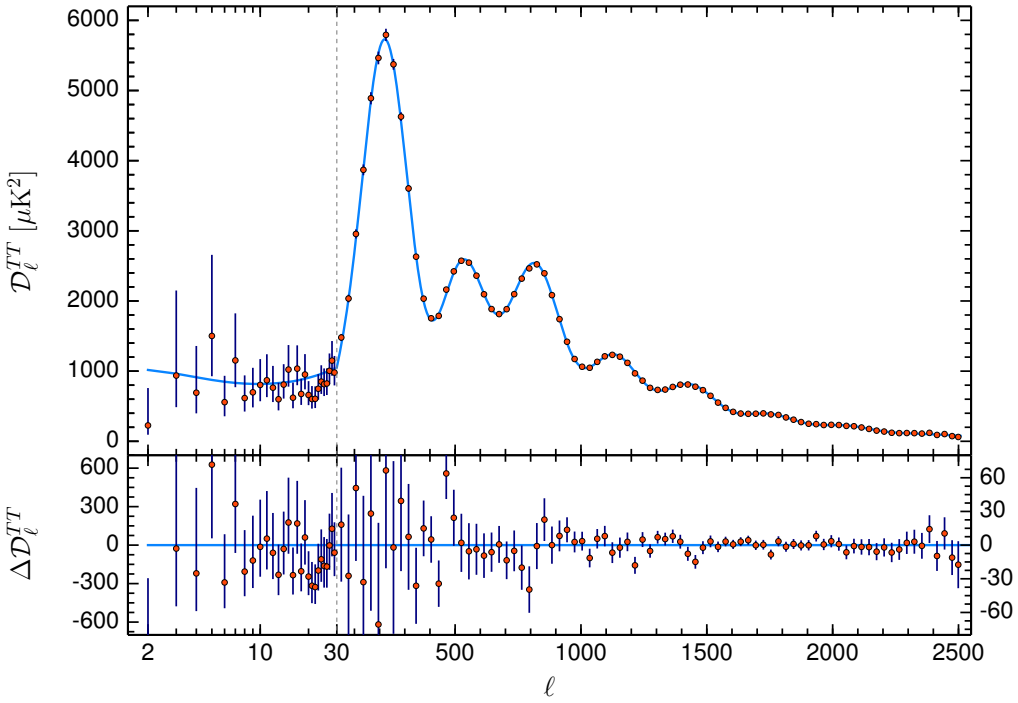

Figure 1.9: *Planck* 2018 temperature power spectrum. The vertical axis shows $\mathcal{D}_\ell \equiv \ell(\ell+1)C_\ell/(2\pi)$. Blue points are the observed data and the red line shows the best fit ΛCDM cosmology. Scales change from logarithmic to linear at $\ell = 30$. The lower plot shows residuals with respect to the best fit. Image credit: [1].

$$c_s^2(z) = \frac{1}{3}\left[1 + \frac{3}{4}\frac{\rho_b(z)}{\rho_\gamma(z)}\right]^{-1}. \tag{1.3.7}$$

The sound horizon serves as a standard ruler, and the position of the acoustic peaks can therefore constrain parameters such as Ω_m, Ω_b, Ω_r, Ω_k and H_0.

– The *Silk damping tail* [73] affects small scales: The mean free path of photons before recombination is not actually zero. Before scattering at recombination, photons follow a random walk within the baryon-photon fluid. This random walk mixes cold and hot photons in the plasma, and therefore smooths the anisotropies on scales below the *Silk scale* [74]:

$$\lambda_D \sim \sqrt{N}\lambda_c \sim \sqrt{\eta_\star \lambda_c}, \tag{1.3.8}$$

where N is the number of steps in the random walk, λ_c is the mean-free path to Compton scattering, and $\eta_\star$ is the conformal time at recombination. The Silk

scale corresponds to an angular scale $\ell \sim 1000$. At higher multipoles, the CMB anisotropies are suppressed by Silk damping.

- **Secondary Anisotropies**: While the three main features driven by recombination physics dominate the shape of the temperature power spectrum, the propagation of the CMB photons between recombination and the present time is affected by a series of processes that alter the CMB power spectrum, and provide useful information about the Universe at $z < 1100$:
  - *Integrated Sachs-Wolfe effect* (ISW) [75]: Photons that propagate through a changing gravitational potential are redshifted or blueshifted, which imprints an extra anisotropy. As previously mentioned, gravitational potentials are constant during matter domination, but they vary if there is a significant contribution from radiation or dark energy, which is the case for early and late times respectively.
  - *CMB lensing*: The path of photons as they propagate is affected by the large-scale structure through gravitational lensing. This has the effect of smoothing the acoustic peaks of the CMB spectra. CMB lensing can be used as a cosmological probe on its own, and will, therefore, be further discussed in Sec. 1.3.5.
  - *Reionization*: Reionization was introduced in the previous section: At $z \lesssim 10$ the formation of the first stars ionizes the Universe. The presence of free electrons from this point onward means that a fraction $(1 - e^{-\tau_{\rm re}})$ of CMB photons undergo Thomson scattering after reionization, where $\tau_{\rm re}$ is the optical depth to reionization defined as the line-of-sight opacity of the CMB radiation with respect to Thomson scattering with free electrons:

$$\tau_{\rm re} = \int_0^{\chi_{\rm re}} \sigma_T n_e \mathrm{d}\chi, \tag{1.3.9}$$

    where $\chi_{\rm re}$ is the comoving distance to reionization, σ_T is the Thomson scattering cross-section and n_e is the number density of free electrons. As a consequence, the power spectrum on scales that enter the horizon before reionization is damped by $e^{-2\tau_{\rm re}}$.
  - *Sunyaev-Zel'dovich effect*: CMB photons undergo inverse Thomson scattering with high energy electrons in galaxy clusters [76; 77; 78]. There are two types of SZ effect: Thermal SZ, where the photons are boosted in energy via Compton scattering with the electrons in the cluster gas, and a subdominant kinematic SZ where the source is the bulk motion of the clusters. The thermal SZ effect increases the energy of the CMB photons and therefore distorts its spectrum to higher frequencies. While the thermal SZ can be detected via its frequency dependence, the kinematic SZ is frequency independent.

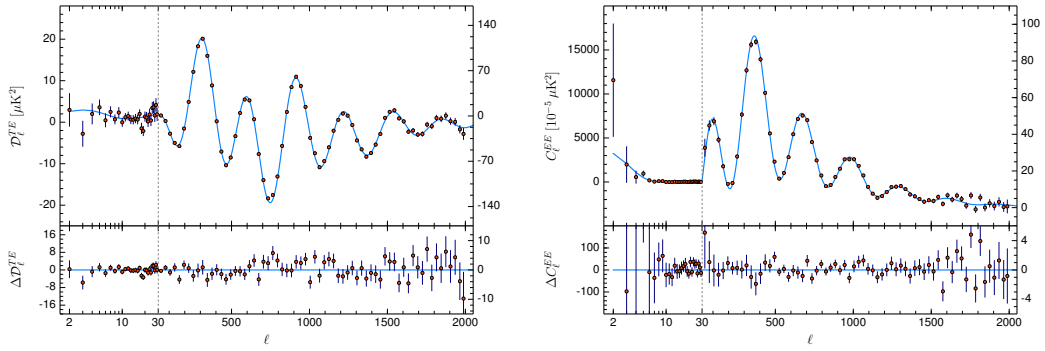

Figure 1.10: *Planck* 2018 temperature power spectrum. The vertical axis on the left plot shows $\mathcal{D}_\ell \equiv \ell(\ell+1)C_\ell/(2\pi)$. Red points are the observed data and the blue line shows the best fit ΛCDM cosmology. Scales change from logarithmic to linear at $\ell = 30$. The lower panels show residuals with respect to the best fits. Image credit: [1].

- **Polarization**: Temperature anisotropies are not the only source of information from CMB radiation. Their polarization pattern provides complementary information to the temperature anisotropies. In the rest frame of the electrons, scalar perturbations to the metric generate a quadrupolar component of the radiation field. This leads to a *linear* polarization of the scattered radiation through Thomson scattering at recombination. Tensor perturbations, which originate from gravitational waves, also produce polarization (for a more detailed discussion about CMB polarization see [79; 80]).

  For a given choice of spatial coordinates $\{\hat{x}, \hat{y}, \hat{z}\}$, the electric field for electromagnetic radiation of angular frequency ω traveling in the $\hat{z}$ direction can be expressed as:

$$E_x = a_x \cos(\omega t - \phi_x), \qquad E_y = a_y \cos(\omega t - \phi_y). \tag{1.3.10}$$

This polarization can then be decomposed into four Stokes parameters:

$$I = a_x^2 + a_y^2, \tag{1.3.11a}$$
$$Q = a_x^2 - a_y^2, \tag{1.3.11b}$$
$$U = 2a_x a_y \cos(\phi_x - \phi_y), \tag{1.3.11c}$$
$$V = 2a_x a_y \sin(\phi_x - \phi_y). \tag{1.3.11d}$$

The first parameter is the intensity, Q and U are the linear-polarization parameters, and V is the circular-polarization parameter, which is always zero in the case of the CMB radiation as Thomson scattering does not create circular polarization. The quantities

$(Q \pm iU)(\hat{n})$ are spin-2 objects, i.e. under a rotation of the reference frame around $\hat{n}$ by an angle θ:

$$(Q \pm iU)(\hat{n}) \to e^{\mp 2i\theta}(Q \pm iU)(\hat{n}). \tag{1.3.12}$$

A spin-2 object on the sphere can be expanded in a basis of spin-2 spherical harmonics[a]:

$$(Q \pm iU)(\hat{n}) = \sum_{\ell=0}^{\infty} \sum_{m=-\ell}^{\ell} (E_{\ell m} \pm iB_{\ell m})_{\pm 2}Y_{\ell m}(\hat{n}). \tag{1.3.14}$$

The names of the E and B components originate from the analogy with electric and magnetic fields, since these modes are curl and divergence free respectively. In the CMB, scalar perturbations only generate E-mode polarization because of their parity, as long as gravitational lensing is neglected [82; 83]. This means that a detection of B-modes in the CMB polarization pattern after correcting for lensing would be a detection of primordial gravitational waves[b], which are predicted by some models of inflation. At the moment of writing this thesis, no such detection has been made, though the B-modes generated by lensing have been detected. For the rest of this thesis, primordial B-mode polarization will therefore be ignored. In analogy with the temperature case, the E-mode or polarization power spectrum is defined as:

$$\langle E^{\star}_{\ell m} E_{\ell' m'} \rangle = \delta_{\ell\ell'}\delta_{mm'} C_{\ell}^{EE}. \tag{1.3.15}$$

Finally, further information can be obtained from the cross-correlation between temperature and polarization anisotropies, defined as:

$$\langle T^{\star}_{\ell m} E_{\ell' m'} \rangle = \delta_{\ell\ell'}\delta_{mm'} C_{\ell}^{TE}. \tag{1.3.16}$$

The three spectra (1.3.4), (1.3.15) and (1.3.16) which will henceforth be called TT, EE and TE respectively, are shown in Figs. 1.9 and 1.10.

[a] The spin-weighted spherical harmonics are defined by:

$${}_sY_{\ell m} = \sqrt{\tfrac{(\ell-s)!}{(\ell+s)!}}\, \eth^s Y_{\ell m}, \qquad s \geq 0, \tag{1.3.13a}$$

$${}_sY_{\ell m} = \sqrt{\tfrac{(\ell+s)!}{(\ell-s)!}}\, (-1)^s \bar{\eth}^{-s} Y_{\ell m}, \qquad s \leq 0; \tag{1.3.13b}$$

where $|s| \leq l$, and $\eth\eta$ and $\bar{\eth}\eta$ are the spin raising and lowering operators respectively [81]:

$$\eth\eta = -(\sin\theta)^s \left\{ \frac{\partial}{\partial\theta} + \frac{i}{\sin\theta}\frac{\partial}{\partial\phi} \right\} \left[(\sin\theta)^{-s}\eta \right], \qquad \bar{\eth}\eta = -(\sin\theta)^{-s} \left\{ \frac{\partial}{\partial\theta} - \frac{i}{\sin\theta}\frac{\partial}{\partial\phi} \right\} \left[(\sin\theta)^{s}\eta \right]. \tag{1.3.13c}$$

[b] Topological defects that could form in symmetry-breaking transitions in the early Universe, such as monopoles, strings and domain walls, would also generate both vector and tensor modes [84; 85; 86; 87; 88; 89], and as a consequence would also generate a B-mode signal [90].

Parameter	Symbol	Best fit value and 68% limits
Cold dark matter density	$\Omega_c h^2$	0.1202 ± 0.0014
Baryon density	$\Omega_b h^2$	0.02236 ± 0.00015
Hubble parameter	h	0.6727 ± 0.0060
Optical depth to reionization	$\tau_{\rm re}$	$0.0544^{+0.0070}_{-0.0081}$
Scalar spectrum amplitude	$\log\left(10^{10} A_s\right)$	3.045 ± 0.016
Scalar spectral index	n_s	0.9649 ± 0.0044

Table 1.2: Best fit values and 68% limits for the constraints from *Planck* 2018 TT+TE+EE+lowE [1].

- **The *Planck* cosmology**: The CMB is the only cosmological probe that can simultaneously constrain all six parameters in the standard ΛCDM model of cosmology[a] $\left\{\Omega_b h^2, \Omega_c h^2, H_0, \tau_{\rm re}, A_s, n_s\right\}$ where $h \equiv H_0/100$. Note that different combinations of these six parameters are commonly used to parameterize ΛCDM. The strongest constraints on these parameters come from observations of the *Planck* satellite, and are shown in table 1.2 obtained from the 2018 Planck Legacy Archive (PLA) tables[b]. *Planck* is a space telescope that observes the whole sky in nine different frequencies between 30 and 857 GHz to produce maps of temperature and polarization anisotropies as well as to clean different foreground contamination and systematics. The standard ΛCDM model of cosmology with the *Planck* best-fit parameters will be henceforth referred to simply as the *Planck* cosmology. The remaining chapters of this thesis will explore inconsistencies in derived parameters between *Planck* and other experiments and assess their significance, since differences in parameters could reflect new physics beyond standard ΛCDM.

1.3.2 Weak Galaxy Lensing

Gravitational lensing is the deflection of light by an intervening gravitational field along the light of sight. The term *strong lensing* refers to cases where lensing is within or close to the Einstein radius [91; 92] and therefore the lensing effect of a single source can be detected. The opposite case is weak lensing, in which the lensing effect is significantly smaller, and frequently distortions on the galaxy images cannot be differentiated from the intrinsic ellipticity of individual galaxies, and lensing has to be measured through correlations in the shapes and orientations of galaxy images. This subsection focuses on gravitational lensing by the large-scale structure of the Universe, also known as *cosmic shear*, as it provides extensive information about cosmology. The effect of lensing by the large-scale structure on galaxy images is a distortion of order one percent and therefore falls in the category of weak lensing.

[a] The term standard or 'vanilla' ΛCDM refers to a flat Universe $\Omega_k = 0$ with a power law primordial power spectrum.

[b] http://www.cosmos.esa.int/web/planck/pla.

There are numerous available reviews on the theory and observations of weak gravitational lensing [e.g. 93; 94; 95; 96].

- **Lensing potential**: All weak lensing quantities can be defined as a function of a lensing potential ϕ:

$$\phi(\hat{n}, \chi) = 2 \int_0^{\chi} \mathrm{d}\chi' \frac{S(\chi - \chi')}{S(\chi) S(\chi')} \Phi(\hat{n}, \chi'), \tag{1.3.17}$$

  where $\Phi(\hat{n}, \chi)$ is the gravitational potential at an angular point $\hat{n}$ and a time $z(\chi)$, and $S(\chi)$ is given by Eq. (1.1.12). The integration of this potential along the line of sight and weighted with a redshift distribution function $n(\chi)$ yields:

$$\phi(\hat{n}) = \int \mathrm{d}\chi n(\chi) \phi(\hat{n}, \chi) = 2 \int \frac{\mathrm{d}\chi'}{S(\chi')} q(\chi') \Phi(\hat{n}, \chi'), \tag{1.3.18}$$

  where the weight function or lensing efficiency $q(\chi)$ is defined as[a]:

$$q(\chi') = \int_0^{\chi'} \mathrm{d}\chi \frac{S(\chi - \chi')}{S(\chi)} n(\chi). \tag{1.3.19}$$

  The deflection angle is obtained as the angular gradient of the lensing potential $\alpha(\hat{n}) = \nabla\phi(\hat{n})$. Weak lensing surveys measure the effect of lensing at different redshifts using tomographic bins, which translate into different redshift distributions $n^i(\chi)$.
- **Lensing correlation function**: The gravitational potential can be expanded in a basis of spherical harmonics (1.3.1):

$$\phi(\hat{n}) = \sum_{\ell=0}^{\infty} \sum_{m=-\ell}^{\ell} \phi_{\ell m} Y_\ell^m(\hat{n}). \tag{1.3.20}$$

  The lensing correlation function or lensing angular power spectrum is defined in the same manner as the CMB case:

$$\langle \phi^\star_{\ell m} \phi_{\ell' m'} \rangle = \delta_{\ell\ell'} \delta_{mm'} C_\ell^{\phi\phi}. \tag{1.3.21}$$

  Using (1.3.18) combined with Poisson's equation, and the Limber and flat-sky approximations (see Chapter 5 for an extended discussion about these approximations and their effects), the lensing correlation function can be expressed in terms of the matter spectrum (1.2.43) and cosmological parameters:

$$C_\ell^{\phi\phi}(i, j) = \frac{4}{(\ell + 1/2)^4} \left(\frac{3 H_0^2 \Omega_m}{2} \right)^2 \int \mathrm{d}\chi \left[1 + z(\chi)\right]^2 q^i(\chi) q^j(\chi) P_\delta \left(\frac{\ell + 1/2}{S(\chi)}, z(\chi) \right), \tag{1.3.22}$$

[a] Note that our lensing efficiency is defined as a dimensionless quantity, as opposed what is frequently done in the literature [e.g. 97; 98].

where i, j denote the tomographic redshift bins.

- **Shear**: The observable in weak lensing is the shear, related to the gravitational potential through the spin-raising operator (1.3.13c):

$$\gamma = \frac{\eth^2 \phi}{2}. \tag{1.3.23}$$

Shear is a spin-2 object, and can therefore be decomposed in E and B modes:

$$\gamma(\hat{\boldsymbol{n}}) = \sum_{\ell m} (\epsilon_{\ell m} + i\beta_{\ell m})\, {}_2Y_{\ell m}(\hat{\boldsymbol{n}}), \tag{1.3.24a}$$

$$\gamma^*(\hat{\boldsymbol{n}}) = \sum_{\ell m} (\epsilon_{\ell m} - i\beta_{\ell m})\, {}_{-2}Y_{\ell m}(\hat{\boldsymbol{n}}). \tag{1.3.24b}$$

Gravitational lensing only produces E-modes, therefore the E-mode power spectrum contains all the information about the shear and is usually called *shear power spectrum*:

$$C_\ell^{\epsilon\epsilon}(i,j) = \left(\frac{3H_0^2\Omega_m}{2}\right)^2 \int \mathrm{d}\chi\, [1+z(\chi)]^2\, q^i(\chi) q^j(\chi) P_\delta\left(\frac{\ell+1/2}{S(\chi)}, z(\chi)\right), \tag{1.3.25}$$

where we have used the flat-sky approximation.

- **Shear correlation functions:** In the context of weak lensing it is common to work in real space instead of multipole space. This is achieved through the shear correlation functions, which using flat-sky approximations are:

$$\xi_+(\theta) = \frac{1}{2\pi} \int \mathrm{d}\ell \ell J_0(\ell\theta) C_\ell^{\epsilon\epsilon}, \tag{1.3.26a}$$

$$\xi_-(\theta) = \frac{1}{2\pi} \int \mathrm{d}\ell \ell J_4(\ell\theta) C_\ell^{\epsilon\epsilon}, \tag{1.3.26b}$$

where J_0 and J_4 are the Bessel functions of the first kind[a].

- **Intrinsic alignments**: Weak lensing measurements are affected by a large number of systematics. Amongst the the most significant are intrinsic alignments, which are correlations in the physical orientations and shapes of galaxies. The observed shear spectrum has a contribution for lensing shear (LL), one from intrinsic alignments (II) and one from the cross-correlation of both effects (LI):

$$C_\ell^{\epsilon\epsilon} = C_\ell^{LL} + C_\ell^{LI} + C_\ell^{II}, \tag{1.3.28}$$

[a]The Bessel functions of the first kind are defined as:

$$J_\nu(x) = \left(\frac{x}{2}\right)^\nu \sum_{k=0}^{\infty} \frac{(-1)^k}{\Gamma(k+1)\Gamma(\nu+k+1)} \left(\frac{x}{2}\right)^{2k}, \tag{1.3.27}$$

where Γ is the Gamma function.

where C_ℓ^{LL} is given by Eq. (1.3.25). Intrinsic alignments are not a well understood phenomenon, and as a consequence there are several models for the terms C_ℓ^{II} and C_ℓ^{LI}. [99] presents two models, one that assumes galaxies whose mean ellipticities are linear functions of the tidal gravitational field, and one that assumes a quadratic relation. The linear model, initially proposed by [100], is most commonly used. In this model, the last two terms in Eq. (1.3.28) are [101]:

$$\begin{aligned} C_\ell^{\rm II}(i,j) &= \int_0^{\chi_{\rm H}} d\chi \, \frac{n_i(\chi) n_j(\chi) F_i(\chi) F_j(\chi)}{[S(\chi)]^2} \, P_\delta\left(\frac{\ell+1/2}{S(\chi)}, \chi\right), \\ C_\ell^{\rm LI}(i,j) &= \left(\frac{3H_0^2\Omega_m}{2}\right) \int_0^{\chi_{\rm H}} d\chi \, [1+z(\chi)] \, F(\chi) \left\{\frac{q_i(\chi) n_j(\chi) + q_j(\chi) n_i(\chi)}{S(\chi)}\right\} P_\delta\left(\frac{\ell+1/2}{S(\chi)}, \chi\right), \end{aligned} \tag{1.3.29}$$

and:

$$F(z) = -A_{IA} C \rho_c \frac{\Omega_m}{D(z)}, \tag{1.3.30}$$

where $D(z)$ is the linear growth rate of perturbations (Eq. 1.2.44) normalized to unity at the present day, and C is a normalizing constant, usually chosen to be $C = 5 \times 10^{-14} h^{-2} M_\odot^{-1} \mathrm{Mpc}^3$ to make the amplitude parameter A_{IA} of order unity. A_{IA} will be positive if the alignment of the galaxies is coherent with the tidal field as expected. Note that this is a very simplified model, that does not consider possible differences in intrinsic alignments depending on galaxy types and luminosities. Some analysis include a luminosity dependence in the intrinsic alignment amplitude to account for some of these effects [97]. Intrinsic alignments will be further discussed in Chapter 6.

- **Galaxy clustering and galaxy-galaxy lensing**: One way of breaking degeneracies between cosmological parameters and systematic effects that affect cosmic shear such as intrinsic alignments is to use additional statistics. Galaxy clustering is a measurement of the overdensities in the galaxy distribution, which is related to the clustering of matter. The two-point correlation function at an angular separation θ is given by:

$$w(\theta) = b^2 \int \frac{\mathrm{d}\ell}{2\pi} J_0(\ell\theta) \int \mathrm{d}\chi \frac{n_L^2(\chi)}{S(\chi)^2 H(z)} P_\delta\left(\frac{\ell+1/2}{S(\chi)}, \chi\right), \tag{1.3.31}$$

where $n_L(\chi)$ is the redshift distribution of galaxies, and b is called the linear bias, defined as the ratio of the galaxy overdensity over the matter overdensity[a] [103; 104; 105]. Galaxy-galaxy lensing is weak lensing of galaxy images caused by the gravitational field of other galaxies. For source galaxies j being lensed by lens galaxies i, the shear is given by:

[a] Using a linear relation between galaxy and matter distribution, while accurate, is only an approximation [102].

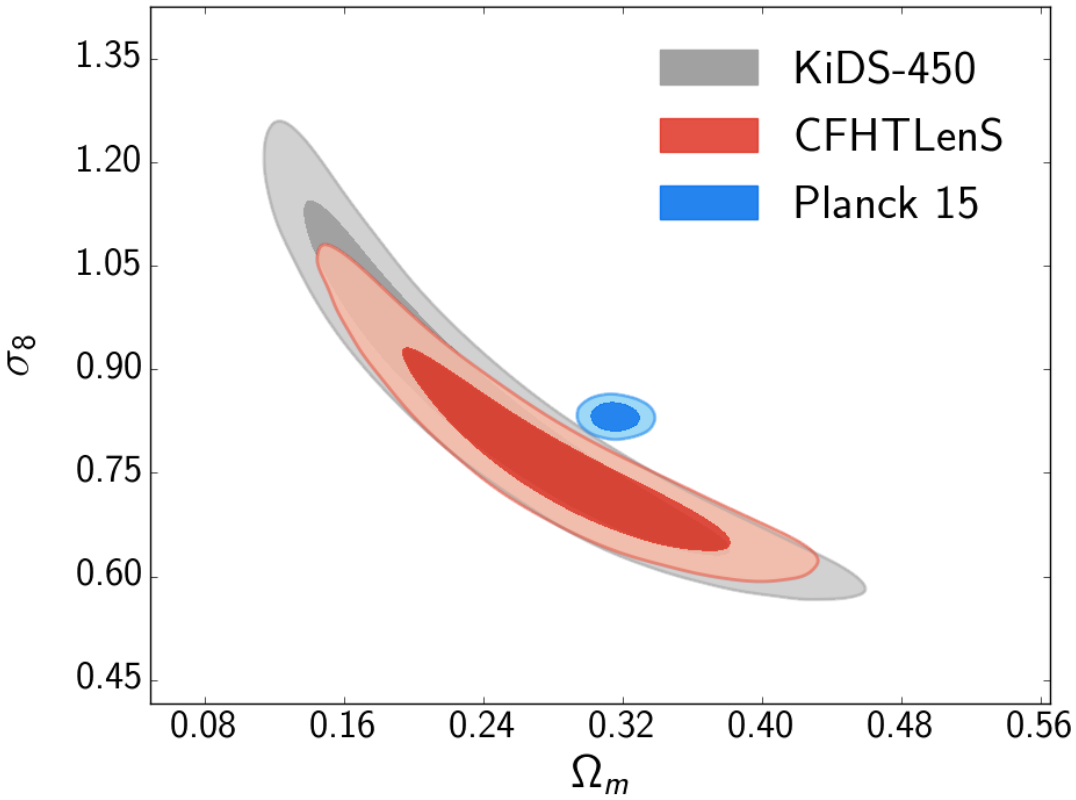

Figure 1.11: Marginalized posterior likelihoods showing 68% and 95% confidence contours. In grey, the results from CHFTLenS [106], in red the results from the KiDS 450-degree analysis in real space [98], in blue, the *Planck* 2015 results using the TT+TE+EE+lowTEB likelihood [21].

$$\gamma^{ij}(\theta) = b^i \left(\frac{3H_0^2\Omega_m}{2}\right) \int \frac{\mathrm{d}\ell}{2\pi} J_2(\ell\theta) \int \mathrm{d}\chi n_L^i(\chi) \left[1 + z(\chi)\right] \frac{q^j(\chi)}{H(z)S(\chi)} P_\delta \left(\frac{\ell + 1/2}{S(\chi)}, \chi\right). \tag{1.3.32}$$

- **Observations**: Cosmic shear was not observed until the year 2000 [107; 108; 109; 110]. The best measurements of cosmic shear to date come from the Canada-France-Hawaii Telescope Lensing Survey (CFHTLenS) [106], the Kilo Degree Survey (KiDS) [98; 111] and the Dark Energy Survey (DES) [97]. Because cosmic shear is related to the matter power spectrum, it is sensitive to the density and clustering of matter parameterized by Ω_m and σ_8 respectively, where σ_8 is the root-mean-square amplitude of the mass fluctuations in spheres of radius $8h^{-1}$ Mpc. Tension has been reported between weak lensing and CMB constraints on these parameters, and in particular in the combination $S_8 \equiv \sigma_8(\Omega_m/0.3)^{0.5}$. This reported tension, illustrated in Fig. 1.11, motivates the discussions of Chapters 5 and 6.

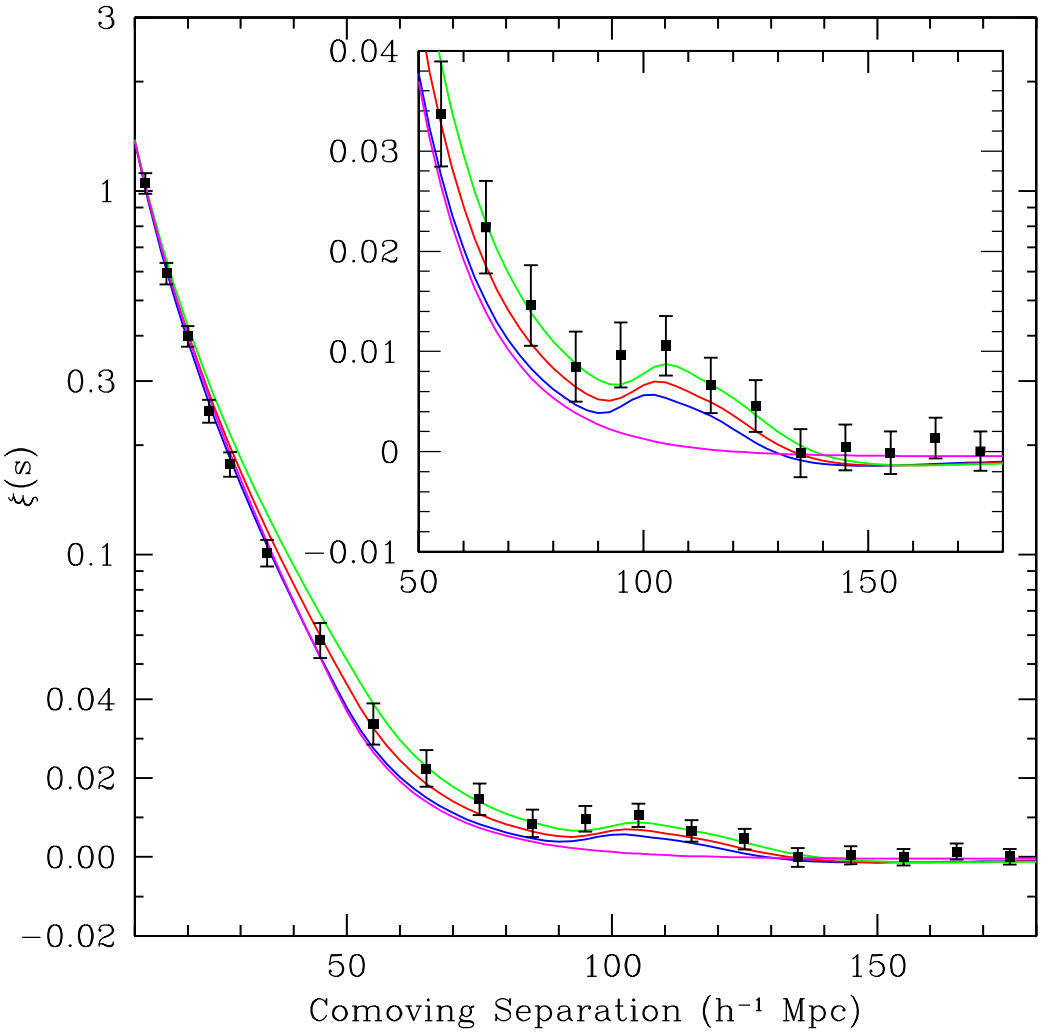

Figure 1.12: First detection of the BAO peak in the galaxy correlation function. The different lines represent different cosmologies: $\Omega_m h^2 = 0.12$ in green, $\Omega_m h^2 = 0.13$ in red, $\Omega_m h^2 = 0.14$, all of them with $\Omega_b h^2 = 0.024$. The magenta line is a pure CDM model $\Omega_m h^2 = 0.105$ which lacks the acoustic peak. Image credit [113].

1.3.3 Baryon Acoustic Oscillations

Baryon acoustic oscillations (BAO) are oscillations in the baryon-photon fluid that leave an imprint in the large-scale structure of the Universe when they freeze at recombination [112]. The mechanism behind these oscillations was introduced in the previous section: Because of the inertia of the baryons, the acoustic peak structure becomes imprinted in the dark matter distributions, which can be measured by using galaxies as a tracer of the dark matter distribution.

- **Galaxy correlation function**: The BAO peak can be observed in the galaxy correlation function, which can be obtained as the Fourier transform of the matter power spectrum:

$$\xi(r) = \int_0^\infty \frac{k^3 \mathrm{d}\log k}{2\pi^2} j_0(kr) P_\delta(k), \tag{1.3.33}$$

where j_0 is a spherical Bessel function[a] , and we have assumed an isotropic matter power spectrum. The imprint of BAO in large-scale structure can be used as a standard ruler in the form of a preferred angular separation between galaxies, corresponding to the sound horizon at radiation drag $r_d \approx 150$ Mpc as shown in Fig. 1.12. Spectroscopic surveys measure this feature in the correlation function with respect to a chosen fiducial cosmology in the directions parallel and perpendicular to the line of sight, which are often characterized by the parameters $\alpha_\parallel$ and $\alpha_\perp$. These parameters are related to the Hubble parameter and the angular diameter distance (Eq. 1.1.39) by:

$$\alpha_\parallel = \frac{H^{\rm fid}(z) r_d^{\rm fid}}{H(z) r_s}, \qquad \alpha_\perp = \frac{d_A(z) r_d^{\rm fid}}{d_A^{\rm fid}(z) r_d}, \tag{1.3.35}$$

where the superscript 'fid' refers to the fiducial cosmology. These parameters can be combined to form a volume averaged distance given by:

$$d_V = \left[(1+z)^2 z \frac{d_A^2(z)}{H(z)} \right]^{\frac{1}{3}}. \tag{1.3.36}$$

- **Alcock-Paczynski effect**: There is a difference in the distortion in the correlation function in the radial direction and the distortion in the transverse direction arising from the geometry of the Universe. This is called the Alcock-Paczynski effect [114] and it is parameterized by the Alcock-Paczynski parameter that measures the ratio of the distortion along the line of sight and the perpendicular direction:

$$F_{AP} = (1+z) D_A(z) H(z). \tag{1.3.37}$$

- **Observations**: The first observations of the BAO peak were reported at similar times by the Baryon Oscillation Spectroscopic Survey (BOSS, [113]) and the 2dF Galaxy Redshift Survey (2dFGRS, [115]). The best constraints on galaxy BAO at the present time come from BOSS DR12 Consensus measurements [116] probing a redshift range $0.35 < z < 0.65$.

[a]The spherical Bessel functions of the first kind $j_n(x)$ are related to the Bessel functions J_n by:

$$j_n(x) = \sqrt{\frac{\pi}{2x}} J_{n+\frac{1}{2}}(x). \tag{1.3.34}$$

- **Quasar BAO** Quasars or quasi-stellar objects are extremely luminous active galactic nuclei that constitute some of the most luminous sources in the Universe, and as a consequence they can be observed at very high redshifts. Their high luminosity means that a measurement of the BAO peak of quasars provides information about the large-scale structure of the Universe at $z > 1$. Such measurements were recently performed by the extended Baryon Oscillation Spectroscopic Survey (eBOSS) [117].
- **Lyman-α BAO**: An alternative tracer of the matter distribution of the Universe that can be used to measure the BAO peak at a redshift even higher than the quasar BAO measurement are observations of the Lyman-α (Lyα) forest [118]. The Lyα forest consists on a series of absorption lines in the spectra of distant objects that maps the distribution of neutral hydrogen in the intergalactic medium, and as a consequence can trace the matter distribution of the Universe at high redshift. The most accurate measurements of the Lyα BAO feature to date come from BOSS DR12 [119] at $z = 2.3$. Furthermore, additional information can be obtained from the cross-correlation between Lyα and quasar BAO [120].

1.3.4 Type Ia Supernovae

- **Constraints on density parameters**: Type Ia Supernovae (SNe) are supernovae occurring in binary systems in which one of the members is a carbon-oxygen white dwarf that accretes enough mass to approach the Chandrasekhar limit of $1.44 M_\odot$ [121]. Before reaching this limit, the high temperature of the core ignites carbon fusion, which causes the supernova explosion. While the details of the physical mechanism behind this explosion are not well established (see [122] for a review), the stability on the peak luminosities of type Ia SNe has led to their use as a standard candle. Measurements of their apparent magnitude m for a given absolute magnitude M prove the luminosity distance d_L through:

$$m = 5 \log_{10} \left(\frac{d_L(z)}{\text{pc}} \right) + M - 5. \tag{1.3.38}$$

  d_L constrains the dimensionless density parameters Ω_I through the relations (1.1.28) and (1.1.37). Alternatively, low-redshift supernovae can be used to constrain the deceleration and jerk parameters q_0 and j_0 defined by Eqs. (1.1.14b) and (1.1.14c) using a low-redshift expansion such as Eq. (1.1.13).
- **Constraints on the Hubble parameter**: Note that the luminosity distance is proportional to H_0^{-1}, which means that the Hubble constant acts as a normalization factor in Eq. (1.3.38). This causes a degeneracy between the Hubble constant and the absolute

magnitude M which cannot be accurately modelled or constrained through observations. Therefore, SNe alone cannot constrain the Hubble parameter. Constraints on H_0 require calibration of the SNe measurements through what is called the *cosmic distance ladder* [123]: Using measurements of nearby objects whose distances can be accurately measured to calibrate the luminosity of a standard candle, which can then be used to calibrate another standard candle. The use of the cosmic distance ladder requires very high accuracy, as inaccuracies in one of the steps propagate through all the measurements.

- **Observations**: The main result from SNe cosmology is the discovery of the accelerated expansion of the Universe [16; 17], where the relation between observed luminosities and redshift of SNe, commonly known as a *Hubble diagram* (Fig. 1.13) clearly rejected a matter dominated Universe in favour of an accelerating Universe, which requires the existence of dark energy or a cosmological constant.

  Present day observations of SNe are also an interesting topic and central to this thesis. In particular, cosmic distance ladder constraints using SNe to measure the Hubble parameter have been in tension with the CMB predictions since the first CMB measurements. The most accurate constraints to date are those obtained by the Supernovae, H_0, for the Equation of State of dark energy (SH0ES) [125] who used a three-step cosmic distance ladder consisting on local distance anchors, Cepheid stars and SNe, and obtained $H_0 = 73.48 \pm 1.66$ km s^{-1}Mpc^{-1}, in tension with the latest *Planck* CMB constraints at the 3.5σ level. This is the biggest tension in cosmology at the present time, and it is of particular interest because while CMB measurements need to use a cosmological model to derive a value of H_0, SNe measurements are independent of the cosmology. As a consequence, there have been numerous attempts to solve this tension introducing extensions to the ΛCDM cosmology [e.g. 126; 127; 128; 129; 130]. So far, no simple extension of ΛCDM capable of solving this tension has been found [1].
- **Inverse distance ladder**: SNe can be used to obtain constraints on H_0 using high redshift measurements as an alternative calibration. As previously described, BAO measurements are calibrated by the sound horizon at radiation drag, which is accurately measured by the CMB or by measurements of primordial deuterium abundance [131; 132; 133]. Therefore, the combination of SNe and BAO calibrated by r_d provides constraints on the Hubble parameter. This method is called the inverse distance ladder [134; 135; 136; 137], and it will be used to address the tension in H_0 in Chapter 7.

1.3.5 CMB lensing

Similarly to the lensing of galaxy images described previously, the CMB radiation is also lensed by large-scale structure. The main effect of lensing on the CMB spectra is a smoothing

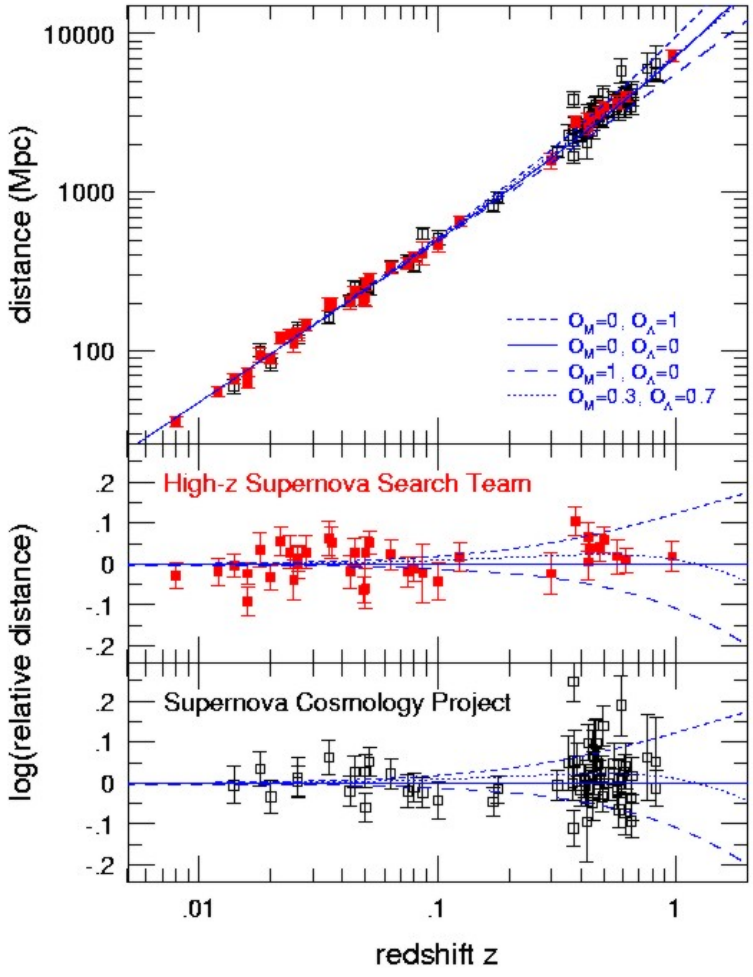

Figure 1.13: Hubble diagram showing distance versus redshift for Type Ia SNe. In red are the points measured by the High-z Supernovae Search Team [17] and in black those measured by the Supernovae Cosmology Project [16]. The different lines show different models of the Universe. In the lower panels, the horizontal line at zero represents an empty Universe, and relative distances to this model are plotted on a logarithmic scale. Image credit: [124]

of the acoustic peaks. Another significant consequence of CMB lensing is that it can convert E-modes into B-modes. For these reasons, correcting for the effect of CMB lensing (a process known as 'delensing') is fundamental to searches for gravitational wave B-modes with CMB measurements.

CMB lensing should not be thought of as a contaminant of the CMB signal, as it provides complimentary information about the Universe. CMB lensing can be seen as a remapping of the CMB signal θ:

$$\theta(\hat{n}) \rightarrow \tilde{\theta}(\hat{n}) = \theta(\hat{n} + \nabla\phi), \tag{1.3.39}$$

where $\tilde{\theta}$ is the lensed signal, and ϕ is the lensing potential. Using the statistical properties of the unlensed CMB, the CMB lensing potential can be reconstructed [138; 139; 140; 141]. This reconstruction provides information about the large-scale structure of the Universe at $z \sim 2$.

1.3.6 Redshift-space distortions

Redshift-space distortions (RSD) are caused by the peculiar motion of galaxies. Spectroscopic surveys use measurements of the redshift of galaxies to estimate their radial distance, but part of the measured redshift is caused by peculiar motions. Comparisons between the transverse and line-of-sight anisotropies in the positions of galaxies can be used to isolate the effect of peculiar velocities, and therefore provide measurements of the growth rate of structure [142] through the parameter combination $f\sigma_8$, where the growth factor f is defined as:

$$f(z) \equiv \frac{\mathrm{d}\log D}{\mathrm{d}\log a}, \tag{1.3.40}$$

with D the linear growth rate introduced in (1.2.44). In ΛCDM the growth factor can be approximated by $f(z) \approx \Omega_m(z)^{0.55}$. While accurate measurements of RSD are highly challenging, BOSS recently reported measurements at 6% precision in the redshift range $z = 0.38 - 0.61$ [116].

1.3.7 Standard sirens

A technique that has recently become available to cosmology and has potential to become a powerful probe in the future is the detection of gravitational waves with electromagnetic counterparts, also known as standard sirens. The recent first detection of gravitational waves [143] followed by the first detection of an electromagnetic counterpart [144; 145] have opened a new window of astronomical observations. Because the luminosity distance can be constrained using only the gravitational wave signal, additional redshift information using spectroscopy can constrain the Hubble parameter H_0 with no dependence on the cosmological model and no need

for calibration. While present-day constraints are not precise ($H_0 = 70.0^{+12.0}_{-8.0}$ km s^{-1}Mpc^{-1}), standard sirens could potentially arbitrate the tension between CMB and direct measurement of the Hubble parameter in the future, especially if the radio and X-ray afterglows of the merger event are used [146].

Part II

Tests at High Redshifts

CHAPTER 2

USING *PLANCK* DATA TO EXPLORE OSCILLATIONS AND FEATURES IN THE PRIMORDIAL POWER SPECTRUM

2.1 Introduction

As described in the introduction, inflation was originally introduced to explain the flatness, homogeneity and lack of magnetic monopoles in the Universe, but it gained importance as an explanation for the formation of overdensities that eventually evolve into the large-scale structure we observe today. In addition, the theory predicts a nearly flat, homogeneous and isotropic Universe; a prediction that is strongly supported by measurements of the temperature anisotropies in the CMB. The most precise all-sky measurements of the CMB today have been performed by the *Planck* Satellite [147; 148].

The results from *Planck* are consistent with a spatially flat, ΛCDM Universe; with a nearly scale-invariant spectrum of adiabatic fluctuations. The *Planck* data give no evidence for non-Gaussianity or isocurvature modes. These results are consistent with simple single-field models of inflation [1; 21; 30; 149]. However, the observed *Planck* spectra (Temperature, E-mode polarization and their cross-correlation, henceforth referred to as TT, EE and TE respectively) show a number of features that do not fit well with ΛCDM. In particular, there is a lack of power in the TT quadrupole and at multipoles $\ell \sim 20$, and oscillatory residuals in the TE and EE spectra, as illustrated in Fig. 2.1. While these features in isolation do not conflict at high significance with ΛCDM, we will investigate theoretical models of the primordial power spectrum that can

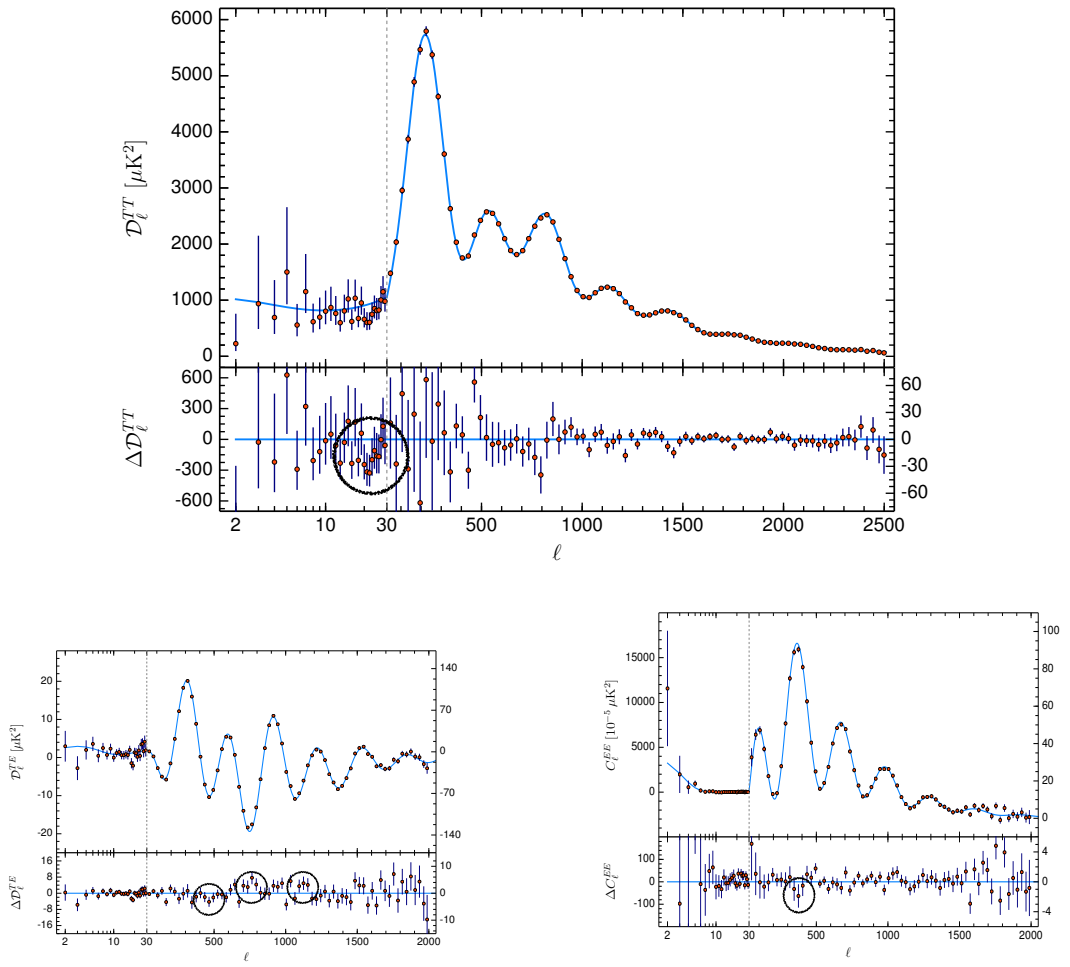

Figure 2.1: Spectra (top) and residuals (bottom) corresponding to the best fit *Planck* cosmology, obtained from Figs. 1 and 2 in [1] . The red dots correspond to the observed data, and the blue line is the best fit ΛCDM model. The top plot is the TT spectrum, bottom left is TE, and bottom right EE. The black circles highlight the features described in the text.

potentially account simultaneously for several of these features, thus significantly improving the fit to the data. Our analysis focuses on two theoretically well motivated inflationary scenarios: Axion monodromy inflation [150; 151; 152] and models which produce a localised oscillatory feature in the primordial power spectrum.

Axion monodromy inflation was originally formulated as a theory of large field inflation ($\Delta\phi > M_P$, where ϕ is the inflation potential and M_P the Planck mass[a]) in string theory inspired models, evading the Baumann-McAllister bound [153]. In this theory, a super Planckian

[a] $M_P = \sqrt{\hbar c/G}$ where $\hbar$ is the reduced Planck constant, c is the speed of light in vacuum, and G is the gravitational constant.

inflaton field range is achieved through a field winding many times around nearby closed paths in configuration space. The underlying periodicity leads to a sinusoidal modulation of the effective inflation potential which, in turn, will produce oscillations in the power spectrum. The shape of the effective potential, and the amplitude, frequency and wavenumber dependence cannot be predicted reliably through theory. Therefore, axion monodromy models as analysed here, should be thought of as phenomenological models that introduce sinusoidal modulations of the curvature power spectrum over the entire wavenumber range accessible to observations. The amplitude and frequency of oscillations are free parameters to be constrained by the data. Axion monodromy models were already tested against *Planck* data [30; 149], finding a marginal improvement for oscillations with certain frequencies. The present work uses the latest data from *Planck* and includes the latest constraints on the optical depth at reionization [154], and analyses the individual fit to the temperature and polarization spectra using the `CamSpec` temperature and polarization likelihoods.

The second type of model that we have tested involves localised oscillatory features in the power spectrum, and will be referred to as the 'pulse' model. There are many theoretical models of inflation that can produce these pulses, such as models with a sharp step in the inflationary potential [64; 155; 156; 157], inflationary models in which the sound speed changes suddenly [158; 159; 160], excitations of heavy fields [161; 162], particle production during inflation [163; 164; 165], or a sharp bending on the trajectory of the inflaton [166; 167; 168; 169]. Features in the primordial power spectrum have previously been explored using CMB data, both from WMAP [170; 171; 172; 173; 174; 175] and from *Planck* [175; 176; 177], including reports of models that provide marginal improvements in the fit to the data. Patterns of oscillations in the power spectrum have also been introduced as a potential tool to distinguish between inflation and alternative theories of the early universe [178; 179]. Our analysis is motivated by the potential of localized oscillations in the primordial power spectrum to fit several of the features in the Planck spectrum shown in Fig. 2.1. Therefore, we will use a phenomenological, model-independent parameterization of such localized oscillations.

The chapter is structured as follows: Sec. 2.2 briefly introduces the theoretical framework behind both inflationary scenarios and motivates the templates that will be used for parameter estimation. Sec. 2.3 presents the results from this analysis, and our conclusions are presented in Sec. 2.4.

2.2 Models

2.2.1 Axion monodromy inflation

Axion monodromy inflation solves the problem of UV sensitivity present in models of large field inflation using the shift symmetry of axions $\phi \to \phi +$ constant. This shift symmetry is continuous, and valid at all orders in perturbation theory. However, it can be weakly broken by non-perturbative effects (or explicitly, through the presence of branes) leading to a discrete shift symmetry $\phi \to \phi + 2\pi f$, where f is the axion decay constant[a]. Generally, models exhibiting a similar weakly broken symmetry are described by a Lagrangian of the form:

$$\mathcal{L} = -\frac{1}{2}(\partial\phi)^2 - V_0(\phi) - \Lambda^4(\phi)\cos\left[a(\phi)\right], \tag{2.2.1}$$

where ϕ is the inflaton field, Λ is a constant with dimension of mass, $V_0(\phi)$ is the leading term in the inflaton potential and $a(\phi)$ is the underlying periodic axion variable. In axion monodromy inflation, the shift symmetry is broken through $V_0 = \mu^{4-p}\phi^p$ with p a constant:

$$\mathcal{L} = -\frac{1}{2}(\partial\phi)^2 - \mu^{4-p}\phi^p - \Lambda^4\cos\left[\frac{\phi}{f}\right], \tag{2.2.2}$$

where μ is a constant mass scale. The power spectrum for primordial fluctuations can be derived from this potential. The calculation assumes a number of e-foldings of inflation $N \sim 60$, slow roll regime and $f \ll M_p$ (for details of this derivation, see [180]), and yields:

$$\Delta^2_\zeta(k) = A_s\left(\frac{k}{k_0}\right)^{n_s-1}\left[1 + \delta n_s\cos\left(\frac{\phi_k}{f} + \Delta\phi\right)\right], \tag{2.2.3}$$

where A_s and n_s are the amplitude and tilt of the primordial power spectrum from Eq. 1.2.30, k_0 is the pivot scale; and ϕ_k and ϕ_* are the values of the inflation when the modes of length k^{-1} and k_*^{-1} leave the Hubble horizon respectively, $\Delta\phi$ is the phase of the oscillation, and δn_s is their amplitude. The frequency dependence is given by:

$$\phi_k = M_P\sqrt{2p\left(N_0 - \log\frac{k}{k_0}\right)}, \tag{2.2.4}$$

with $N_0 = N_* + (\phi_{end}/M_P)^2/2p$ and ϕ_{end} the value of the inflaton field ϕ at the end of inflation. There are some physically motivated constraints on these parameters: The amplitude of the oscillations δn_s must be small, to keep the oscillations as a perturbative effect; the axion decay constant has an upper limit ($f \sim M_p$) and a lower limit ($f > m_\phi$) since the theory is obtained integrating out scales heavier than the inflaton, and therefore can only describe dynamics on

[a]Note that f is used throughout this work as the axion decay constant, which is inversely proportional to the frequency of the oscillations.

smaller mass scales. Our power spectrum template is based on a more general model derived in [181], that allows for a constant drifting in the frequency of the modulations by adding an extra parameter p_f, since the frequency of the oscillations can vary dynamically during inflation. While it is possible that the amplitude of the oscillations can also vary during inflation, we do not add an amplitude modulation parameter, to limit the degeneracies between the parameters. The power spectrum for this model is:

$$\Delta^2_\zeta(k) = A_s \left(\frac{k}{k_0}\right)^{n_s-1} \left\{1 + \delta n_s \cos\left[\frac{\phi_0}{f}\left(\frac{\phi_k}{\phi_0}\right)^{p_f+1} + \Delta\phi\right]\right\}. \tag{2.2.5}$$

This primordial power spectrum is shown in Fig. 2.2. The value of the inflaton at inflation end for a power-law potential ($V \propto \phi^p$) is [182]:

$$\phi_{end} \approx \left(\frac{2p-1}{2\sqrt{2}}\right) M_P. \tag{2.2.6}$$

This approximation is valid in our case as the amplitude of the oscillations is required to be small to make sure these are a perturbation to the power law potential. In addition, [182] provides a formula to calculate the number of e-folds between the pivot scale and the end of inflation, which assuming instant reheating is:

$$N_* = 66.9 - \log\left(\frac{k_0}{a_0 H_0}\right) + \frac{1}{4}\log\left(\frac{V_*^2}{M_P^4 \rho_{\rm end}}\right) - \frac{1}{12}\log g_{\rm reh}, \tag{2.2.7}$$

where a_0 and H_0 are the scale factor and Hubble parameter today, $\rho_{\rm end}$ is the energy density at the end of inflation, V_* is the inflationary energy density at the pivot scale and $g_{\rm reh}$ is the number of equivalent bosonic degrees of freedom after reheating.

2.2.2 Inflation with localised features in the power spectra

In this section we want to explore models with a single localised pulse injected somewhere in the power spectra. These models have greater flexibility to model localised features in the CMB power spectra. This is because axion monodromy models are strongly constrained to low amplitudes by the low multipoles of the TT power spectrum. This is not the case for pulse models, which can fit high amplitude features at high multipoles because of the restricted range of wavenumbers for the oscillations. Our template for the power spectrum, shown in Fig. 2.3, follows the idea introduced in [177; 183] of adding a piece-wise perturbation to the primordial power spectrum, However, we use oscillations and parameters similar to those introduced in the monodromy template (Eq. 2.2.3), with the objective of comparing both models. This is a phenomenological choice of template, that is not based in any specific underlying mechanism causing oscillations. Therefore, our template has the form of the power spectrum for a baseline

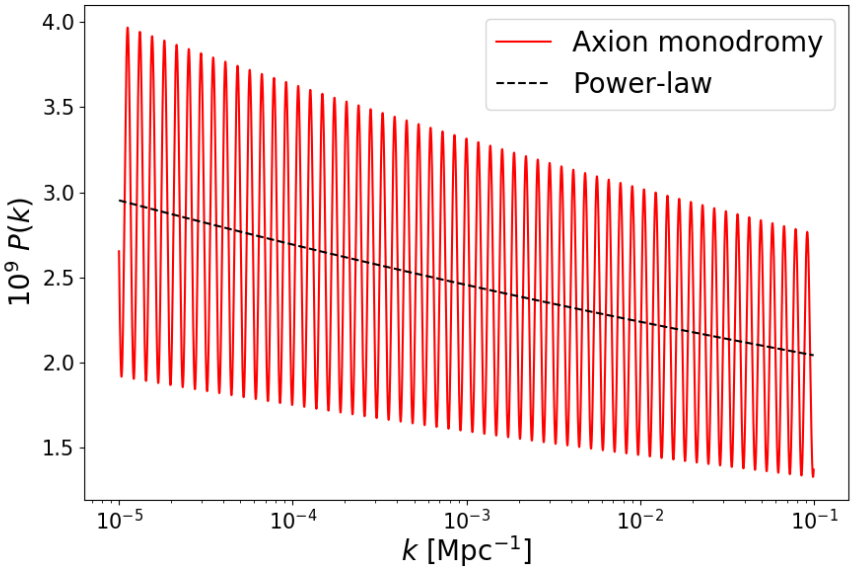

Figure 2.2: The primordial power spectrum for axion monodromy inflation in red, compared to a power-law power spectrum shown as a dotted black line. Both spectra have $n_s = 0.96$ and $A_s = 2.1 \times 10^{-9}$. The values of the parameters specific to axion monodromy correspond to the centre of the priors used in the analysis (Table 2.1).

ΛCDM model (Eq. 1.2.30), with a perturbation that corresponds to the oscillations caused by the pulse:

$$\Delta^2_\zeta(k) = \Delta^2_{\zeta,0}(k) + \delta\Delta^2_\zeta(k) \qquad \text{where} \qquad \Delta^2_{\zeta,0}(k) = A_s \left(\frac{k}{k_0}\right)^{n_s-1}, \tag{2.2.8}$$

and:

$$\delta\Delta^2_\zeta(k) = \begin{cases} 0 & k < k_f \\ \delta n_s \left(\frac{k}{k_f}\right)^{-\alpha} \cos\left[\frac{\phi_k}{f} + \Delta\phi\right] & k \geq k_f. \end{cases} \tag{2.2.9}$$

Note that while f does not have an interpretation as a decay constant in this template, it is still used as the inverse frequency for similarity with the axion monodromy template. Instead of treating the parameter α describing the damping of the amplitude as a free parameter, we study two possible values: $\alpha = 1.5$ and $\alpha = 3$. The reason to not treat α as a free parameter is to limit the degeneracies in parameter space. As we will show in the following sections, the choice of fixed values of α is sufficient to show that we find unphysical results from the *Planck* polarization likelihoods. The parameter k_f refers to the wavenumber at which the feature in the potential occurs, and will be treated as a free parameter.

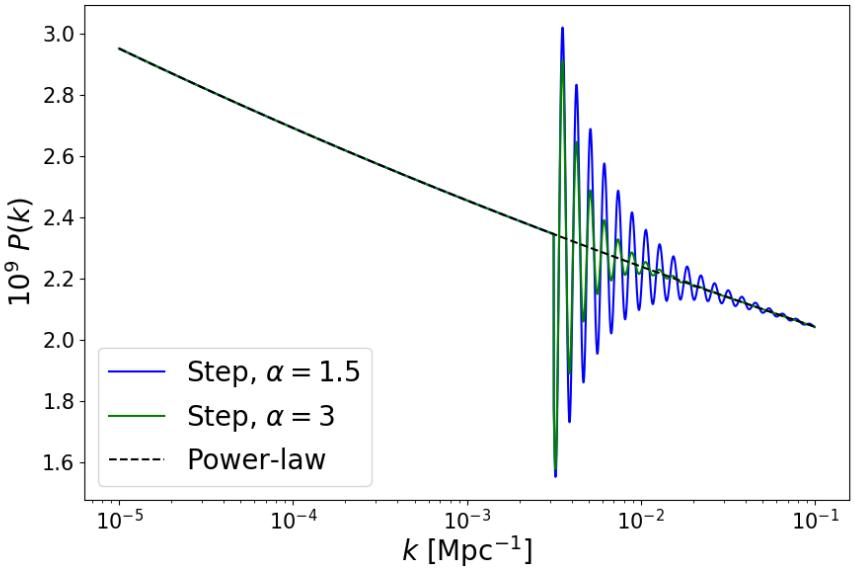

Figure 2.3: The primordial power spectrum for inflation with localized oscillations in the primordial power spectrum with $\alpha = 1.5$ in blue and $\alpha = 3$ in green, compared to a power-law power spectrum shown as a dotted black line. Both spectra have $n_s = 0.96$ and $A_s = 2.1 \times 10^{-9}$. The values of the parameters specific to the pulse model correspond to the centre of the priors used in the analysis (Table 2.1).

2.3 Results

2.3.1 Nested sampling analysis

This section presents the comparison between the inflationary models introduced in the previous section and ΛCDM fitted to the *Planck* 2018 data. We use the nested sampling algorithm `PolyChord` [184; 185] in combination with the Markov Chain Monte Carlo (MCMC) `CosmoMC` package [186], both publicly available. `PolyChord` is a nested sampling algorithm, which uses sliced sampling, as opposed to the rejection sampling method used by `MultiNest` [187; 188; 189]. It also uses a clustering algorithm, to identify posteriors with multiple localised maxima; and in its application within `CosmoMC` is adapted to use the fast and slow parameters hierarchy [190]. This hierarchy between fast and slow parameters is one of the main advantages of `PolyChord` over `MultiNest` for this problem. The resolution of the algorithm is given by the parameter `nlives`, which indicates the number of live points that are used during the nested sampling, in our case `nlives` = 1000. We use the latest `CamSpec` *Planck* likelihood at high multipoles ($\ell > 29$). At low multipoles ($\ell \leq 29$) for the temperature and full analyses, we use the `commander` low-ℓ 2015 TT likelihood, but we add a prior on the reionization optical depth $\tau = 0.055 \pm 0.009$ based on [154].

Parameter	Minimum	Maximum
$\Omega_b h^2$	0.005	0.1
$\Omega_c h^2$	0.001	0.99
$\theta_{\rm MC}$	0.5	10
n_s	0.8	1.2
$\log\left(10^{10} A_s\right)$	1.61	3.91
δn_s	0	0.7
$\log_{10}(f/M_P)$	-5	-1
$\Delta\phi$	-3.14	3.14
p_f	-0.75	1
$\log_{10} k_f$[Mpc]	-4	-1

Table 2.1: Limits of the flat priors used on cosmological parameters for the monodromy and pulse templates (Eqs. 2.2.5, 2.2.9). Note that the parameter p_f is only used on the monodromy template, and $\log_{10} k_f$ is only used on the pulse template.

We start by testing the template (2.2.5). This adds four parameters to the baseline ΛCDM analysis: The axion decay constant f, the amplitude δn_s, the phase $\Delta\phi$, and the frequency modulation p_f. Following [181], we fix $p = 4/3$. We choose a pivot scale $k_0 = 0.05$ Mpc^{-1}, which assuming instant reheating and using Eq. (2.2.6) and (2.2.7) implies $\phi_{end} \approx -0.59 M_P$ and $N_* \approx 57.5$. Finally, we set the fiducial value of the scalar field to $\phi_0 = 12.38 M_P$. In the case of the template for inflation with a pulse (Eq. 2.2.9), the number of parameters introduced is the same, with the difference that instead of a frequency modulation, the location of the sharp feature is added as a free parameter. Due to our lack of prior knowledge, we apply a uniform prior in $\log_{10} k_f$ over the range $[-4, -1]$ where k_f is in units Mpc^{-1}. We use flat priors in all cosmological parameters, with the exception of the optical depth to reionization. These priors are specified specified in Table 2.1.

2.3.2 Best-fit values

Our main result is shown in Table 2.2, that shows the improvement in goodness of fit for each model and each likelihood with respect to the *Planck* best fit for the corresponding likelihood. We find reductions of χ^2 larger than eight for all models in the TE and EE likelihoods. Fig. 2.4 shows the degeneracy between the frequency and its modulation, in the form of 'bands' in the marginalized two-dimensional posterior likelihood. Despite this degeneracy, Fig. 2.5 illustrates how certain values of the frequency and its modulation clearly maximize the EE likelihood. In particular, there is a clear tendency to high values of the axion decay constant (low frequencies). The same trend is observed in the case of the pulse, where the best fit to the data is obtained again from a low frequency (Fig. 2.6).

These parameter combinations are modelling the oscillatory residuals in the *Planck* EE

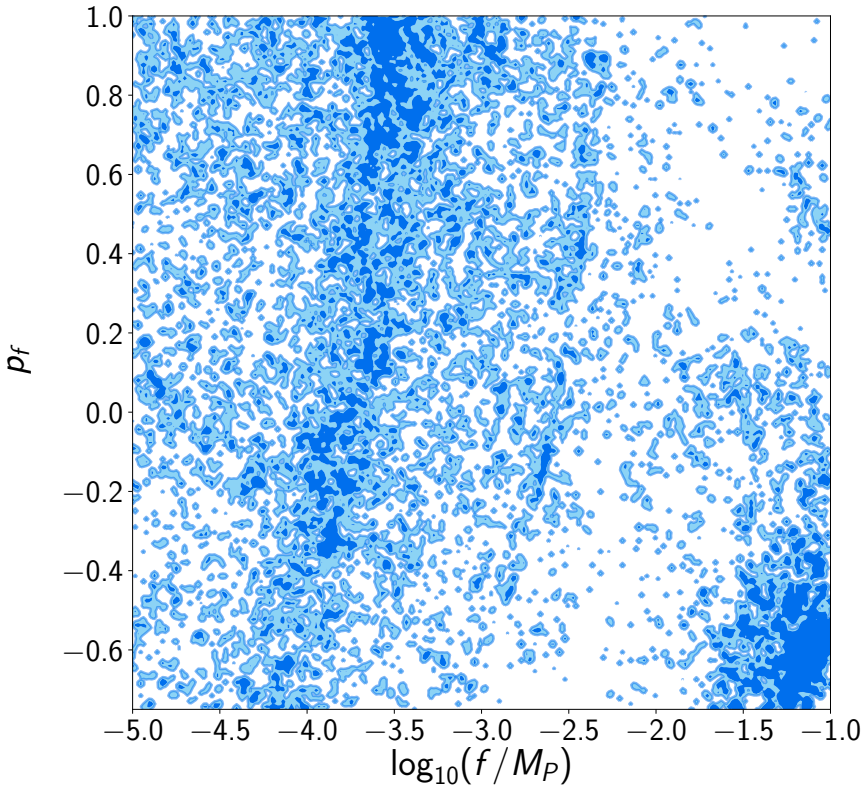

Figure 2.4: Marginalized two-dimensional posterior likelihood for the frequency and its modulation in the axion monodromy template with the EE likelihood. The figure has no smoothing in order to highlight the degeneracy directions.

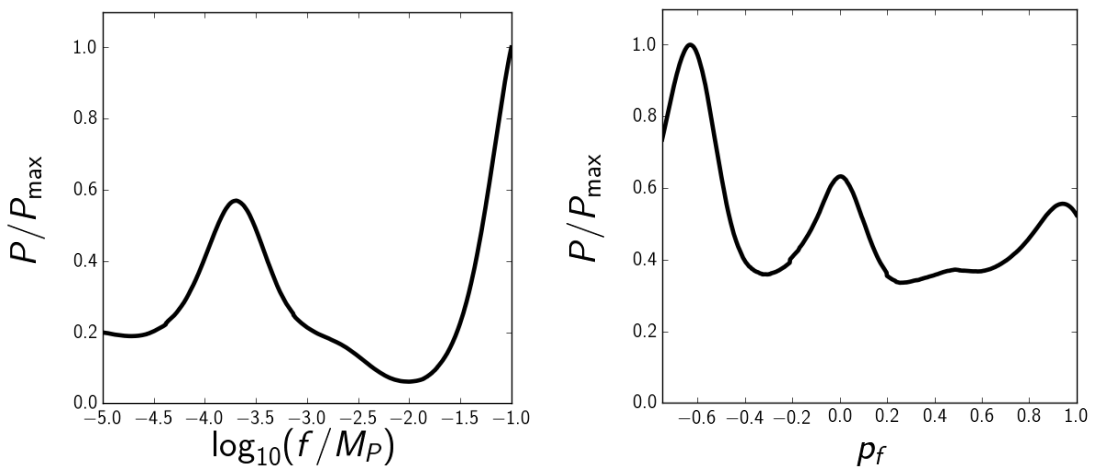

Figure 2.5: Marginalized one-dimensional posterior likelihoods for the frequency (left) and the frequency modulation (right) for axion monodromy inflation with the EE likelihood.

Likelihood	Monodromy		Pulse ($\alpha = 1.5$)		Pulse ($\alpha = 3$)	
	$\Delta\chi^2$	PTE	$\Delta\chi^2$	PTE	$\Delta\chi^2$	PTE
TT	6.62	0.16	5.75	0.22	4.95	0.29
TE	**10.39**	**0.034**	**13.97**	**0.0074**	**12.64**	**0.012**
EE	**10.19**	**0.037**	**12.07**	**0.017**	**13.14**	**0.011**
TT+TE+EE	7.03	0.13	5.76	0.22	6.13	0.19

Table 2.2: Improvement in goodness of fit measured by $\Delta\chi^2 = \chi^2_{\Lambda\mathrm{CDM}} - \chi^2_{\mathrm{model}}$ where 'model' refers to axion monodromy or inflation with localized oscillations in the primordial power spectrum, and $\chi^2 = -2\log(\mathrm{Likelihood})$. The columns show the values of $\Delta\chi^2$ obtained from the best fit values for each model and likelihood with respect to the corresponding *Planck* best fit, and the corresponding probability to exceed (PTE). In bold font those values that provide a PTE below 0.05, corresponding to a significant improvement.

Parameter	Pulse $\alpha = 1.5$ TE BF	Pulse $\alpha = 3$ EE BF
$\Omega_b h^2$	0.0226	0.0232
$\Omega_c h^2$	0.116	0.122
H_0	69.2	66.7
n_s	0.988	0.960
$\log\left(10^{10} A_s\right)$	3.04	3.10
δn_s	0.330	0.689
$\log_{10}(f/M_P)$	-4.96	-1.55
$\Delta\phi$	0.624	-2.51
$\log_{10} k_f$[Mpc]	-1.59	-2.36

Table 2.3: Best-fit values of cosmological parameters for the points in parameter space that produce the largest improvements in χ^2, as shown in Table 2.2.

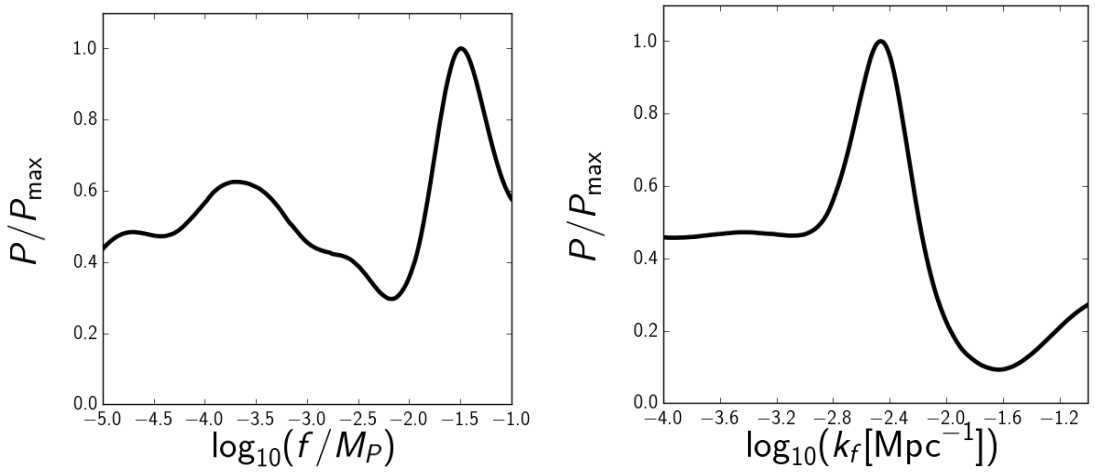

Figure 2.6: Marginalized one-dimensional posterior likelihoods for the frequency (left) and location of the pulse (right) for a primordial power spectrum presenting localized oscillations for $\alpha = 1.5$ and the EE likelihood.

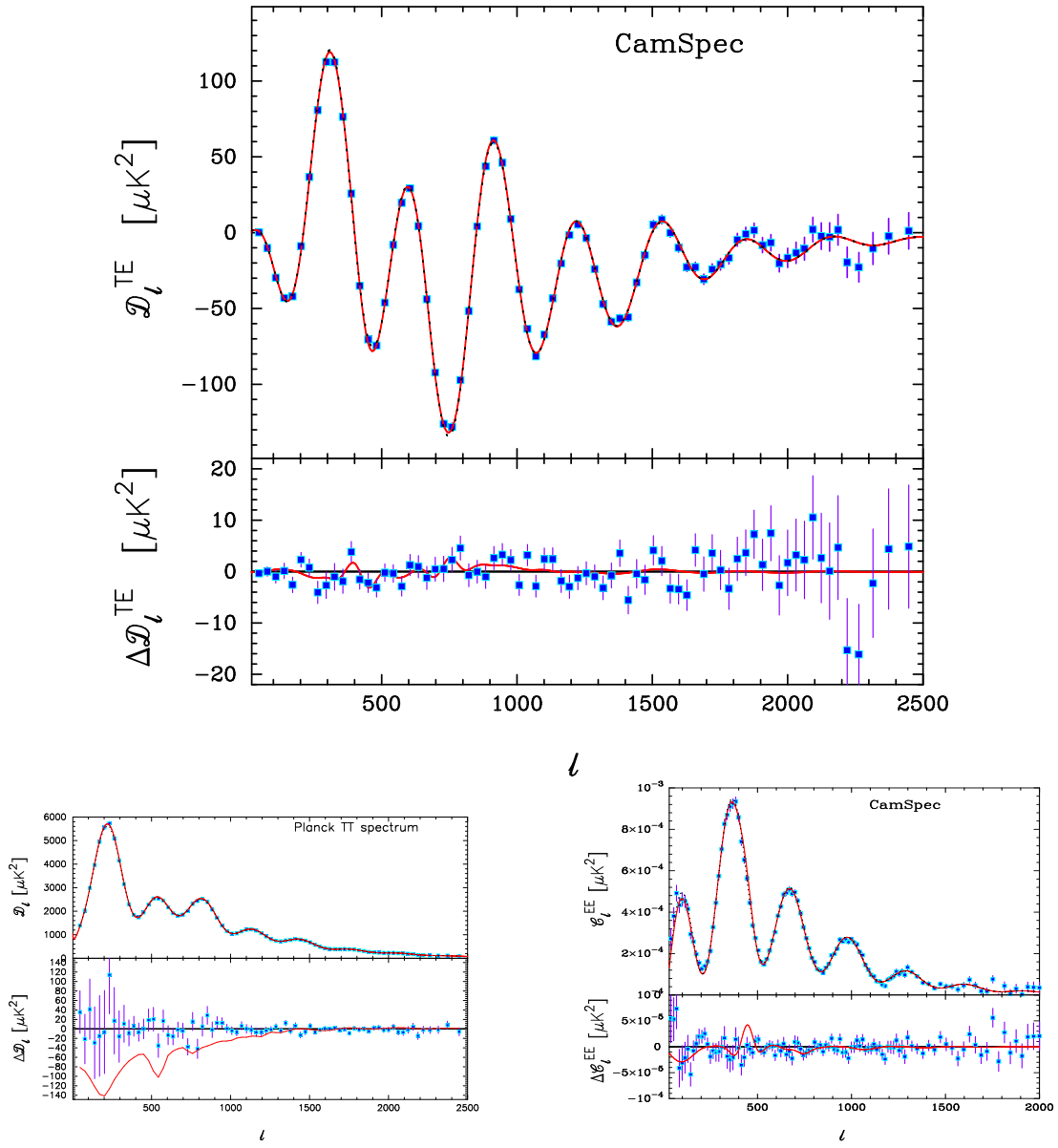

Figure 2.7: Spectra (top) and residuals (bottom) corresponding to the best fit parameters observed in the TE posterior probability for the pulse model with $\alpha = 1.5$. The blue dots correspond to the observed data, the black lines are the best fit ΛCDM models for each likelihood, and the red one to the pulse model. The top plot is the TE spectrum, bottom left is TT, and bottom right EE. The vertical axis for the TT and TE spectra shows $\mathcal{D}_\ell \equiv \ell(\ell+1)C_\ell/(2\pi)$. The lower panels show $\Delta\mathcal{D}_\ell$ for TT and TE, and ΔC_ℓ for EE.

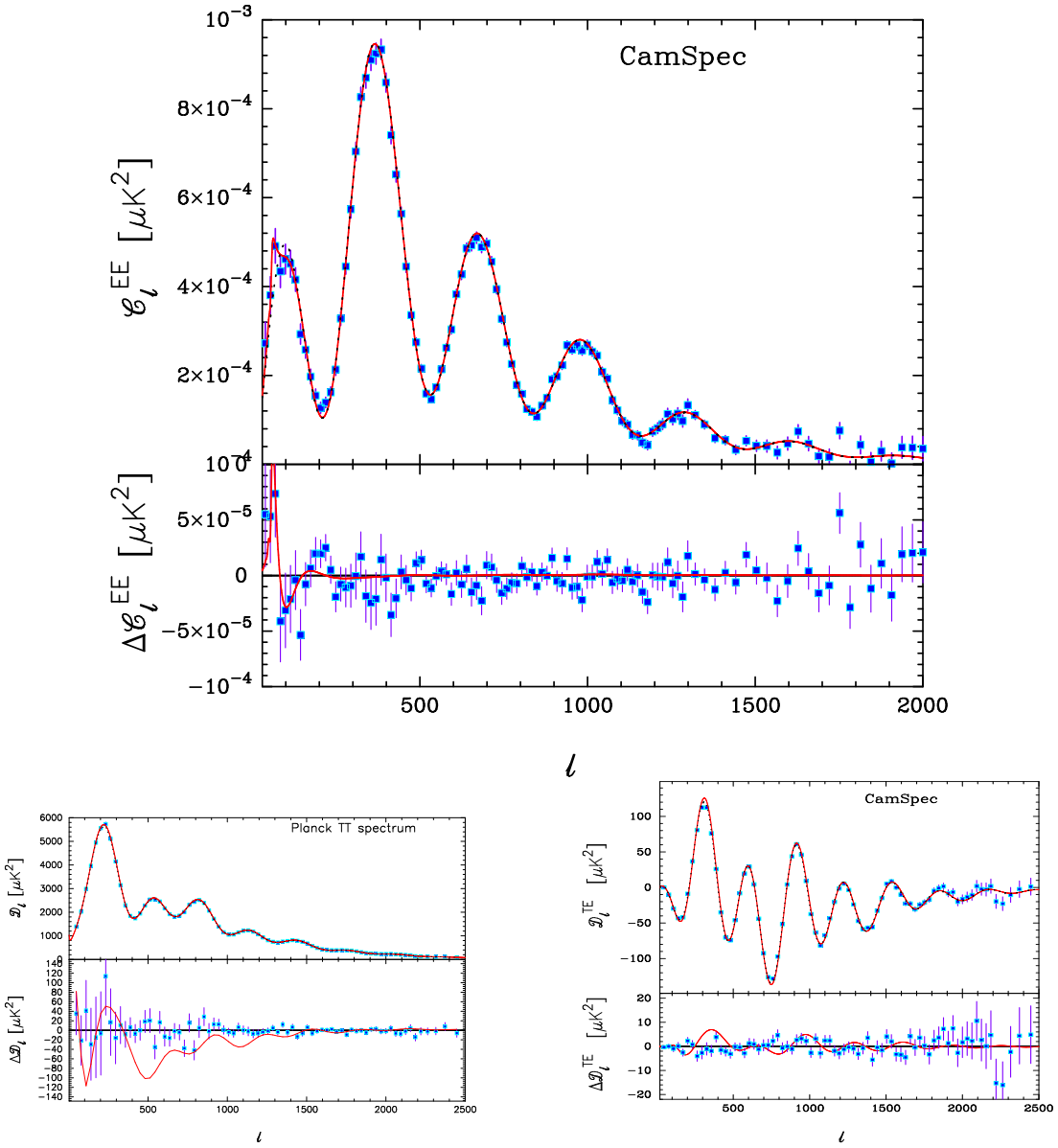

Figure 2.8: Spectra (top) and residuals (bottom) corresponding to the best fit parameters observed in the EE posterior probability for the pulse model with $\alpha = 3$. The blue dots correspond to the observed data, the black lines are the best fit ΛCDM models for each likelihood, and the red one to the pulse model. The top plot is the EE spectrum, bottom left is TT, and bottom right TE. The vertical axis for the TT and TE spectra shows $\mathcal{D}_\ell \equiv \ell(\ell+1)C_\ell/(2\pi)$. The lower panels show $\Delta\mathcal{D}_\ell$ for TT and TE, and ΔC_ℓ for EE.

and TE spectra (Fig. 2.1). However, they provide significantly worse fits to the temperature spectrum than ΛCDM. As shown in Table 2.2, the greatest improvements in χ^2 are obtained by the pulse model on the TE and EE likelihoods, with probabilities to exceed (PTEs) below 0.01. In the case of the TE likelihood, shown in Fig. 2.7, the improvement comes from fitting features at $\ell \sim 400$, $\ell \sim 800$ and $\ell \sim 1000$. However, the bottom panels of this figure illustrate the poor fit that these parameters produce in the TT and EE likelihoods, explaining why these parameters produce a poor fit to the combined TT+TE+EE likelihood. A similar situation is found for the best fit to the EE likelihood (Fig. 2.8): The best fit model reproduces features at low multipoles, but produces a very poor fit to the TT and TE likelihoods.

It is important to stress that these improvements in the different likelihoods correspond to completely different parameter values, as illustrated by Table 2.3. The bottom line of Table 2.2 shows that there is no point in parameter space for any of these models that produces a significant improvement in the fit to the combined TT+TE+EE likelihood. However, the large improvements in χ^2 in the TE and EE likelihoods indicate problems with these two likelihoods. These results are clearly showing that it is possible to greatly improve the fit to these two spectra. While it is possible that some exotic new physics that affects only polarization could fit these features, no such model exists at the present time. Another possible explanation are unknown systematics in polarization, but the fact that most of these features are present across the different *Planck* spectra goes against this idea [148]. The most likely explanation is an underestimation of the contribution of noise to the *Planck* TE and EE spectra at low multipoles. This possibility will be discussed in detail in [191].

We now turn back to the best fits to the full TT+TE+EE likelihood. Table 2.4 shows the best fit parameters for ΛCDM, axion monodromy inflation and inflation with a pulse with $\alpha = 3$. We do not consider the case of the $\alpha = 1.5$ throughout the rest of this subsection, as $\alpha = 3$ provides a larger improvement in goodness of fit. The bottom part of the table shows how, for axion monodromy inflation, the improvement in χ^2 in the full likelihood comes from an improvement in fit to the temperature, while in the case of the pulse there are small improvements in both the temperature and the temperature-cross-polarization spectra. In both cases, the improvement in the full likelihood is obtained from low values of the inverse frequency f, which provide worse fits to the polarization spectrum. Figs. 2.9 and 2.10 show the theoretical model and the data compared to ΛCDM. Again, we see how while in the case of axion monodromy most of the improvement comes from a better fit to the temperature likelihood alone, the pulse model visibly reproduces residuals in all three spectra, but it does not model the residuals in TT as accurately as axion monodromy. We now asses whether these improvements in χ^2 are statistically significant.

Parameter	ΛCDM	Axion monodromy	Pulse ($\alpha = 3$)
$\Omega_b h^2$	0.0224	0.0222	0.0223
$\Omega_c h^2$	0.119	0.120	0.121
H_0	67.6	67.5	67.2
n_s	0.969	0.963	0.965
$\log\left(10^{10} A_s\right)$	3.07	3.03	3.05
δn_s	–	0.0433	0.110
$\log_{10}(f/M_P)$	–	-3.35	-4.50
$\Delta\phi$	–	2.44	2.62
p_f	–	-0.482	–
$\log_{10} k_f$[Mpc]	–	–	-1.44
χ^2_{TT}	7064.54	7057.20	7062.38
χ^2_{TE}	2578.53	2574.54	2576.44
χ^2_{EE}	1892.73	1894.64	1893.51
$\chi^2_{TT+TE+EE}$	11513.04	11505.33	11506.28

Table 2.4: Best-fit values of cosmological parameters for each model. Dashes represent parameters that are not used for the corresponding model. Note that the *Planck* values differ from [1] since we have used slightly different likelihoods.

Bayes factor R

Likelihood	Monodromy	Pulse ($\alpha = 1.5$)	Pulse ($\alpha = 3$)
TT	8.8 ± 3.8	5.3 ± 2.3	8.1 ± 3.5
TE	3.32 ± 0.86	1.45 ± 0.37	1.38 ± 0.35
EE	2.26 ± 0.55	0.62 ± 0.15	0.82 ± 0.20
TT+TE+EE	8.1 ± 4.5	5.8 ± 3.2	8.9 ± 3.4

Table 2.5: Bayes factor $R \equiv \mathcal{Z}_{\Lambda CDM}/\mathcal{Z}_{\text{model}}$ where 'model' refers to axion monodromy or inflation with a pulse, and $\mathcal{Z}$ is the Bayesian evidence. A value $R > 1$ means that ΛCDM is preferred by the data, while $R < 1$ means the corresponding model is preferred.

2.3.3 Bayesian model comparison

In this section, we use Bayesian model comparison to asses the validity of this models. In a Bayesian framework, models are compared using the Bayes factor or evidence ratio, formed as the ratio of Bayesian evidences.

$$\mathcal{Z} \equiv P(D|M) = \int \mathrm{d}\theta P(D|\theta, M) P(\theta|M), \tag{2.3.1}$$

where D represents the data, M the model, and θ the parameters of the model. The terms inside the integral are the likelihood $P(D|\theta, M)$ and the prior $P(\theta|M)$. For the comparison between the ΛCDM cosmology and a second model M, the Bayes factor is given by:

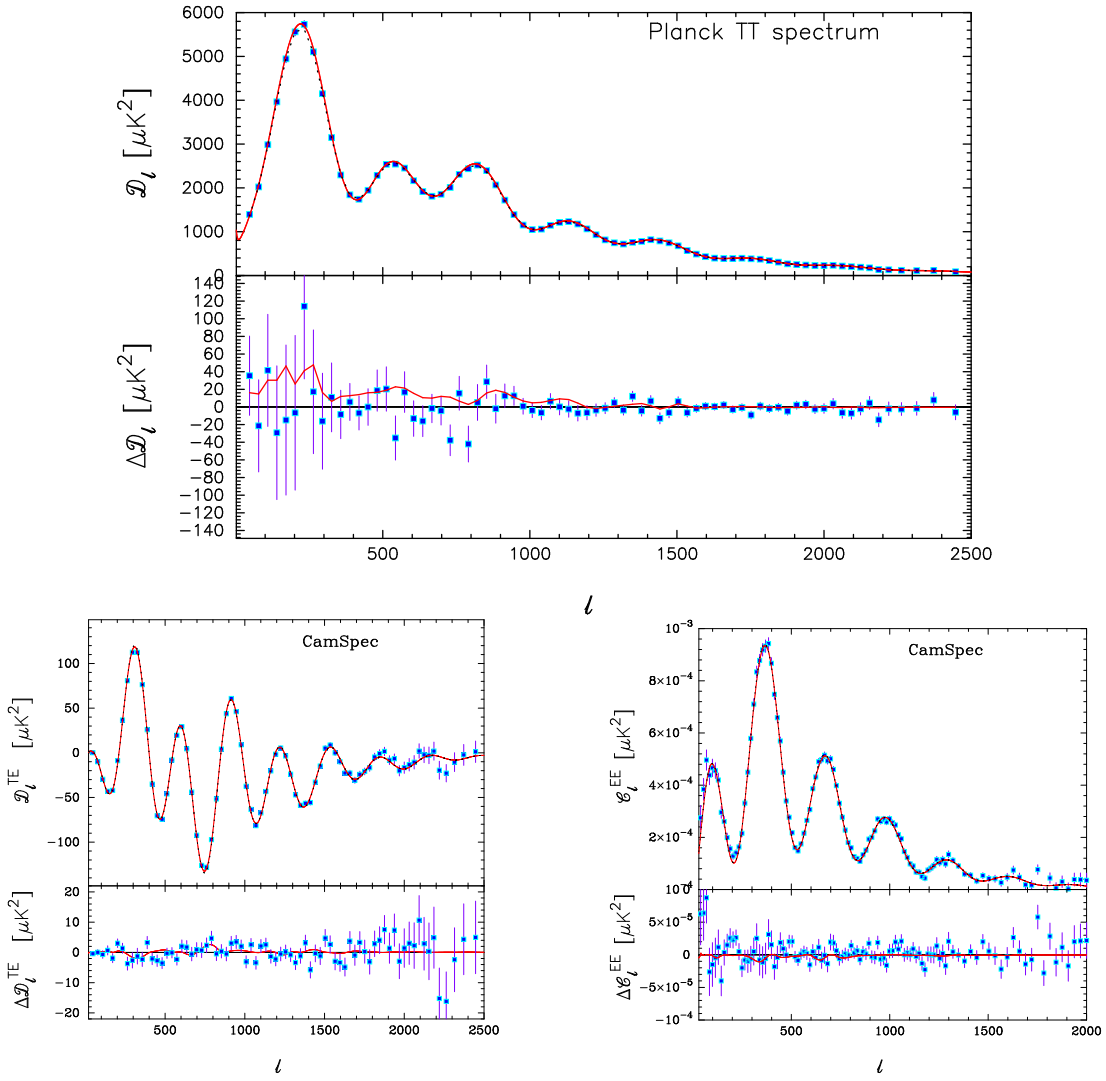

Figure 2.9: Spectra (top) and residuals (bottom) corresponding to the best fit parameters observed in the TT+TE+EE posterior probability for axion monodromy inflation. The blue dots correspond to the observed data, the black line is the best fit ΛCDM model to the TT+TE+EE likelihood, and the red one to axion monodromy inflation. The top plot is the TT spectrum, bottom left is TE, and bottom right EE. The vertical axis for the TT and TE spectra shows $\mathcal{D}_\ell \equiv \ell(\ell+1)C_\ell/(2\pi)$. The lower panels show $\Delta\mathcal{D}_\ell$ for TT and TE, and ΔC_ℓ for EE.

$$R = \frac{P(D|\Lambda CDM)}{P(D|M)} = \frac{P(\Lambda CDM|D)}{P(M|D)}\frac{P(\Lambda CDM)}{P(M)}. \tag{2.3.2}$$

Lacking any prior beliefs on either model $P(\Lambda CDM) = P(M)$, the Bayes factor provides a measure of the ratio of probabilities between the models given the data. Therefore, a Bayes factor $R > 1$ favours ΛCDM while a value $R < 1$ favours the alternative model. Table 2.5 shows the value of the Bayes factor for each likelihood and inflationary model in comparison

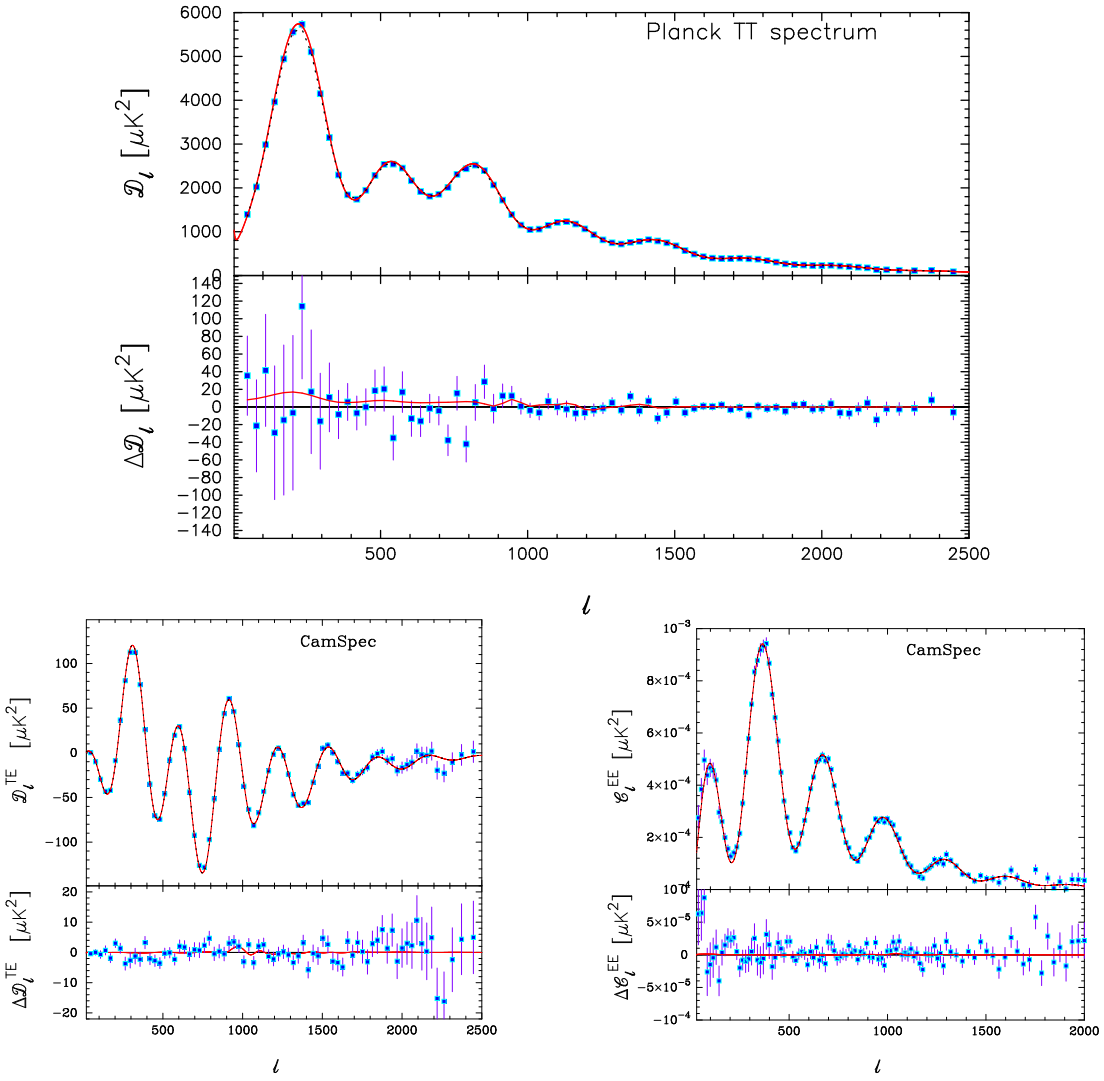

Figure 2.10: Spectra (top) and residuals (bottom) corresponding to the best fit parameters observed in the TT+TE+EE posterior probability for the pulse model with $\alpha = 3$. The blue dots correspond to the observed data, the black line is the best fit ΛCDM model to the TT+TE+EE likelihood, and the red one to inflation with a pulse in the primordial power spectrum. The top plot is the TT spectrum, bottom left is TE, and bottom right EE. The vertical axis for the TT and TE spectra shows $\mathcal{D}_\ell \equiv \ell(\ell+1)C_\ell/(2\pi)$. The lower panels show $\Delta\mathcal{D}_\ell$ for TT and TE, and ΔC_ℓ for EE.

with ΛCDM. While it is true that in some cases the Bayes factor indicates that the data is more compatible with the alternative model, in particular for the pulse model in the EE likelihood, it is worth noticing that the evidence ratio is not small enough to support claims of evidence for departures from ΛCDM. Even if we use a Jeffreys scale [192], which is not at all stringent, we need $R < 0.31$ for 'substantial evidence', which is not the case here. On the cases where the Bayes ratio is bigger than one, a Jeffreys scale requires $R > 3.2$ for substantial evidence, and

$R > 10$ for strong evidence. Only in the case of the TT and TT+TE+EE likelihoods the evidence can be considered substantial, as expected from Table 2.2. The conclusion from this section is that *Planck* 2018 does not provide strong evidence for either monodromy or for localized oscillatory features, and in fact presents substantial evidence against these models.

2.4 Conclusions

We have studied alternative models of inflation with oscillations in the primordial power spectrum using *Planck* 2018 data. After a brief introduction of the mechanisms that could generate such oscillations and a motivation of the assumptions and priors that have been used in the analysis, we present the results of comparing them to the *Planck* 2018 data using a nested sampling algorithm. Although these models can produce significant improvements in the E-mode polarization and cross temperature-polarization likelihoods by modelling some of the oscillatory residuals of these spectra, we find that the parameters that give us this improvement correspond to a worse fit in the full likelihood, indicating that this improvement is not a consequence of new physics. This claim is supported by the fact that the fit to the temperature and the combined TT+TE+EE likelihoods does not significantly improve the ΛCDM model.

A more careful analysis indicates that the improvements in the combined TT+TE+EE likelihood have different origins for each spectra: While in axion monodromy most of the improvements come from the temperature only likelihood, inflation with a localized oscillations in the primordial power spectrum can model the residuals in all three individual spectra, but does not significantly improve the fit to the temperature spectrum. Using Bayesian model comparison we conclude that despite its very high accuracy, *Planck* 2018 data cannot provide strong evidence to favour these models over ΛCDM, and in fact slightly favors ΛCDM. It will be necessary to wait for next-generation CMB experiments [193; 194] to make stronger claims about models of this type. While a more careful study of these models could be performed, for instance allowing for a modulation of the amplitude, or changes in the power of the inflaton p in the case of the monodromy, and for modulation on frequency and amplitude in our pulse model; the results of this work discourage us from performing a more careful analysis at the present time.

Despite not finding evidence in favour of this models, this analysis provides important information. Monodromy models are limited to low amplitudes primarily by the temperature spectrum. Models with localized oscillations in the primordial power spectrum have greater flexibility to fit localized oscillations in the spectra. These pulse models give improvements with PTEs smaller than 0.02 on the TE and EE likelihoods, but with parameters that provide poor fits to the temperature data. While we cannot rule out the possibility of unknown systematics

or exotic new physics being the reason behind the features in these spectra, they are more likely to be caused by an underestimation of the noise at low multipoles in the *Planck* polarization spectra.

Our main conclusion is that the *Planck* 2018 temperature measurements provide strong constraints on models of inflation which produce oscillations in the primordial power spectrum, and as a consequence *Planck* does not favour these models. However, there are oscillations at low multipoles in the TE and EE spectra measured by *Planck* 2018, which are most likely to be a symptom of an underestimation of noise in polarization.

CHAPTER 3

GENERALIZED SLOW-ROLL INFLATION ON PLANCK 2018 DATA

3.1 Introduction

Chapter 2 studied possible departures from a two-parameter primordial power spectrum (Eq. 1.2.30) in the form of oscillations. This chapter studies the possibility of features in the primordial power spectrum in a model-independent way, using an approach called 'Generalized Slow Roll' (GSR) [173; 195; 196; 197] which allows deviations of the base ΛCDM spectrum of order unity. We want to investigate if deviations from a power-law primordial power spectrum can account for some the features in the *Planck* spectra introduced in the previous chapter (Fig. 2.1), and improve the fit to the data. GSR was already applied to *Planck* 2015 data [21; 198; 199] finding a significant deviation from the simple two-parameter primordial power spectrum, and non-negligible shifts in the values of cosmological parameters. In this chapter, we apply GSR to *Planck* 2018. We do this using nested sampling [200], as in the previous chapter, to sample the GSR parameter space, as opposed to previous analyses which used Markov Chain Monte Carlo (MCMC) methods. The chapter is organised as follows: Sec. 3.2 describes GSR from a theoretical point of view, Sec. 3.3 describes the data that we use and the statistical techniques used to perform the analysis. We present our results in Sec. 3.4 and we finish with conclusions in Sec. 3.5.

3.2 The Generalized Slow Roll Formalism

This section presents an overview of the GSR formalism. We start by describing the theoretical basis, and then define the parameterization used in this chapter. We finish this section by introducing the use of principal component analysis (PCA) to calculate the extra degrees of freedom added by GSR. This formalism was first introduced by [195]. Our framework, notation, as well as the way it is parameterized, are based on the analysis of *Planck* 2015 data by [198; 199; 201].

3.2.1 Theory

As described in Sec. 1.2.1, slow-roll inflation (henceforth referred to as 'ordinary' slow-roll as opposed to generalized slow-roll) predicts a two-parameter power spectrum, which to first order in slow-roll parameters can be parameterized as (Eq. 1.2.30):

$$\Delta^2_\zeta(k) = A_s \left(\frac{k}{k_0}\right)^{n_s-1}. \tag{3.2.1}$$

In ordinary slow-roll, the Hubble slow-roll parameters ϵ_H and η_H introduced in Eq. 1.2.10 are small during inflation:

$$\epsilon_H \equiv \frac{\dot\phi^2}{2M_P^2H^2}, \qquad \eta_H \equiv -\frac{\dot\epsilon_H}{H\epsilon_H}, \tag{3.2.2}$$

where ϕ is the inflaton field, M_P is the reduced Planck mass, and H the Hubble parameter. As a result, the usual slow-roll expression for n_s in terms of ϵ and η (Eq. 1.2.31) is obtained. In GSR we relax the requirement of a small η_H, and allow it to become large for a fraction of an e-fold [196]. This produces features of order unity in the primordial power spectrum through the function [195; 202]:

$$G(\log s) = -2\log f + \frac{2}{3}(\log f)', \tag{3.2.3}$$

where $'$ denotes $\mathrm{d}/\mathrm{d}\log s$ and

$$f = 2\pi z_M \sqrt{c_s} s, \tag{3.2.4}$$

with c_s the sound speed, z_M the Mukhanov variable $z_M \equiv a\dot\phi/H$, and s the sound horizon:

$$s = \int_a^{a_{\rm end}} \frac{\mathrm{d}a'}{a'} \frac{c_s}{a'H(a')}, \tag{3.2.5}$$

with $a_{\rm end}$ the scale factor at the end of inflation. The effect of this change on the curvature power spectrum is obtained using Green function techniques [196; 203]:

$$\log \Delta^2_\zeta(k) = G(\log s_*) + \int_{s_*}^{\infty} \frac{\mathrm{d}s}{s} W(ks) G'(\log s) + \log\left[1 + I_1^2(k)\right], \tag{3.2.6}$$

where s_* is an arbitrary epoch during the period of inflation such that $k s_* << 1$ for all relevant k-modes, and:

$$I_1(k) = \frac{1}{\sqrt{2}} \int_0^{\infty} \frac{\mathrm{d}s}{s} G'(\log s) X(ks). \tag{3.2.7}$$

The window functions at leading and second order are given, respectively, by:

$$W(x) = \frac{3\sin(2x)}{2x^3} - \frac{3\cos(2x)}{x^2} - \frac{3\sin(2x)}{2x}, \qquad X(x) = \frac{3}{x^3}(\sin x - x\cos x)^2. \tag{3.2.8}$$

For this to be a good approximation, we limit features in the primordial power spectrum to order unity by requiring that $\max(|I_1|) < 1/\sqrt{2}$ [173].

3.2.2 Parameterization

Having introduced the theoretical framework, we now describe the way it is parameterized and applied in this chapter. Given that $G'(\log s) = 1 - n_s$ recovers the expression for ordinary slow-roll inflation (Eq. 3.2.1) we look for deviations from ordinary slow-roll described by:

$$\delta G'(\log s) \equiv G'(\log s) - (1 - n_s). \tag{3.2.9}$$

We parameterize these deviations by defining a set of spline basis functions $\{B_i(\log s)\}$ with coefficients $\{p_i\}$ [199; 201]:

$$\delta G' = \sum_i p_i B_i(\log s). \tag{3.2.10}$$

We limit our analysis to the range $s \in [200, 20000]$ Mpc, since we cannot observe scales larger than the present-day Hubble radius, and we want to study fluctuations that appear on scales larger than the acoustic scale at recombination. We sample $\{\log s_i\}$ with twenty points spaced equally along this range. The spline basis functions are given by:

$$B_i(\log s_j) = \begin{cases} 1 & i = j \\ 0 & i \neq j, \end{cases} \tag{3.2.11}$$

and the spline coefficients are just given by $p_i = \delta G'(\log s_i)$. With this spline basis, the GSR window functions (3.2.8) become:

$$W_i(k) \int_{s_*}^{\infty} \frac{\mathrm{d}s}{s} W(ks) B_i(\log s), \qquad X_i(k) \int_{s_*}^{\infty} \frac{\mathrm{d}s}{s} X(ks) B_i(\log s), \tag{3.2.12}$$

and we choose the arbitrary epoch s_* as the large-scale endpoint of our sampling grid. Using this parameterization, the curvature power spectrum is:

$$\log \Delta^2_\zeta = \log A_s \left(\frac{k}{k_0}\right)^{n_s-1} + \sum_i p_i [W_i(k) - W_i(k_0)] + \log\left[\frac{1 + I_1^2(k)}{1 + I_1^2(k_0)}\right], \tag{3.2.13}$$

with

$$I_1(k) = \frac{\pi}{2\sqrt{2}}(1 - n_s) + \frac{1}{\sqrt{2}} \sum_i p_i X_i(k). \tag{3.2.14}$$

In Eq. 3.2.13, we have absorbed the factor $G(\log s_*)$ into the amplitude of the power spectrum $A_s = \Delta^2_\zeta(k_0)$. The main advantage of this approach is that we can pre-compute the window functions (Eq. 3.2.12) on a grid in k-space, and then vary the spline coefficients $\{p_i\}$ to sample the different features on the power spectra.

3.2.3 Principal Component Analysis

The choice of twenty spline parameters greatly oversamples the features in the spectra. To interpret our results, we want to know how many degrees of freedom are really needed to describe significant deviations from the base ΛCDM primordial spectrum. We do this using a principal component analysis from the covariance matrix of the spline coefficients $C_{ij} = \langle p_i p_j \rangle - \langle p_i \rangle \langle p_j \rangle$ derived from the nested sampling chain. We diagonalize this matrix and obtain an orthonormal matrix of eigenvectors S_{ik} related to the original by:

$$C_{ij} = \sum_k S_{ik} \sigma_k^2 S_{jk}. \tag{3.2.15}$$

We can then define the principal component parameters as:

$$m_k = \sum_i S_{ik} p_i. \tag{3.2.16}$$

These principal components are independent, i.e. their covariance matrix is diagonal with values $\{\sigma_i\}$:

$$\langle m_i m_j \rangle - \langle m_i \rangle \langle m_j \rangle = \delta_{ij} \sigma_i^2. \tag{3.2.17}$$

We use PCA to calculate the number of independent degrees of freedom added by GSR. We take this to be the number of principal components that differ from zero by more than one standard deviation, since for N of such parameters we can reconstruct the deviation from Eq. 3.2.9 as:

Parameter	Minimum	Maximum
$\Omega_b h^2$	0.005	0.1
$\Omega_c h^2$	0.001	0.99
$\theta_{\rm MC}$	0.5	10
n_s	0.8	1.2
$\log\left(10^{10} A_s\right)$	1.7	5
$p_i \ \{i \in [1, 20]\}$	-2.5	2.5

Table 3.1: Limits on the flat priors used in this analysis.

$$\delta G'_{N,\rm PC}(\log s_i) = \sum_{k=1}^{N} m_k S_{ik}. \tag{3.2.18}$$

This, in turn, can be then used to reconstruct Δ^2_ζ.

3.3 Data and Analysis

We now apply this method to *Planck* 2018 data. We use the same likelihood employed in the previous chapter: *Planck* 2018 `CamSpec` likelihood [1] with a prior on the optical depth at reionization $\tau = 0.055 \pm 0.009$ based on *Planck* low multipole polarization measurements [154]. In [199], the authors used a MCMC analysis to obtain posterior distribution for the parameters, using the publicly available code `CosmoMC` [186; 190], which for the likelihood evaluations uses the Boltzmann solver `CAMB` [204]. In this analysis, we also use `CosmoMC`, but due to the high number of parameters and the complexity of the parameter space with several degeneracies between the spline and cosmological parameters, the Metropolis algorithm of `CosmoMC` is not very efficient at sampling this likelihood. Therefore, we use the nested sampling algorithm `Polychord` [184; 185] which has already been adapted to work with `CosmoMC` as described in Chapter 2.

Our analysis samples over the same six cosmological parameters for ΛCDM used in the previous chapter: the baryon and cold dark matter densities $\Omega_b h^2$ and $\Omega_c h^2$, the optical depth to reionization τ, an approximation of the ratio of the sound horizon to the angular diameter distance at recombination $\theta_{\rm MC}$, and the amplitude and tilt of the power-law primordial power spectrum A_s and n_s. In addition, for the GSR formalism, we add twenty spline parameters $\{p_i\}$. We use flat priors on these parameters, specified in Table 3.1, with the exception of τ, for which we use a Gaussian prior as previously described. As usual, we take an effective number of neutrinos $N_{\rm eff} = 3.046$ consisting of three massive neutrinos with a combined mass $\sum m_\nu = 0.06$ eV. We choose the pivot scale to be at $k_0 = 0.05$ Mpc, and as mentioned in the

	ΛCDM		**GSR**	
Parameter	best fit	68% CL	best fit	68% CL
$\Omega_b h^2$	0.02201	0.00019	0.02201	0.00020
$\Omega_c h^2$	0.1205	0.0021	0.1211	0.0019
H_0 [km s^{-1}Mpc^{-1}]	66.93	0.89	66.61	0.85
τ	0.0679	0.0073	0.0575	0.0065
n_s	0.9618	0.0060	0.9569	0.0060
$\log\left(10^{10} A_s\right)$	3.055	0.015	3.067	0.014

Table 3.2: Best fit values and 1σ errors of cosmological parameters for 6-parameter ΛCDM (left) and for GSR (right) for the TT likelihood. Note that the *Planck* values differ from [1] since we have used different likelihoods.

	ΛCDM		**GSR**	
Parameter	best fit	68% CL	best fit	68% CL
$\Omega_b h^2$	0.02215	0.00014	0.02239	0.00015
$\Omega_c h^2$	0.1199	0.0013	0.1195	0.0013
H_0 [km s^{-1}Mpc^{-1}]	67.20	0.57	67.62	0.55
τ	0.0624	0.0083	0.0550	0.0067
n_s	0.9632	0.0040	0.9641	0.0048
$\log\left(10^{10} A_s\right)$	3.055	0.015	3.051	0.015

Table 3.3: Best fit values and 1σ errors of cosmological parameters for 6-parameter ΛCDM (left) and for GSR (right) for the TT+TE+EE likelihood. Note that the *Planck* values differ from [1] since we have used different likelihoods.

previous section impose a prior $\max(|I_1|) < 1/\sqrt{2}$ to limit the departures from a power-law spectrum to be of order unity.

3.4 Results

3.4.1 Effect on Cosmological Parameters

Tables 3.2 and 3.3 show best fit values for the TT and full (TT+TE+EE) *Planck* 2018 likelihoods respectively, using a 6-parameter ΛCDM cosmology on the left column, and GSR inflation on the right. None of the parameter shifts are very drastic, with changes below a 1σ significance level for all parameters and both likelihoods, with the exception of the optical depth to reionization τ, which is lowered by around 1σ when GSR is used. When more flexibility in the primordial power spectrum is allowed, τ is dominated by the Gaussian prior at $\tau = 0.055 \pm 0.009$.

We then use the PCA analysis described in Sec. 3.2.3 to estimate how many extra degrees of freedom are being added on each spectrum, which we define to be the number of principal

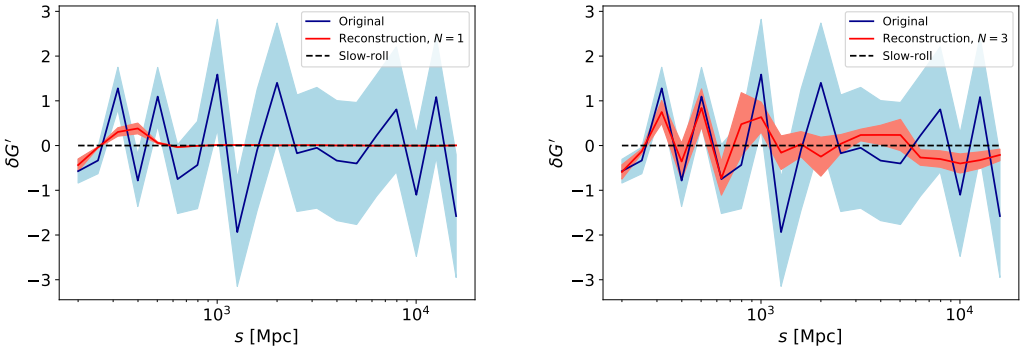

Figure 3.1: PCA reconstruction of the departures from ordinary slow roll using the best fit spline parameters to the EE likelihood, using a number of principal components $N = 1$ (left panel) and $N = 3$ (right panel). In blue, the full twenty parameter departure from slow roll parameterized by $\delta G'$ (Eq. 3.2.9) with the best fit as a solid line, and the 68% confidence intervals as bands. In red, the same for the PCA reconstruction. The black solid line is ordinary slow-roll. As expected, in this case three parameters are needed to reproduce the main features within the error margins.

components that deviate from zero by at least one standard deviation. The results are shown in Table 3.4. The first relevant result is that, from the TT spectrum, all principal components are consistent with zero at the 68% confidence level. This indicates that deviations in the primordial power spectrum cannot significantly improve the fit to the temperature spectrum, as long as they are consistent with the GSR formalism. This is not the case for the TE and EE spectra: We find one principal component that is non-zero at the 1σ level for TE, and three for EE, including one component that is non-zero at more than 3σ. In the full TT+TE+EE spectrum, we find two non-zero principal component parameters. We want to stress that the relevance of these numbers is that they provide an estimate of the number of extra degrees of freedom added in each case, which will be used in the following section[a]. This is illustrated in Fig. 3.1, showing the PCA reconstruction of the deviation to ordinary slow roll (3.2.9) in the case of the best fit parameters to the EE spectrum. The right panel of the figure illustrates that three principal components can reproduce the main features of $\delta G'$, while the left panel illustrates that one principal component is not enough.

3.4.2 Comparison of best fits

Model comparison using Bayesian evidences is not feasible in this case, as the twenty spline parameters increase the prior volume by 5^{20} with respect to ΛCDM. Therefore, in this section

[a]Note that we are choosing this number in a conservative way. If we had instead set the number of degrees of freedom as the number of principal components that are non-zero at the 2σ level, only the EE likelihood would have one significant component, as shown by table 3.4.

	TT			**TE**			**EE**			**TT+TE+EE**		
Parameter	Mean	68% CL	N_σ	Mean	68% CL	N_σ	Mean	68% CL	N_σ	Mean	68% CL	N_σ
m_1	0.049	0.061	0.81	**-0.30**	**0.21**	**1.4**	**0.65**	**0.21**	**3.2**	**-0.66**	**0.48**	**1.4**
m_2	-0.09	0.16	0.59	0.11	0.14	0.77	**-1.17**	**0.81**	**1.4**	**0.095**	**0.085**	**1.1**
m_3	0.27	0.50	0.53	-0.7	1.1	0.69	**-1.35**	**1.1**	**1.2**	-0.20	0.22	0.91

Table 3.4: Means and standard deviations for the first three principal components obtained for each likelihood, sorted by their value of N_σ, which measures the amount of standard deviations by which parameter differs from zero. In bold, those parameters that differ from zero by more than 1σ. Note that the parameters m_1, m_2 and m_3 shown in the table are formed by a different linear combinations of the spline parameters for each column.

Likelihood	$N_{\text{D.o.F.}}$	$\Delta\chi^2$	PTE
TT	0	-0.5	–
TE	1	5.5	0.019
EE	3	16.4	0.00094
TT+TE+EE	**2**	**2.7**	**0.26**

Table 3.5: Goodness of fit for GSR compared to ΛCDM, measured by $\Delta\chi^2 \equiv \chi^2_{\text{Planck}} - \chi^2_{\text{GSR}}$, where $\chi^2 \equiv -2\log\mathcal{L}$ and $\mathcal{L}$ is the likelihood. The second column measures the number of extra degrees of freedom, calculated as the number of principal components that differ from zero at more than one standard deviation, given by Table 3.4. The last column is the corresponding probability to exceed (PTE). Note that the PTE is not defined for the TT case, as no extra degrees of freedom are added.

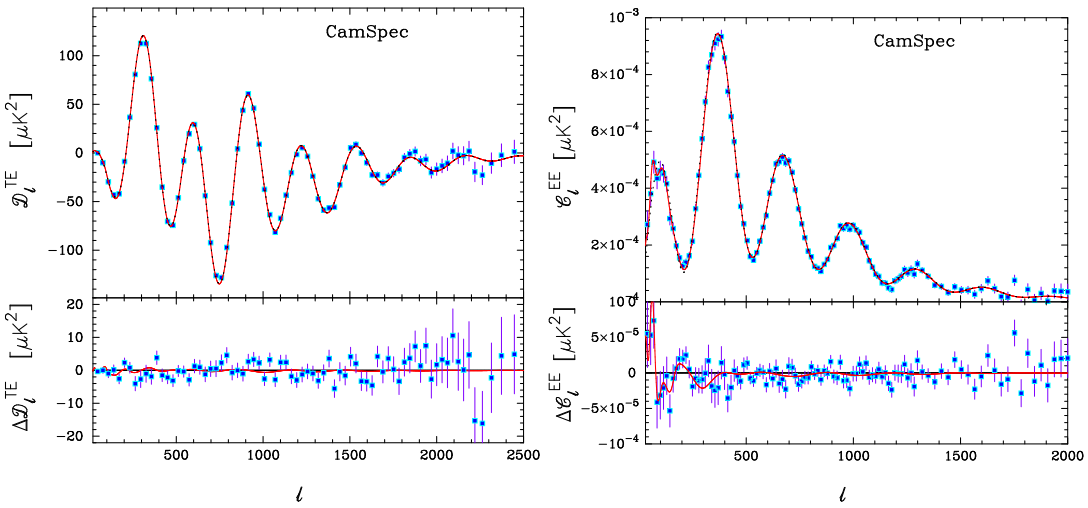

Figure 3.2: Spectra and residuals corresponding to the best fit parameters observed in the TE and EE likelihoods on the left and right panels respectively. The blue dots correspond to the observed data, the black line is the best fit ΛCDM model, and the red one to GSR. The vertical axis in the left plot shows $\mathcal{D}_\ell \equiv \ell(\ell+1)C_\ell/(2\pi)$. The lower panels show $\Delta\mathcal{D}_\ell$ and ΔC_ℓ for the TE and EE spectra respectively.

we compare the models by evaluating the χ^2 values obtained by the best fits to the data using GSR and 6-parameter ΛCDM as theoretical models. Table 3.5 shows the difference in goodness of fit for the best fit parameters to each individual likelihood, and the combined TT+TE+EE likelihood. The table shows no improvement in the χ^2 for the TT likelihood, as we expected from the PCA analysis in the previous section, where we found that all principal components were consistent with zero. The TE likelihood shows a significant improvement, with a PTE of 0.019 corresponding to more than a 2σ significance. The left panel of Fig. 3.2 shows how this best fit compares to the residuals of the *Planck* data for a 6-parameter ΛCDM cosmology. The figure illustrates how GSR tracks some of the oscillatory features in the *Planck* residuals, but does not provide a significantly better fit compared to the base ΛCDM model.

The most statistically significant result in this chapter is the large improvement in goodness of fit obtained for the EE spectrum, with a PTE of 0.00094, corresponding to more than a 3σ improvement. This large improvement is illustrated in the right panel in Fig. 3.2: Allowing for a GSR inflation, the spectrum can perfectly fit the large residuals at low multipoles, and in particular it reproduces the feature at $\ell \sim 200$. The GSR and ΛCDM spectra agree at high multipoles. Despite this large improvement in the fit to the polarization likelihood, there is no combination of parameters that significantly improves the fit to the combined TT+TE+EE likelihood, with a PTE of 0.26 corresponding to a marginal improvement. This is caused by the lack of improvement to the temperature spectrum. The best fit to the combined likelihood in all spectra is shown in Fig. 3.3, where we see that the marginal improvement comes mostly from fitting some of the residuals at low multipoles in polarization. From this, we conclude that *Planck* 2018 data disfavors departures from a power-law primordial power spectrum.

However, this analysis also provides important information about possible problems in the TE and EE likelihoods. The best fit to these individual likelihoods gives non-negligible improvements when features in the primordial power spectrum are allowed as shown by Table 3.5, especially for the EE likelihood. This agrees with the results from Chapter 2, with even larger improvements in χ^2 caused by the higher freedom allowed in the primordial spectrum. As discussed in Chapter 2, the possibility of new physics that affects only polarization is an unlikely explanation, since there are no simple models of new physics that can account for these features in the TE and EE spectra. The features are observed at different frequencies in the *Planck* measurements [148] which makes systematics unlikely. A possible explanation for this is an underestimation of the *Planck* noise in polarization at low multipoles. More specifically, we believe there could be a contribution from correlated noise to *Planck* that has not been included in the likelihood, which could be modeled via end-to-end simulations, a possibility that will be further explored in [191].

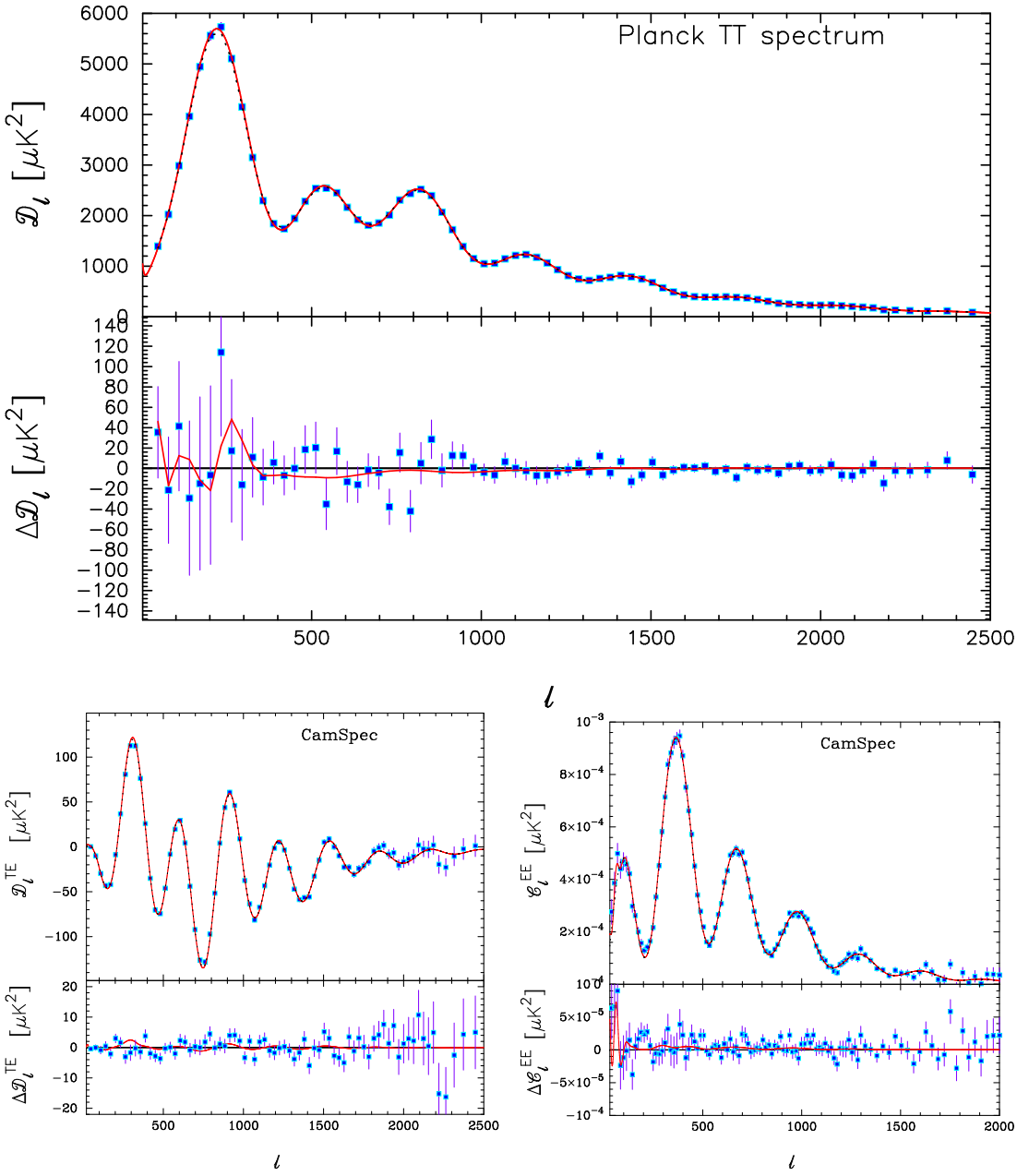

Figure 3.3: Spectra (top) and residuals (bottom) corresponding to the best fit parameters observed in the full TT+TE+EE posterior probability for GSR with respect to ΛCDM. The blue dots correspond to the observed data, the black line is the best fit ΛCDM model, and the red one to GSR inflation. The top figure is the TT spectrum, bottom left is TE, and bottom right EE. The vertical axis for the TT and TE spectra shows $\mathcal{D}_\ell \equiv \ell(\ell+1)C_\ell/(2\pi)$. The lower panels show $\Delta\mathcal{D}_\ell$ for TT and TE, and ΔC_ℓ for EE.

3.5 Conclusions

We have studied the possibility of departures from a power-law primordial power spectrum in the context of generalised slow-roll inflation using the different *Planck* 2018 spectra. We used twenty spline parameters in addition to the six parameters of the baseline ΛCDM cosmology. Since these parameters are highly degenerate we used a principal component analysis to calculate the number of degrees of freedom added for each likelihood. We found that GSR produces no improvements to the temperature likelihood, and as a consequence of this, no significant improvements are found in the combined TT+TE+EE likelihood. However, we find a large improvement in the goodness of fit for the EE likelihood. This was already observed for oscillatory power spectra in the previous chapter. While this indicates that *Planck* 2018 data is consistent with ΛCDM as opposed to models containing features in the primordial power spectrum, the large improvement in the polarization likelihood most likely reflects problems with *Planck* polarization. We believe that the most likely reason behind the large residuals causing these improvements in χ^2 is an underestimation of the *Planck* noise at low multipoles in polarization. The conclusion from Chapters 2 and 3 is that the TE and EE likelihoods seem to be inconsistent with the TT likelihood at low multipoles. Further work needs to be done, particularly on modelling noise in *Planck*. As a consequence, evidence for new physics based on the *Planck* polarization likelihoods needs to be treated with caution.

CHAPTER 4

THE TENSION BETWEEN SPTPOL 500 SQUARE DEGREES AND PLANCK 2015 POLARIZATION RESULTS

4.1 Introduction

This chapter focuses on the results published by the South Pole Telescope (SPT) collaboration on temperature anisotropies and E-mode polarization of the CMB from the 500 square degrees analysis of their SPTpol instrument ([205], hereafter H18). H18 used 150 GHz data from three seasons of observations and produced power spectra for the E-mode polarization (EE) and the temperature-E-mode cross-spectrum (TE) shown in Fig. 4.1. The main advantage of SPTpol with respect to *Planck* is its higher resolution, which allows it to measure much smaller scales, covering a multipole range $50 < \ell \leq 8000$, as opposed to *Planck*'s $2 < \ell \leq 1996$ in polarization. However, because of its smaller sky coverage, SPTpol cannot obtain information on large scales, and as a consequence produces parameter constraints that are much weaker than those from *Planck*[a]. H18 obtains a best fit that is in mild tension with the 6-parameter ΛCDM cosmology, and with the *Planck* parameters within that model at more than a 2σ significance. To understand this tension, H18 split the SPTpol data into high and low multipoles, using $\ell = 1000$ as the cutoff, and obtained good agreement with the *Planck* ΛCDM cosmology derived from

[a]This analysis was done before the *Planck* 2018 likelihood was completed, and therefore uses *Planck* 2015 spectra [21]. The chapter focuses on the SPTpol likelihood, and only uses the parameter constraints from *Planck* as comparison. Because parameter constraints do not change significantly between *Planck* 2015 and *Planck* 2018, the analysis was not updated with the latest likelihood.

temperature anisotropies when only low multipoles were used. They argued that this could hint at new physics at high multipoles, beyond the reach of *Planck*. In this chapter, we investigate the validity of the SPTpol analysis to understand the origin of this tension. We find several errors in the analysis of the SPT data, which increase the error bars on their cosmological parameters. We also find that the parameters of the SPTpol cosmology have converged by $\ell \sim 2500$, and higher multipoles do not significantly alter the parameters within the ΛCDM model. More data will be necessary to asses whether multipoles $\ell > 2500$ are consistent with the 6-parameter ΛCDM model, since they are well beyond the range of multipoles accessible to *Planck*. We argue that the remaining difference between SPTpol and *Planck* is not significant, and is likely to originate from outliers in the SPTpol TE and EE spectra, which could be caused by problems in the error model.

In Sec. 4.2 we discuss some problems in the likelihood used by H18, and publicly available in the SPT website[a]. In Sec. 4.3 we discuss the effect on cosmological parameters of altering the priors in some of the SPT calibration parameters and the validity of the prior ranges used in their analysis. Sec. 4.4 repeats the cosmological analysis for different multipole ranges, to find the cause of the tension with *Planck*, and assesses the level of tension between the experiments. Finally, we present our conclusions in Sec. 4.5.

4.2 Corrections to the SPTpol likelihood

In this section, we discuss some issues we found in the publicly available SPTpol likelihood, how to correct them, and their effect on cosmological parameters. H18 calculated cosmological parameters using the Markov Chain Monte Carlo (MCMC) package `CosmoMC` [186; 190] which uses the Boltzmann code `CAMB` [204]. Their analysis consists of dividing the SPTpol TE and EE data in 56 bandpowers spanning the multipole range $50 < \ell \leq 8000$. Information about these bandpowers can be found in Table 2 of H18.

For their analysis, they parameterize the ΛCDM cosmology using the same parameters used in Chapters 2 and 3: The density of baryonic matter $\Omega_b h^2$, the density of cold dark matter $\Omega_c h^2$, θ_{MC} an approximation of the ratio of the sound horizon to the angular diameter distance at recombination, the optical depth to reionization τ and the amplitude and tilt of the primordial power spectrum A_s and n_s. The CMB spectrum is degenerate in the parameter combination $A_s e^{-2\tau}$ that measures the overall amplitude of the spectrum, except at very low multipoles which are not measured by SPT. Therefore, instead of providing constraints on each of these two parameters, the SPT team presents results on $A_s e^{-2\tau}$, and we will do the same. H18 also uses a Gaussian prior on the optical depth to reionization $\tau = 0.078 \pm 0.019$ based on

[a] http://pole.uchicago.edu/public/data/henning17/

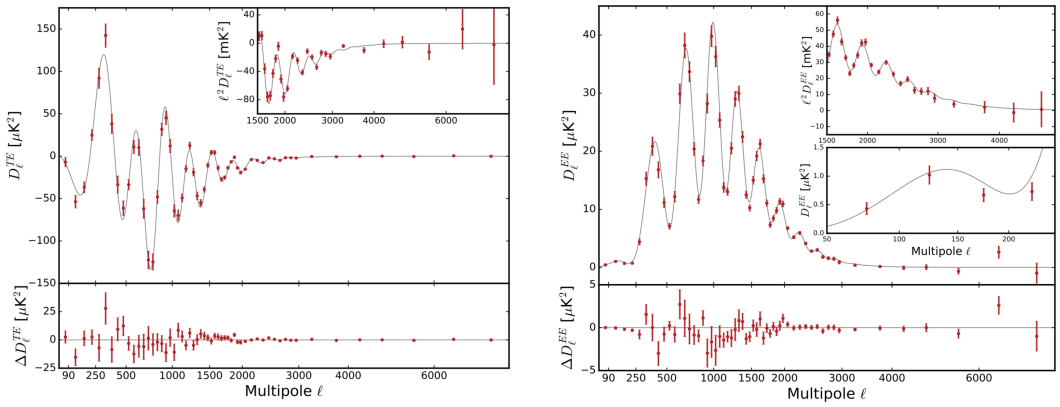

Figure 4.1: The SPTpol 500deg^2 power spectra. On the left, the temperature-polarization cross correlation (TE) and on the right the polarization auto-correlation (EE). The solid gray lines are the *Planck* 2015 best-fit ΛCDM cosmology, obtained with the `base_plikHM_TT_lowTEB` likelihood. In both plots, the sub-panels show residuals to the best fit model, while the top right plot has bandpowers scaled by an additional ℓ^2 to highlight features at higher multipoles. On the right plot, the lower inset plot zooms in on low multipoles to highlight the corresponding features. Image credit: H18.

Parameter	Symbol	Prior
Cold dark matter density	$\Omega_c h^2$	[0.001,0.99]
Baryon density	$\Omega_b h^2$	[0.005,0.1]
$100 \times \theta_{MC}$	$100\theta_{MC}$	[0.5,10]
Scalar spectrum amplitude	$\log\left(10^{10} A_s\right)$	[2,4]
Scalar spectral index	n_s	[0.8,1.2]

Table 4.1: Uniform priors used by H18 and in our analysis. Priors on calibration and foreground parameters can be found in Table 3 of H18 and are discussed in the text.

the *Planck* LFI likelihood [206], since SPTpol cannot constrain this parameter. Although the *Planck* collaboration released tighter constraints on this parameter recently [154], we will use this same prior for consistency. Since SPTpol is not sensitive to low multipoles, the value of τ is not very important unless we want to infer the amplitude A_s. The remaining parameters have flat priors specified in Table 4.1. These priors will be used everywhere in this analysis.

H18 also uses five parameters to measure foreground contributions from dust and other sources, and two more to correct for super-sample lensing variance [207] and beam errors. These are also included in our analysis, with the same priors used by the SPT team, which can be found in Table 3 of H18. There are two more nuisance parameters in the SPTpol analysis, $T_{\rm cal}$ and $P_{\rm cal}$, which will be discussed in depth in the next section.

In this section, we discuss two issues that we found in the publicly available `CosmoMC` module used in the H18 analysis. The first one concerns the way the separate TE and EE analyses are

performed. The way this is done in the original analysis is by multiplying the elements of the covariance matrix that are not to be used by a large factor, therefore increasing their error to the extent that their contribution to χ^2 becomes negligible. This, although valid in theory, is not implemented correctly in their code. In particular, they do this by multiplying the diagonal block by a factor of 10^{24} and the non-diagonal blocks by the square root of that factor, i.e. 10^{12}. Some simple algebra, however, can show that this is incorrect. Let us define $\alpha = 10^{12}$, and the covariance matrix by

$$\begin{bmatrix} A & C \\ C & B \end{bmatrix},$$

where in this case A is the block corresponding to the 56 TE datapoints, B is the block corresponding to EE, and C are the blocks corresponding to their cross-correlation. The inverse of this will be

$$\begin{bmatrix} \tilde{A} & \tilde{C} \\ \tilde{C} & \tilde{B} \end{bmatrix},$$

where, using the Woodbury formula [208],

$$\tilde{A} = A^{-1} + (A^{-1}C)(B - CA^{-1}C)^{-1}(CA^{-1}). \tag{4.2.1}$$

In H18, if they want to study the separate TE likelihood which corresponds to eliminating the B and C blocks, they multiply C by α and B by α^2 respectively. This yields:

$$\tilde{A} = A^{-1} + (\alpha A^{-1}C)(\alpha^2 B - \alpha^2 CA^{-1}C)^{-1}(\alpha CA^{-1}), \tag{4.2.2}$$

therefore, the α factors cancel out. What this is doing is eliminate the direct contributions from the unwanted blocks, but due to this cancellation, there are unwanted contributions to the errors in the data of interest. An easy solution to this issue is to multiply the off-diagonal blocks by zero. These changes produce reductions in the value of χ^2 corresponding to the best-fit SPTpol cosmology to the separate TE and EE likelihoods of order $\Delta\chi^2 \sim 5$.

The second issue concerns the aberration correction [209]. Aberration refers to the effect of our proper motion with respect to the last scattering surface of the CMB. This motion induces a dipole which requires an angle dependent rescaling of the multipole moments. The aberration correction implemented in the publicly released SPTpol likelihood differs from the correction described in the chapter: H18 uses the same aberration correction on the power spectrum used by the ACTPol collaboration [210]

$$\left(\frac{\Delta C_\ell}{C_\ell}\right)_{\rm H18} = -\frac{{\rm d}\ln C_\ell}{{\rm d}\ln \ell}\beta\langle\cos\theta\rangle. \tag{4.2.3}$$

However, the public likelihood code uses

$$\Delta D_\ell = -\frac{{\rm d}D_\ell}{{\rm d}\ell}\beta\ell\langle\cos\theta\rangle \Rightarrow \left(\frac{\Delta C_\ell}{C_\ell}\right)_{\rm code} = -\frac{{\rm d}\ln(\ell^2 C_\ell)}{{\rm d}\ln\ell}\beta\langle\cos\theta\rangle, \tag{4.2.4}$$

where as usual $D_\ell = \frac{\ell(\ell+1)}{2\pi}C_\ell \approx \frac{\ell^2}{2\pi}C_\ell$ since for SPTpol we have $\ell \geq 50$. The formula 4.2.4 used in the public likelihood is correct, since it gives a zero aberration correction for a scale invariant spectrum, unlike Eq. 4.2.3. However, Eq. 4.2.3 can be found in the literature as a formula for aberration corrections. The issue arises from a misunderstanding of the effects of aberration and modulation, the latter being the change of the temperature in the Lorentz transformation between the two frames.

To understand the difference between these formulae, we clarify the difference between aberration and modulation: Let us define $T_{\rm CMB}$ as the actual temperature of the CMB and $T_{\rm obs}$ as the temperature observed after aberration. These two quantities are related by a Lorentz transformation that remaps the points. Let A be the remapping function such that point $\hat{n}$ is transformed into point $A\hat{n}$. Then:

$$T_{\rm obs}(\hat{n}) = T_{\rm CMB}(A\hat{n}). \tag{4.2.5}$$

Such that the Fourier transform yields:

$$T_{\rm obs}(\hat{\ell}) = \int {\rm d}^2\hat{n}\, T_{\rm CMB}(A\hat{n})e^{i\hat{\ell}\cdot\hat{n}}. \tag{4.2.6}$$

This generates a contribution from a Jacobian term. This remapping is called aberration, but there is a second effect, which is the change in temperature caused by the Lorentz transformation itself, called modulation. If one were to measure the blackbody temperature directly along each line of sight, the modulation would cancel the Jacobian factor. However, real measurements of temperature anisotropies are derived from measurements of the intensity within a certain bandpass, which makes the modulation effect frequency dependent [211], and means that the Jacobian and the modulation do not cancel exactly. The use of the correct frequency dependent modulation yields:

$$\frac{\Delta C_\ell}{C_\ell} = -\left[\frac{{\rm d}\ln C_\ell}{{\rm d}\ln\ell} + 2(1-b_\nu)\right]\beta\langle\cos\theta\rangle, \tag{4.2.7}$$

where b_ν is a frequency dependent factor given by

$$b_\nu = \frac{\nu}{\nu_0}\coth\left(\frac{\nu}{2\nu_0}\right) - 1, \tag{4.2.8}$$

	TE		EE		TEEE	
Parameter	Default	Extended	Default	Extended	Default	Extended
$100\Omega_b h^2$	2.333 ± 0.073	2.330 ± 0.074	2.24 ± 0.12	2.23 ± 0.012	2.295 ± 0.048	2.302 ± 0.050
$\Omega_c h^2$	0.1202 ± 0.0074	0.1203 ± 0.0076	0.1045 ± 0.0077	0.1051 ± 0.083	0.1099 ± 0.048	0.1093 ± 0.050
n_s	0.972 ± 0.032	0.972 ± 0.032	1.038 ± 0.045	1.037 ± 0.047	0.997 ± 0.024	0.996 ± 0.024
H_0^*	67.7 ± 2.7	67.6 ± 2.8	73.4 ± 3.7	73.2 ± 3.9	71.3 ± 2.1	71.5 ± 2.2
$A_s e^{-2\tau}$	1.862 ± 0.075	1.84 ± 0.12	1.712 ± 0.070	1.69 ± 0.15	1.779 ± 0.054	1.802 ± 0.084
$T_{\rm cal}$	1.0000 ± 0.0034	0.9993 ± 0.0099	1.0000 ± 0.0034	0.9996 ± 0.0098	1.0000 ± 0.0034	0.9992 ± 0.0099
$P_{\rm cal}$	1.000 ± 0.011	0.992 ± 0.047	1.000 ± 0.011	0.992 ± 0.045	1.003 ± 0.010	1.010 ± 0.019

Table 4.2: Best fit values and one sigma errors for each cosmological parameter using the default and extended priors on the calibration parameters $P_{\rm cal}$ and $T_{\rm cal}$, for the TE and EE likelihoods alone, and their combination TEEE. H_0 has units of km s^{-1}Mpc^{-1}.

with $\nu_0 \equiv k_B T_0/h \approx 57$GHz. The value $b_\nu = 1$ corresponds to actually measuring the temperature instead of measuring intensity within a bandpass. If we now go back to Eq. 4.2.4 and expand it, we get:

$$\left(\frac{\Delta C_\ell}{C_\ell}\right)_{\rm code} = -\left[\frac{{\rm d}\ln C_\ell}{{\rm d}\ln \ell} + 2\right]\beta\langle\cos\theta\rangle, \tag{4.2.9}$$

which is equivalent to the exact expression of Eq. 4.2.7 for $b_\nu = 0$, i.e. no modulation correction. We conclude that Eq. 4.2.4 used in the SPTpol likelihood code accounts for aberration alone (no modulation), while Eq. 4.2.3 which is mentioned in H18, as well as other works such as [210] accounts for both aberration and modulation corrections, assuming $b_\nu = 1$. It is important to point out, however, that b_ν can present significant departures from unity. In fact, for *Planck* at 150 GHz, b_ν is of order two, and at 217 GHz of order three. Since the effect of these changes in the amplitude of the local power spectrum is tied up with exactly how the calibration is done, we will keep using Eq. 4.2.4 in the rest of this analysis.

We find a similar problem with the super-sample lensing correction, for which the equation on H18,

$$(\Delta C_\ell)_{\rm H18} = -\frac{\partial[\ell^2 C_\ell^{XY}({\rm p})]}{\partial \ln \ell}\frac{\kappa}{\ell^2}, \tag{4.2.10}$$

is correct, but the public likelihood code calculates the wrong quantity:

$$(\Delta C_\ell)_{\rm code} = -\frac{\partial[\ell^3 C_\ell^{XY}({\rm p})]}{\partial \ln \ell}\frac{\kappa}{\ell^2}. \tag{4.2.11}$$

This has been corrected in the rest of this analysis. Although the aberration, modulation and super-sample lensing corrections should be used correctly, they do not significantly affect the parameter constraints or values of χ^2 for SPTpol.

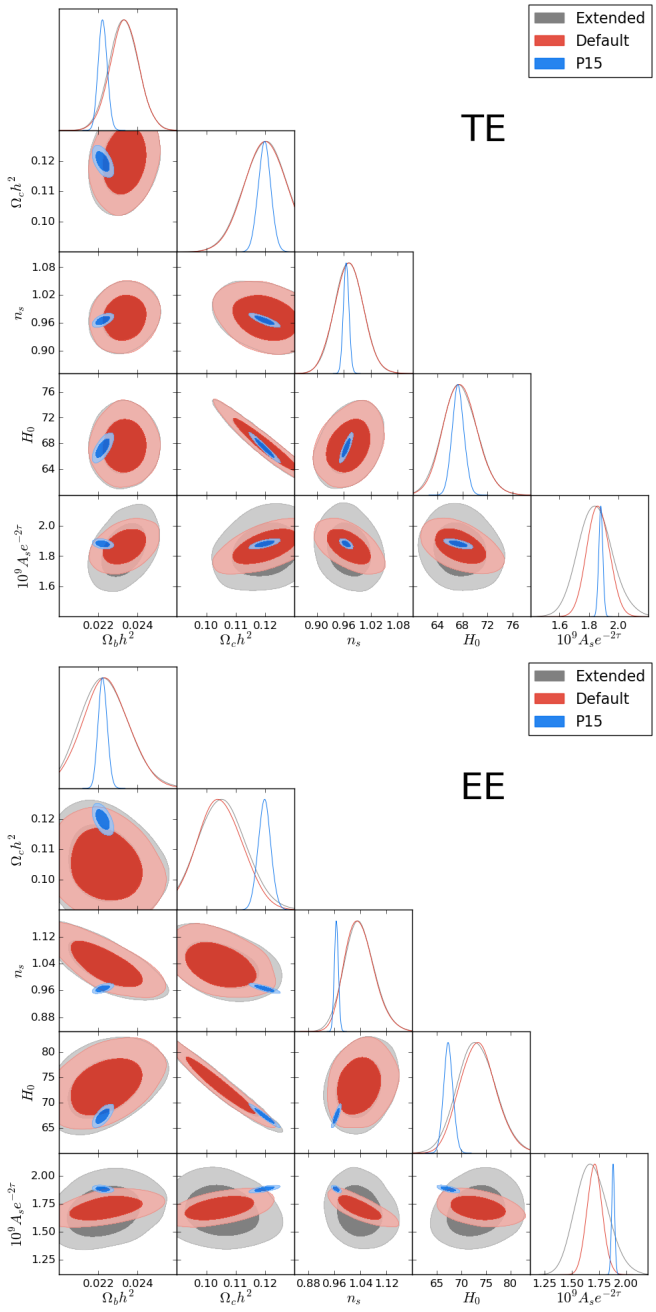

Figure 4.2: Posterior distributions of the ΛCDM model parameters using the default and extended priors in the calibrations in red and grey respectively for the TE and EE only likelihoods on the top and bottom plots respectively. In blue are the parameter constraints from *Planck* 2015 using the `base_plikHM_TT_lowTEB` likelihood. Units of km s^{-1}Mpc^{-1} are assumed for H_0. In this plot, and throughout the rest of this thesis, the contours show 68% and 95% confidence levels.

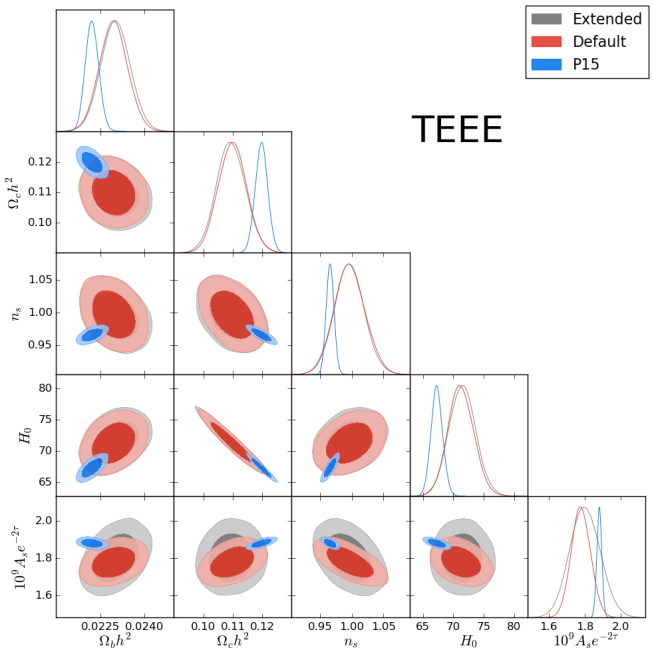

Figure 4.3: Posterior distributions of the ΛCDM model parameters using the default and extended priors in the calibrations in red and grey respectively for the TE+EE likelihood. In blue are the parameter constraints from *Planck* 2015 using the `base_plikHM_TT_lowTEB` likelihood. Units of km s^{-1}Mpc^{-1} are assumed for H_0.

4.3 Priors in calibration parameters

In this section, we discuss the effect of the calibration parameters and their priors on the cosmological parameter estimation of H18. The SPT team calibrates their TE and EE spectra multiplying their theoretical predictions which are being compared to the data by $1/(T_{\rm cal}^2 P_{\rm cal})$ and $1/(T_{\rm cal}^2 P_{\rm cal}^2)$ respectively, where $P_{\rm cal}$ and $T_{\rm cal}$ are nuisance parameters that are varied in the MCMC analysis. This parameterization was already used in the 100 Square Degrees SPTpol analysis [212]. $T_{\rm cal}$ and $P_{\rm cal}$ are expected to be close to unity, so Gaussian priors centred on one are used for both parameters. The prior used by H18 for $T_{\rm cal}$ has a standard deviation of 0.0034 based on matching beam amplitudes as discussed in their paper. The case of $P_{\rm cal}$ is more complicated, as this parameter is degenerate with the polarization efficiency. H18 corrects for polarization efficiency by comparing their 150 GHz polarization maps to *Planck* 143 GHz at the map level, and obtains $P_{\rm cal} = 1.06 \pm 0.01$. H18 explains that this discrepancy is 'the subject of ongoing study', and they deal with this issue by applying the 1.06 calibration factor to their E-mode maps and using a Gaussian prior on $P_{\rm cal}$ with a standard deviation of 0.01. The problem with this is that the *Planck* 143 GHz maps were calibrated with the ground based polarization efficiencies, which have large errors of $\sim 1\%$ at the map level. As noted

by H18, the $P_{\rm cal} = 1.06 \pm 0.01$ calibration is surprising: a 6% correction at the map level is much larger than expected for the SPTpol detectors, but in fact from the *Planck* 2018 analysis [1; 148], we estimate that the *Planck* 143 GHz polarization efficiency is actually too high by $\sim 1.5\%$. This exacerbates the problem with SPTpol since it implies that $P_{\rm cal} \sim 1.075$ calibrated against *Planck* 143 GHz. Evidently, the polarization calibration of SPTpol is not understood. We are concerned that applying a $P_{\rm cal} = 1.06 \pm 0.01$ calibration with such a small error can lead to inconsistencies between the SPTpol TE and EE likelihoods, and biases using the combined TE+EE likelihood.

We therefore investigate what happens if we impose less restrictive priors: We repeat the analysis, extending the priors on $T_{\rm cal}$ and $P_{\rm cal}$, to study the effect of wider priors on parameter constraints. We do this using the corrections on the covariance matrix and on the aberration and super-sample lensing corrections described in the previous section. We use priors $T_{\rm cal} = 1.0 \pm 0.01$ and $P_{\rm cal} = 1.0 \pm 0.05$, and refer to this analysis as 'extended' as opposed to the 'default' analysis using the H18 prior. Our results are summarized in Figs. 4.2 and 4.3, and in Table 4.2.

The first thing we see in the figures is that extending the priors in the calibration parameters increases the errors in the parameter estimates. In particular, it has a very significant effect on the errors on the amplitude parameter $A_s e^{-2\tau}$, which as mentioned in H18 is the parameter most in tension with *Planck*, since SPTpol obtains a value significantly lower, especially when the EE likelihood only is used. We can see in Figs. 4.2 and 4.3 how by using wider priors on the calibration parameters the tension with *Planck* is reduced to below 2σ making these parameter constraints consistent. We also notice how extending the priors in $T_{\rm cal}$ and $P_{\rm cal}$ breaks the degeneracy directions in the parameter combinations involving $A_s e^{-2\tau}$. These problems with the SPT polarization calibration mean that amplitude parameters determined from SPTpol should be treated with caution.

4.4 Multipole cuts

The goal of this section is to identify the multipole range that causes both the bad fit to the SPTpol data obtained from a 6-parameter ΛCDM cosmology, and the differences in parameter constraints with the *Planck* 2015 results within the framework of ΛCDM. This is done with a repetition of the analysis from H18 in which high and low multipoles are analysed separately, using different multipole cuts and comparing each cosmology with *Planck*, as well as studying the goodness of fit of each multipole range. In H18 this is done using a single cut to separate between low and high multipoles at $\ell = 1000$. Since the cosmology they obtain for $\ell \geq 1000$ is in tension with *Planck*, they claim that the cause for the tension could be new physics at high

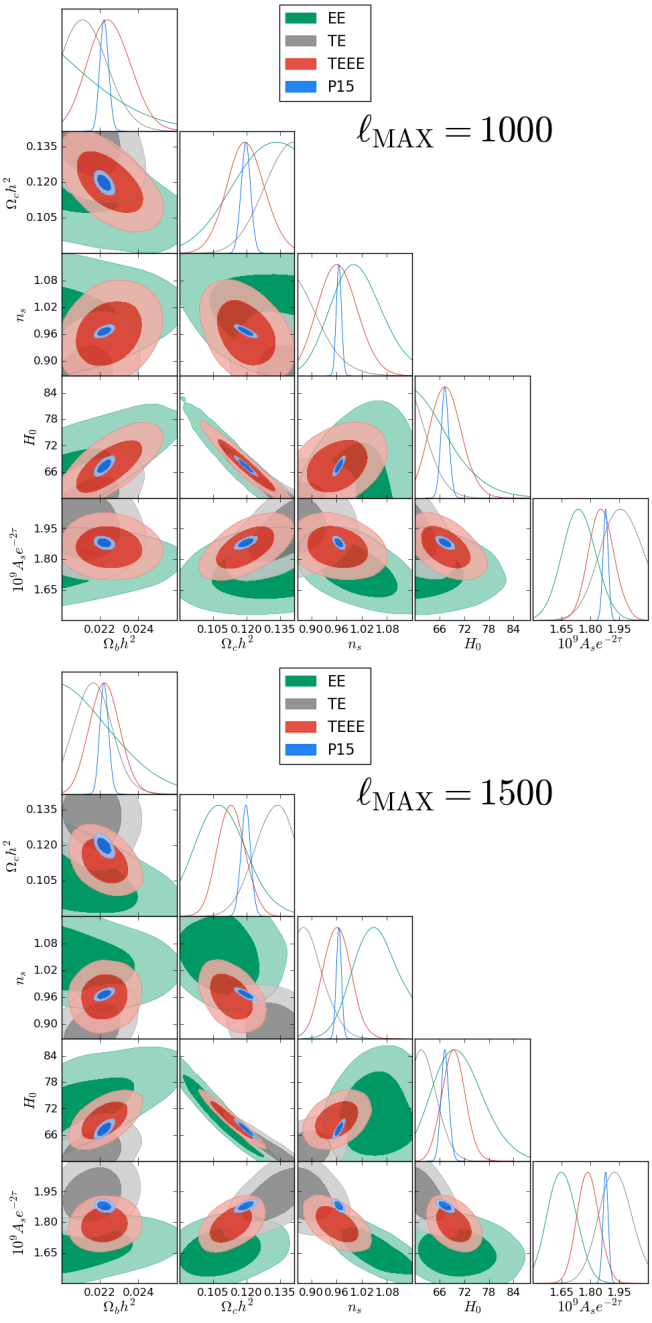

Figure 4.4: Posterior distributions of the ΛCDM model parameters using multipole cuts $\ell_{\rm max} = 1000$ (top) and $\ell_{\rm max} = 1500$ (bottom). In green we show the EE only likelihood, in gray the TE only, and in red the TE+EE combination. In blue are the parameter constraints from *Planck* 2015 using the `base_plikHM_TT_lowTEB` likelihood. Units of km s^{-1}Mpc^{-1} are assumed for H_0.

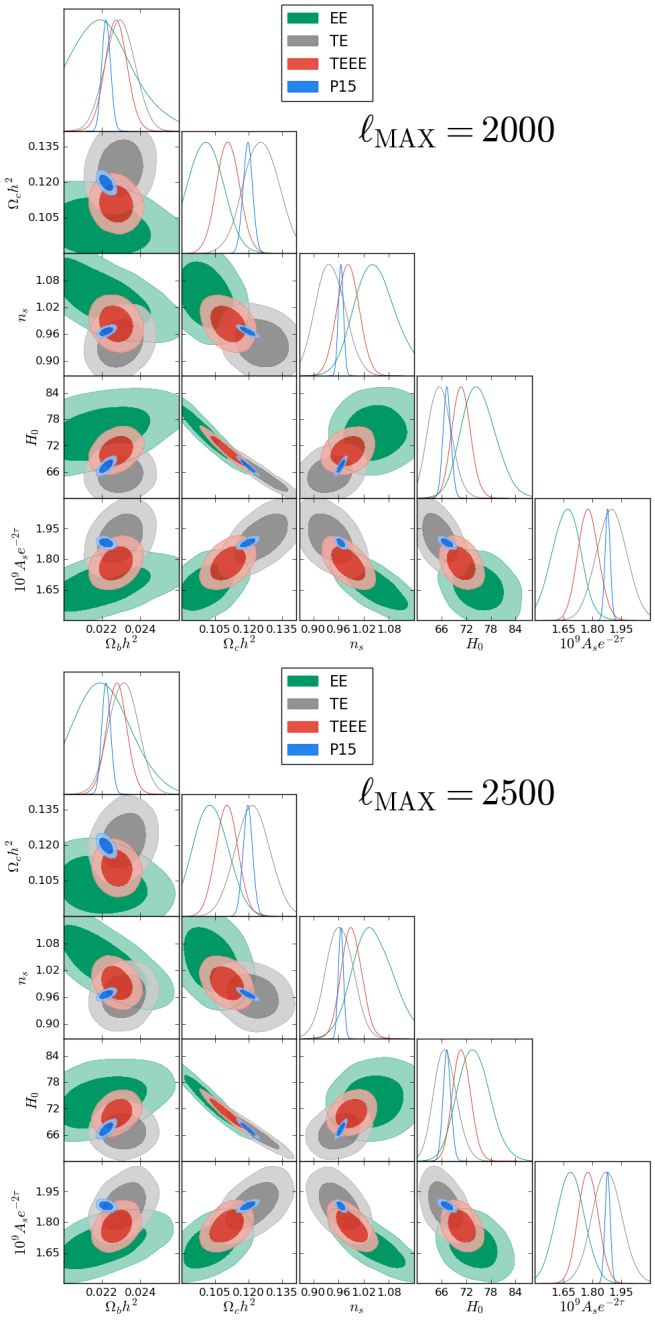

Figure 4.5: Posterior distributions of the ΛCDM model parameters using multipole cuts $\ell_{\rm max} = 2000$ (top) and $\ell_{\rm max} = 2500$ (bottom). In green we show the EE only likelihood, in gray the TE only, and in red the TE+EE combination. In blue are the parameter constraints from *Planck* 2015 using the `base_plikHM_TT_lowTEB` likelihood. Units of km s^{-1}Mpc^{-1} are assumed for H_0.

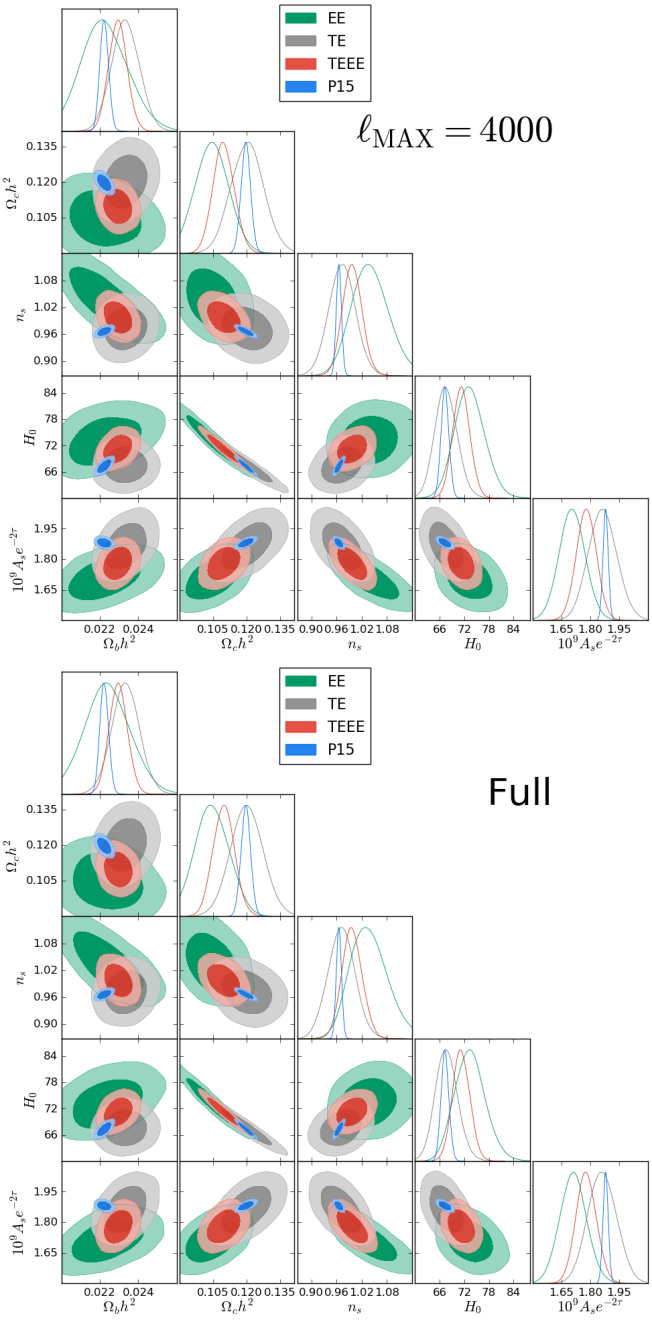

Figure 4.6: Posterior distributions of the ΛCDM model parameters using a multipole cut $\ell_{\rm max} = 4000$ (top) and for the full spectrum (bottom). In green we show the EE only likelihood, in gray the TE only, and in red the TE+EE combination. In blue are the parameter constraints from *Planck* 2015 using the `base_plikHM_TT_lowTEB` likelihood. Units of km s^{-1}Mpc^{-1} are assumed for H_0.

Parameter	$\ell_{\rm max} = 1000$	$\ell_{\rm max} = 1500$	$\ell_{\rm max} = 2000$	$\ell_{\rm max} = 2500$	$\ell_{\rm max} = 4000$	Full	*Planck* 2015
			TE				
$100\Omega_b h^2$	2.12 ± 0.13	2.165 ± 0.099	2.295 ± 0.077	2.314 ± 0.076	2.332 ± 0.072	2.332 ± 0.073	2.222 ± 0.022
$\Omega_c h^2$	0.142 ± 0.014	0.1334 ± 0.0098	0.1258 ± 0.0079	0.1218 ± 0.0076	0.1204 ± 0.0074	0.1202 ± 0.0074	0.1197 ± 0.0022
n_s	0.874 ± 0.053	0.888 ± 0.042	0.940 ± 0.035	0.961 ± 0.032	0.973 ± 0.032	0.972 ± 0.032	0.9655 ± 0.0062
H_0[km s^{-1}Mpc^{-1}]	58.3 ± 4.7	62.2 ± 3.4	65.6 ± 2.8	67.0 ± 2.7	67.6 ± 2.7	67.7 ± 2.7	67.31 ± 0.96
$A_s e^{-2\tau}$	1.97 ± 0.11	1.932 ± 0.088	1.901 ± 0.079	1.879 ± 0.078	1.864 ± 0.075	1.863 ± 0.075	1.880 ± 0.014
χ^2 (N_b)	14.2 (19)	25.4 (29)	42.2 (39)	55.4 (42)	67.8 (48)	70.2 (56)	$\chi^2_p = 3.38$
N_σ	0.7	0.7	1.4	2.6	3.1	2.3	PTE = 0.64
			EE				
Parameter	$\ell_{\rm max} = 1000$	$\ell_{\rm max} = 1500$	$\ell_{\rm max} = 2000$	$\ell_{\rm max} = 2500$	$\ell_{\rm max} = 4000$	Full	*Planck* 2015
$100\Omega_b h^2$	1.78 ± 0.34	2.00 ± 0.26	2.21 ± 0.18	2.20 ± 0.15	2.22 ± 0.12	2.24 ± 0.12	2.222 ± 0.022
$\Omega_c h^2$	0.136 ± 0.020	0.108 ± 0.012	0.1010 ± 0.0082	0.1033 ± 0.0081	0.1049 ± 0.0077	0.1042 ± 0.0077	0.1197 ± 0.0022
n_s	1.010 ± 0.062	1.054 ± 0.055	1.045 ± 0.049	1.043 ± 0.047	1.041 ± 0.044	1.040 ± 0.045	0.9655 ± 0.0062
H_0[km s^{-1}Mpc^{-1}]	60.4 ± 8.2	70.7 ± 6.2	75.0 ± 4.2	73.7 ± 3.9	73.2 ± 3.6	73.5 ± 3.7	67.31 ± 0.96
$A_s e^{-2\tau}$	1.746 ± 0.088	1.659 ± 0.077	1.671 ± 0.077	1.688 ± 0.074	1.707 ± 0.068	1.708 ± 0.068	1.880 ± 0.014
χ^2 (N_b)	23.8 (19)	35.4 (29)	45.8 (39)	49.0 (42)	54.8 (48)	63.3 (56)	$\chi^2_p = 8.21$
N_σ	2.7	2.2	1.9	1.8	1.7	1.6	PTE = 0.14
			TEEE				
Parameter	$\ell_{\rm max} = 1000$	$\ell_{\rm max} = 1500$	$\ell_{\rm max} = 2000$	$\ell_{\rm max} = 2500$	$\ell_{\rm max} = 4000$	Full	*Planck* 2015
$100\Omega_b h^2$	2.25 ± 0.11	2.226 ± 0.079	2.276 ± 0.058	2.280 ± 0.053	2.295 ± 0.049	2.295 ± 0.049	2.222 ± 0.022
$\Omega_c h^2$	0.1200 ± 0.086	0.1134 ± 0.0062	0.1110 ± 0.0051	0.1103 ± 0.0050	0.1098 ± 0.0048	0.1098 ± 0.0048	0.1197 ± 0.0022
n_s	0.963 ± 0.047	0.961 ± 0.033	0.982 ± 0.027	0.991 ± 0.025	0.997 ± 0.023	0.997 ± 0.024	0.9655 ± 0.0062
H_0[km s^{-1}Mpc^{-1}]	67.4 ± 3.9	69.4 ± 2.8	70.8 ± 2.2	70.9 ± 2.2	71.3 ± 2.1	71.3 ± 2.1	67.31 ± 0.96
$A_s e^{-2\tau}$	1.860 ± 0.068	1.790 ± 0.058	1.781 ± 0.054	1.780 ± 0.053	1.780 ± 0.053	1.779 ± 0.053	1.880 ± 0.014
χ^2 (N_b)	50.6 (38)	77.4 (58)	100.0 (78)	109.8 (84)	129.9 (96)	139.9 (112)	$\chi^2_p = 9.85$
N_σ	2.7	2.7	2.5	2.7	3.1	2.5	PTE = 0.08

Table 4.3: Mean values and one sigma errors for each cosmological parameter predicted by SPTpol using different multipole cuts for the TE and EE likelihoods alone, and their combination TEEE. The right column are the predictions from *Planck* 2015 using the using the `base_plikHM_TT_lowTEB` likelihood. χ^2 measures the goodness of fit of the best fit parameters, and N_b the corresponding number of bands. N_σ and χ^2_p are introduced in the text.

multipoles, above $\ell \sim 2000$, which is the highest measured by *Planck* polarization. However, within the framework of ΛCDM, parameters should converge to almost their true values by $\ell \approx 2000$.

Our results are shown in figures 4.4, 4.5, 4.6 and in Table 4.3. Here we use the default priors on the calibration parameters $P_{\rm cal}$ and $T_{\rm cal}$ as opposed to the extended priors discussed in the previous section. Our reason to do this is that we want to understand the origin of the differences between SPTpol and *Planck* pointed out in H18. Therefore we maintain their priors in these two parameters. The figures illustrate the multipole range causing the tension between SPTpol and *Planck*. As mentioned in H18, for a multipole cut of $\ell_{\rm max} = 1000$ the results from SPTpol are very compatible with *Planck*. However, we notice that as soon as we move to $\ell_{\rm max} = 1500$ the tensions start to arise, and these keep increasing for $\ell_{\rm max} = 2000$. Higher multipole cuts do not seem to change the parameter constraints significantly. This goes against the idea from H18 that the tension comes from something that is happening at multipoles high enough that they cannot be measured by *Planck*. Instead, the tension originates in multipoles between 1000 and 2000.

This idea is further reinforced by the results shown in Table 4.3, which shows how the parameter constraints experience big changes between $\ell_{\rm max} = 1000$ and $\ell_{\rm max} = 2000$, but the changes between this point and $\ell_{\rm max} = 4000$ are insignificant. In particular, the table shows how the EE likelihood shows larger changes for different multipole cuts. In any case, it is clear that the differences between SPTpol and *Planck* do not originate at multipoles above $\ell \sim 2000$. To quantify the significance of these differences in parameter values between SPTpol and *Planck* within the framework of ΛCDM , we can asses the significance of such parameter differences in the following manner: Let us define the vector $\mathbf{\Delta p}$ as the difference between the cosmological parameters on SPT and Planck, and calculate

$$\chi^2_p = \mathbf{\Delta p}^T \mathbf{C_P}^{-1} \mathbf{\Delta p}, \tag{4.4.1}$$

where $\mathbf{C_P}$ is the covariance matrix for SPTpol cosmological parameters, and we are neglecting the contribution from errors in the *Planck* parameters as they are a lot smaller. The corresponding PTE is obtained using 5 degrees of freedom corresponding to the five cosmological parameters. The results are shown in the right column of Table 4.3. We get a PTE of 0.64 for the TE spectrum alone, and of 0.14 for the EE spectrum, which is indicating that TE is perfectly consistent while the differences in EE are not significant. Not even the differences in the full spectra are significant, with a PTE of 0.08, i.e. less than 2σ. Therefore, the parameter differences between SPTpol and *Planck* within this cosmology are not significant.

We now turn to the problem of the poor fit of the SPTpol data to a 6-parameter ΛCDM cosmology. To do this, we explore the different values of χ^2, also shown in Table 4.3. In this

		Planck		SPTpol			
SPTpol spectrum	N_b	$\chi^2_{\rm min}$	N_σ	$\chi^2_{\rm min}$	N_σ	χ^2_p	PTE
TE+EE	112	149.5	3.2	138.5	2.4	9.37	0.10
TE	56	72.6	2.5	71.2	2.4	3.03	0.70
EE	56	68.7	2.1	61.1	1.3	7.55	0.18

Table 4.4: Chi squared values for the best fit *Planck* and SPTpol cosmologies on the SPTpol TE+EE, TE and EE likelihoods using wide priors on the calibration parameters $P_{\rm cal}$ and $T_{\rm cal}$, the meaning of each column is explained in the text. The *Planck* cosmology is obtained using the `base_plikHM_TT_lowTEB` likelihood.

table, N_b gives the number of bandpowers in each spectrum and $\chi^2_{\rm min}$ is calculated using Eq. 4.4.1. N_σ is an estimate of the deviation from the expectation $\langle\chi^2_{\rm min}\rangle = N_{\rm dof}$ where $N_{\rm dof}$ is the number of degrees of freedom, and as in H18 it is given by the number of bandpowers minus 8, corresponding to 5 cosmological parameters and three nuisance parameters with flat priors. It is obtained as

$$N_\sigma = \frac{\chi^2_{\rm min} - N_{\rm dof}}{\sqrt{2N_{\rm dof}}}. \tag{4.4.2}$$

The values of χ^2 clearly highlight the difference between the TE and EE likelihoods. The former provide a good fit to the data at low multipoles, that gets worse as higher multipoles are included, reaching the 2σ level at $\ell_{\rm max} = 2500$, and the 3σ level at $\ell_{\rm max} = 4000$. The inclusion of multipoles between 4000 and 8000 improves the fit to the TE data, bringing the tension back to 2.3σ for the full multipole range. In the case of EE, ΛCDM provides a poor fit to the data at low multipoles, but the goodness of fit improves as higher multipoles are included, with $N_\sigma < 2$ for multipoles above 2000. The combined TE+EE likelihood gives a poor fit to ΛCDM for the entire multipole range, driven by the EE spectrum at low multipoles, and the TE spectrum at high multipoles. This trend of the SPTpol data to disfavour both the ΛCDM cosmology and the *Planck* parameter values within that cosmology is partially driven by a small number of outliers in the data. A careful look at the spectra shows such outliers with more than a 2σ deviation from the best-fit cosmology at $\ell = 124, 1874, 2449$, and 3249 for TE and $\ell = 1974, 6499$ for EE. Note that, while these outliers match the trend in χ^2 for TE, they do not account for the poor fit of the EE spectrum at low multipoles. As shown by Table 4.3, the SPT spectra have a high χ^2 per degree of freedom, therefore the fact that there are several points showing residuals at more than 2.5σ raises the issue of possible problems with the SPTpol error model. This may explain why the differences at the parameter level between SPTpol and *Planck* (Eq. 4.4.1) are much less significant: This statistic uses differences in χ^2 rather than its absolute value, therefore it is less sensitive to the normalization of χ^2.

Finally, we turn to the effects of the priors on the SPTpol calibration parameters introduced in Sec. 4.3, and repeat the assessment of tension with *Planck* and goodness of fit with wider priors on $P_{\rm cal}$ and $T_{\rm cal}$. As mentioned in Sec. 4.3, widening the priors is expected to reduce the tension between *Planck* and SPTpol, through an increase in the error of the amplitude parameter $A_s e^{-2\tau}$, which is driving most of this tension. We repeat the study of differences in parameter values with respect to *Planck* using Eq. 4.4.1 for default and wide priors. Although it would be possible to use this method to compare the SPTpol likelihoods with default and wide priors directly, this would not be as simple as using Eq. 4.4.1. This is because of three reasons: First, if we were to do this, we would need to account for correlations between both likelihoods; second, it would require considering not only the five cosmological parameters but also the calibration and nuisance parameters; and finally, we would need to take into account the covariance matrices from both likelihoods, while in our analysis we can safely neglect the contribution from errors in *Planck*.

Table 4.4 shows the same numbers shown in Table 4.3 but using the wide priors in $P_{\rm cal}$ and $T_{\rm cal}$. We see how the values of N_σ are slightly reduced, but widening the priors does not have a large impact on the goodness of fit, which could have been expected, since Sec. 4.3 showed that the main effect of widening the priors is an increase of the errors. There are some minimal improvements in the N_σ from the *Planck* best fit, since now a high value of the amplitude $A_s e^{-2\tau}$ is less 'punished' by the wider priors. As expected, there are improvements in χ^2_P: widening the priors reduces the tension with *Planck* in every case.

4.5 Conclusions

In this chapter, we have performed several analyses on the SPTpol likelihood to try to gain a better understanding of possible tensions with *Planck*. We have found some problems and errors with the public SPTpol likelihood used in H18, in particular concerning the way the separate TE and EE analyses are performed, and the aberration and super-sample lensing corrections. These changes produce significant reductions in χ^2 for the individual TE and EE spectra.

We have also discussed problems with the polarization calibration used by SPTpol. We have motivated the choice of a wider prior in the polarization calibration, and shown that this significantly changes the errors in cosmological parameters, in particular, the parameter combination $A_s e^{-2\tau}$, which drives the tension in parameter values with *Planck*. By widening the priors in the calibration parameters, especially in the polarization parameter $P_{\rm cal}$, this tension is significantly reduced.

We explore the origin of the tension between SPTpol and *Planck* by repeating the H18 analysis with different cuts on the multipole range, to determine where this tension originates.

The SPTpol analysis [205] suggests that the difference could come from multipoles above the maximum measured by *Planck* in polarization ($\ell = 1996$). However, multipoles $\ell > 2000$ from SPTpol do not provide strong constraints on cosmological parameters. By using different multipole cuts, we find that the difference with *Planck* is mainly caused by points in the SPTpol spectra in the multipole range $1000 \lesssim \ell \lesssim 2000$. Evaluating the importance of the parameter differences, we find that these are not significant within the framework of ΛCDM .

The different multipole cuts are also used to understand the high values of χ^2 reported by H18. Marginal evidence (below 3σ) of poor fits to ΛCDM is found from both the TE and EE spectra. The combined TE+EE likelihood disfavours the *Planck* cosmology at more than 3σ. This poor fit is likely to be caused by outliers in the data with respect to a ΛCDM cosmology. These could be indicative of problems in the SPTpol error model.

The main conclusion is that the claims by H18 that multipoles $\ell > 2500$ are the main cause for the tension between SPTpol and both *Planck* and ΛCDM are not supported by our results. Outliers in the data with respect to a ΛCDM cosmology are present over the full multipole range. While the origin of these outliers is not clear, it is possible that they are caused by problems with the error model applied by SPTpol. Future data releases from ACTPol and SPTpol should clarify this issue.

Part III

Tests at Low Redshifts

Chapter 5

The effect of Limber and flat-sky approximations on galaxy weak lensing

5.1 Introduction

The amplitude and shape of the mass fluctuation spectrum are of fundamental importance to cosmology. The mass fluctuation spectrum can be used to test the physics of the early Universe, its contents, and the nature of gravity. In addition, it determines the timescales and evolutionary paths for the formation of non-linear objects such as galaxies and galaxy clusters that we see in the Universe today.

Observations of the cosmic microwave background (CMB) [21; 47] have led to precision measurements of the shape of the fluctuation spectrum and via gravitational lensing of the CMB can constrain its amplitude down to redshifts $z \sim 2$. Determining the amplitude at lower redshifts is, however, challenging. Weak gravitational lensing of galaxies is a particularly promising technique. Several weak lensing analyses [98; 213; 214; 215; 216] have reported constraints on the amplitude of the fluctuation spectrum as measured by the parameter σ_8.[a] The results from two surveys, CFHTLenS [215] and KiDS [98], are discrepant with the Planck constraints on the parameter combination $\sigma_8 \Omega_m^{0.5}$, where Ω_m is the present-day matter density parameter, at about the $2.5\,\sigma$ level, assuming the standard six-parameter ΛCDM cosmology (which we will refer to as the base-ΛCDM model). The possibility of new physics beyond base-ΛCDM [106] merits close scrutiny of both the weak lensing and CMB data.

[a] Here, σ_8 is the rms amplitude of the mass fluctuations in spheres of radius $8h^{-1}$ Mpc, where h is the Hubble constant in units of $100\,\mathrm{km\,s^{-1}\,Mpc^{-1}}$.

Recently, Ref. [217] investigated the Limber approximation [218] and a number of other small-angle approximations used to relate weak lensing observables to the three-dimensional matter power spectrum. The first version of that paper concluded that such approximations could contribute significantly to the tension between the CMB measurements and weak lensing data. This conclusion, if correct, would have important implications for cosmology and motivated the analysis presented in this chapter.

The chapter is structured as follows. In Sec. 5.2 we derive the full two-point statistics for weak galaxy lensing in different tomographic redshift bins in full generality, i.e., without using flat-sky or Limber-like approximations (extending the work of Refs [219; 220]). We then compare the exact formulae to small-angle approximations. Section 5.3 applies these formulae to the latest tomographic weak lensing data from CFHTLenS[a] [215] and assesses the impact of these approximations on cosmological parameters and on the tension with the base-ΛCDM constraints from Planck. Our conclusions are presented in Sec. 5.4. Appendix A provides more detail on some of the results used in the main text.

5.2 Two-point statistics

Our aim in this section is to present exact expressions for two-point weak lensing statistics and then to apply small-angle approximations. Further details of the calculations that underlie these results are given in Appendix A. Throughout, we assume a spatially-flat universe.

We start from the definition of the lensing potential $\phi(\hat{\boldsymbol{n}})$ as a function of the gravitational potential $\Phi(\boldsymbol{x}, \chi)$ at (comoving) position $\boldsymbol{x}$ and look back time χ, integrated along the line-of-sight $\hat{\boldsymbol{n}}$ and weighted by a redshift distribution $n(\chi)$ of lensing sources introduced in Sec. 1.3.2 (Eq. 1.3.18):

$$\phi(\hat{\boldsymbol{n}}) = \frac{2}{c^2}\int \frac{\mathrm{d}\chi}{\chi} q(\chi)\Phi(\chi\hat{\boldsymbol{n}}, \chi), \tag{5.2.1}$$

where χ is the comoving radial distance. In this equation $n(\chi)$ is normalized so that $\int n(\chi)\, d\chi = 1$ and $q(\chi)$ is the lensing efficiency:

$$q(\chi) = \int_{\chi}^{\chi_H} \mathrm{d}\chi' \left(\frac{\chi' - \chi}{\chi'}\right) n(\chi'), \tag{5.2.2}$$

where χ_H is the distance to the particle horizon.

We are interested in the two-point statistic

$$\langle\phi(\hat{\boldsymbol{n}})\phi(\hat{\boldsymbol{n}}')\rangle = \left(\frac{2}{c^2}\right)^2 \int \frac{\mathrm{d}\chi}{\chi} q(\chi) \int \frac{\mathrm{d}\chi'}{\chi'} q(\chi') \left\langle\Phi(\chi\hat{\boldsymbol{n}}, \chi)\Phi(\chi'\hat{\boldsymbol{n}}', \chi')\right\rangle . \tag{5.2.3}$$

[a]The data used in this chapter is publicly available at https://github.com/sjoudaki/cfhtlens_revisited.

Expanding the two-dimensional lensing potential ϕ in spherical harmonics, and the gravitational potential in Fourier modes, and using Poisson's equation, we can relate the lensing angular power spectrum $C_\ell^{\phi\phi}$,

$$\langle \phi_{\ell m} \phi_{\ell' m'} \rangle = C_\ell^{\phi\phi} \delta_{\ell\ell'} \delta_{mm'}, \tag{5.2.4}$$

to the unequal-time dimensional matter power spectrum $P_\delta(k; \chi, \chi')$. If we further approximate the unequal-time power spectrum as separable (which is exact in linear theory; see [221] for the impact of non-linear evolution), i.e.,

$$P_\delta(k; \chi, \chi') \approx \left[P_\delta(k; \chi) P_\delta(k; \chi') \right]^{1/2}, \tag{5.2.5}$$

for two tomographic redshift bins (r, s) with redshift distributions $n^r(\chi)$ and $n^s(\chi)$ we find

$$C_\ell^{\phi\phi}(r, s) = \frac{8}{\pi} \left(\frac{3\Omega_m H_0^2}{2c^2} \right)^2 \int \frac{\mathrm{d}k}{k^2} I_\ell^r(k) I_\ell^s(k), \tag{5.2.6a}$$

where

$$I_\ell^r(k) = \int \frac{\mathrm{d}\chi}{\chi} \left[1 + z(\chi) \right] q^r(\chi) j_\ell(k\chi) \left[P_\delta(k; \chi) \right]^{1/2}. \tag{5.2.6b}$$

The main observable in weak galaxy lensing surveys is the shear, which can be described by the spin-2 field $\gamma = \eth^2 \phi / 2$, where $\eth$ is the spin-raising operator (Eq. 1.3.13c). The expansions of the shear, and its complex conjugate, in spin ± 2 spherical harmonics are given by Eqs. 1.3.24a and 1.3.24b:

$$\gamma(\hat{\boldsymbol{n}}) = \sum_{\ell m} (\epsilon_{\ell m} + i \beta_{\ell m}) {}_2Y_{\ell m}(\hat{\boldsymbol{n}}), \tag{5.2.7}$$

$$\gamma^*(\hat{\boldsymbol{n}}) = \sum_{\ell m} (\epsilon_{\ell m} - i \beta_{\ell m}) {}_{-2}Y_{\ell m}(\hat{\boldsymbol{n}}), \tag{5.2.8}$$

where $\epsilon_{\ell m}$ are the multipoles of the E-mode of the shear and $\beta_{\ell m}$ for the B-modes. For lensing in the Born approximation, as considered here, the gravitational shear has only E-modes with $\epsilon_{\ell m} = \sqrt{(\ell+2)!/(\ell-2)!}\, \phi_{\ell m}/2$. The angular power spectrum of the lensing potential, Eq. (5.2.6a), can easily be related to the E-mode power spectrum of the shear field by

$$C_\ell^{\epsilon\epsilon} = \frac{1}{4} \frac{(\ell+2)!}{(\ell-2)!} C_\ell^{\phi\phi}. \tag{5.2.9}$$

The shear γ is defined relative to the θ and ϕ directions. The two-point functions of the shear in real space are simplest when the shear at the two points, $\hat{\boldsymbol{n}}_1$ and $\hat{\boldsymbol{n}}_2$, are rotated onto bases generated by the great circle through the two points (and the orthogonal directions). If we denote the rotated shear by an overbar, e.g., $\bar{\gamma}(\hat{\boldsymbol{n}}_1)$, the shear correlation functions for tomographic bins r and s are defined as

$$\xi_+(\theta; r, s) = \langle \bar{\gamma}_r^*(\hat{\boldsymbol{n}}_1) \bar{\gamma}_s(\hat{\boldsymbol{n}}_2) \rangle, \qquad \xi_-(\theta; r, s) = \langle \bar{\gamma}_r(\hat{\boldsymbol{n}}_1) \bar{\gamma}_s(\hat{\boldsymbol{n}}_2) \rangle, \tag{5.2.10}$$

where θ is the angle between $\hat{\boldsymbol{n}}_1$ and $\hat{\boldsymbol{n}}_2$. The correlation functions $\xi_\pm$ can be expressed in terms of the shear power spectrum as[a]

$$\xi_+(\theta; r, s) = \sum_\ell \frac{2\ell+1}{4\pi} C_\ell^{\epsilon\epsilon}(r, s) d^l_{2\,2}(\theta), \tag{5.2.11a}$$

$$\xi_-(\theta; r, s) = \sum_\ell \frac{2\ell+1}{4\pi} C_\ell^{\epsilon\epsilon}(r, s) d^\ell_{2\,-2}(\theta), \tag{5.2.11b}$$

where d^ℓ_{mn} are the reduced Wigner D-matrices. The equations above are all exact and make no use of the Limber or flat-sky approximations.

5.2.1 Limber approximation

The exact expressions for the power spectra, Eqs. (5.2.6a) and (5.2.6b) are time consuming to evaluate accurately at high multipoles due to the rapid oscillations of the spherical Bessel functions. Many analyses adopt the Limber approximation instead, which is accurate at large ℓ and much easier to compute. In the Limber approximation, we effectively replace the spherical Bessel function in Eq. (5.2.6b) with a delta-function,

$$j_\ell(k\chi) \to \sqrt{\frac{\pi}{2\nu}} \delta_D(\nu - k\chi), \tag{5.2.12}$$

where $\nu = \ell + 1/2$. The wavenumber k is then related to radial distance χ via the relation $k\chi = \nu$. This approximation is accurate if the rest of the integrand in Eq. (5.2.6b) is slowly varying compared to the spherical Bessel function, which is generally the case at large ℓ (see [219] for a careful discussion). Making this approximation in Eq. (5.2.6b), and using Eqs. (5.2.6a) and (5.2.9), we recover the familiar Limber formula for the shear power spectrum

$$C_\ell^{\epsilon\epsilon}(r, s) = \frac{(\ell+2)!}{\nu^4(\ell-2)!} \left(\frac{3\Omega_m H_0^2}{2c^2}\right)^2 \int \mathrm{d}\chi \, [1 + z(\chi)]^2 \, q^r(\chi) q^s(\chi) P_\delta(\nu/\chi; \chi). \tag{5.2.13}$$

5.2.2 Flat-sky approximations

Mathematically, the flat-sky approximations consist of replacing the expansion in spherical harmonics by an expansion in Fourier modes. The relation between shear and lensing power spectra, Eq. (5.2.9), is then

$$C_\ell^{\epsilon\epsilon} \approx \frac{\ell^4}{4} C_\ell^{\phi\phi}. \tag{5.2.14}$$

The reduced D-matrices for high multipoles can be approximated by Bessel functions [223]:

$$d^\ell_{2\,+2}(\theta) \approx J_0(\ell\theta) \qquad d^\ell_{2\,-2}(\theta) \approx J_4(\ell\theta), \tag{5.2.15}$$

[a] Equation (48) of Ref. [222] incorrectly has the $d^\ell_{2\,\pm2}$ replaced by Legendre polynomials in these expressions for the spherical correlation functions.

and together with the Limber-approximated expression (5.2.13), we obtain the usual expression for the shear power spectrum [224] mentioned in the introduction (Eq. 1.3.25)

$$C_\ell^{\epsilon\epsilon}(r,s) = \left(\frac{3\Omega_m H_0^2}{2c^2}\right)^2 \int \mathrm{d}\chi \; [1+z(\chi)]^2 \, q^r(\chi) q^s(\chi) P_\delta(\nu/\chi;\chi), \tag{5.2.16a}$$

and the correlation functions (Eqs. 1.3.26a and 1.3.26b)

$$\xi_+(\theta,r,s) = \frac{1}{2\pi}\int \mathrm{d}\ell\ell J_0(\ell\theta) C_\ell^{\epsilon\epsilon}(r,s), \tag{5.2.16b}$$

$$\xi_-(\theta,r,s) = \frac{1}{2\pi}\int \mathrm{d}\ell\ell J_4(\ell\theta) C_\ell^{\epsilon\epsilon}(r,s). \tag{5.2.16c}$$

Note that we have replaced ν by ℓ in the prefactor of the Limber-approximated power spectrum, Eq. (5.2.13), and also in the expressions (5.2.11a) and (5.2.11b) for the correlation functions $[(2\ell+1)/(4\pi) \to \ell/(2\pi)]$. We have, however, retained ν in the argument of the matter power spectrum.

In this chapter, we compare exact results with two flat-sky approximations: (i) Equations (5.2.16a–5.2.16c) with $\nu = (\ell + 1/2)$ in the argument of the matter power spectrum, which is the approximation used in the tomographic analysis of CFHTlenS and KiDS weak lensing data[a] (we call this 'flat-sky no prefactor'); and (ii) Equations (5.2.13), and (5.2.16b–5.2.16c) with $\nu = (\ell + 1/2)$ in both the prefactor and the matter power spectrum (which we call 'flat-sky with prefactor'). These two approximations differ from each other only in the prefactor of the shear power spectrum. The spectrum with the prefactor is smaller by a factor of approximately $1 - 5/(2\ell^2)$. We shall compare each of these approximations to the exact expressions (5.2.6a–5.2.6b) and (5.2.11a–5.2.11b).

5.3 Application to CFHTLenS data

In this section we investigate the impact of the small-angle approximations on current weak lensing parameter constraints using the CFHTLenS survey as an example. CFHTLenS is based on imaging data from the Canada-France-Hawaii telescope in five photometric bands. In the reanalysis of [215], the data is divided into seven tomographic redshift bins with photometric redshifts spanning the range $0.15 < z < 1.30$. We use the calibrated redshift distributions to compute the exact shear power spectrum, as well as the 'flat-sky no prefactor' and the 'flat-sky with prefactor' spectra, using the formulae presented in the previous section assuming the best-fit parameters of [215]. Figure 5.1 shows the resulting shear power spectra for the third and fourth tomographic redshift bins. This shows that the small-angle approximations have

[a]Note that Eq. (4) in [98] uses $\nu = \ell$ in the argument of the matter power spectrum; however, the public KiDS likelihood code uses $\nu = \ell + 1/2$.

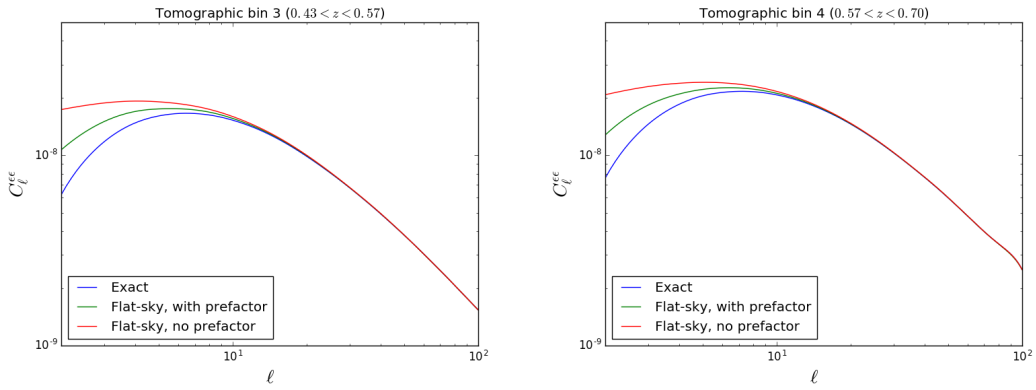

Figure 5.1: Shear power spectra for the third (left) and fourth (right) tomographic redshift bins of the revised CFHTLenS data set assuming the best-fit parameters of [215], illustrating the effects of the small-angle approximations discussed in the text. The red lines use the same approximations as in the tomographic analyses of the CFHTlenS and KiDS weak lensing data, while the blue lines are from the exact calculation.

negligible impact except at multipoles $\ell \lesssim 10$. However, the CFHTLenS analyses are insensitive to these multipoles.

We can see explicitly that the small-angle approximations have negligible impact on the CFHTLenS analysis by looking at the shear correlation functions ξ_+ and ξ_-. Figure 5.2 shows the predictions for ξ_+ and ξ_- for the various approximations assuming the best-fit parameters of [215] for tomographic redshift bin 3, together with the data points and 1 σ errors from [215]. Compared to the large errors on the CFHTLenS data points, the effects of adopting small-angle approximations are negligible over the angular scales probed by the data.

As a final test, we perform parameter estimation (with CosmoMC [186; 190]) sampling the CFHTlenS likelihood as in [215] comparing the 'flat-sky prefactor' with the 'flat-sky no prefactor' approximations.[a] As expected from Fig. 5.1, the impact of these approximations on cosmological parameters such as σ_8 and Ω_m is undetectable within the convergence errors of the parameter chains (and therefore well below the 1 σ errors on cosmological parameters).

5.4 Conclusions

The analysis presented here shows that the small-angle Limber and flat-sky approximations that are typically used in the analysis of galaxy weak lensing have no significant impact on

[a] We have not tested the exact calculation since it is too slow to be used in CosmoMC. However, the differences between the exact correlation functions and those with the 'flat-sky no prefactor' approximation are about twice as large as the differences between the two flat-sky approximations, so our analysis should still be representative of the actual errors introduced by the small-angle approximations.

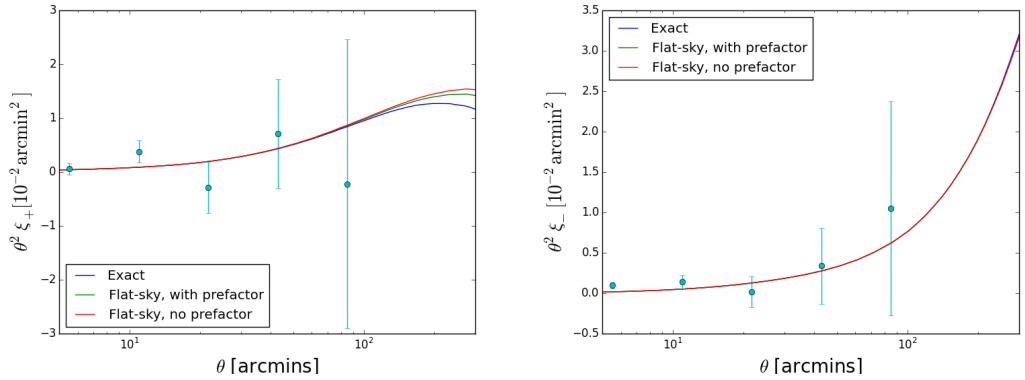

Figure 5.2: Shear correlation functions ξ_+ (left) and ξ_- (right) for the third tomographic redshift bin of CFHTLenS. The points show the CFHTLenS measurements together with $1\,\sigma$ errors. The model curves show the effects of the small-angle approximations described in the text, assuming the best-fit parameters of [215].

cosmological parameters derived from current data. Kilbinger et al. [222] have reached similar conclusions recently, as does the revised version of [217]. Three independent analyses are therefore in agreement that small-angle approximations have no bearing on the discrepancy between the amplitude of the mass fluctuation spectrum inferred from the CFHTLenS or KiDS galaxy weak lensing data and that measured from the CMB assuming the base-ΛCDM cosmology.

Chapter 6

Statistical inconsistencies in the KiDS-450 data set

6.1 Introduction

This chapter continues the work of the previous chapter, trying to understand the reported tension in the parameter combination $S_8 \equiv \sigma_8(\Omega_m/0.3)^{0.5}$, between galaxy weak lensing surveys and the *Planck* 2016 value[ab] $S_8 = 0.850 \pm 0.024$ [21, Henceforth, P16] derived from the Planck temperature power spectrum and low multipole polarization (TT+lowTEB, in the notation of P16). Several ambitious deep imaging projects have reported results recently. These include the Canada France-Hawaii Telescope Lensing Survey [CFHTLenS, 213; 214; 215], Deep Lens Survey [DLS, 225], Dark Energy Survey [DES, 97; 216; 226] and Kilo Degree Survey [KiDS, 98; 111]. Weak lensing analysis of these surveys can be used to constrain the parameter combination S_8, with results which span a range of values. The reanalysis of CFHTlenS by [215] finds $S_8 = 0.732^{+0.029}_{-0.031}$; [225] find $S_8 = 0.818^{+0.034}_{-0.026}$ from DLS; [216] find $S_8 = 0.81 \pm 0.06$ from the DES Science Verification data; [98] (hereafter H17) find $S_8 = 0.745 \pm 0.039$ from a tomographic correlation function analysis of KiDS while [111] (hereafter K17) find $S_8 = 0.651 \pm 0.058$ from a tomographic power spectrum analysis of KiDS. The DES Year 1 weak lensing analysis[c] [226] gives $S_8 = 0.789^{+0.024}_{-0.026}$. Some of these values are

[a] Unless stated otherwise, we quote $\pm 1\sigma$ errors on parameters.

[b] This work was performed before the publication of the *Planck* 2018 results [1] . Because the parameter S_8 does not change significantly ($S_8 = 0.840 \pm 0.024$ for *Planck* 2018 using the TT+lowE likelihood), the analysis was not repeated using the latest *Planck* data.

[c] DES Year 1 results [97; 226] appeared after this work was done and so will not be discussed in detail.

in tension with *Planck*. For example, H17 find a 2.3σ discrepancy between KiDS and *Planck*, while K17 find a 3.2σ discrepancy. However, the results from these different surveys do not agree particularly well with each other (even when using the same shear catalogue), showing differences in the value of S_8 at the $\sim 1.4\sigma$ level. There is also a 2.3σ discrepancy between the results from K17 and the KiDS+GAMA analysis of [227].

A statistically significant tension between the *Planck* ΛCDM cosmology and weak galaxy lensing could have important consequences for fundamental physics [e.g. 106]. But how seriously should we take the weak lensing results? A minimal requirement is that a cosmic shear data set should be internally self-consistent. The main purpose of this chapter is to show that this does not seem to be the case with KiDS if we use the covariance matrix computed of H17. We discuss in Appendix B how our results change if we use a more accurate covariance matrix from [4].

Before we begin, we make a few remarks concerning cosmic shear analysis. Most analyses involve estimation of correlation functions ξ_+ and ξ_- as a function of relative angular separation θ, or of the cosmic shear E-mode power spectrum $C_\ell^{\epsilon\epsilon}$ as a function of multipole ℓ. The relation between these quantities was established in the introduction (Eqs. 1.3.26a and 1.3.26b):

$$\xi_\pm = \frac{1}{2\pi}\int d\ell\ell C_\ell^{\epsilon\epsilon} J_{0,4}(\ell\theta). \tag{6.1.1}$$

As discussed in Chapters 1 and 5, for a cross-power spectrum between redshift bins i and j, the shear power spectrum is related to the non-linear matter power spectrum P_δ by Eq. 1.3.25:

$$C_\ell^{\epsilon\epsilon}(i,j) = \left(\frac{3}{2}\frac{H_0^2}{c^2}\Omega_m\right)^2 \int \mathrm{d}\chi\, [1+z(\chi)]^2\, q^i(\chi) q^j(\chi) P_\delta\left(\frac{\ell+1/2}{S(\chi)}, z(\chi)\right), \tag{6.1.2}$$

where, as explained in the introduction, χ is the comoving radial distance, $S(\chi)$ is the comoving angular diameter distance to distance χ, and $q_i(\chi)$ is the lensing efficiency for tomographic redshift bin i (Eq. 1.3.19):

$$q_i(\chi') = \int_0^{\chi_H} \mathrm{d}\chi \frac{S(\chi-\chi')}{S(\chi)} n_i(\chi), \tag{6.1.3}$$

where χ_H is the comoving Hubble distance and $n_i(\chi)$ is the effective (weighted) number density of galaxies in redshift bin i normalized so that $\int n_i(\chi) d\chi = 1$. Even if the image analysis is assumed to be free of systematic errors and biases, inferences on cosmology require an accurate model of the redshift distribution $n_i(\chi)$, which in turn requires accurate calibration of the photometric redshifts used to define the redshift bin i. A key test of the accuracy of the photometric redshift calibrations would be to demonstrate consistency between distinct cross-correlations i, j. However, this is not straightforward because of intrinsic ellipticity alignments between neighbouring galaxies (II term) and between gravitation shear and intrinsic shear (LI

term) described in Sec. 1.3.2. The power spectra[a] of these terms are usually modelled as (Eqs. 1.3.29 and 1.3.30):

$$C_\ell^{\rm II}(i,j) = \int_0^{\chi_H} d\chi F^2(z) \frac{n_i(\chi) n_j(\chi)}{[S(\chi)]^2} P_\delta\left(\frac{(\ell+1/2)}{S(\chi)}, \chi\right), \tag{6.1.4}$$

$$C_\ell^{\rm LI}(i,j) = \left(\frac{3H_0^2\Omega_m}{2c^2}\right) \int_0^{\chi_H} d\chi F(z)\,[1+z(\chi)]\, \frac{\left[q_i(\chi) n_j(\chi) + n_i(\chi) q_j(\chi)\right]}{S(\chi)} P_\delta\left(\frac{(\ell+1/2)}{S(\chi)}, \chi\right),$$

[99; 101]. In these equations,

$$F(z) = -A_{IA} C \rho_c \frac{\Omega_m}{D(z)}, \tag{6.1.5}$$

where, as mentioned in the introduction, $D(z)$ is the linear growth rate of perturbations (Eq. 1.2.44) normalized to unity at the present day, and $C = 5\times10^{-14} h^{-2} M_\odot^{-1}{\rm Mpc}^3$ is a normalizing constant. With this choice, the intrinsic alignment amplitude is expected to be of order unity (and positive if intrinsic ellipticities are aligned with the stretching axis of the tidal field). This model of intrinsic alignments is heuristic and simplified (see [228] for a more complex alignment model). Even in the context of this model, the intrinsic alignment amplitude may vary with redshift, luminosity, and galaxy type. For current weak lensing surveys, intrinsic alignments are not benign. The contributions of Eqs. 6.1.4 are comparable to any claimed tensions between the *Planck* value of S_8 and those inferred from cosmic shear surveys (with positive A_{IA} raising the value of S_8 and negative values lowering S_8). How can we test the intrinsic alignment model? The conventional solution is to introduce additional nuisance parameters to characterize uncertainties in the intrinsic alignment model [e.g. 229], relying on the redshift dependence of the measured signals to disentangle true cosmic shear from intrinsic alignments. This, of course, requires accurate knowledge of the redshift distributions and their errors.

Current cosmic shear data is still relatively sparse, with a small number of measurements in coarse redshift bins. The number of internal consistency checks of the data and the various components of the model (including nuisance parameters) is therefore limited[b]. In Sec. 6.2 we perform consistency tests of the KiDS data from H17. In Sec. 6.3 we compare the KiDS results with *Planck* and measurements of redshift space distortions and rich cluster abundances, which provide independent measures of the amplitude of the matter fluctuations at similar redshifts to those of the KiDS galaxies. Sec. 6.4 compares the results from various weak lensing analyses. Our main conclusions are presented in Sec. 6.5.

[a] Neglecting B-modes.

[b] The situation is very different to the CMB, where there is a large amount of information to separate a high amplitude frequency independent cosmological signal with a distinctive power spectrum from low amplitude foregrounds with smooth power spectra.

Parameter	Symbol	H17 prior	Extended prior
Cold dark matter density	$\Omega_c h^2$	[0.01,0.99]	[0.01,0.99]
Baryon density	$\Omega_b h^2$	[0.019,0.026]	[0.019,0.026]
100 x approximation to θ_{MC}	$100\theta_{MC}$	[0.5,10]	[0.5,10]
Scalar spectrum amplitude	$\log\left(10^{10}A_s\right)$	[1.7,5]	[1.7,5]
Scalar spectral index	n_s	[0.7,1.3]	[0.1,2]
Hubble parameter	h	[0.64,0.82]	[0.50,3]
IA amplitude	A_{IA}	[-6,6]	[-6,6]
Feedback amplitude	B	[2,4]	[2,4]

Table 6.1: Uniform priors used by H17 and in our extended analysis

6.2 Tests of the KiDS data

We use the KiDS cross-correlation measurements of ξ_+ and ξ_- in four tomographic redshift bins as reported by H17 together with the associated `CosmoMC` likelihood module and covariance matrix[a]. For reference, the four redshift bins span the following ranges in photometric redshift z_B: $0.1 < z_B \leq 0.3$ (bin 1), $0.3 < z_B \leq 0.5$ (bin 2), $0.5 < z_B \leq 0.7$ (bin 3), $0.7 < z_B \leq 0.9$ (bin 4).

6.2.1 Extended priors

We start by repeating the original analysis performed by H17, but extending their 'fiducial' priors (first entry on their Table 4) on some of the cosmological parameters. Our priors are given in table 6.1. This is motivated by the fact that, in the posterior distributions shown in Figures F1 and F2 of H17, the parameter H_0 seems to be constrained only by the prior, showing a clear preference for high values. Similarly, the analysis presented in H17 reports a best fit value for the scalar spectral index n_s that is bigger than one, as opposed to the value obtained by Planck. Our results are shown in Figs. 6.1 and 6.2 and Table 6.2.

The main effect is a displacement in the posteriors of the parameters shown in Table 6.2 at a level of significance above 1σ when wider priors are allowed. In the case of the Hubble parameter, the displacement is greater than 2σ, and the prior extends well into the regime of non-physical values. Indeed, with our extended priors, the best fit value of H_0 chosen by the data is more than 2σ away from the value of $73.24 \pm 1.74 \mathrm{kms}^{-1}\mathrm{Mpc}^{-1}$ obtained by the latest direct measurements of Riess et al [230]. When we allow H_0 to go to higher values, the scalar spectral index n_s goes down below unity through the degeneracy illustrated in Fig. 6.1. This preference of the data for values of the parameters that are clearly unphysical is an indicator that there is a problem with the data.

[a]Downloaded from http://kids.strw.leidenuniv.nl.

Parameter	H17 best fit	'Extended prior' best fit	N_σ
$\Omega_c h^2$	0.115 ± 0.042	0.38 ± 0.19	1.36
H_0 [km s^{-1}Mpc^{-1}]	74.7 ± 5.0	203 ± 58	2.21
n_s	1.09 ± 0.13	0.82 ± 0.22	1.06
σ_8	0.85 ± 0.16	1.45 ± 0.38	1.46
Ω_m	0.249 ± 0.078	0.108 ± 0.057	1.46

Table 6.2: Best fit values for the parameters $\left\{\Omega_c h^2, H_0, n_s\right\}$ and the derived parameters σ_8 and Ω_m. The second and third columns are the best fit values and 1σ errors for the 'fiducial' analysis of H17 and our analysis with extended priors, the fourth column is the number of standard deviations by which these differ, obtained as $N_\sigma = (|\bar{x} - \bar{y}|)/\sqrt{\sigma_x^2 + \sigma_y^2}$.

Fig. 6.2 shows the constraints on σ_8 and Ω_m with 'fiducial' and 'extended' priors, and the corresponding constraints from the *Planck* TT+lowTEB+lensing likelihood. We see how allowing for wider priors in the parameters displaces the KiDS results along the degeneracy direction further away from Planck, increasing the tension between surveys. However, the parameter combination S_8 does not change significantly with this change in priors from $S_8 = 0.745 \pm 0.039$ (fiducial) to $S_8 = 0.797 \pm 0.053$ (extended). The effect of the choice of priors in the tension in the $\Omega_m - \sigma_8$ plane between KiDS and *Planck*, which is one of the main results of H17, stresses the importance of motivating and justifying the choice of priors. As a final remark, the intrinsic alignment parameter is also not affected by this change, other than by an increase in the error (from $A_{IA} = 1.11 \pm 0.64$ to $A_{IA} = 1.33 \pm 0.91$).

This section has demonstrated the sensitivity of the KiDS data to the choice of priors. If the priors allow it, the data favour values of cosmological parameters that differ significantly from the expected values. This should not be the case if the data was free of systematics and the ΛCDM model was the correct theory. Henceforth, we will use the 'default' KiDS priors and test internal consistency of KiDS.

6.2.2 Removal of redshift bins

In this section, we study internal consistency of the KiDS data through the removal of different redshift bins. We used the same angular ranges, photometric redshift calibrations and errors, nuisance parameters and priors as in 'fiducial' analysis in H17 (first entry in their Table 4). We verified that we recovered the identical best-fit χ^2 (162.8) and constraint on S_8 ($S_8 = 0.745 \pm 0.039$). We then removed all cross-correlations involving one of the photometric redshift bins. The results are summarized in Table 6.3 and in Fig. 6.3.

The first point to note is that the intrinsic alignment amplitude is reasonably stable to the removal of photometric redshift bins. All of the posteriors shown in Fig. 6.3 are consistent

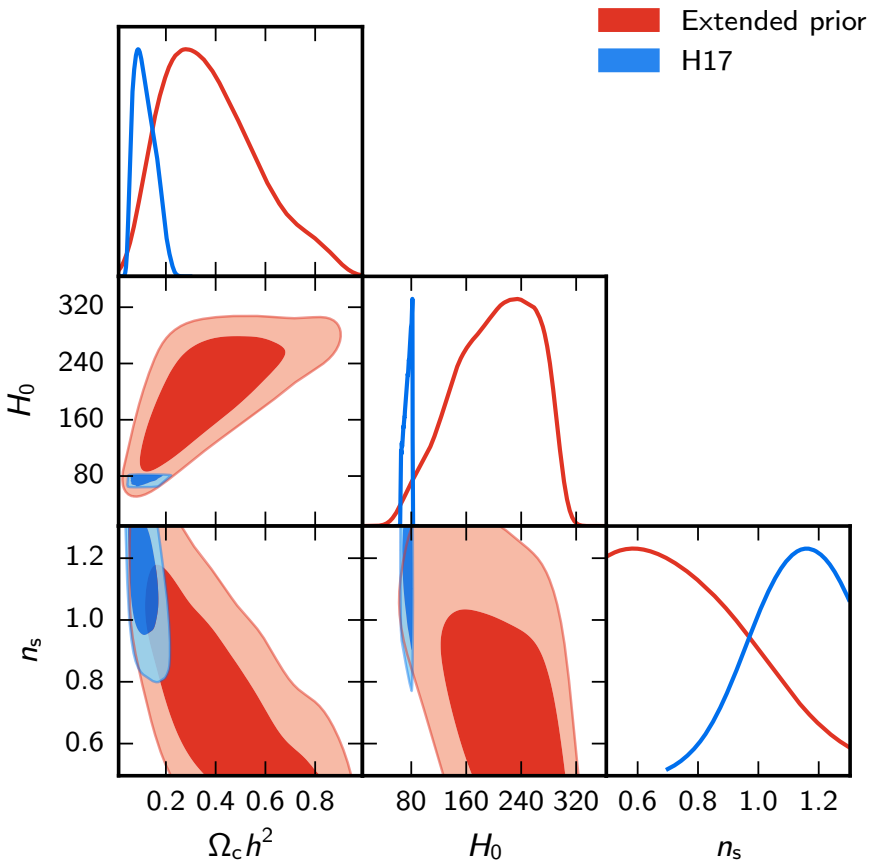

Figure 6.1: Posterior distributions of the model parameters $\left\{\Omega_c h^2, H_0, n_s\right\}$. In blue the posteriors obtained from the 'fiducial' priors of H17, in red our extended priors. The rest of the primary parameters are not affected by the new priors.

Table 6.3: Conditional χ^2 tests removing photometric redshift bins

$\mathbf{y}^D$	S_8	A_{IA}	$\chi^2_{\rm cond}$	$N_{\sigma_{\rm cond}}$
minus z-bin 1	0.745 ± 0.040	1.14 ± 0.85	61.0 (52)	0.89
minus z-bin 2	0.754 ± 0.042	1.24 ± 0.80	66.3 (52)	1.40
minus z-bin 3	0.771 ± 0.039	1.25 ± 0.57	78.2 (52)	2.60
minus z-bin 4	0.684 ± 0.071	-0.1 ± 1.7	87.9 (52)	3.52
minus ξ_-	0.778 ± 0.040	1.10 ± 0.73	89.7 (60)	2.71
minus ξ_+	0.705 ± 0.048	0.92 ± 0.97	84.1 (70)	1.20

Notes: The first column defines the portion of the data vector ($\mathbf{y}^D$) used to fit the model. The second and third columns give the marginalised mean values of S_8, A_{IA} and their 1σ errors. The fourth column gives the conditional $\chi^2_{\rm cond}$, as defined in Eq. 6.2.9, for the rest of data vector, $\mathbf{x}^D$. The numbers in parentheses list the length, $N_{\rm x}$, of the vector $\mathbf{x}^D$. The fifth column gives the number of standard deviations by which $\chi^2_{\rm cond}$ differs from $N_{\rm x}$, $N_{\sigma_{\rm cond}} = (\chi^2_{\rm cond} - N_{\rm x})/\sqrt{2N_{\rm x}}$.

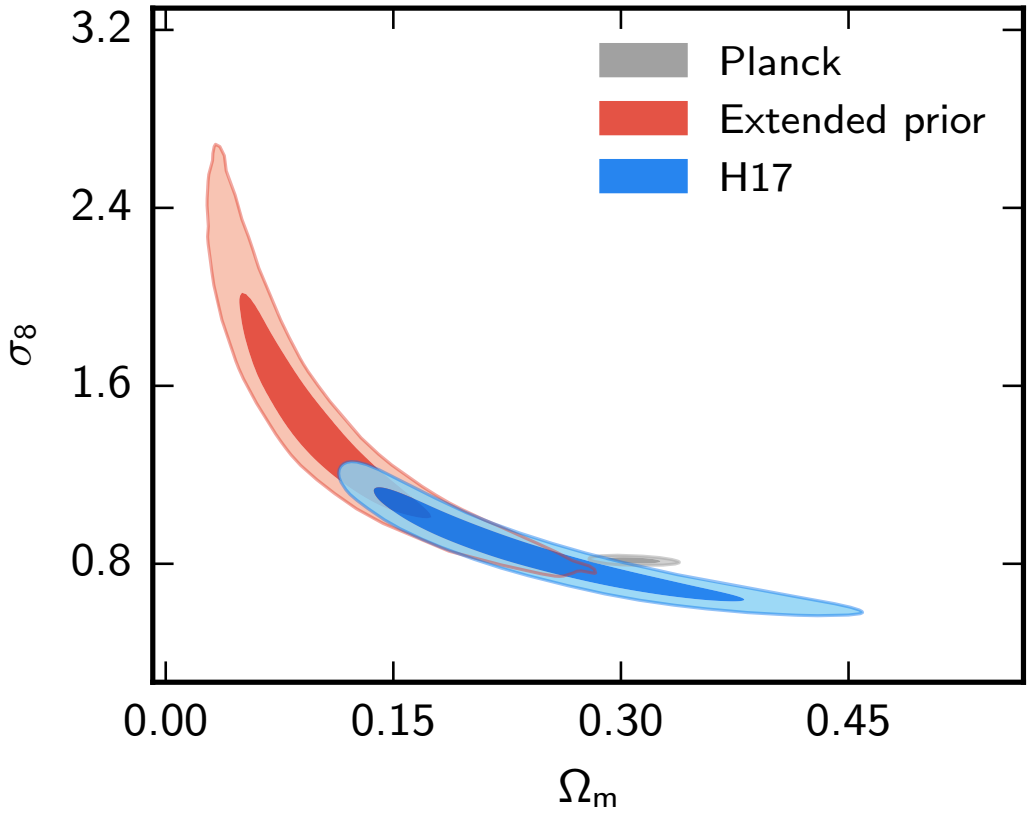

Figure 6.2: Marginalized 2D posterior distributions of the parameters σ_8 and Ω_m. In blue the posteriors obtained from the 'fiducial' priors of H17, in red our extended priors, in grey Planck TT+lowTEB+lensing.

with the intrinsic alignment solution from the full dataset ($A_{IA} = 1.10^{+0.68}_{-0.54}$). However, it is also clear that redshift bin 4 carries a high weight in fixing A_{IA}. With redshift bin 4 removed, the posterior distribution develops a long tail to negative values that is cut-off by the lower end of the A_{IA} prior (uniform between $-6 < A_{IA} < 6$). As a consequence of this long tail, the best fit value of S_8 with bin 4 removed is driven to lower values and its error increases substantially compared to the full sample (lower panel of Fig. 6.3 and Table 6.3). Redshift bin 4 is therefore critical in pinning down the intrinsic alignment solution and reducing the error on S_8.

If redshift bin 3 is removed, S_8 rises and the constraints in the $S_8 - \Omega_m$ plane become compatible with *Planck* (Fig. 6.3). This is not unexpected, because one can see from Fig. 5 of H17 that the best-fit fiducial model tends to sit high for all cross-spectra involving tomographic redshift bin 3 (particularly for ξ_-). With redshift bin 3 removed, there is substantial overlap in the posteriors in the $S_8 - \Omega_m$ plane with those from the full sample and with the other subsets of the data summarized in Table 6.3. However, these various estimates of S_8 are highly correlated

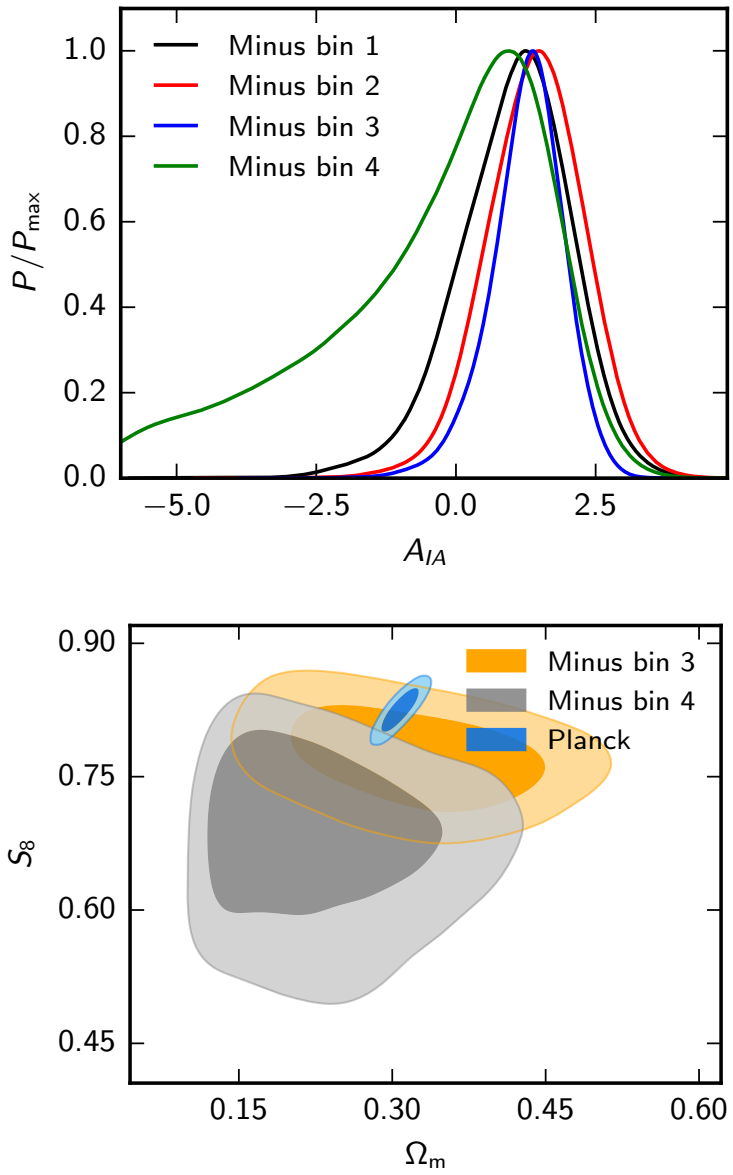

Figure 6.3: The upper panel shows the posteriors for the intrinsic alignment parameter A_{IA} (Eq. 6.1.5) as we remove all cross-correlations involving a particular redshift bin. The lower panel shows the 68 and 95% constraints on S_8 for the data minus redshift bin 3 (orange) and minus redshift bin 4 (grey). The blue contours show the *Planck* constraints from the TT+lowTEB+lensing data combination as given in P16.

since they share common data. Are the parameter shifts seen in these subsets statistically reasonable? We turn to this question next.

We can perform a more elaborate statistical consistency test by dividing the data vector into two components:

$$\mathbf{z}^D = (\mathbf{x}^D, \mathbf{y}^D). \tag{6.2.1}$$

We can then fit $\mathbf{y}^D$ to a model (including nuisance parameters), $\hat{\mathbf{y}}$. The model parameters also make a theory prediction for the data partition $\mathbf{x}^D$, which we denote $\hat{\mathbf{x}}$. We can then write the theory vector for $\mathbf{z}^D$ as

$$\hat{\mathbf{z}} = (\lambda\hat{\mathbf{x}}, \hat{\mathbf{y}}), \tag{6.2.2}$$

introducing a new parameter λ. Evidently, if the data partitions and model are consistent, the new parameter λ should be consistent with unity[a]. The tests described in this Section are all based on the ΛCDM model, *but with a free amplitude*. Since cosmic shear measurements have very limited ability to fix shape parameters, and the data cuts that we apply cover similar redshift ranges, it seems reasonable to interpret differences in λ as indicative of systematic errors in the data. To recap, we run MCMC chains to determine the model parameters from a data partition $\mathbf{y}^D$ and determine a single amplitude parameter λ by fitting to the rest of the data $\mathbf{x}_D$. The posterior distributions of λ for the data cuts of Table 6.3 are shown in Fig. 6.4.

The upper plot in Fig. 6.4 compares the amplitudes λ_- (fitting the model parameters to ξ_+) and λ_+ (fitting the model parameters to ξ_-). This agrees with the visual impression given by Fig. 5 of H17, namely that ξ_- wants a low amplitude while ξ_+ prefers a high amplitude. Integrating these distributions,

$$\int_0^1 P(\lambda_-)d\lambda_- = 2.9 \times 10^{-3}, \tag{6.2.3}$$

$$\int_1^\infty P(\lambda_+)d\lambda_+ = 4.2 \times 10^{-2}. \tag{6.2.4}$$

A value of $\lambda = 1$ therefore lies in the tails of both posterior distributions. These results show that ξ_- sits about 2.8σ low compared to the best fit ΛCDM cosmology determined from ξ_+.

The lower plot in Fig. 6.4 tests consistency between photometric redshift bins including both ξ_+ and ξ_- in the fits. The parameters λ_i (with i running from $1-4$) are computed for data partitions in which $\mathbf{y}^D$ excludes all cross-correlations involving photometric redshift bin i. In this test, photometric redshift bin 3 is an outlier with

$$\int_0^1 P(\lambda_3)d\lambda_3 = 1.3 \times 10^{-2}, \tag{6.2.5}$$

[a]Note that this is a very simplified consistency test, based only on allowing the amplitude of the spectra to vary. After this work was produced, [231] introduced a similar, more general method called posterior predictive distribution (PPD). However, our very simplified test is enough to highlight the issues in the KiDS-450 data.

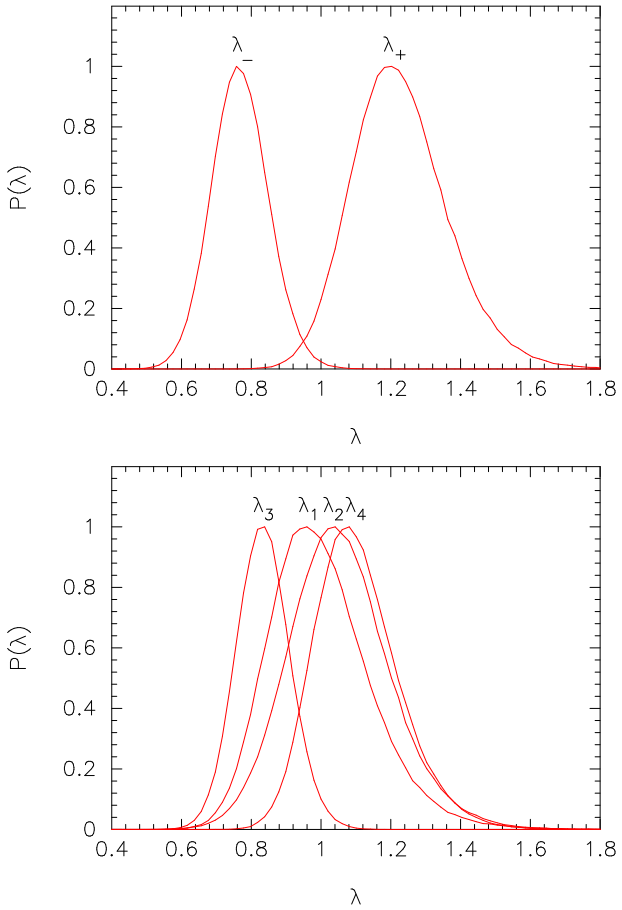

Figure 6.4: Posterior distributions of the parameter λ defined in Eq. 6.2.2. The upper figure shows the distributions if the model parameters are fitted to ξ_+ (denoted λ_-) and to ξ_- (denoted λ_+). The lower figure shows the posterior distributions of λ for partitions of the data in which all cross-correlations involving a particular tomographic redshift bin are removed from the fit to the theoretical model (e.g. λ_3, corresponds to a theoretical model fitted to all cross-correlations that do not involve tomographic redshift bin 3).

suggesting that the data involving photometric redshift bin 3 is inconsistent with the rest of the data at about the 2.2σ level. Again, this accords with the visual impression from Fig. 5 of H17, which shows that cross-correlations in both ξ_+ and ξ_- involving photometric redshift bin 3 tend to lie below their best fit model.

Instead of using an amplitude parameter λ, we can and calculate the most likely data vector $\mathbf{x}^D$ conditional on the fit to $\mathbf{y}^D$

$$\mathbf{x}^{\rm cond} = \hat{\mathbf{x}} + \mathbf{C}_{xy}\mathbf{C}_{yy}^{-1}(\mathbf{y}^D - \hat{\mathbf{y}}). \tag{6.2.6}$$

If the best-fit model is known exactly, the covariance of $\mathbf{x}^{\rm cond}$ is

$$\mathbf{C}_{xx}^{\rm cond} = \mathbf{C}_{xx} - \mathbf{C}_{xy}\mathbf{C}_{yy}^{-1}\mathbf{C}_{yx}. \tag{6.2.7}$$

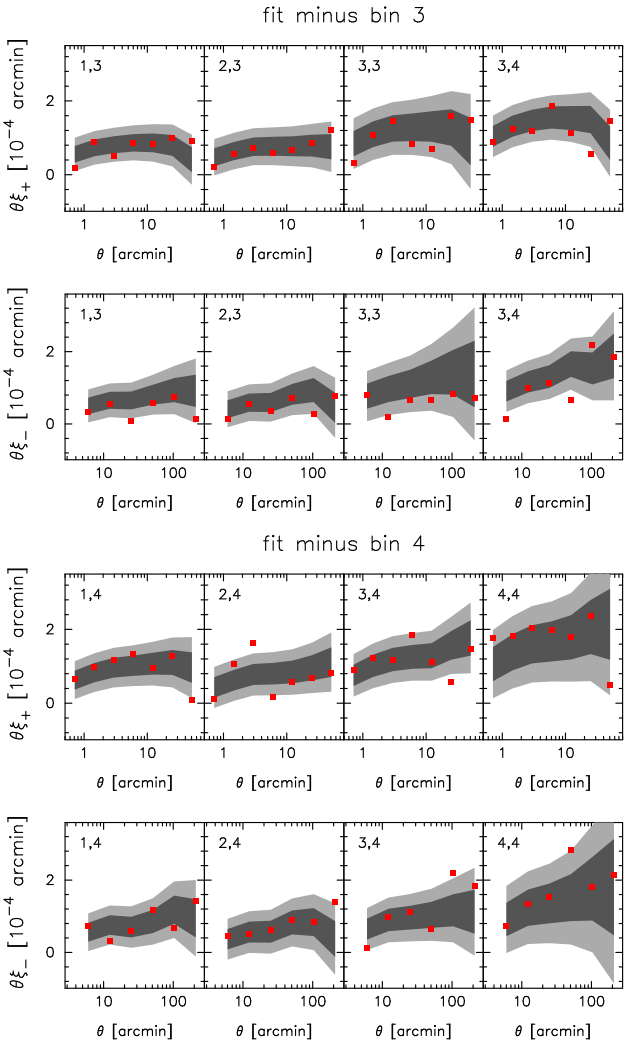

Figure 6.5: The upper two panels show cross-correlations ξ_+ and ξ_- involving tomographic redshift bin 3 (red points). The numbers in each plot identify the cross-correlation (e.g. 1, 3 denotes redshift bin 1 crossed with redshift bin 3). The grey bands show the allowed $\pm 1\sigma$ (dark grey) and $\pm 2\sigma$ (light grey) ranges allowed by the fits to the rest of the data. The lower two panels show the equivalent plots, but for cross-correlations involving tomographic redshift bin 4.

However, in our application the best-fit model is determined by fitting the data vector $\mathbf{y}^D$ and so the uncertainty in the best-fit model contributes an additional variance to $\mathbf{C}_{xx}^{\rm cond}$:

$$\mathbf{C}'^{\rm cond}_{xx} = \mathbf{C}^{\rm cond}_{xx} + \mathbf{\Delta C}^{\rm cond}_{xx}, \tag{6.2.8}$$

which we determine empirically by sampling over the MCMC chains. In our application, $\mathbf{\Delta C}^{\rm cond}_{xx}$ is a small correction to $\mathbf{C}^{\rm cond}_{xx}$.

As a test of the consistency of the data we compute a conditional χ^2:

$$\chi^2_{\rm cond} = (\mathbf{x}^D - \mathbf{x}^{\rm cond})^T (\mathbf{C}'^{\rm cond}_{xx})^{-1} (\mathbf{x}^D - \mathbf{x}^{\rm cond}). \tag{6.2.9}$$

The results of these tests are summarized in Table 6.3 and are consistent with the λ-tests shown in Fig. 6.4[a]. Eliminating ξ_- leads to a substantial increase in S_8 that is incompatible with ξ_- at about 2.7σ. The redshift bin 3 component of the data vector is inconsistent with the rest of the data vector at about 2.6σ. However, the $\chi^2_{\rm cond}$ reveals a new inconsistency: the redshift bin 4 component of the data vector is inconsistent with the rest of the data vector at about 3.5σ.

The origin of the high values of $\chi^2_{\rm cond}$ for these various partitions of the data vector is clear from Fig. 6.5. The figure shows the data vector (red points) for all cross-correlations involving redshift bin 3 (upper two panels) and those involving redshift bin 4 (lower two panels) compared to the expectations $\mathbf{x}^{\rm cond}$ conditional on the rest of the data (Eq. 6.2.6). The grey bands show ± 1 and $\pm 2\sigma$ ranges around $\mathbf{x}^{\rm cond}$ computed from the diagonal components of Eq. 6.2.8. The top two panels of Fig. 6.5 show that cross-correlations involving redshift bin 3 want a lower amplitude than the rest of the data. This problem is particularly acute for ξ_- for the $(3, 3)$ and $(3, 4)$ redshift bin cross-correlations. These two cross-correlations carry quite high weight in fits to the full data vector (driving S_8 down), yet they are inconsistent at nearly $\sim 2.6\sigma$ with the rest of the data. A possible explanation for this discrepancy is an inaccuracy in the calibration of the photometric redshifts for bin 3. In fact [227] present evidence for a 2.3σ negative shift of $\Delta z \approx -0.06$ for this redshift bin. They find no evidence for significant shifts in the other redshift bins.

As summarized in Table 6.3, removing redshift bin 4 lowers the value of S_8 but increases the errors on S_8 substantially because the intrinsic alignment amplitude is less well constrained. From Fig. 6.5 this low amplitude solution appears to match reasonably well with the general shape of the rest of the data vector, but now we see a high value of $\chi^2_{\rm cond}$ arising from *outliers*. In the lower two panels of this figure, 8 out of 52 data points sit outside the conditional $\pm 2\sigma$ range[b]. Several of these outliers are at large angular scales and are not obvious in plots using errors computed from the diagonals of the full covariance matrix (e.g. Fig. 5 of H17). However, the KiDS covariance matrix tells us that the data vector should be correlated across different tomographic redshift bins. What Fig. 6.5 shows is that the KiDS correlation functions display significantly higher variance than expected from the KiDS covariance matrix, particularly at large angular scales and for correlations involving redshift bin 4. This excess variance is a serious problem because it means that the KiDS errors on cosmological parameters are systematically underestimated, especially if data at small angular scales is excluded.

Our analysis shows strong evidence for a statistical inconsistency between the KiDS estimates of ξ_+ and ξ_-. H17 and [227] find evidence for non-zero B-modes in the KiDS data at small angular scales ($\theta < 4.2'$), indicative of systematics. If systematic errors contribute

[a] This conditional χ^2 neglects possible non-Gaussian tails. A full PPD analysis [231] would possibly produce small changes in the results from Table 6.3, but is not expected to change the conclusions.

[b] Assuming Gaussian statistics, the $p-$value for this is about 2.4×10^{-3}.

equally to the tangential and cross distortions (and this has not been demonstrated for KiDS), then the B-modes will affect ξ_+, but not ξ_-. Eliminating ξ_+ entirely from the fits lowers S_8 to 0.705 ± 0.048 (see Table 6.3) with $\chi^2 = 82.2$ for 50 degrees of freedom (a 3.2σ excess). In other words, if one argues that the difference between ξ_+ and ξ_- is indicative of systematic errors in ξ_+, then the tension between KiDS and *Planck* is exacerbated.

6.3 Comparison with other techniques for measuring the amplitude of the fluctuation spectrum

The results of the previous section show that there are some worrying internal inconsistencies in the KiDS dataset as analysed in H17. These inconsistencies suggest that we should be cautious in interpreting the KiDS constraints on cosmology. However, the tests in themselves do not tell us the causes of the inconsistencies, or their impact on the estimates of S_8. Is the amplitude of the matter fluctuations at redshifts $z \lesssim 1$ really lower than expected in the *Planck* ΛCDM cosmology?

Another way of studying the amplitude of the matter power spectrum is via redshift space distortions [RSD, 232] as discussed in Sec. 1.3.6. RSD provide a measurement of the parameter combination $f\sigma_8$, where f is the logarithmic derivative of the linear growth rate with respect to the scale factor (Eq. 1.3.40)

$$f = \frac{\mathrm{d}\ln D}{\mathrm{d}\ln a}, \tag{6.3.1}$$

and $a = (1+z)^{-1}$. In the ΛCDM model, $f \approx \Omega_m(z)^{0.55}$ and so RSD measure the parameter combination $\sigma_8\Omega_m^{0.55}$, *i.e.* similar to the parameter combination S_8 up to a known constant. Measurements of RSD from the DR12 analysis of the Baryon Oscillation Spectroscopy Survey (BOSS) have been reported by [116]. These measurements are for three redshift slices with effective redshifts $z_{\rm eff} = 0.38$, $z_{\rm eff} = 0.51$ and $z_{\rm eff} = 0.61$, substantially overlapping with the redshift range of the KiDS survey. [233] have recently used the Supercal Type Ia supernova compilation [234] together with independent distance measurements of galaxies [235] to measure $f\sigma_8$ at $z_{\rm eff} = 0.02$. The *Planck* ΛCDM cosmology is in excellent agreement with these measurements of $f\sigma_8$ over the entire redshift range $z = 0.02 - 0.61$. The consistency between *Planck* and the RSD measurements is illustrated in Fig. 6.6, where we have combined the BOSS and Supercal RSD measurements to produce constraints in the $\sigma_8 - \Omega_m$ plane[a]. The RSD constraints are in mild tension with the KiDS correlation function analysis of H17, and in

[a]This is done using the final_consensus_dV_FAP_fsig data files and covariance matrix downloaded from https://sdss3.org/science/boss_publications.php. We then scanned the likelihood, using uniform priors in H_0 and $\Omega_m h^2$ to rescale the BOSS distance D_V and Alcock-Paczynski [114] parameter F_{AP} to the fiducial sound horizon used in the BOSS analysis, fixing $\Omega_b h^2$ to the P16 ΛCDM value.

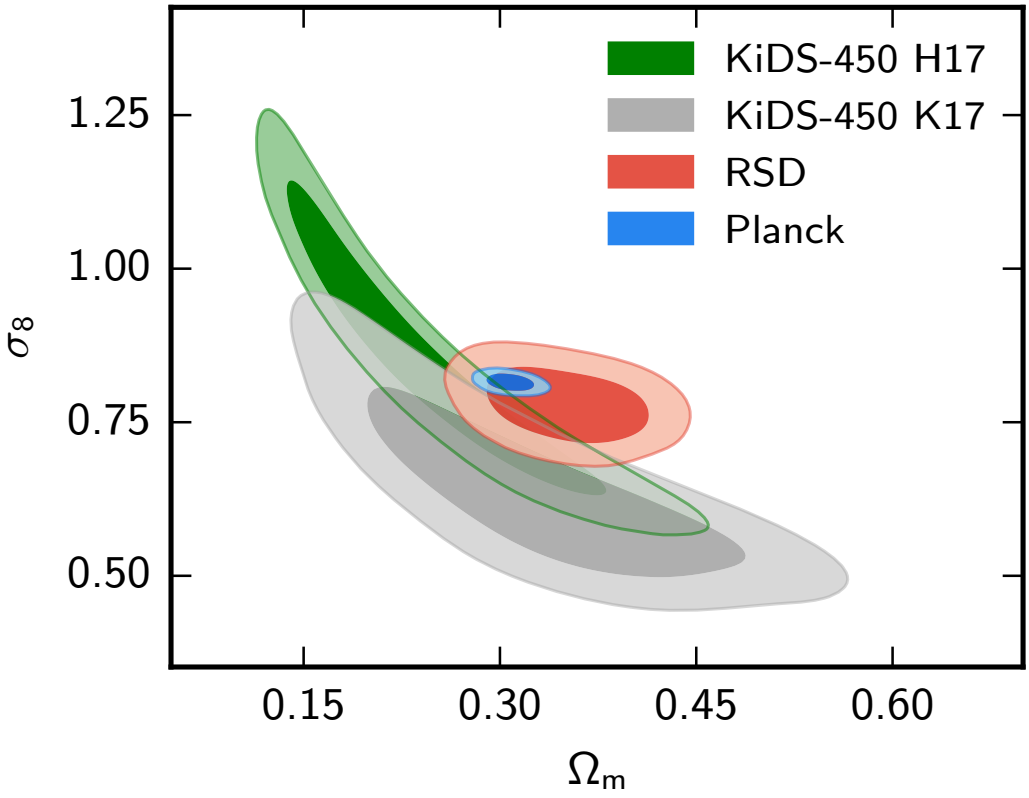

Figure 6.6: Constraints in the $\sigma_8 - \Omega_m$ plane assuming the spatially flat ΛCDM cosmology. The 68% and 95% contours from *Planck* are shown in blue. The constraints from the H17 fiducial KiDS analysis are shown in green. The grey contours show the constraints from the power-spectrum analysis of KiDS reported by K17. The red contours show the constraints from redshift-space distortions (RSD) as discussed in the text.

even greater tension with the tomographic power-spectrum analysis of KiDS described by K17 *using the same shear catalogue*.

The abundance of rich clusters of galaxies (selected at various wavelengths) has been used in a number of studies to constrain the amplitude of the fluctuations spectrum at low redshift [e.g. 236; 237; 238; 239; 240; 241; 242]. As summarized in several of these papers, calibration of cluster masses is a major source of uncertainty in this type of analysis. Two recent studies [240; 242] use weak gravitational lensing mass estimates from the 'Weighing the Giants' programme [243; 244; 245] to calibrate cluster scaling relations. [240] use an X-ray selected sample of clusters from the ROSAT All-Sky Survey covering the redshift range $0 < z < 0.5$, finding $\sigma_8(\Omega_m/0.3)^{0.17} = 0.81 \pm 0.03$. [242] use a sample of clusters identified with the South Pole Telescope with median redshift $z_{\rm med} = 0.53$ to infer $\sigma_8(\Omega_m/0.27)^{0.3} =$

0.797 ± 0.031. Both of these estimates are consistent with the Planck P16 ΛCDM cosmology obtained from the TT+lowTEB+lensing data combination: $\sigma_8(\Omega_m/0.3)^{0.17} = 0.818 \pm 0.009$, $\sigma_8(\Omega_m/0.27)^{0.3} = 0.848 \pm 0.012$. Thus, there is no convincing evidence for any discrepancy between rich cluster counts and the expectations from the *Planck*-ΛCDM cosmology. The [242] study is particularly interesting because it covers a similar redshift range to those of the BOSS RSD and KiDS measurements, yet is consistent with *Planck* and RSD.

6.4 Comparison of weak lensing estimates of S_8: the importance of intrinsic alignments

Fig. 6.6 shows a discrepancy between the H17 and K17 analyses, which are based on the same shear catalogue. There is little doubt that the H17 and K17 analyses are incompatible, since not one of the 14,469 samples in the K17 MCMC likelihood chain[a] has parameters close to those of the best fit found by H17. In fact, [227] (hereafter vU17) have computed cross power-spectra from ξ_+ and ξ_- for the KiDS data using the identical redshift bins to those used in K17. Their auto-spectrum for the highest redshift bin differs substantially from the quadratic estimate of K17. The origin of this difference is not understood[b]. Another pointer that the K17 results are affected by systematic errors comes from the intrinsic alignment solution. K17 find $A_{IA} = -1.72^{+1.49}_{-1.25}$ which has the opposite (and from the theoretical perspective, counterintuitive) sign to that found by H17. This difference drives down the amplitude of S_8 in the K17 analysis. Both the direct comparison of spectra reported by [227] and the shift to a negative intrinsic alignment amplitude suggest that the K17 analysis is suspect.

The key point that we want to emphasise here is that the intrinsic alignment parameter A_{IA} is not a benign 'nuisance' parameter [for reviews see e.g. 246; 247]. The modelling of intrinsic alignments is degenerate with the cosmological parameters of interest, σ_8, Ω_m, and S_8, and so the model and associated parameters matter. Systematic errors in the data can be absorbed by the intrinsic alignment model and this will have an impact on cosmology. For example, [227] have noted that the parameter A_{IA} can absorb systematic errors in the calibrations of photometric redshift distributions. (This can also be inferred from Fig. 6.3 which shows the sensitivity of the intrinsic alignment solution for the KiDS data to the highest photometric redshift bin). Implausible (e.g. strongly negative) values of A_{IA} suggest systematic errors and should therefore be followed up.

[a] KiDS450_QE_EB_4bins_3zbins_basez_ia_bary_nu.txt, downloaded from http://kids.strw.leidenuniv.nl.

[b] Note that the quadratic estimator used by K17 is sensitive to noise estimation, particularly if there are B-mode systematics (which are known to be present in the KiDS data). Inaccurate noise estimation would primarily affect the auto-spectra, where the noise levels are high compared to the cosmological signal (see Fig. 4 of H17).

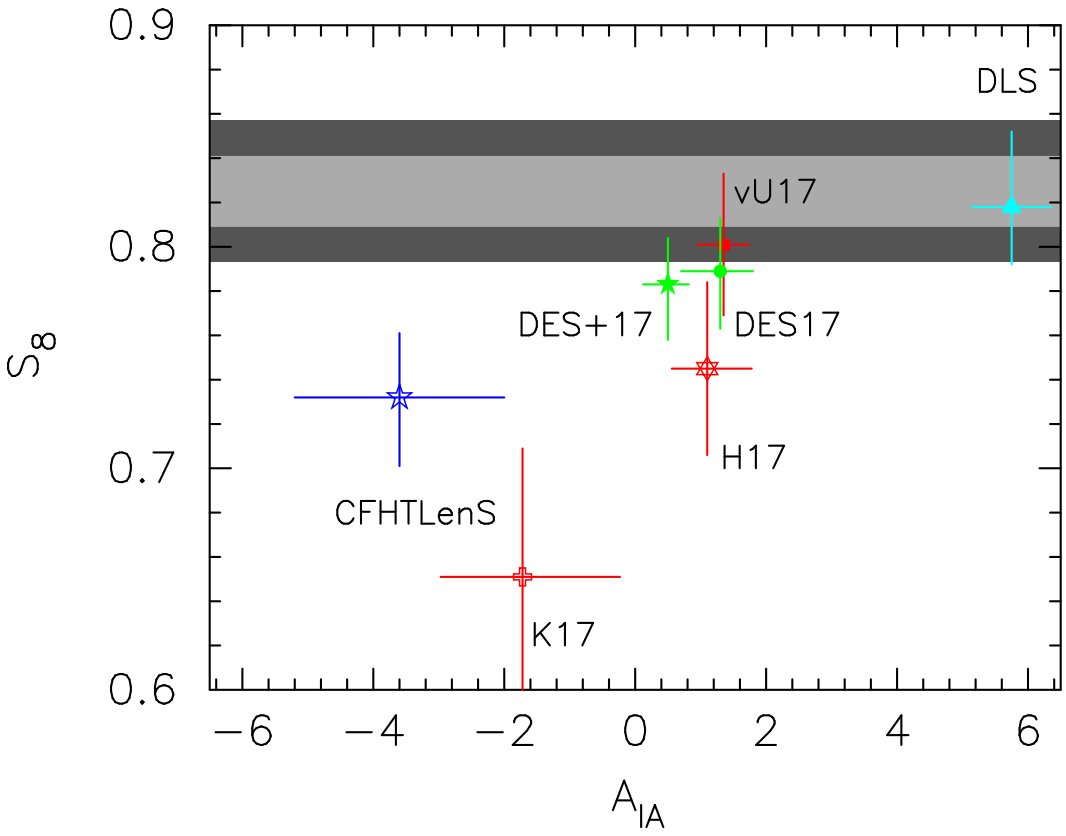

Figure 6.7: S_8 plotted against the intrinsic alignment amplitude for various surveys together with 1σ errors on S_8 and A_{IA}. The grey bands show the 1σ and 2σ constraints from *Planck*. The data points are as follows: CFHTLenS [215]; DLS [225][a]; K17 shows the power spectrum analysis of KiDS [111]; H17 shows the correlation function analysis of KiDS [98]; vU17 shows the constraints from combining P^{gg}, P^{gm} and P^{E} measurements from KiDS and GAMA data [227]; DES17 shows the cosmic shear constraints from DES year 1 data [226] (note that the DES analyses uses a redshift dependent model of intrinsic alignments, as described in the text); DES+17 shows the combination of DES year 1 cosmic shear results with galaxy-galaxy and galaxy-shear measurements [97].

As an example, one of the lowest weak lensing determinations of S_8 comes from the reanalysis of the revised CFHTLenS data [106]. However, these authors find a strongly negative value of $A_{IA} = -3.6 \pm 1.6$, a value which seems unlikely for any reasonable mix of galaxy types. The recent DES analysis of [226] uses a redshift dependent amplitude: $A_{IA}[(1+z)/(1.62)]^{\eta}$, finding $A_{IA} = 1.3^{+0.5}_{-0.6}$, $\eta = 3.7^{+1.0}_{-2.3}$ [b]. [226] also test a more elaborate 'mixed' alignment

[a] Note that the [225] 'baseline' analysis of DLS use a luminosity dependent model of intrinsic alignments and impose a flat prior of $5.14 < A_{IA} < 6.36$, motivated by the results of [248]. However, they find that their results on S_8 are insensitive to A_{IA} (see their Fig. 12), presumably because of the huge depth of DLS.

[b] These constraints become $A_{IA} = 0.5^{+0.32}_{-0.38}$, $\eta = 0^{+2.7}_{-2.8}$ with the addition of galaxy-galaxy and galaxy-shear data, [97]). These authors argue that an amplitude of $A_{IA} \sim 0.5$ is consistent with their selection criteria if only red

model based on the work of [228]. This model leads to a downward shift of S_8 by about 1σ, demonstrating that uncertainties in the modelling of intrinsic alignments makes a non-negligible contribution to the errors in cosmological parameters.

Returning to the KiDS survey, one way of achieving better control of intrinsic alignments and photometric redshift calibration errors is to add additional types of data. vU17 have analysed the shear power spectra from KiDS, P^E (constructed by integrating over ξ_+ and ξ_-). In addition, they use the Galaxies Mass Assembly (GAMA) redshift survey [249; 250] to compute the galaxy-mass power-spectra, P^{gm} by cross-correlating the KiDS shear measurements with GAMA galaxies, and the galaxy-galaxy power spectra P^{gg}. From $P^{gm} + P^{gg}$, they find $S_8 = 0.853 \pm 0.042$. Combining with P^E, they find $A_{IA} = 1.30 \pm 0.40$ and $S_8 = 0.801 \pm 0.032$ (consistent with the *Planck* and RSD results shown in Fig. 6.6).

Fig. 6.7 gives a summary of the results discussed in this Section. The two analyses that are most discrepant with the S_8 value from Planck (CFHTLenS and K17) both have strongly negative intrinsic alignment solutions. The H17 results are in tension with *Planck* but become consistent with *Planck* with the addition of galaxy-galaxy and galaxy-mass data (vU17). The DES year 1 analyses plotted in Fig. 6.7 are both consistent with *Planck*. The intrinsic alignment solutions of vU17 and [97] (i.e. $A_{IA} \sim 1$) seem physically plausible given the mix of galaxy types expected in these surveys.

6.5 Conclusions

The main purpose of this chapter has been to highlight and quantify internal inconsistencies in the KiDS cosmic shear analysis. Our main conclusion is that more effort is needed to resolve inconsistencies in the KiDS data. This includes understanding the origin of the B-modes, systematic differences between ξ_+ and ξ_-, the parameter shifts seen by excluding photometric redshift bin 3, the large excess χ^2 and scatter at large angular scales. Until this is done, it seems premature to draw inferences on new physics from KiDS.

Comparison of *Planck* with other measures of the amplitude of the mass fluctuations, principally redshift space distortions from BOSS, reveals no evidence for any inconsistencies with the *Planck* base-ΛCDM cosmology. We have also reviewed cosmic shear constraints on S_8, emphasising the degeneracy between intrinsic alignments and cosmology. As summarized in Fig. 6.7 the two analyses which yield the lowest values of S_8 both have strongly negative values of A_{IA}. The DES 1 year analyses are consistent with the *Planck* ΛCDM value for S_8 [97; 226] and give physically plausible values for A_{IA}. The H17 value of S_8 from KiDS sits about 2.3σ low compared to *Planck*, but is pulled upwards with the addition of galaxy-galaxy, galaxy-mass

galaxies contribute to the intrinsic alignments.

data (vU17). Overall, we conclude there is no strong evidence for any inconsistency between the *Planck* ΛCDM cosmology and measures of the amplitude of the fluctuation spectrum at low redshift.

All the internal inconsistencies found in the KiDS data in this chapter used the covariance matrix from H17. Appendix B repeats the internal consistency tests described in this chapter to the KiDS data using the corrected covariance matrix described in [4]. As described by Appendix B, this corrected covariance matrix, combined with a correction of the effective centres of the tomographic angular bins, raises the value of the parameter combination S_8, and increases the errors in parameter constraints, alleviating the tension with *Planck* as well as some of the internal inconsistencies described in this chapter.

After this work was done, members of the KiDS collaboration published a paper in response [251]. In this paper, the authors use a different statistical method to asses internal consistency. Their method is a variation of the posterior predictive distribution [231], that they call translated predictive distribution (TPD). This methods obtains less significance in the differences between redshift bins, but a higher significance in the difference between the separate ξ_+ and ξ_- analyses. The authors of [251] agree that the corrections of the covariance matrix introduced in [4] solve all internal inconsistencies in the KiDS-450 dataset.

CHAPTER 7

MODEL INDEPENDENT $H(z)$ RECONSTRUCTION USING THE COSMIC INVERSE DISTANCE LADDER

7.1 Introduction

The *Planck* satellite has provided strong evidence in support of the ΛCDM cosmology and has measured the six parameters that define this model to high precision [21; 47, hereafter P16 and P14 respectively]. In particular, P16[a] found a value of the Hubble constant of $H_0 = 67.27 \pm 0.66$ km s^{-1}Mpc^{-1}. As pointed out in P16, other data combinations give similar values of H_0, for example combining WMAP and BAO data gives $H_0 = 68.0 \pm 0.7$ km s^{-1}Mpc^{-1}. A 'low' value of H_0 is therefore not solely driven by high multipole CMB anisotropies measured by *Planck* but is necessary if the ΛCDM cosmology is to fit a range of cosmological data.

In contrast, direct measurements of the cosmic distance scale have consistently found a higher value of H_0. The SH0ES[b] project uses Cepheid period-luminosity relations, together with local distance anchors, to calibrate distances to Type Ia SNe host galaxies. The SH0ES programme has reported measurements of H_0 of increasing precision over the last few years [125; 230; 252; 253]. The latest value from the SH0ES collaboration[c] is $H_0 = 73.48 \pm 1.66$ km s^{-1}Mpc^{-1} [125, hereafter R18], which is consistent with but has a much smaller error

[a] This value is for the full temperature and polarization analysis in P16. It is consistent with the value $H_0 = 67.36 \pm 0.54$ km s^{-1}Mpc^{-1} from the latest *Planck* analysis [1] derived for the TT,TE,EE+lowE+lensing likelihood combination.

[b] Supernovae and H_0 for the Equation of State.

[c] As this work was nearing completion, [254] reported new Hubble Space Telescope photometry of long period Milky Way Cepheids. Together with GAIA parallaxes [255] these measurements increase the tension between *Planck* and the distance ladder estimate of H_0 to 3.8σ.

than earlier determinations from the Hubble Space Telescope key project [256].

The 3.5σ difference between the SH0ES determination of H_0 and the value inferred from *Planck* for the ΛCDM cosmology is one of the most intriguing problems in modern cosmology. Perhaps unsurprisingly, there have been many attempts to solve the problem by introducing new (and sometimes highly speculative) physics [e.g. 126; 127; 128; 129; 130]. There have also been several reanalyses of the SH0ES data [257; 258; 259; 260] which, apart from minor details, agree well with the analyses by the SH0ES collaboration, though [261] conclude that the Gaussian likelihood assumption used in the SH0ES analysis may overestimate the statistical significance of the discrepancy.

In this chapter, we apply the inverse ladder [134; 135; 136; 137; 262; 263; 264] to derive an estimate of H_0. In our application, we combine SNe data from the Pantheon sample [265] with BAO measurements from the 6dF Galaxy Survey (6dFGS) [266], Baryon Oscillation Spectroscopic Survey (BOSS) [116] and Sloan Digital Sky Survey (SDSS) quasars [117; 119; 120]. To calibrate the inverse distance ladder, we impose priors on the sound horizon at the end of the radiation drag epoch, r_d. However, instead of assuming a particular cosmological model, we fit a flexible parametric model describing the evolution of the Hubble parameter $H(z)$. The FRW metric then fixes the luminosity distance $D_L(z)$ in terms of $H(z)$; the extrapolation of $H(z)$ to $z = 0$ is then independent of the low redshift properties of dark matter and dark energy, as in the important analysis of [262]. Note that this extrapolation only relies on the FRW metric, and does not assume the equations of General Relativity.

The analysis presented here is similar to recent analyses by [231], who parameterized $D_L(z)$ with a third-order Taylor expansion (characterized by the deceleration and jerk parameters q_0 and j_0), by [267], who parameterized $H(z)$ on a discrete grid in z and by [263] who reconstruct $H(z)$ by interpolating piece-wise cubic splines specified by a small number of knots. In this chapter, we parameterize $H(z)$ as a smooth function of redshift. Our analysis is closely related to that of [263], except that we use more recent (and more constraining) BAO and supernova data to extrapolate to a value of H_0 rather than fixing the sound horizon, and we demonstrate explicitly that the discrepancy with the direct measurement of H_0 is insensitive to whether the BAO scale is normalized using priors on the sound horizon derived from *Planck* or WMAP.

The layout of this chapter is as follows: In Section 7.2 we introduce our parameterization of $H(z)$ and the priors on r_d that we use to calibrate the distance scale. The datasets used in this analysis are described in Section 7.3 and our results are presented in Section 7.4. Section 7.5 presents our conclusions.

7.2 Inverse distance ladder

7.2.1 $H(z)$ parameterizations

According to the FRW metric, the Hubble parameter $H(z)$ fixes the luminosity distance $D_L(z)$ introduced in Section 1.1.5 and comoving angular diameter distance $D_M(z)$ according to

$$D_L(z) = c(1+z)\int_0^z \frac{dz'}{H(z')}, \quad D_M(z) = \frac{D_L(z)}{(1+z)}, \tag{7.2.1}$$

where we have assumed that a spatially flat geometry is an accurate description of our Universe. We adopt the following parametric form for $H(z)$:

$$H^2(z) = H_{\rm fid}^2\left[A(1+z)^3 + B + Cz + D(1+z)^\epsilon\right], \tag{7.2.2}$$

with A, B, C, D and ϵ as free parameters. We refer to this parameterization as the 'epsilon' model. The normalising factor $H_{\rm fid}$ is fixed at $H_{\rm fid} = 67$ km s^{-1}Mpc^{-1} and is introduced so that the free parameters A to D are dimensionless and of order unity. In the base ΛCDM cosmology,

$$H(z) = H_0\left[\Omega_m(1+z)^3 + (1-\Omega_m)\right]^{1/2}, \tag{7.2.3}$$

where Ω_m is the present day total matter density in units of the critical density. Equation (7.2.3) applies at low redshifts when contributions to the energy density from photons and neutrinos can be ignored. This equation is reproduced by the parameterization of equation (7.2.1) if

$$A = \left(\frac{H_0}{H_{\rm fid}}\right)^2\Omega_m, \qquad B = \left(\frac{H_0}{H_{\rm fid}}\right)^2(1-\Omega_m), \qquad C = D = 0, \qquad \epsilon \neq 0, \tag{7.2.4}$$

with a degeneracy between B and D for $\epsilon = 0$.

The base ΛCDM model assumes that dark energy is a cosmological constant with equation of state $w = p/(\rho c^2) = -1$. In models of evolving dark energy, the equation of state is often parameterized as

$$w(z) = w_0 + w_a\frac{z}{1+z}. \tag{7.2.5}$$

With this equation of state, and arbitrary curvature Ω_k,

$$H^2(z) = H_0^2[\Omega_m(1+z)^3 + \Omega_k(1+z)^2 + \Omega_{\rm DE}(1+z)^{-3(1+w_0+w_a)}e^{-3w_a z/(1+z)}], \tag{7.2.6}$$

where $\Omega_{\rm DE} = 1 - \Omega_m - \Omega_k$. In our application of the inverse distance ladder, the data that we use spans the redshift range $0.1 - 2.4$ (see Section 7.3). Over this redshift range, the parameterization of equation (7.2.2) accurately reproduces equation (7.2.6) for extreme values of w_0, w_a and Ω_k. Provided $H(z)$ is a smoothly varying function of z, with no abrupt jumps, the epsilon model provides an accurate description of the evolution of $H(z)$ in a wide variety

Dataset	$z_{\rm eff}$	Measurement	Constraint
6dFGS	0.106	$r_d/D_V(z_{\rm eff})$	0.336 ± 0.015
BOSS DR12	0.38	$D_M(z_{\rm eff})r_{d,\rm eff}/r_d$	1512 ± 25 Mpc
		$H(z_{\rm eff})r_d/r_{d,\rm eff}$	81.2 ± 2.4 km s^{-1}Mpc^{-1}
	0.51	$D_M(z_{\rm eff})r_{d,\rm eff}/r_d$	1975 ± 30 Mpc
		$H(z_{\rm eff})r_d/r_{d,\rm eff}$	90.9 ± 2.3 km s^{-1}Mpc^{-1}
	0.61	$D_M(z_{\rm eff})r_{d,\rm eff}/r_d$	2307 ± 37 Mpc
		$H(z_{\rm eff})r_d/r_{d,\rm eff}$	99.0 ± 2.5 km s^{-1}Mpc^{-1}
eBOSS DR14 QSO	1.52	$D_A(z_{\rm eff})r_{d,\rm eff}/r_d$	1850^{+90}_{-115} Mpc
		$H(z_{\rm eff})r_d/r_{d,\rm eff}$	159^{+12}_{-13} km s^{-1}Mpc^{-1}
BOSS DR12 Lyα	2.33	$D_M(z_{\rm eff})/r_d$	37.8 ± 2.1
		$c/(H(z_{\rm eff})r_d)$	9.07 ± 0.31
BOSS DR12 QSOxLyα	2.40	$D_M(z_{\rm eff})/r_d$	35.7 ± 1.7
		$c/(H(z_{\rm eff})r_d)$	9.01 ± 0.36

Table 7.1: BAO measurements used in this chapter. $z_{\rm eff}$ gives the effective redshift for each measurement. The BOSS DR12 and eBOSS DR14 QSO analyses adopt a fiducial sound horizon of $r_{d,\rm eff} = 147.78$ Mpc. Note that [266] use the [268] formulae to calculate r_d.

of theories involving dynamical dark energy and interactions between dark energy, dark matter and baryons.

As we will see in Section 7.4, the parameters of the epsilon model are strongly degenerate. We have therefore also implemented a simpler parameterization, which we refer to as the 'log' model:

$$H^2(z) = H^2_{\rm fid}\left[A'(1+z)^3 + B' + C'z + D'\ln(1+z)\right]. \tag{7.2.7}$$

This is a less flexible parameterization than the epsilon model but the four free parameters in equation (7.2.7) are less degenerate. In fact, we will find that the data constrain $H(z)$ to be so close to the form expected in the base ΛCDM cosmology that the epsilon and log models give nearly identical results for H_0.

7.2.2 The sound horizon

The principal datasets used in this analysis are Type Ia supernovae, for which we require the luminosity distance $D_L(z)$, and BAO data which return joint estimates of $D_M(z)/r_d$ and $H(z)r_d/c$. Here r_d is the sound horizon at the epoch z_d when baryons decouple from the photons (Eq. 1.3.6):

$$r_d = \int_{z_d}^{\infty} \frac{c_s(z)}{H(z)}{\rm d}z, \tag{7.2.8}$$

where c_s is the sound speed in the photon-baryon fluid (Eq. 1.3.7)

$$c_s^2(z) = \frac{c^2}{3}\left[1 + \frac{3}{4}\frac{\rho_b(z)}{\rho_\gamma(z)}\right]^{-1}, \tag{7.2.9}$$

and ρ_b and ρ_γ are the energy densities of baryons and radiation respectively. CMB experiments such as *Planck* and WMAP [46] lead to precise determinations of r_d, assuming the validity of the ΛCDM model at high redshift. From the 2015 Planck Legacy Archive (PLA) tables[a] we have

$$r_d = 147.27 \pm 0.31 \text{ Mpc}, \quad \text{Planck}, \tag{7.2.10}$$

$$r_d = 148.5 \pm 1.2 \text{ Mpc}, \quad \text{WMAP9}, \tag{7.2.11}$$

where the *Planck* value is for the likelihood combination TE+TE+EE+lowTEB in the notation of P16.[b] We use the PLA value for the nine-year WMAP estimate, rather than the value quoted in [46], since (7.2.11) is calculated consistently using the Boltzmann solver `CAMB` [204].

The estimates of r_d in (7.2.10) and (7.2.11) are extremely insensitive to physics at low redshifts [136] (since the physical densities $\Omega_m h^2$ and $\Omega_c h^2$ which enter in equation (7.2.8) are fixed mainly by the relative heights of the CMB acoustic peaks) but assume the base ΛCDM cosmology at high redshifts. By using these values as priors in the inverse distance ladder, we are implicitly assuming that the base ΛCDM model is correct at high redshift though we allow deviations from the model at low redshifts via the parameterizations of equations (7.2.2) or (7.2.7). However, as discussed in P14 and P16, the parameters of the base ΛCDM found by *Planck* are consistent with Big Bang Nucleosynthesis (BBN) constraints on $\Omega_b h^2$ inferred from deuterium abundance measurements in low metallicity systems at high redshift [131; 132; 133]. As emphasised by [269], BBN constraints can be used together with BAO data to provide a consistency check of r_d and H_0 assuming the base ΛCDM model. We will revisit this constraint in Section 7.4.2.

7.3 Data

The BAO measurements used in this chapter are summarized in Table 7.1. We use the BAO measurements from the 6dF Galaxy Survey (6dFGS) [266] which constrains r_d/D_V, where

$$D_V(z) = \left[D_M^2(z) \frac{cz}{H(z)} \right]^{1/3}. \tag{7.3.1}$$

Note that [266] use the [268] formulae to calculate r_d. The `CAMB` code gives values that are lower by a factor 1.027 and so the [266] numbers in Table 1 have been corrected to account for this difference (for a more detailed discussion see Appendix B of [270]). We use the BOSS DR12 consensus BAO measurements [116] on $D_M(z)$ and $H(z)$ in three redshift bands together

[a] `http://www.cosmos.esa.int/web/planck/pla`.

[b] This is consistent with the value $r_d = 147.09 \pm 0.26$ Mpc derived for the *Planck* 2018 TT,TE,EE+lowE+lensing likelihood combination [1].

with the associated 6×6 covariance matrix[a]. We also use the eBOSS BAO measurements from quasars in DR14 [117], from BOSS DR12 analyses of Lyman-α absorption in quasar spectra [119] and BAO constraints from a Lyα-quasar cross-correlation analysis with BOSS DR12 [120]. The high redshift measurements are less accurate than the BOSS DR12 galaxy measurements, but serve to anchor the parameterizations (7.2.2) and (7.2.7) at redshifts greater than unity. Note also that since the likelihoods for these high redshift measurements were not available to us, and these data are relatively unimportant for fixing H_0, we sampled over $D_M(z)$ and $H(z)$ assuming that they are Gaussian distributed and uncorrelated. The mild tension between Lyman-α BAO and *Planck* reported by [119] has no significant impact on our results, since supernovae data constrains the expansion history very tightly.

For the supernovae (SNe) data, we use the new Pantheon sample[b] [265]. This dataset contains SNe spanning the redshift range $0.01 < z < 2.3$ drawn from a number of surveys: The Pan-Starrs1 survey [271; 272], CfA1-CfA4 [16; 273; 274; 275], CSP [276; 277; 278], SNLS [279; 280], SDSS [281; 282], SCP survey [283], GOODS [284] and CANDELS/CLASH survey [285; 286; 287]. We also used the Joint Light-Curve Analysis (JLA) sample [288]. The JLA compilation gives almost identical results for H_0 as the Pantheon sample, so we do not present those results here.

7.4 Results

7.4.1 Constraints on the expansion history

We use the `CosmoMC` package[c] [186; 190] to sample the free parameters of the models. For r_d, we adopt Gaussian priors with dispersions as given in equations (7.2.10) and (7.2.11). For the epsilon model, the parameters A, B and D are constrained to be positive and we impose the constraint that $\epsilon > -5$. For the log model we impose the conditions that A' and B' should be positive.

The constraints on the parameters of each model are illustrated in Figure 7.1. The parameters in the epsilon model show complex degeneracies in comparison to the parameters of the log model. Nevertheless, the expansion histories $H(z)$ allowed by the two models are almost identical as shown in Fig. 7.2. The overall scaling of $H(z)$ is set by the r_d prior. The BAO and SNe data then strongly constrain the redshift dependence with the SNe and are particularly important in fixing the slope of $H(z)$ at low redshifts (as will be discussed in more detail below).

[a] BAO_consensus_covtot_dM_Hz.txt downloaded from http://www.sdss3.org/science/BOSS_publications.php.

[b] The files are publicly available as a `CosmoMC` module at http://kicp.uchicago.edu/~dscolnic/Pantheon_Public.tar.

[c] https://cosmologist.info/cosmomc.

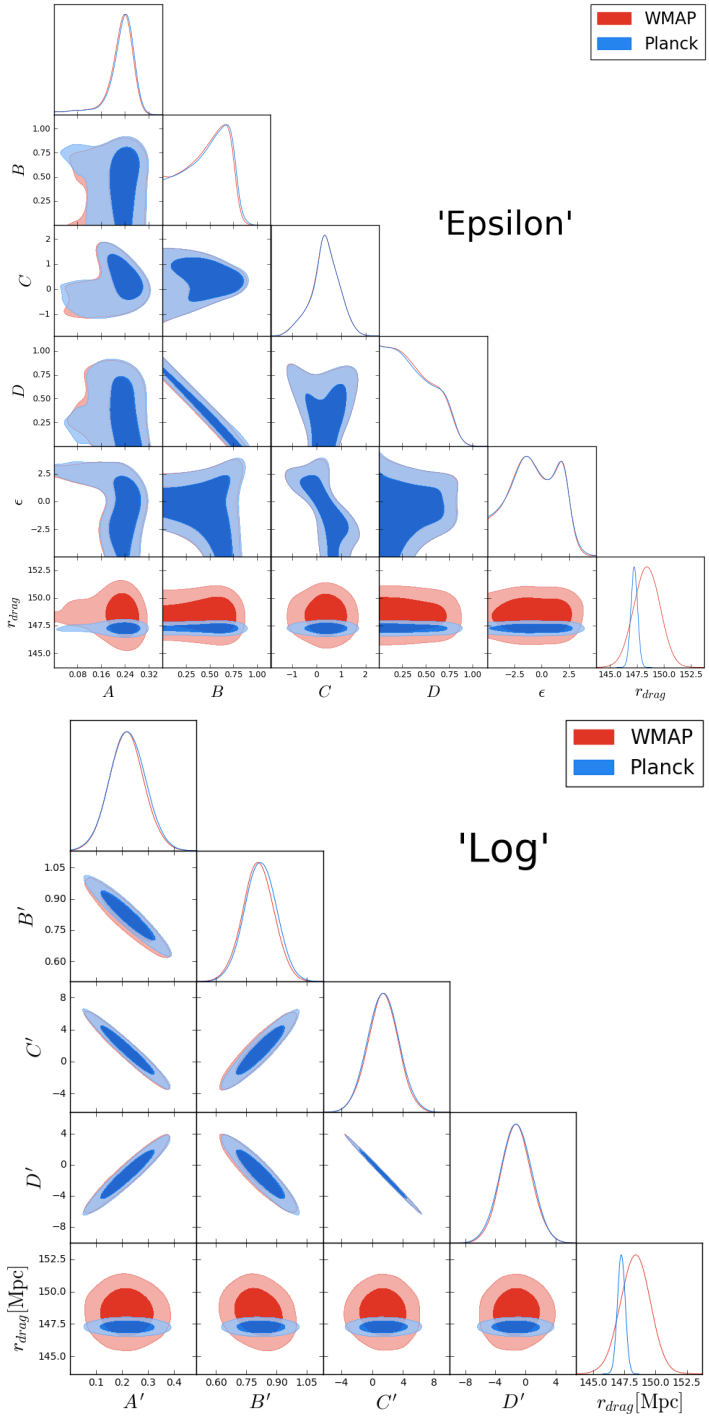

Figure 7.1: Posterior likelihoods for the 'epsilon' (above) and 'log' (below) parameterizations of $H(z)$. Blue contours show 68% and 95% constraints using the *Planck* prior on r_d. The red contours (largely hidden by the blue contours) show the constraints using the WMAP prior on r_d.

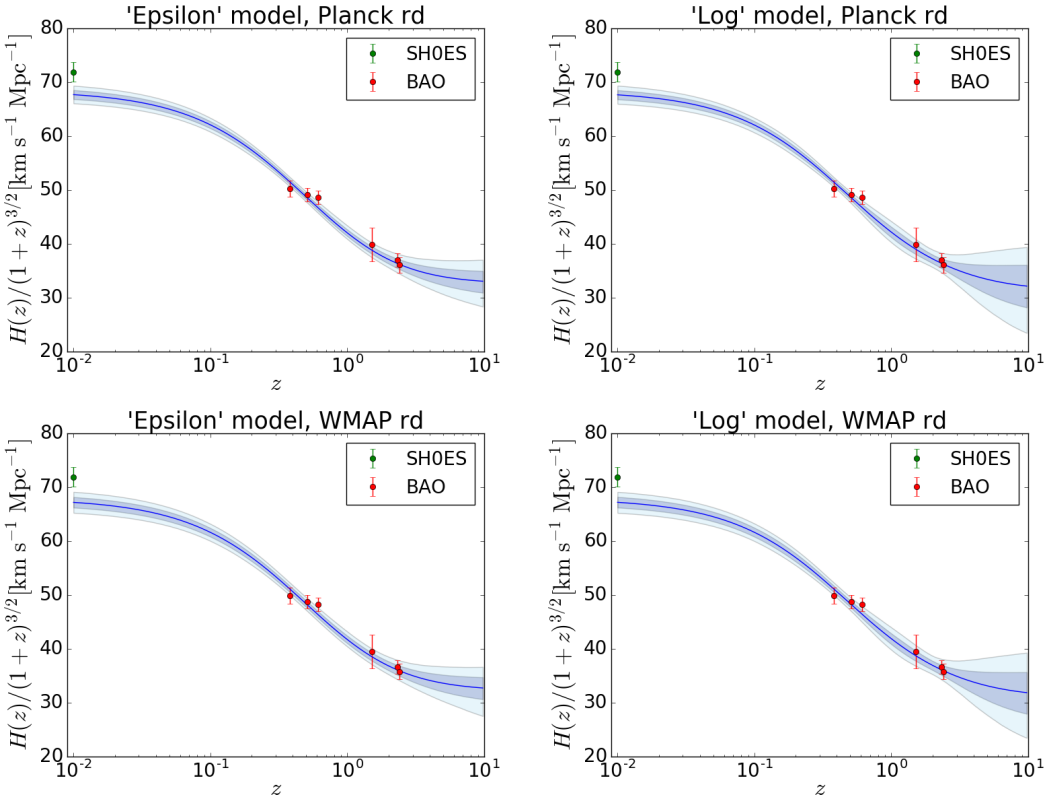

Figure 7.2: $H(z)$ reconstruction for the epsilon model (left hand panels) and log model (right hand panels) for the *Planck* and WMAP priors on r_d: The blue lines show the best fits, and the bands show the allowed one and two sigma ranges. The red points show the BAO estimates on $H(z)$ from Table 7.1 plotted assuming the central values of the priors on r_d. The R18 SH0ES forward distance ladder estimate of $H_0 = 73.48 \pm 1.66$ km s^{-1}Mpc^{-1} is plotted as the green point in each panel.

The epsilon and log models give almost identical results, differing at redshifts $z > 2.4$ where the models become unconstrained by the BAO and SNe data.

The main results of this chapter are illustrated in Fig. 7.3 which shows posteriors on H_0 for the epsilon model. We find

$$H_0 = 68.42 \pm 0.88 \ \text{km s}^{-1}\text{Mpc}^{-1}, \text{Planck } r_d \text{ prior}, \tag{7.4.1}$$

$$H_0 = 67.9 \pm 1.0 \ \text{km s}^{-1}\text{Mpc}^{-1}, \quad \text{WMAP9 } r_d \text{ prior}. \tag{7.4.2}$$

The estimate (7.4.1) is about 1σ lower, and has a smaller error, than the similar analysis of [263] (which gives $H_0 = 69.4 \pm 1$ km s^{-1}Mpc^{-1}) because of differences in methodology and improvements in the BAO and SNe data. Both estimates (7.4.1) and (7.4.2) are much closer to the *Planck* ΛCDM estimate of H_0 than the SH0ES estimate of R18. The value inferred using the Planck and WMAP r_d priors are respectively 1σ and 0.5σ higher than *Planck* estimate

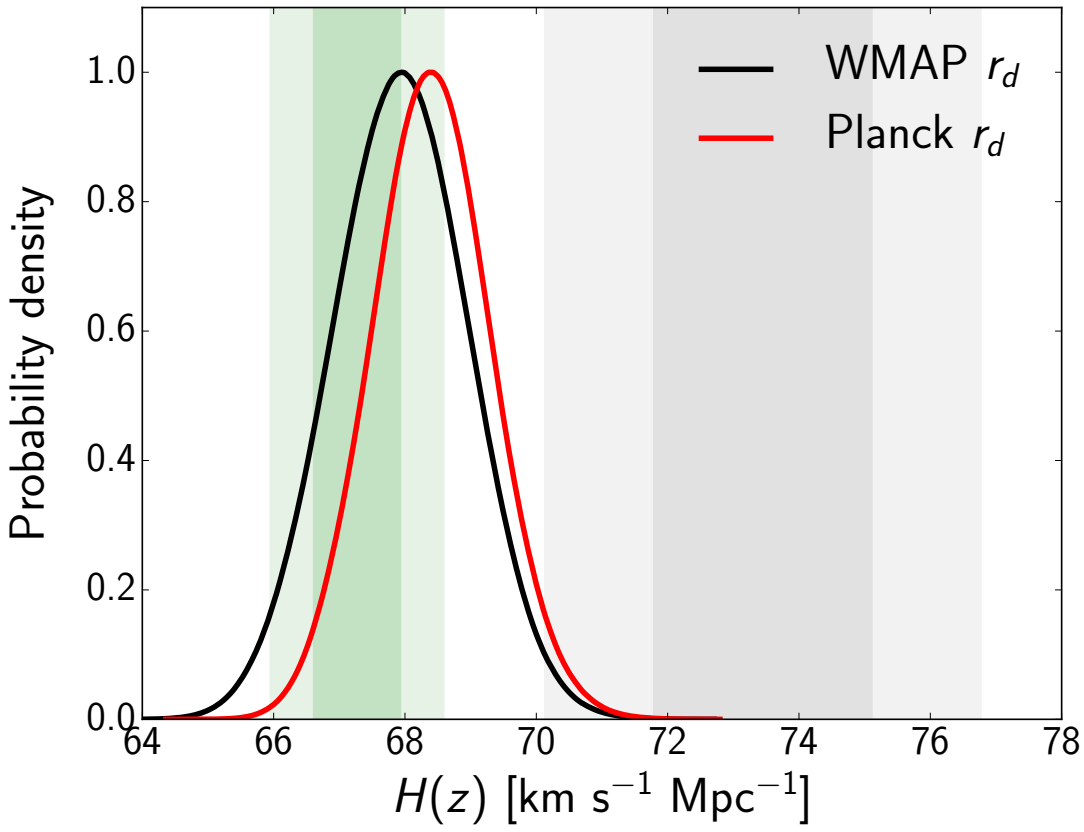

Figure 7.3: Posteriors for the Hubble constant H_0 derived from the epsilon model using the WMAP and *Planck* r_d priors. The grey bands show the one and two sigma errors for the value obtained by R18, while the green bands show the *Planck* base ΛCDM value from P16.

and 2.7σ and 2.9σ lower than the R18 value. Evidently, provided the FRW metric is valid, the discrepancy with the R18 estimate of H_0 is unlikely to be a consequence of new physics at redshifts $z \lesssim 1$.

These results are in excellent agreement with those of [231], who used an $H(z)$ expansion in terms of the present day values of the deceleration and jerk parameters introduced in Section 1.1.2 (Equations. 1.1.14b and 1.1.14c),

$$q \equiv -\frac{a\ddot{a}}{\dot{a}^2}, \qquad j \equiv \frac{\dddot{a}a^2}{\dot{a}^3}, \tag{7.4.3}$$

where a is the scale factor of the Friedman-Robinson-Walker metric and dots denote differentiation with respect to time. Expanding to second order in z:

$$H(z) = H_0[1 + (1 + q_0)z + (j_0 - q_0^2)\frac{z^2}{2}], \tag{7.4.4}$$

$$D_L(z) = \frac{cz}{H_0}[1 + (1 + q_0)\frac{z}{2} + (1 - q_0 - 3q_0^2 + j_0)\frac{z^2}{6}]. \tag{7.4.5}$$

For the base ΛCDM model with $\Omega_m = 0.31$, $q_0 = 1 - 3\Omega_m/2 = -0.535$ and $j_0 = 1$ and the expressions (7.4.4) and (7.4.5) agree well with the exact forms of $H(z)$ and $D_L(z)$ out to a redshift $z \approx 0.6$ (covering the redshift range of the BOSS DR12 galaxy measurements). Fig. 7.4 shows our constraints on q_0 and j_0, which are determined mainly by the Pantheon SNe sample and so are nearly independent of r_d. These distributions are consistent with the values expected in base ΛCDM. Although these distributions have extended tails, the gradient $dH(z)/dz$ at low redshifts is tightly constrained by the Pantheon SNe (Fig. 7.2) which is why it is not possible to match the BAO $H(z)$ measurements with the SH0ES estimate of H_0. It is also worth noting that the SH0ES methodology matches Cepheid-based distance measurements of SNe host galaxies to more distant supernovae assuming the relation (7.4.5) with $q_0 = -0.55$ and $j_0 = 1$, based on fits to the SNe magnitude-redshift relation. It is inconsistent, therefore, to apply the R18 H_0 measurement as a fixed prior, independent of the underlying cosmological model, and to infer a cosmology that conflicts with the SNe magnitude-redshift relation since the SNe magnitude-redshift relation is a fundamental part of the H_0 determination. This inconsistency needs to be borne in mind when using the direct measurement of H_0 to set a scale for the sound horizon [e.g. 262; 263].

7.4.2 Consistency of r_d with high redshift physics

The inverse distance ladder constraints on H_0 derived in this chapter assume that there is no new physics at high redshift that can alter CMB estimates of r_d. BBN provides a strong test of new physics at high redshift and can, in principle, be used to test the consistency of CMB estimates of r_d. The most recent estimates [133] of the deuterium to hydrogen ratio D/H, based on seven low metallicity damped Lyα systems, give

$$10^5(\mathrm{D/H}) = 2.527 \pm 0.030. \tag{7.4.6}$$

Assuming three (non-degenerate) neutrino families and BBN, the estimate (7.4.6) can be converted into a constraint on $\Omega_b h^2$. This conversion is, however, dependent on uncertainties in the $d(p,\gamma)^3$He reaction rate[a]. [133] use the theoretical reaction rate from [289] and the

[a] As discussed in [1], these estimates are also sensitive to the BBN code used, as well as other reaction rates in addition to the $d(p,\gamma)^3$He rate.

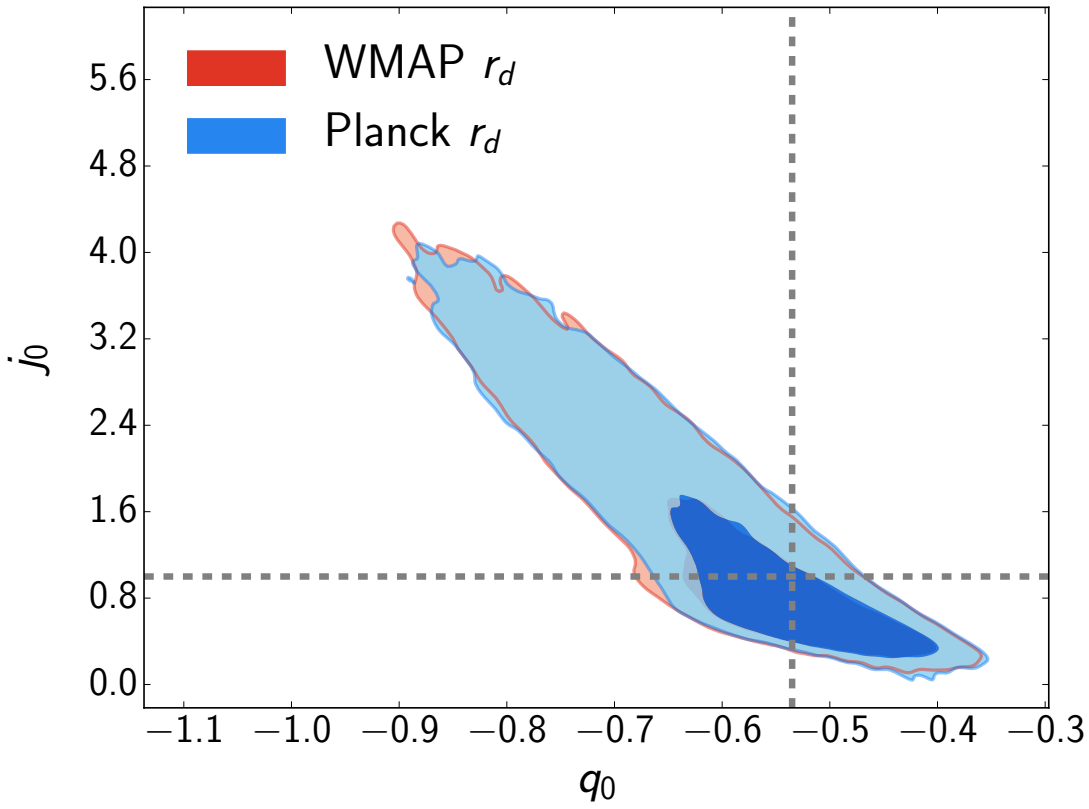

Figure 7.4: 68% and 95% constraints on the q_0 and j_0 parameters determined from the epsilon model. These constraints are set mainly by the Pantheon SNe sample and are almost independent of the prior on r_d. The lines give the values of j_0 and q_0 expected in the base ΛCDM model with $\Omega_m = 0.31$.

experimental value from [290] to illustrate the sensitivity of $\Omega_b h^2$. They find:

$$100\Omega_b h^2 = 2.166 \pm 0.019, \quad \text{Marcucci et al.,} \tag{7.4.7}$$

$$100\Omega_b h^2 = 2.235 \pm 0.037, \quad \text{Adelberger et al.,} \tag{7.4.8}$$

where the error in (7.4.8) is dominated by the error in the [290] cross-section. The estimate (7.4.7) is lower by 2.4σ compared to the P16 TT+TE+EE+lowP value of $100\Omega_b h^2 = 2.225 \pm 0.016$ for the base ΛCDM cosmology, whereas (7.4.8) is consistent with the P16 value to within 0.25σ. We consider these two values and associated error estimates in the analysis below.

We then follow [137] and [269] in using these BBN estimates together with supplementary astrophysical data to infer r_d assuming the base ΛCDM cosmology. Here we have combined the BBN constraints with the BAO measurements and the Pantheon SNe sample, as described in Section 7.3. The posteriors on r_d are shown in Fig. 7.5 and are consistent with the r_d constraints from WMAP and *Planck*. To the extent that BBN probes early Universe physics,

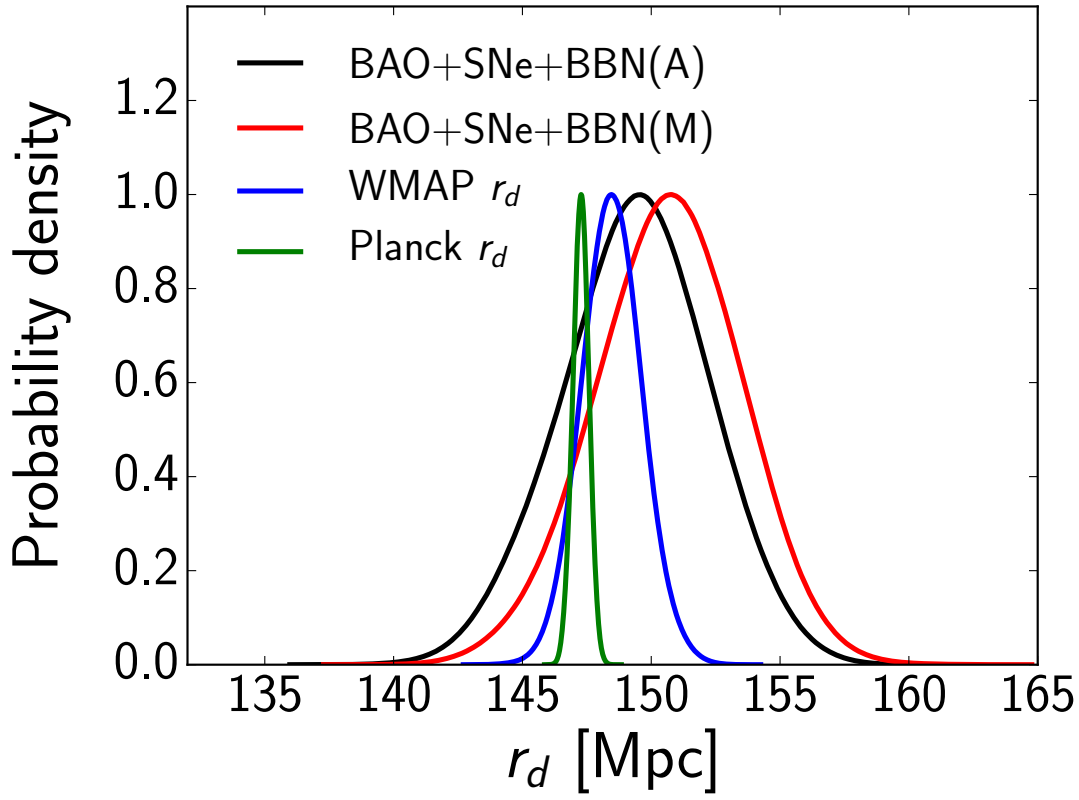

Figure 7.5: The CMB constraints on the sound horizon r_d from WMAP and *Planck* used in this chapter. The black and red curves show the posteriors on r_d determined by fitting to the BAO and Pantheon SNe data assuming the base ΛCDM cosmology and BBN constraints on $\Omega_b h^2$. The curve labelled BBN(M) assumes the [289] $d(p,\gamma)^3$He reaction rate. The curve labelled BBN(A) uses the experimental rate from [290].

we find no evidence for any inconsistency with the values of the sound horizon inferred from CMB measurements.

[263] suggested that the H_0 tension can be partially relieved by invoking extra relativistic degrees of freedom in addition to the $N_{\rm eff} = 3.046$ expected in the standard model. This solution is disfavoured by the latest *Planck* analysis. Allowing $N_{\rm eff}$ to vary as an extension to the base-ΛCDM cosmology, [1] find $N_{\rm eff} = 2.99 \pm 0.17$, $H_0 = 67.3 \pm 1.1$ km s^{-1}Mpc^{-1} and $r_d = 147.9 \pm 1.8$ Mpc for the TT,TE,EE+lowE+BAO+lensing likelihood combination. Additional relativistic degrees of freedom are therefore tightly constrained by the latest data.

7.5 Conclusions

The precision and redshift reach of BAO measurements has improved substantially over the last few years. Together with SNe data, it is now possible to reconstruct the time evolution of $H(z)$

accurately without invoking any specific model of the physics of the late time Universe other than the validity of the FRW metric. If we assume that there is no new physics at early times, then CMB measurements constrain the sound horizon, r_d, and this in turn fixes the absolute scale of $H(z)$ allowing an extrapolation to $z = 0$ to infer H_0. Our results disagree with the direct measurement of H_0 from the SH0ES collaboration and are in much closer agreement with the H_0 value determined by *Planck* assuming the base ΛCDM cosmology. This conclusion holds irrespective of whether we use a prior on r_d from WMAP or from *Planck*.

Our results are consistent with previous work on the inverse distance ladder [e.g 134; 135; 231, P16]. In agreement with [263], we reach this conclusion without having to assume any specific model for the time evolution of dark energy or its interaction with dark matter and baryons. As long as there is no new physics in the early Universe that can alter the CMB value of the sound horizon, the new BAO measurements from BOSS provide accurate absolute measurements of $H(z)$ in the redshift range $0.38 - 2.4$. The SNe data then provide a strong constraint on the gradient of $H(z)$ at lower redshifts, which is compatible with the gradient expected in the base ΛCDM cosmology. The data therefore do not allow a rise in $H(z)$ at low redshift with which to match the SH0ES direct measurement of H_0. We conclude that it is not possible to reconcile CMB estimates of H_0 and the SH0ES direct measurements by invoking new physics at low redshifts.

If the tension between the CMB estimates of H_0 and direct measurements is a signature of new physics, then we need to introduce new physics in the early Universe. This new physics must lower the sound horizon by about 9% (i.e. to about 135 Mpc) compared to the values used in this chapter while preserving the structure of the temperature and polarization power spectra measured by CMB experiments. This new physics also needs to preserve the consistency between BBN and observed abundances of light elements. These requirements pose interesting challenges for theorists.

Part IV

Conclusions

Conclusions

Conclusions

The goal of this thesis has been to test the *Planck* base ΛCDM cosmology. Following the latest data release [1; 148], *Planck* has made measurements of the temperature and polarization of the cosmic microwave background which are compatible with the standard ΛCDM model of cosmology, and provided accurate estimates of the six parameters that define this model. In this thesis, we have put the robustness of the *Planck* cosmology to a test, from a theoretical and observational point of view, and using the high and low redshift Universe.

In the first part of this thesis, we focused on high redshifts. In Chapters 2 and 3 we tested the goodness of fit of the ΛCDM model to the *Planck* data compared with models of inflation that alter the power-law primordial power spectrum. Although we found problems with the *Planck* polarization likelihoods which are not understood and may be caused by errors in the *Planck* noise model at low multipoles, the main result of this analysis is that *Planck* does not favour any changes from a pure power-law spectrum of fluctuations. In Chapter 4, we studied the tension between *Planck* and SPTpol, and the possibility of departures from ΛCDM from the SPTpol measurements at multipoles $\ell > 2500$. We found that absolute values of χ^2 are strongly dependent on the SPTpol covariance matrix. We demonstrated that SPTpol parameters have converged by $\ell = 2000$. We conclude that, while SPTpol results are uncertain because of problems with calibration and polarization efficiencies, there are no significant differences comparing *Planck* and SPT at the parameter level, and the high values of χ^2 reported by SPTpol are at least partially driven by several outliers in the data spanning the entire SPTpol multipole range, which could reflect problems with the SPTpol error model.

In the second part, we studied the low redshift Universe. In Chapter 5, we reviewed the effect of the small-angle approximations commonly used in weak lensing surveys, and their possible contributions to differences between weak lensing and CMB estimates of the amplitude and shape of the matter power spectrum. We found that these approximations have a negligible effect in cosmological parameter estimation with the accuracy of present-day experiments. In Chapter 6, we found statistical inconsistencies in the KiDS-450 data. A revision of the KiDS

covariance matrix eases these inconsistencies by increasing the errors, especially on large angular scales. However, this does not mean that the KiDS data are free of systematics (for example, the data shows a spurious B-mode). Finally, in Chapter 7, we studied the tension in the expansion rate of the Universe between *Planck* and direct measurements, through an inverse distance ladder analysis with a model-independent parameterization of the expansion history of the Universe, and using baryon acoustic oscillations and supernovae data. We found that this data produces values of the Hubble parameter compatible with *Planck* and in tension with direct measurements, independently of the expansion history at low redshifts. We conclude that if this tension is real, it requires an extension to the ΛCDM model at high redshifts that reduces the sound horizon.

The conclusion of all these tests is that the six-parameter ΛCDM model of the Universe with parameter values measured by *Planck* remains the most robust model of the Universe. Our tests show that any possible deviations from the ΛCDM cosmology at high or low redshifts must be small. In this so-called era of precision cosmology, it is fundamental for cosmological surveys to critically evaluate their data, and all possible systematics that affect it, before claiming new physics.

Appendix

Appendix A

Galaxy weak lensing two-point statistics

A.1 Introduction

In this appendix we summarise results for the two-point statistics of the weak lensing observables, namely convergence and shear, on the spherical sky and also in the flat-sky limit. These results are valid for both weak lensing of galaxies and of the CMB. As in Chapter 5, we assume a flat universe throughout.

As explained in Sec. 1.3.2, the lensing potential $\phi(\hat{\boldsymbol{n}}, \chi)$ for sources at comoving distance χ is given by:

$$\phi(\hat{\boldsymbol{n}}, \chi) = \frac{2}{c^2} \int_0^{\chi} \mathrm{d}\chi' \, \frac{\chi - \chi'}{\chi \chi'} \Phi(\chi' \hat{\boldsymbol{n}}, \chi'), \tag{A.1.1}$$

where $\Phi(\boldsymbol{x}, \chi)$ is the gravitational potential at comoving position $\boldsymbol{x}$ and conformal lookback time χ.

If we average observables over sources with a redshift distribution $n(\chi)$, normalised such that $\int n(\chi)\, \mathrm{d}\chi = 1$, the relevant 2D lensing potential is given by Eq. 1.3.18:

$$\phi(\hat{\boldsymbol{n}}) = \int \mathrm{d}\chi \, n(\chi) \phi(\hat{\boldsymbol{n}}, \chi) = \frac{2}{c^2} \int \frac{\mathrm{d}\chi'}{\chi'} q(\chi') \Phi(\chi' \hat{\boldsymbol{n}}, \chi'), \tag{A.1.2}$$

where $q(\chi)$ is the lensing efficiency defined in Eq. (1.3.19). In the case of CMB lensing, the source distribution can be approximated by a delta-function at the surface of last scattering: $n(\chi) = \delta_D(\chi - \chi_*)$. The lensing potential is a scalar field and can be expanded in spherical harmonics as described by Eq. 1.3.20. The basic observables in weak lensing are the convergence κ and the components γ_1 and γ_2 of the shear, defined in terms of the second derivatives

of the lensing potential as

$$\nabla_i \nabla_j \phi = \kappa g_{ij} + \frac{1}{2}(\gamma_1 + i\gamma_2)(\boldsymbol{m}_- \otimes \boldsymbol{m}_-)_{ij} + \frac{1}{2}(\gamma_1 - i\gamma_2)(\boldsymbol{m}_+ \otimes \boldsymbol{m}_+)_{ij}, \tag{A.1.3}$$

where g_{ij} is the metric on the sphere and the null vectors $\boldsymbol{m}_\pm = \hat{\boldsymbol{\theta}} \pm i\hat{\boldsymbol{\phi}}$. Here, $\hat{\boldsymbol{\theta}}$ and $\hat{\boldsymbol{\phi}}$ are unit vectors along the θ and ϕ coordinate directions of a spherical-polar coordinate system. The convergence $\kappa = \nabla^2\phi/2$ describes isotropic magnification/dilation and is a scalar field. The shear describes area-preserving distortions; the complex shear $\gamma = \gamma_1 + i\gamma_2$ is a spin-2 field related to the lensing potential via

$$\gamma = \frac{1}{2}(\boldsymbol{m}_+ \otimes \boldsymbol{m}_+)_{ij}\nabla^i\nabla^j\phi = \frac{1}{2}\eth^2\phi, \tag{A.1.4}$$

where $\eth$ is the spin-raising operator (Eq. 1.3.13c). The spherical-harmonic expansions of the convergence and shear follow from Eq. (1.3.20):

$$\kappa(\hat{\boldsymbol{n}}) = -\frac{1}{2}\sum_{\ell,m} \ell(\ell+1)\phi_{\ell m} Y_\ell^m(\hat{\boldsymbol{n}}), \tag{A.1.5a}$$

$$\gamma_1(\hat{\boldsymbol{n}}) \pm i\gamma_2(\hat{\boldsymbol{n}}) = \frac{1}{2}\sum_{\ell,m} \sqrt{\frac{(\ell+2)!}{(\ell-2)!}}\phi_{\ell m}\, {}_{\pm2}Y_\ell^m(\hat{\boldsymbol{n}}). \tag{A.1.5b}$$

Generally, a spin 2 field can be expanded in E and B-modes, for example,

$$(\gamma_i \pm i\gamma_2)(\hat{\boldsymbol{n}}) = \sum_{\ell,m} (\epsilon_{\ell m} \pm i\beta_{\ell m})\, {}_{\pm2}Y_\ell^m(\hat{\boldsymbol{n}}), \tag{A.1.6}$$

where $\epsilon_{\ell m}$ are the E-mode multipoles and $\beta_{\ell m}$ are the B-mode multipoles. These transform oppositely under parity: $\epsilon_{\ell m} \to (-1)^\ell \epsilon_{\ell m}$ and $\beta_{\ell m} \to (-1)^{\ell+1}\beta_{\ell m}$. However, we see from Eq. (A.1.5b) that the gravitational shear has no B-modes (in the Born approximation that we are assuming here), while $\epsilon_{\ell m} = \sqrt{(\ell+2)!/(\ell-2)!}\,\phi_{\ell m}/2$.

The angular power spectrum of the lensing potential is defined by

$$\langle \phi_{\ell m} \phi^*_{\ell' m'} \rangle = \delta_{\ell\ell'}\delta_{mm'} C_\ell^{\phi\phi}. \tag{A.1.7}$$

We can similarly define the convergence and shear power, which are related to $C_\ell^{\phi\phi}$ by

$$C_\ell^{\kappa\kappa} = \frac{\ell^2(\ell+1)^2}{4} C_\ell^{\phi\phi}, \tag{A.1.8a}$$

$$C_\ell^{\epsilon\epsilon} = \frac{1}{4}\frac{(\ell+2)!}{(\ell-2)!} C_\ell^{\phi\phi}. \tag{A.1.8b}$$

In the flat-sky approximation, we project onto the tangent plane at the centre of the observed field and denote positions in this plane with a 2D vector $\boldsymbol{\theta}$. Expansions in spherical harmonics are replaced by Fourier expansions, so that for the gravitational potential

$$\phi(\boldsymbol{\theta}) = \int \frac{\mathrm{d}^2\boldsymbol{l}}{(2\pi)^2}\, \phi(\boldsymbol{l}) e^{i\boldsymbol{l}\cdot\boldsymbol{\theta}}. \tag{A.1.9}$$

The expansions of the convergence and shear become

$$\kappa(\boldsymbol{\theta}) = -\frac{1}{2}\int \frac{\mathrm{d}^2\boldsymbol{l}}{(2\pi)^2}\, l^2\phi(\boldsymbol{l})e^{i\boldsymbol{l}\cdot\boldsymbol{\theta}} \tag{A.1.10a}$$

$$(\gamma_1 \pm i\gamma_2)(\boldsymbol{\theta}) = -\frac{1}{2}\int \frac{\mathrm{d}^2\boldsymbol{l}}{(2\pi)^2}\, l^2\phi(\boldsymbol{l})e^{\pm 2i(\psi_{\boldsymbol{l}}-\psi_{\boldsymbol{\theta}})}e^{i\boldsymbol{l}\cdot\boldsymbol{\theta}}, \tag{A.1.10b}$$

where $\psi_{\boldsymbol{l}}$ and $\psi_{\boldsymbol{\theta}}$ are the angles that $\boldsymbol{l}$ and $\boldsymbol{\theta}$, respectively, make with the x-axis. Note that the components of the shear are defined relative to a polar-coordinate basis in the plane; rotating to a global Cartesian basis removes the factors of $e^{\mp 2i\psi_{\boldsymbol{\theta}}}$.

In the flat-sky approximation, the power spectra are related simply by

$$C_\ell^{\kappa\kappa} = \frac{\ell^4}{4}C_\ell^{\phi\phi} = \frac{\ell^4}{4}C_\ell^{\epsilon\epsilon}. \tag{A.1.11}$$

A.2 Relation to the matter power spectrum

We can relate the lensing angular power spectra to the 3D matter power spectra as follows. We begin by expanding the gravitational potential in Eq. (A.1.2) in Fourier modes $\Phi(\boldsymbol{k},\chi)$ and using the plane-wave expansion to find

$$\phi_{\ell m} = i^\ell \frac{8\pi}{c^2}\int \frac{\mathrm{d}^3\boldsymbol{k}}{(2\pi)^3}\left(\int \frac{\mathrm{d}\chi}{\chi}\, q(\chi)j_\ell(k\chi)\Phi(\boldsymbol{k},\chi)\right)Y_\ell^{m*}(\hat{\boldsymbol{k}})\,. \tag{A.2.1}$$

The two-point correlator of the gravitational potential is

$$\langle\Phi(\boldsymbol{k},\chi)\Phi^*(\boldsymbol{k}',\chi')\rangle = (2\pi)^3 P_{\Phi}(k;\chi,\chi')\delta_D^{(3)}(\boldsymbol{k}-\boldsymbol{k}'), \tag{A.2.2}$$

where $P_{\Phi}(k;\chi,\chi')$ is the unequal-time power spectrum of the gravitational potential. It follows from Eq. (A.2.1) that, for redshift distributions $q^r(\chi)$ and $q^s(\chi)$,

$$C_\ell^{\phi\phi}(r,s) = \left(\frac{8\pi}{c^2}\right)^2\int \frac{k^2\mathrm{d}k}{(2\pi)^3}\int \frac{\mathrm{d}\chi}{\chi}q^r(\chi)j_\ell(k\chi)\int \frac{\mathrm{d}\chi'}{\chi'}q^s(\chi')j_\ell(k\chi')P_{\Phi}(k;\chi,\chi'). \tag{A.2.3}$$

This simplifies if we adopt the approximation made in Chapter 5,

$$P_{\Phi}(k;\chi,\chi') \approx \left[P_{\Phi}(k;\chi)P_{\Phi}(k;\chi')\right]^{1/2}, \tag{A.2.4}$$

to give

$$C_\ell^{\phi\phi}(r,s) = \frac{8}{\pi c^4}\int k^2\mathrm{d}k\, \hat{I}_\ell^r(k)\hat{I}_\ell^s(k), \tag{A.2.5}$$

where

$$\hat{I}_\ell^r(k) = \int \frac{\mathrm{d}\chi}{\chi}q^r(\chi)j_\ell(k\chi)\left[P_{\Phi}(k,\chi)\right]^{1/2}. \tag{A.2.6}$$

Finally, we can relate the 3D power spectrum of the gravitational potential to the 3D matter power spectrum using Poisson's equation, i.e.,

$$P_{\Phi}(k;\chi) = \left(\frac{3}{2}\Omega_m H_0^2\,[1+z(\chi)]\right)^2 \frac{P_\delta(k;\chi)}{k^4}, \tag{A.2.7}$$

to obtain our final result

$$C_\ell^{\phi\phi}(r,s) = \frac{8}{\pi}\left(\frac{3\Omega_m H_0^2}{2c^2}\right)^2 \int \frac{\mathrm{d}k}{k^2}\, I_\ell^r(k) I_\ell^s(k), \tag{A.2.8a}$$

$$I_\ell^r(k) = \int \frac{\mathrm{d}\chi}{\chi}\,[1+z(\chi)]\,q^r(\chi) j_\ell(k\chi)\,[P_\delta(k,\chi)]^{1/2}\,. \tag{A.2.8b}$$

A.3 Spherical correlation functions

Expressions for the spherical correlation functions of the gravitational shear from the angular power spectrum can be obtained following the methods used for CMB polarization (also a spin-2 field) in Refs. [291; 292]. To maintain generality, we give results including B-modes although, as noted above, these are expected to vanish for the gravitational shear.

As discussed in Chapter 5, the correlation functions of the shear for lines of sight $\hat{\boldsymbol{n}}_1$ and $\hat{\boldsymbol{n}}_2$ are simplest when the shear is expressed at each point in bases generated by the great circle through the two points. If α_1 is the angle required to rotate $\hat{\boldsymbol{\theta}}_1$ in a right-handed sense about $\hat{\boldsymbol{n}}_1$ onto the tangent to the great circle there, the rotated shear is $\bar{\gamma}(\hat{\boldsymbol{n}}_1) = e^{-2i\alpha_1}\gamma(\hat{\boldsymbol{n}}_1)$. For redshift distributions $q^r(\chi)$ and $q^s(\chi)$, the two-point correlation functions of the rotated shear are

$$\xi_+(\theta;r,s) = \langle \bar{\gamma}_r^*(\hat{\boldsymbol{n}}_1)\bar{\gamma}_s(\hat{\boldsymbol{n}}_2)\rangle = \sum_\ell \frac{2\ell+1}{4\pi}\left[C_\ell^{\epsilon\epsilon}(r,s) + C_\ell^{\beta\beta}(r,s)\right] d^l_{2\,2}(\theta), \tag{A.3.1a}$$

$$\xi_-(\theta;r,s) = \langle \bar{\gamma}_r(\hat{\boldsymbol{n}}_1)\bar{\gamma}_s(\hat{\boldsymbol{n}}_2)\rangle = \sum_\ell \frac{2\ell+1}{4\pi}\left[C_\ell^{\epsilon\epsilon}(r,s) - C_\ell^{\beta\beta}(r,s)\right] d^\ell_{2\,-2}(\theta), \tag{A.3.1b}$$

where d^ℓ_{mn} are the reduced Wigner D-matrices, and θ is the angle between $\hat{\boldsymbol{n}}_1$ and $\hat{\boldsymbol{n}}_2$. The correlation coefficients for the shear components follow from these expressions (noting that the right-hand sides are real-valued):

$$\langle \bar{\gamma}_{1,r}(\hat{\boldsymbol{n}}_1)\bar{\gamma}_{1,s}(\hat{\boldsymbol{n}}_2)\rangle = \frac{1}{2}\left[\xi_+(\theta;r,s) + \xi_-(\theta;r,s)\right], \tag{A.3.2a}$$

$$\langle \bar{\gamma}_{2,r}(\hat{\boldsymbol{n}}_1)\bar{\gamma}_{2,s}(\hat{\boldsymbol{n}}_2)\rangle = \frac{1}{2}\left[\xi_+(\theta;r,s) - \xi_-(\theta;r,s)\right]. \tag{A.3.2b}$$

Correlations between mixed components, e.g., $\langle \bar{\gamma}_{1,r}(\hat{\boldsymbol{n}}_1)\bar{\gamma}_{2,s}(\hat{\boldsymbol{n}}_2)\rangle$, vanish since we are assuming that parity invariance holds in the mean (so that $C_\ell^{\epsilon\beta}(r,s) = 0$).

APPENDIX B

CORRECTIONS TO THE KiDS-450 COVARIANCE MATRIX

After the work described in Chapter 6 was done, [4, henceforth T18] reported errors in the covariance matrix used in the KiDS-450 analysis of H17. In particular, they studied the effect of shape noise in the analytical covariance matrix beyond simple geometrical approximations used in the KiDS-450 analysis, and found that a more careful treatment increases the effect of shape noise by a factor of three, thus greatly increasing the errors and alleviating the tension with *Planck*. They also used a different implementation of multiplicative shear bias, and found a mistake in the estimation of effective angular bin centres used in H17. In this section, we repeat the tests to the KiDS data presented in Sec. 6.2 with the corrected covariance matrix of T18, and evaluate the effect of these corrections on the internal inconsistencies in the KiDS data.

It is worth noting that the analysis of T18 pointed out some other differences with respect to the original KiDS analysis. In particular, T18 use the code `CosmoSIS` [293] instead of `CosmoMC` for their MCMC analysis. This code uses a different parameterization of ΛCDM, using the Hubble parameter H_0 instead of $\theta_{\rm MC}$ is a free parameter. They also introduced photometric redshift bias parameters to account for errors in the calibration of photometric redshift distributions, instead of using bootstrapping with multiple realizations as done in H17. We confirmed that none of these minor differences affect the results in any significant way, as claimed by T18, by reproducing the left-hand panel of figure 2 in T18 (Figure B.1). The change in the covariance matrix does however produce a rise in S_8 that alleviates the tension with *Planck*. We now review

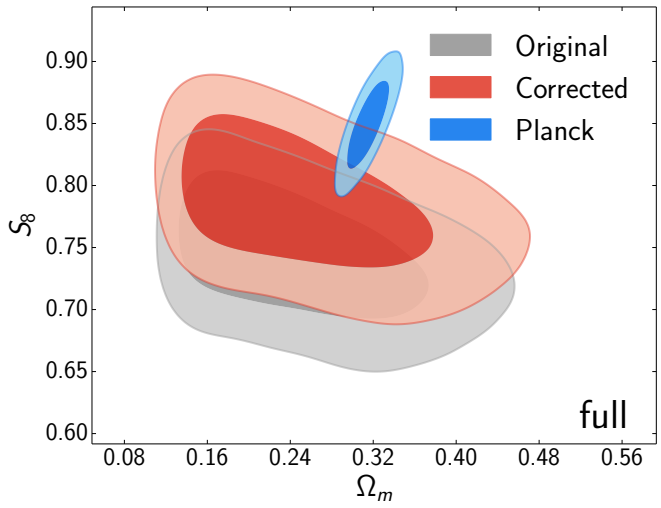

Figure B.1: The plot $S_8 - \Omega_m$ for the full likelihood. In blue, the *Planck* contours, obtained with the `TT+lowTEB` 2015 likelihood; In grey the original results from H17, in red the contours using the T18 covariance matrix. As expected, the plot is similar to the left-hand plot in Figure 2 in T18, despite the using a different MCMC sampler and accounting differently for errors in the photometric redshift distributions.

	Original				**Corrected**			
$\mathbf{y}^D$	S_8	A_{IA}	$\chi^2_{\rm cond}$	$N_{\sigma_{\rm cond}}$	S_8	A_{IA}	$\chi^2_{\rm cond}$	$N_{\sigma_{\rm cond}}$
minus z-bin 1	0.745 ± 0.040	1.14 ± 0.85	61.0 (52)	0.89	0.771 ± 0.037	1.57 ± 0.82	47.9 (52)	−0.41
minus z-bin 2	0.754 ± 0.042	1.24 ± 0.80	66.3 (52)	1.40	0.774 ± 0.041	1.25 ± 0.78	49.3 (52)	−0.26
minus z-bin 3	0.771 ± 0.039	1.25 ± 0.57	78.2 (52)	2.60	0.793 ± 0.038	1.41 ± 0.56	61.4 (52)	0.92
minus z-bin 4	0.684 ± 0.071	-0.1 ± 1.7	87.9 (52)	3.52	0.712 ± 0.069	0.2 ± 1.5	66.5 (52)	1.42
minus ξ_-	0.778 ± 0.040	1.10 ± 0.73	89.7 (60)	2.71	0.779 ± 0.040	1.14 ± 0.69	62.0 (60)	0.18
minus ξ_+	0.705 ± 0.048	0.92 ± 0.97	84.1 (70)	1.20	0.732 ± 0.049	1.2 ± 1.1	81.4 (70)	0.96

Table B.1: Reproduction of Table 6.3, using the original covariance matrix on the left, and the corrected covariance matrix on the right.

its effects on the internal inconsistencies of H17.

B.1 Removal of redshift bins and separate ξ_+ and ξ_- analyses

Our main result is shown in Table B.1, which compares the effect of removing the different redshift bins and separating ξ_+ and ξ_- on the original and corrected analyses. We see how after correcting the covariance matrix, the different redshift bins are consistent with the rest of the data, with differences below the 2σ level in all cases. Table B.1 also illustrates the very significant improvement in goodness of fit after the covariance matrix has been corrected. Similarly, separate ξ_+ and ξ_- analyses are consistent with the rest of the data within 1σ.

This is further illustrated by Figure B.2, which reproduces Figure 6.5 for the original and corrected covariance matrices in the left and right-hand sides respectively. Figure B.2 highlights

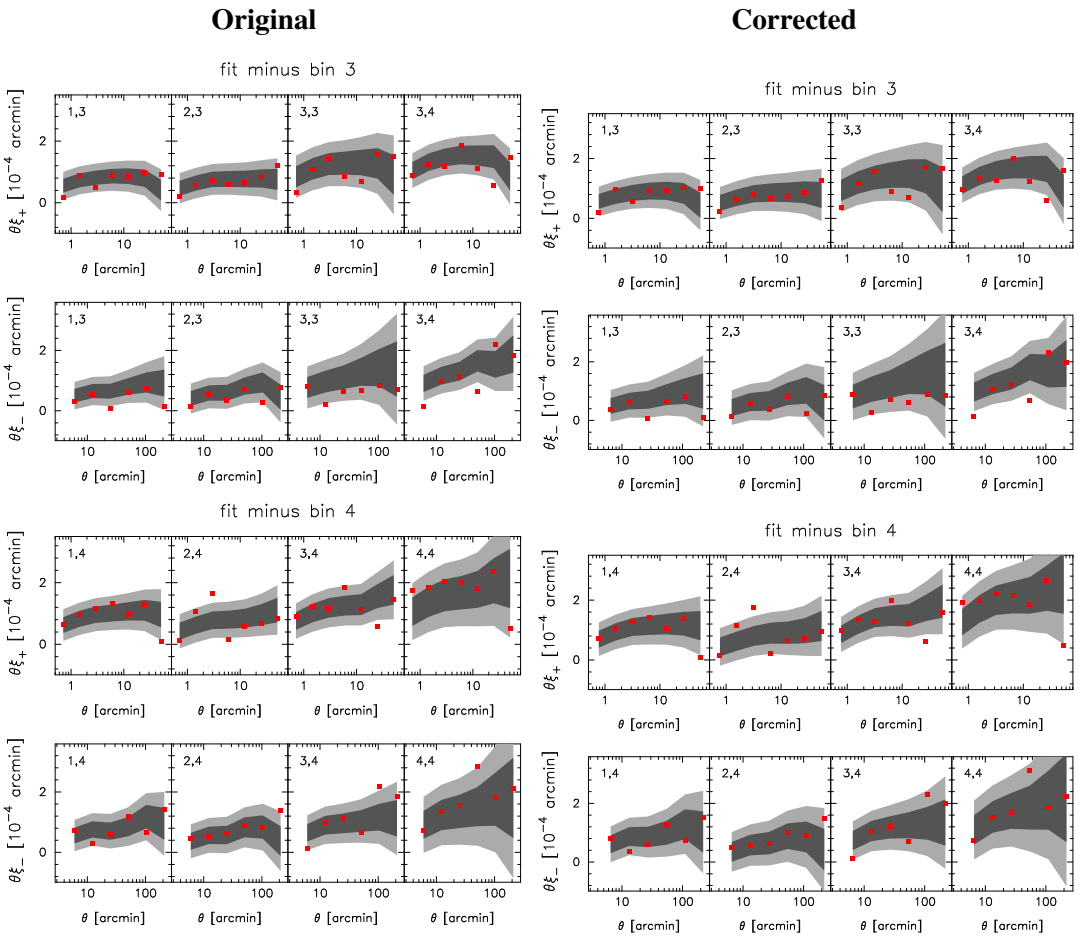

Figure B.2: Reproduction of figure 6.5, using the original covariance matrix on the left, and the corrected covariance matrix on the right.

Parameter	H17 best fit	'Extended prior' best fit	N_σ
$\Omega_c h^2$	0.119 ± 0.044	0.61 ± 0.22	2.19
H_0 km s^{-1}Mpc^{-1}	74.8 ± 4.9	270 ± 82	2.38
n_s	1.09 ± 0.13	0.59 ± 0.24	1.83
σ_8	0.89 ± 0.17	1.59 ± 0.50	1.33
Ω_m	0.254 ± 0.081	0.100 ± 0.050	1.62

Table B.2: Reproduction of Table 6.2, using the corrected covariance matrix.

the two main effects of the corrections to the covariance matrix: An increase in amplitude, and a widening of the error bars. We see how this changes greatly reduce the number of outliers in the data, and their significance.

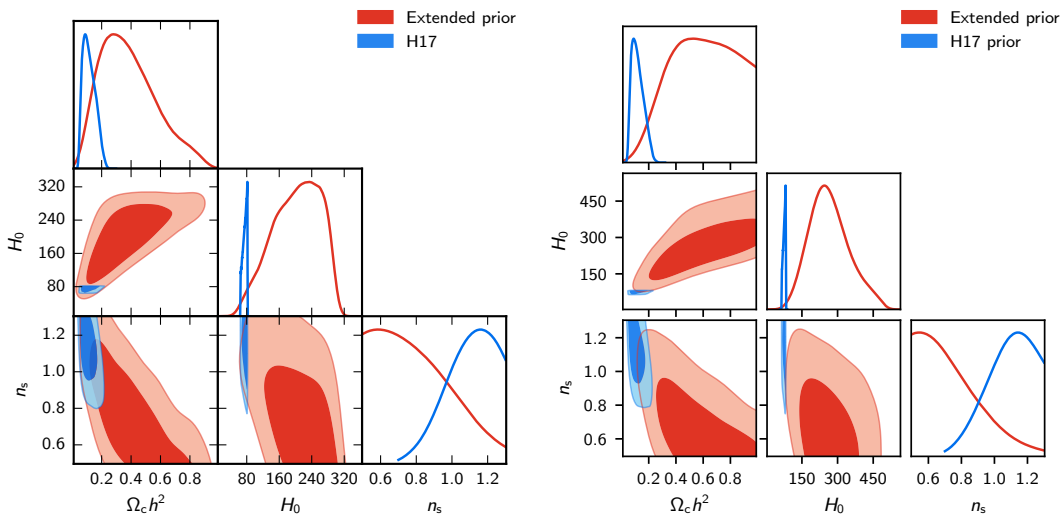

Figure B.3: Reproduction of figure 6.1, using the original covariance matrix on the left, and the corrected covariance matrix on the right.

B.2 Extended priors

We now explore the effect of the corrected covariance matrix on the extended priors test, by repeating the analysis with the corrected covariance matrix using the priors from Table 6.1. Table B.2 shows the effect of extended priors on the parameters that were in tension in Sec. 6.2, as shown by Table 6.2. Table B.2 clearly shows how the corrections to the covariance matrix increase the tension between default and wide priors. Figure B.3 shows the effect of the extended priors on cosmological parameters for the default and corrected covariance matrices. We see how the corrected covariance matrix allows $\Omega_c h^2$ to go to even higher values, being limited only by the physically motivated prior at $\Omega_c h^2 = 1$. This in turn pushes H_0 to higher values, and decreases n_s, due to existing degeneracies between these parameters. Therefore, the issue with the priors does not disappear with the corrections to the covariance matrix.

B.3 Conclusions

After repeating the internal consistency tests to the KiDS data used in Sec. 6.2 with the corrected covariance matrix from T18, we find that the internal inconsistencies observed when removing tomographic redshifts bins or performing a separate analysis using only ξ_+ or ξ_- become insignificant, due to the significant increase on both the errors, and the amplitude of the signal. This also alleviates the tension between KiDS and *Planck*, as observed by T18.

The problem with extended priors preferring unexpected values of cosmological parameters still remains, and it is in fact increased by the wider priors. This effect, combined with the

problems with photometric redshifts and the observed B-modes which are not understood, indicates that the errors in the covariance matrix were not the only issue in the KiDS analysis of H17. There seem to be other systematic effects that are not being taken into account, and that are displacing the parameters to values that differ from the expected values if allowed by the priors, however, we lose sensitivity to these effects after the increase in the errors on the T18 covariance matrix. Given the accuracy of present-day experiments, it is important to understand the origin of these problems, since they could be caused by systematics effects that are present in other weak lensing surveys.

Bibliography

Bibliography

[1] Planck Collaboration, N. Aghanim, Y. Akrami, M. Ashdown, J. Aumont, C. Baccigalupi, M. Ballardini, A. J. Banday, R. B. Barreiro, N. Bartolo, et al. Planck 2018 results. VI. Cosmological parameters. *ArXiv e-prints*, July 2018.

[2] P. Lemos, A. Challinor, and G. Efstathiou. The effect of Limber and flat-sky approximations on galaxy weak lensing. *J. Cosmology Astropart. Phys.*, 5:014, May 2017.

[3] G. Efstathiou and P. Lemos. Statistical inconsistencies in the KiDS-450 data set. *MNRAS*, 476:151–157, May 2018.

[4] M. A. Troxel, E. Krause, C. Chang, T. F. Eifler, O. Friedrich, D. Gruen, N. MacCrann, A. Chen, C. Davis, J. DeRose, et al. Survey geometry and the internal consistency of recent cosmic shear measurements. *MNRAS*, 479:4998–5004, October 2018.

[5] P. Lemos, E. Lee, G. Efstathiou, and S. Gratton. Model independent $H(z)$ reconstruction using the cosmic inverse distance ladder. *ArXiv e-prints*, June 2018.

[6] Scott Dodelson. *Modern Cosmology*. Academic Press, Elsevier Science, 2003.

[7] A. Liddle. *An Introduction to Modern Cosmology, Second Edition*. Wiley, May 2003.

[8] S. Weinberg. *Cosmology*. Oxford University Press, 2008.

[9] D.H. Lyth and A.R. Liddle. *The Primordial Density Perturbation: Cosmology, Inflation and the Origin of Structure*. Cambridge University Press, 2009.

[10] D Baumann. *Cosmology Lecture Notes - Part III Mathematical Tripos*. Department of Applied Mathematics and Theoretical Physics, University of Cambridge, 2015.

[11] R. M. Wald. *General relativity*. University of Chicago Press, 1984.

[12] J. B. Hartle. *Gravity : an introduction to Einstein's general relativity*. Addison Wesley, 2003.

[13] S. M. Carroll. *Spacetime and geometry. An introduction to general relativity*. Addison-Wesley, 2004.

[14] M. P. Hobson, G. P. Efstathiou, and A. N. Lasenby. *General Relativity*. Cambridge University Press, December 2005.

[15] A. Einstein. Die Grundlage der allgemeinen Relativitätstheorie. *Annalen der Physik*, 354:769–822, 1916.

[16] A. G. Riess, A. V. Filippenko, P. Challis, A. Clocchiatti, A. Diercks, P. M. Garnavich, R. L. Gilliland, C. J. Hogan, S. Jha, R. P. Kirshner, et al. Observational Evidence from Supernovae for an Accelerating Universe and a Cosmological Constant. *AJ*, 116:1009–1038, September 1998.

[17] S. Perlmutter, G. Aldering, G. Goldhaber, R. A. Knop, P. Nugent, P. G. Castro, S. Deustua, S. Fabbro, A. Goobar, D. E. Groom, et al. Measurements of Ω and Λ from 42 High-Redshift Supernovae. *ApJ*, 517:565–586, June 1999.

[18] S. Weinberg. The Cosmological Constant Problems (Talk given at Dark Matter 2000, February, 2000). *ArXiv Astrophysics e-prints*, May 2000.

[19] A. Avelino and R. P. Kirshner. The Dimensionless Age of the Universe: A Riddle for Our Time. *ApJ*, 828:35, September 2016.

[20] D. Baumann and L. McAllister. *Inflation and String Theory*. Department of Applied Mathematics and Theoretical Physics, University of Cambridge, April 2015.

[21] Planck Collaboration, P. A. R. Ade, N. Aghanim, M. Arnaud, M. Ashdown, J. Aumont, C. Baccigalupi, A. J. Banday, R. B. Barreiro, J. G. Bartlett, et al. Planck 2015 results. XIII. Cosmological parameters. *A&A*, 594:A13, September 2016.

[22] E. Noether. Invariant Variation Problems. *Nachr. D. König. Gesellsch. D. Wiss. Zu Göttingen, Math-phys. Klasse 1918: p. 235-237*, pages 235–237, 1918.

[23] M. Chiara Guzzetti, N. Bartolo, M. Liguori, and S. Matarrese. Gravitational waves from inflation. *ArXiv e-prints*, May 2016.

[24] A. R. Liddle and S. M. Leach. How long before the end of inflation were observable perturbations produced? *Phys. Rev. D*, 68(10):103503, November 2003.

[25] E. M. Lifshitz. On the gravitational stability of the expanding universe. *Zhurnal Eksperimentalnoi i Teoreticheskoi Fiziki*, 16:587–602, 1946.

[26] J. M. Bardeen. Gauge-invariant cosmological perturbations. *Phys. Rev. D*, 22:1882–1905, October 1980.

[27] M. Sasaki. Gauge-Invariant Scalar Perturbations in the New Inflationary Universe. *Progress of Theoretical Physics*, 70:394–411, August 1983.

[28] V. F. Mukhanov. The quantum theory of gauge-invariant cosmological perturbations. *Zhurnal Eksperimentalnoi i Teoreticheskoi Fiziki*, 94:1–11, July 1988.

[29] H. Kodama and M. Sasaki. Cosmological Perturbation Theory. *Progress of Theoretical Physics Supplement*, 78:1, 1984.

[30] Planck Collaboration, Y. Akrami, F. Arroja, M. Ashdown, J. Aumont, C. Baccigalupi, M. Ballardini, A. J. Banday, R. B. Barreiro, N. Bartolo, et al. Planck 2018 results. X. Constraints on inflation. *ArXiv e-prints*, July 2018.

[31] R. Allahverdi, R. Brandenberger, F.-Y. Cyr-Racine, and A. Mazumdar. Reheating in

Inflationary Cosmology: Theory and Applications. *Annual Review of Nuclear and Particle Science*, 60:27–51, November 2010.

[32] A. D. Sakharov. SPECIAL ISSUE: Violation of CP in variance, C asymmetry, and baryon asymmetry of the universe. *Soviet Physics Uspekhi*, 34:392–393, May 1991.

[33] L. Canetti, M. Drewes, and M. Shaposhnikov. Matter and antimatter in the universe. *New Journal of Physics*, 14(9):095012, September 2012.

[34] G. W. Pettinari. *The Intrinsic Bispectrum of the Cosmic Microwave Background*. Springer International Publishing Switzerland, 2016.

[35] Megh Nad Saha D.Sc. Liii. ionization in the solar chromosphere. *The London, Edinburgh, and Dublin Philosophical Magazine and Journal of Science*, 40(238):472–488, 1920.

[36] M. N. Saha. On a Physical Theory of Stellar Spectra. *Proceedings of the Royal Society of London Series A*, 99:135–153, May 1921.

[37] K. H. Kingdon and I. Langmuir. The Removal of Thorium from the Surface of a Thoriated Tungsten Filament by Positive Ion Bombardment. *Physical Review*, 22:148–160, August 1923.

[38] G. F. Smoot. COBE observations and results. In L. Maiani, F. Melchiorri, and N. Vittorio, editors, *3K cosmology*, volume 476 of *American Institute of Physics Conference Series*, pages 1–10, May 1999.

[39] F. Hoyle, G. Burbidge, and J. V. Narlikar. *A different approach to cosmology : from a static universe through the big bang towards reality*. Cambridge University Press, March 2000.

[40] G. Gamow. Expanding Universe and the Origin of Elements. *Physical Review*, 70:572–573, October 1946.

[41] G. Gamow. The Origin of Elements and the Separation of Galaxies. *Physical Review*, 74:505–506, August 1948.

[42] R. A. Alpher, H. Bethe, and G. Gamow. The Origin of Chemical Elements. *Physical Review*, 73:803–804, April 1948.

[43] R. A. Alpher and R. C. Herman. On the Relative Abundance of the Elements. *Physical Review*, 74:1737–1742, December 1948.

[44] A. A. Penzias and R. W. Wilson. A Measurement of Excess Antenna Temperature at 4080 Mc/s. *ApJ*, 142:419–421, July 1965.

[45] G. F. Smoot, C. L. Bennett, A. Kogut, E. L. Wright, J. Aymon, N. W. Boggess, E. S. Cheng, G. de Amici, S. Gulkis, M. G. Hauser, et al. Structure in the COBE differential microwave radiometer first-year maps. *The Astrophysical Journal*, 396:L1–L5, September 1992.

[46] G. Hinshaw, D. Larson, E. Komatsu, D. N. Spergel, C. L. Bennett, J. Dunkley, M. R.

Nolta, M. Halpern, R. S. Hill, N. Odegard, et al. Nine-year Wilkinson Microwave Anisotropy Probe (WMAP) Observations: Cosmological Parameter Results. *ApJS*, 208:19, October 2013.

[47] Planck Collaboration, P. A. R. Ade, N. Aghanim, C. Armitage-Caplan, M. Arnaud, M. Ashdown, F. Atrio-Barandela, J. Aumont, C. Baccigalupi, A. J. Banday, et al. Planck 2013 results. XVI. Cosmological parameters. *A&A*, 571:A16, November 2014.

[48] A. N. Lasenby, A. W. Jones, and Y. Dabrowski. Review of Ground-Based CMB Experiments. *ArXiv Astrophysics e-prints*, October 1998.

[49] J. M. Kovac, E. M. Leitch, C. Pryke, J. E. Carlstrom, N. W. Halverson, and W. L. Holzapfel. Detection of polarization in the cosmic microwave background using DASI. *Nature*, 420:772–787, December 2002.

[50] K. T. Story, C. L. Reichardt, Z. Hou, R. Keisler, K. A. Aird, B. A. Benson, L. E. Bleem, J. E. Carlstrom, C. L. Chang, H.-M. Cho, et al. A Measurement of the Cosmic Microwave Background Damping Tail from the 2500-Square-Degree SPT-SZ Survey. *ApJ*, 779:86, December 2013.

[51] J. L. Sievers, R. A. Hlozek, M. R. Nolta, V. Acquaviva, G. E. Addison, P. A. R. Ade, P. Aguirre, M. Amiri, J. W. Appel, L. F. Barrientos, et al. The Atacama Cosmology Telescope: cosmological parameters from three seasons of data. *J. Cosmology Astropart. Phys.*, 10:060, October 2013.

[52] J. Maldacena. Non-gaussian features of primordial fluctuations in single field inflationary models. *Journal of High Energy Physics*, 5:013, May 2003.

[53] C. T. Byrnes and K.-Y. Choi. Review of Local Non-Gaussianity from Multifield Inflation. *Advances in Astronomy*, 2010:724525, 2010.

[54] N. Bartolo, S. Matarrese, and A. Riotto. Non-Gaussianity in the curvaton scenario. *Phys. Rev. D*, 69(4):043503, February 2004.

[55] M. Zaldarriaga. Non-Gaussianities in models with a varying inflaton decay rate. *Phys. Rev. D*, 69(4):043508, February 2004.

[56] D. H. Lyth and Y. Rodríguez. Inflationary Prediction for Primordial Non-Gaussianity. *Physical Review Letters*, 95(12):121302, September 2005.

[57] D. H. Lyth. Generating the curvature perturbation at the end of inflation. *J. Cosmology Astropart. Phys.*, 11:006, December 2005.

[58] K. Enqvist, A. Jokinen, A. Mazumdar, T. Multamäki, and A. Väihkönen. Non-Gaussianity from preheating. *Physical Review Letters*, 94(16):161301, April 2005.

[59] A. Jokinen and A. Mazumdar. Very large primordial non-Gaussianity from multiple fields: application to massless preheating. *J. Cosmology Astropart. Phys.*, 4:003, April 2006.

[60] K. A. Malik and D. H. Lyth. A numerical study of non-Gaussianity in the curvaton scenario. *J. Cosmology Astropart. Phys.*, 9:008, September 2006.

[61] E. Silverstein and D. Tong. Scalar speed limits and cosmology: Acceleration from D-cceleration. *Phys. Rev. D*, 70(10):103505, November 2004.

[62] M. Alishahiha, E. Silverstein, and D. Tong. DBI in the sky: Non-Gaussianity from inflation with a speed limit. *Phys. Rev. D*, 70(12):123505, December 2004.

[63] M.-X. Huang and G. Shiu. Inflationary trispectrum for models with large non-Gaussianities. *Phys. Rev. D*, 74(12):121301, December 2006.

[64] X. Chen, R. Easther, and E. A. Lim. Large non-Gaussianities in single-field inflation. *J. Cosmology Astropart. Phys.*, 6:023, June 2007.

[65] X. Chen, M.-x. Huang, S. Kachru, and G. Shiu. Observational signatures and non-Gaussianities of general single-field inflation. *J. Cosmology Astropart. Phys.*, 1:002, January 2007.

[66] F. Arroja, S. Mizuno, and K. Koyama. Non-Gaussianity from the bispectrum in general multiple field inflation. *J. Cosmology Astropart. Phys.*, 8:015, August 2008.

[67] X. Chen, B. Hu, M.-x. Huang, G. Shiu, and Y. Wang. Large primordial trispectra in general single field inflation. *J. Cosmology Astropart. Phys.*, 8:008, August 2009.

[68] X. Chen. Primordial Non-Gaussianities from Inflation Models. *Advances in Astronomy*, 2010:638979, 2010.

[69] K. Koyama. Non-Gaussianity of quantum fields during inflation. *Classical and Quantum Gravity*, 27(12):124001, June 2010.

[70] Planck Collaboration, P. A. R. Ade, N. Aghanim, M. Arnaud, F. Arroja, M. Ashdown, J. Aumont, C. Baccigalupi, M. Ballardini, A. J. Banday, et al. Planck 2015 results. XVII. Constraints on primordial non-Gaussianity. *A&A*, 594:A17, September 2016.

[71] M. White, D. Scott, and J. Silk. Anisotropies in the Cosmic Microwave Background. *ARA&A*, 32:319–370, 1994.

[72] W. Hu and M. White. Acoustic Signatures in the Cosmic Microwave Background. *ApJ*, 471:30, November 1996.

[73] J. Silk. Cosmic Black-Body Radiation and Galaxy Formation. *ApJ*, 151:459, February 1968.

[74] W. Hu and M. White. The Damping Tail of Cosmic Microwave Background Anisotropies. *ApJ*, 479:568–579, April 1997.

[75] R. K. Sachs and A. M. Wolfe. Perturbations of a Cosmological Model and Angular Variations of the Microwave Background. *ApJ*, 147:73, January 1967.

[76] Y. B. Zeldovich and R. A. Sunyaev. The Interaction of Matter and Radiation in a Hot-Model Universe. *Astrophysics and Space Science*, 4:301–316, July 1969.

[77] R. A. Sunyaev and Y. B. Zeldovich. The Observations of Relic Radiation as a Test of the Nature of X-Ray Radiation from the Clusters of Galaxies. *Comments on Astrophysics and Space Physics*, 4:173, November 1972.

[78] R. A. Sunyaev and I. B. Zeldovich. The velocity of clusters of galaxies relative to the microwave background - The possibility of its measurement. *MNRAS*, 190:413–420, February 1980.

[79] W. Hu and M. White. A CMB polarization primer. *New Astron.*, 2:323–344, October 1997.

[80] P. Cabella and M. Kamionkowski. Theory of Cosmic Microwave Background Polarization. *ArXiv Astrophysics e-prints*, March 2004.

[81] J. N. Goldberg, A. J. Macfarlane, E. T. Newman, F. Rohrlich, and E. C. G. Sudarshan. Spin-s Spherical Harmonics and ð. *Journal of Mathematical Physics*, 8:2155–2161, November 1967.

[82] M. Kamionkowski, A. Kosowsky, and A. Stebbins. Statistics of cosmic microwave background polarization. *Phys. Rev. D*, 55:7368–7388, June 1997.

[83] M. Zaldarriaga and U. Seljak. All-sky analysis of polarization in the microwave background. *Phys. Rev. D*, 55:1830–1840, February 1997.

[84] T. W. B. Kibble. Topology of cosmic domains and strings. *Journal of Physics A Mathematical General*, 9:1387–1398, August 1976.

[85] M. B. Hindmarsh and T. W. B. Kibble. Cosmic strings. *Reports on Progress in Physics*, 58:477–562, May 1995.

[86] A. Rajantie. Formation of Topological Defects in Gauge Field Theories. *International Journal of Modern Physics A*, 17:1–43, 2002.

[87] K. Kamada, Y. Miyamoto, D. Yamauchi, and J. Yokoyama. Effects of cosmic strings with delayed scaling on CMB anisotropy. *Phys. Rev. D*, 90(8):083502, October 2014.

[88] C. Ringeval, D. Yamauchi, J. Yokoyama, and F. R. Bouchet. Large scale CMB anomalies from thawing cosmic strings. *J. Cosmology Astropart. Phys.*, 2:033, February 2016.

[89] R. P. L. Azevedo and C. J. A. P. Martins. Cosmic strings and other topological defects in nonscaling regimes. *Phys. Rev. D*, 95(4):043537, February 2017.

[90] A. Moss and L. Pogosian. Did BICEP2 See Vector Modes? First B-Mode Constraints on Cosmic Defects. *Physical Review Letters*, 112(17):171302, May 2014.

[91] A. Einstein. Lens-Like Action of a Star by the Deviation of Light in the Gravitational Field. *Science*, 84:506–507, December 1936.

[92] J. Renn, T. Sauer, and J. Stachel. The origin of gravitational lensing: a postscript to Einstein's 1936 Science paper. *Science*, 275:184–186, January 1997.

[93] M. Bartelmann and P. Schneider. Weak gravitational lensing. *Phys. Rep.*, 340:291–472,

January 2001.

[94] D. Munshi, P. Valageas, L. van Waerbeke, and A. Heavens. Cosmology with weak lensing surveys. *Phys. Rep.*, 462:67–121, June 2008.

[95] H. Hoekstra and B. Jain. Weak Gravitational Lensing and Its Cosmological Applications. *Annual Review of Nuclear and Particle Science*, 58:99–123, November 2008.

[96] M. Kilbinger. Cosmology with cosmic shear observations: a review. *Reports on Progress in Physics*, 78(8):086901, July 2015.

[97] DES Collaboration, T. M. C. Abbott, F. B. Abdalla, A. Alarcon, J. Aleksić, S. Allam, S. Allen, A. Amara, J. Annis, J. Asorey, et al. Dark Energy Survey Year 1 Results: Cosmological Constraints from Galaxy Clustering and Weak Lensing. *ArXiv e-prints*, August 2017.

[98] H. Hildebrandt, M. Viola, C. Heymans, S. Joudaki, K. Kuijken, C. Blake, T. Erben, B. Joachimi, D. Klaes, L. Miller, et al. KiDS-450: cosmological parameter constraints from tomographic weak gravitational lensing. *MNRAS*, 465:1454–1498, February 2017.

[99] C. M. Hirata and U. Seljak. Intrinsic alignment-lensing interference as a contaminant of cosmic shear. *Phys. Rev. D*, 70(6):063526, September 2004.

[100] P. Catelan, M. Kamionkowski, and R. D. Blandford. Intrinsic and extrinsic galaxy alignment. *MNRAS*, 320:L7–L13, January 2001.

[101] S. Bridle and L. King. Dark energy constraints from cosmic shear power spectra: impact of intrinsic alignments on photometric redshift requirements. *New Journal of Physics*, 9:444, December 2007.

[102] A. Dekel and O. Lahav. Stochastic Nonlinear Galaxy Biasing. *ApJ*, 520:24–34, July 1999.

[103] N. Kaiser. On the spatial correlations of Abell clusters. *ApJ*, 284:L9–L12, September 1984.

[104] J. M. Bardeen, J. R. Bond, N. Kaiser, and A. S. Szalay. The statistics of peaks of Gaussian random fields. *ApJ*, 304:15–61, May 1986.

[105] H. J. Mo and S. D. M. White. An analytic model for the spatial clustering of dark matter haloes. *MNRAS*, 282:347–361, September 1996.

[106] S. Joudaki, A. Mead, C. Blake, A. Choi, J. de Jong, T. Erben, C. Heymans, H. Hildebrandt, H. Hoekstra, B. Joachimi, et al. KiDS-450: Testing extensions to the standard cosmological model. *ArXiv e-prints*, October 2016.

[107] N. Kaiser, G. Wilson, and G. A. Luppino. Large-Scale Cosmic Shear Measurements. *ArXiv Astrophysics e-prints*, March 2000.

[108] D. M. Wittman, J. A. Tyson, D. Kirkman, I. Dell'Antonio, and G. Bernstein. Detection of weak gravitational lensing distortions of distant galaxies by cosmic dark matter at

large scales. *Nature*, 405:143–148, May 2000.

[109] D. J. Bacon, A. R. Refregier, and R. S. Ellis. Detection of weak gravitational lensing by large-scale structure. *MNRAS*, 318:625–640, October 2000.

[110] L. Van Waerbeke, Y. Mellier, T. Erben, J. C. Cuillandre, F. Bernardeau, R. Maoli, E. Bertin, H. J. McCracken, O. Le Fèvre, B. Fort, et al. Detection of correlated galaxy ellipticities from CFHT data: first evidence for gravitational lensing by large-scale structures. *A&A*, 358:30–44, June 2000.

[111] F. Köhlinger, M. Viola, B. Joachimi, H. Hoekstra, E. van Uitert, H. Hildebrandt, A. Choi, T. Erben, C. Heymans, S. Joudaki, et al. KiDS-450: The tomographic weak lensing power spectrum and constraints on cosmological parameters. *ArXiv e-prints*, June 2017.

[112] D. J. Eisenstein, H.-J. Seo, and M. White. On the Robustness of the Acoustic Scale in the Low-Redshift Clustering of Matter. *ApJ*, 664:660–674, August 2007.

[113] D. J. Eisenstein, I. Zehavi, D. W. Hogg, R. Scoccimarro, M. R. Blanton, R. C. Nichol, R. Scranton, H.-J. Seo, M. Tegmark, Z. Zheng, et al. Detection of the Baryon Acoustic Peak in the Large-Scale Correlation Function of SDSS Luminous Red Galaxies. *ApJ*, 633:560–574, November 2005.

[114] C. Alcock and B. Paczynski. An evolution free test for non-zero cosmological constant. *Nature*, 281:358, October 1979.

[115] S. Cole, W. J. Percival, J. A. Peacock, P. Norberg, C. M. Baugh, C. S. Frenk, I. Baldry, J. Bland-Hawthorn, T. Bridges, R. Cannon, et al. The 2dF Galaxy Redshift Survey: power-spectrum analysis of the final data set and cosmological implications. *MNRAS*, 362:505–534, September 2005.

[116] S. Alam, M. Ata, S. Bailey, F. Beutler, D. Bizyaev, J. A. Blazek, A. S. Bolton, J. R. Brownstein, A. Burden, C.-H. Chuang, et al. The clustering of galaxies in the completed SDSS-III Baryon Oscillation Spectroscopic Survey: cosmological analysis of the DR12 galaxy sample. *ArXiv e-prints*, July 2016.

[117] P. Zarrouk, E. Burtin, H. Gil-Marín, A. J. Ross, R. Tojeiro, I. Pâris, K. S. Dawson, A. D. Myers, W. J. Percival, C.-H. Chuang, et al. The clustering of the SDSS-IV extended Baryon Oscillation Spectroscopic Survey DR14 quasar sample: measurement of the growth rate of structure from the anisotropic correlation function between redshift 0.8 and 2.2. *MNRAS*, February 2018.

[118] P. McDonald and D. J. Eisenstein. Dark energy and curvature from a future baryonic acoustic oscillation survey using the Lyman-α forest. *Phys. Rev. D*, 76(6):063009, September 2007.

[119] J. E. Bautista, N. G. Busca, J. Guy, J. Rich, M. Blomqvist, H. du Mas des Bourboux, M. M. Pieri, A. Font-Ribera, S. Bailey, T. Delubac, et al. Measurement of baryon acoustic

oscillation correlations at z = 2.3 with SDSS DR12 Lyα-Forests. *A&A*, 603:A12, June 2017.

[120] H. du Mas des Bourboux, J.-M. Le Goff, M. Blomqvist, N. G. Busca, J. Guy, J. Rich, C. Yèche, J. E. Bautista, É. Burtin, K. S. Dawson, et al. Baryon acoustic oscillations from the complete SDSS-III Lyα-quasar cross-correlation function at z = 2.4. *A&A*, 608:A130, December 2017.

[121] S. Chandrasekhar. The highly collapsed configurations of a stellar mass. *MNRAS*, 91:456–466, March 1931.

[122] W. Hillebrandt and J. C. Niemeyer. Type IA Supernova Explosion Models. *ARA&A*, 38:191–230, 2000.

[123] M. Rowan-Robinson. *The cosmological distance ladder: Distance and time in the universe*. W H Freeman & Co, 1985.

[124] B. Leibundgut and J. Sollerman. A cosmological surprise: the universe accelerates. *ArXiv Astrophysics e-prints*, April 2002.

[125] A. G. Riess, S. Casertano, W. Yuan, L. Macri, J. Anderson, J. W. MacKenty, J. B. Bowers, K. I. Clubb, A. V. Filippenko, D. O. Jones, et al. New Parallaxes of Galactic Cepheids from Spatially Scanning the Hubble Space Telescope: Implications for the Hubble Constant. *ApJ*, 855:136, March 2018.

[126] M. Wyman, D. H. Rudd, R. A. Vanderveld, and W. Hu. Neutrinos Help Reconcile Planck Measurements with the Local Universe. *Physical Review Letters*, 112(5):051302, February 2014.

[127] M.-M. Zhao, D.-Z. He, J.-F. Zhang, and X. Zhang. Search for sterile neutrinos in holographic dark energy cosmology: Reconciling Planck observation with the local measurement of the Hubble constant. *Phys. Rev. D*, 96(4):043520, August 2017.

[128] E. Di Valentino, C. BÅ‘hm, E. Hivon, and F. R. Bouchet. Reducing the H_0 and σ_8 tensions with dark matter-neutrino interactions. *Phys. Rev. D*, 97(4):043513, February 2018.

[129] J. Solà, A. Gómez-Valent, and J. de Cruz Pérez. The H_0 tension in light of vacuum dynamics in the universe. *Physics Letters B*, 774:317–324, November 2017.

[130] E. Di Valentino, E. V. Linder, and A. Melchiorri. Vacuum phase transition solves the H_0 tension. *Phys. Rev. D*, 97(4):043528, February 2018.

[131] R. J. Cooke, M. Pettini, R. A. Jorgenson, M. T. Murphy, and C. C. Steidel. Precision Measures of the Primordial Abundance of Deuterium. *ApJ*, 781:31, January 2014.

[132] R. J. Cooke, M. Pettini, K. M. Nollett, and R. Jorgenson. The Primordial Deuterium Abundance of the Most Metal-poor Damped Lyman-α System. *ApJ*, 830:148, October 2016.

[133] R. J. Cooke, M. Pettini, and C. C. Steidel. One Percent Determination of the Primordial Deuterium Abundance. *ApJ*, 855:102, March 2018.

[134] W. J. Percival, B. A. Reid, D. J. Eisenstein, N. A. Bahcall, T. Budavari, J. A. Frieman, M. Fukugita, J. E. Gunn, Ž. Ivezić, G. R. Knapp, et al. Baryon acoustic oscillations in the Sloan Digital Sky Survey Data Release 7 galaxy sample. *MNRAS*, 401:2148–2168, February 2010.

[135] É. Aubourg, S. Bailey, J. E. Bautista, F. Beutler, V. Bhardwaj, D. Bizyaev, M. Blanton, M. Blomqvist, A. S. Bolton, J. Bovy, et al. Cosmological implications of baryon acoustic oscillation measurements. *Phys. Rev. D*, 92(12):123516, December 2015.

[136] A. J. Cuesta, L. Verde, A. Riess, and R. Jimenez. Calibrating the cosmic distance scale ladder: the role of the sound-horizon scale and the local expansion rate as distance anchors. *MNRAS*, 448:3463–3471, April 2015.

[137] DES Collaboration, T. M. C. Abbott, F. B. Abdalla, J. Annis, K. Bechtol, B. A. Benson, R. A. Bernstein, G. M. Bernstein, E. Bertin, D. Brooks, et al. Dark Energy Survey Year 1 Results: A Precise H0 Measurement from DES Y1, BAO, and D/H Data. *ArXiv e-prints*, November 2017.

[138] U. Seljak and M. Zaldarriaga. Direct signature of an evolving gravitational potential from the cosmic microwave background. *Phys. Rev. D*, 60(4):043504, August 1999.

[139] W. Hu and T. Okamoto. Mass Reconstruction with Cosmic Microwave Background Polarization. *ApJ*, 574:566–574, August 2002.

[140] C. M. Hirata and U. Seljak. Reconstruction of lensing from the cosmic microwave background polarization. *Phys. Rev. D*, 68(8):083002, October 2003.

[141] J. Yoo and M. Zaldarriaga. Improved estimation of cluster mass profiles from the cosmic microwave background. *Phys. Rev. D*, 78(8):083002, October 2008.

[142] W. J. Percival and M. White. Testing cosmological structure formation using redshift-space distortions. *MNRAS*, 393:297–308, February 2009.

[143] B. P. Abbott, R. Abbott, T. D. Abbott, M. R. Abernathy, F. Acernese, K. Ackley, C. Adams, T. Adams, P. Addesso, R. X. Adhikari, et al. Observation of Gravitational Waves from a Binary Black Hole Merger. *Physical Review Letters*, 116(6):061102, February 2016.

[144] B. P. Abbott, R. Abbott, T. D. Abbott, F. Acernese, K. Ackley, C. Adams, T. Adams, P. Addesso, R. X. Adhikari, V. B. Adya, et al. GW170817: Observation of Gravitational Waves from a Binary Neutron Star Inspiral. *Physical Review Letters*, 119(16):161101, October 2017.

[145] B. P. Abbott, R. Abbott, T. D. Abbott, F. Acernese, K. Ackley, C. Adams, T. Adams, P. Addesso, R. X. Adhikari, V. B. Adya, et al. Multi-messenger Observations of a Binary

Neutron Star Merger. *ApJ*, 848:L12, October 2017.

[146] K. P. Mooley, A. T. Deller, O. Gottlieb, E. Nakar, G. Hallinan, S. Bourke, D. A. Frail, A. Horesh, A. Corsi, and K. Hotokezaka. Superluminal motion of a relativistic jet in the neutron star merger GW170817. *ArXiv e-prints*, June 2018.

[147] Planck Collaboration, R. Adam, P. A. R. Ade, N. Aghanim, Y. Akrami, M. I. R. Alves, M. Arnaud, F. Arroja, J. Aumont, C. Baccigalupi, et al. Planck 2015 results. I. Overview of products and scientific results. *ArXiv e-prints*, February 2015.

[148] Planck Collaboration, Y. Akrami, F. Arroja, M. Ashdown, J. Aumont, C. Baccigalupi, M. Ballardini, A. J. Banday, R. B. Barreiro, N. Bartolo, et al. Planck 2018 results. I. Overview and the cosmological legacy of Planck. *ArXiv e-prints*, July 2018.

[149] Planck Collaboration, P. A. R. Ade, N. Aghanim, M. Arnaud, F. Arroja, M. Ashdown, J. Aumont, C. Baccigalupi, M. Ballardini, A. J. Banday, et al. Planck 2015 results. XX. Constraints on inflation. *ArXiv e-prints*, February 2015.

[150] E. Silverstein and A. Westphal. Monodromy in the CMB: Gravity waves and string inflation. *Phys. Rev. D*, 78(10):106003, November 2008.

[151] L. McAllister, E. Silverstein, and A. Westphal. Gravity waves and linear inflation from axion monodromy. *Phys. Rev. D*, 82(4):046003, August 2010.

[152] M. Berg, E. Pajer, and S. Sjörs. Two-field high-scale inflation in a sub-Planckian region of field space. *Phys. Rev. D*, 81(10):103535, May 2010.

[153] D. Baumann and L. McAllister. A microscopic limit on gravitational waves from D-brane inflation. *Phys. Rev. D*, 75(12):123508, June 2007.

[154] Planck Collaboration. Planck intermediate results. XLVI. Reduction of large-scale systematic effects in HFI polarization maps and estimation of the reionization optical depth. *ArXiv e-prints*, May 2016.

[155] A. A. Starobinskij. Spectrum of adiabatic perturbations in the universe when there are singularities in the inflationary potential. *Soviet Journal of Experimental and Theoretical Physics Letters*, 55:489–494, May 1992.

[156] J. Adams, B. Cresswell, and R. Easther. Inflationary perturbations from a potential with a step. *Physical Review D*, 64(12):123514, December 2001.

[157] P. Adshead, C. Dvorkin, W. Hu, and E. A. Lim. Non-Gaussianity from step features in the inflationary potential. *Phys. Rev. D*, 85(2):023531, January 2012.

[158] Dhiraj Kumar Hazra, Arman Shafieloo, George F. Smoot, and Alexei A. Starobinsky. Inflation with Whip-Shaped Suppressed Scalar Power Spectra. *Phys. Rev. Lett.*, 113(7):071301, 2014.

[159] Dhiraj Kumar Hazra, Arman Shafieloo, George F. Smoot, and Alexei A. Starobinsky. Wiggly Whipped Inflation. *JCAP*, 1408:048, 2014.

[160] Dhiraj Kumar Hazra, Arman Shafieloo, George F. Smoot, and Alexei A. Starobinsky. Primordial features and Planck polarization. *JCAP*, 1609(09):009, 2016.

[161] Laura Covi, Jan Hamann, Alessandro Melchiorri, Anze Slosar, and Irene Sorbera. Inflation and WMAP three year data: Features have a Future! *Phys. Rev.*, D74:083509, 2006.

[162] Ali Akbar Abolhasani, Hassan Firouzjahi, Shahram Khosravi, and Misao Sasaki. Local Features with Large Spiky non-Gaussianities during Inflation. *JCAP*, 1211:012, 2012.

[163] D. J. H. Chung, E. W. Kolb, A. Riotto, and I. I. Tkachev. Probing Planckian physics: Resonant production of particles during inflation and features in the primordial power spectrum. *Phys. Rev. D*, 62(4):043508, August 2000.

[164] N. Barnaby and Z. Huang. Particle production during inflation: Observational constraints and signatures. *Phys. Rev. D*, 80(12):126018, December 2009.

[165] N. Barnaby. Features and non-Gaussianity from inflationary particle production. *Phys. Rev. D*, 82(10):106009, November 2010.

[166] A. Achúcarro, J.-O. Gong, S. Hardeman, G. A. Palma, and S. P. Patil. Features of heavy physics in the CMB power spectrum. *J. Cosmology Astropart. Phys.*, 1:030, January 2011.

[167] Sebastian Cespedes, Vicente Atal, and Gonzalo A. Palma. On the importance of heavy fields during inflation. *JCAP*, 1205:008, 2012.

[168] Xian Gao, David Langlois, and Shuntaro Mizuno. Oscillatory features in the curvature power spectrum after a sudden turn of the inflationary trajectory. *JCAP*, 1310:023, 2013.

[169] T. Noumi and M. Yamaguchi. Primordial spectra from sudden turning trajectory. *J. Cosmology Astropart. Phys.*, 12:038, December 2013.

[170] J. Martin and C. Ringeval. Superimposed oscillations in the WMAP data? *Phys. Rev. D*, 69(8):083515, April 2004.

[171] C. Pahud, M. Kamionkowski, and A. R. Liddle. Oscillations in the inflaton potential? *Phys. Rev. D*, 79(8):083503, April 2009.

[172] M. Benetti, M. Lattanzi, E. Calabrese, and A. Melchiorri. Features in the primordial spectrum: New constraints from WMAP7 and ACT data and prospects for the Planck mission. *Phys. Rev. D*, 84(6):063509, September 2011.

[173] C. Dvorkin and W. Hu. Complete WMAP constraints on band-limited inflationary features. *Phys. Rev. D*, 84(6):063515, September 2011.

[174] D. K. Hazra, A. Shafieloo, and T. Souradeep. Primordial power spectrum: a complete analysis with the WMAP nine-year data. *J. Cosmology Astropart. Phys.*, 7:031, July 2013.

[175] P. D. Meerburg, D. N. Spergel, and B. D. Wandelt. Searching for oscillations in the

primordial power spectrum. I. Perturbative approach. *Phys. Rev. D*, 89(6):063536, March 2014.

[176] M. Benetti. Updating constraints on inflationary features in the primordial power spectrum with the Planck data. *Phys. Rev. D*, 88(8):087302, October 2013.

[177] X. Chen, M. H. Namjoo, and Y. Wang. Models of the Primordial Clock. *J. Cosmology Astropart. Phys.*, 2:027, February 2015.

[178] X. Chen, R. Easther, and E. A. Lim. Generation and characterization of large non-Gaussianities in single field inflation. *J. Cosmology Astropart. Phys.*, 4:010, April 2008.

[179] X. Chen. Primordial Features as Evidence for Inflation. *ArXiv e-prints*, April 2011.

[180] R. Flauger, L. McAllister, E. Pajer, A. Westphal, and G. Xu. Oscillations in the CMB from axion monodromy inflation. *JCAP*, 6:009, June 2010.

[181] R. Flauger, L. McAllister, E. Silverstein, and A. Westphal. Drifting oscillations in axion monodromy. *J. Cosmology Astropart. Phys.*, 10:055, October 2017.

[182] John Ellis, Marcos A. G. Garcia, Dimitri V. Nanopoulos, and Keith A. Olive. Calculations of Inflaton Decays and Reheating: with Applications to No-Scale Inflation Models. *JCAP*, 1507(07):050, 2015.

[183] X. Chen and M. H. Namjoo. Standard Clock in primordial density perturbations and cosmic microwave background. *Physics Letters B*, 739:285–292, December 2014.

[184] W. J. Handley, M. P. Hobson, and A. N. Lasenby. POLYCHORD: nested sampling for cosmology. *MNRAS*, 450:L61–L65, June 2015.

[185] W. J. Handley, M. P. Hobson, and A. N. Lasenby. POLYCHORD: next-generation nested sampling. *MNRAS*, 453:4384–4398, November 2015.

[186] A. Lewis and S. Bridle. Cosmological parameters from CMB and other data: A Monte Carlo approach. *Phys. Rev. D*, 66(10):103511, November 2002.

[187] F. Feroz and M. P. Hobson. Multimodal nested sampling: an efficient and robust alternative to Markov Chain Monte Carlo methods for astronomical data analyses. *MNRAS*, 384:449–463, February 2008.

[188] F. Feroz, M. P. Hobson, and M. Bridges. MULTINEST: an efficient and robust Bayesian inference tool for cosmology and particle physics. *MNRAS*, 398:1601–1614, October 2009.

[189] F. Feroz, M. P. Hobson, E. Cameron, and A. N. Pettitt. Importance Nested Sampling and the MultiNest Algorithm. *ArXiv e-prints*, June 2013.

[190] A. Lewis. Efficient sampling of fast and slow cosmological parameters. *Phys. Rev. D*, 87(10):103529, May 2013.

[191] George Efstathiou. Noise contribution to planck 2018. *To be published*, 2018.

[192] H. Jeffreys. A Treatise on Probability. *Nature*, 109:132–133, February 1922.

[193] K. N. Abazajian, P. Adshead, Z. Ahmed, S. W. Allen, D. Alonso, K. S. Arnold, C. Baccigalupi, J. G. Bartlett, N. Battaglia, B. A. Benson, et al. CMB-S4 Science Book, First Edition. *ArXiv e-prints*, October 2016.

[194] M. H. Abitbol, Z. Ahmed, D. Barron, R. Basu Thakur, A. N. Bender, B. A. Benson, C. A. Bischoff, S. A. Bryan, J. E. Carlstrom, C. L. Chang, et al. CMB-S4 Technology Book, First Edition. *ArXiv e-prints*, June 2017.

[195] E. D. Stewart. Spectrum of density perturbations produced during inflation to leading order in a general slow-roll approximation. *Phys. Rev. D*, 65(10):103508, May 2002.

[196] C. Dvorkin and W. Hu. Generalized slow roll approximation for large power spectrum features. *Phys. Rev. D*, 81(2):023518, January 2010.

[197] C. Dvorkin and W. Hu. CMB constraints on principal components of the inflaton potential. *Phys. Rev. D*, 82(4):043513, August 2010.

[198] G. Obied, C. Dvorkin, C. Heinrich, W. Hu, and V. Miranda. Inflationary vs. Reionization Features from Planck 2015 Data. *ArXiv e-prints*, March 2018.

[199] G. Obied, C. Dvorkin, C. Heinrich, W. Hu, and V. Miranda. Inflationary features and shifts in cosmological parameters from Planck 2015 data. *Phys. Rev. D*, 96(8):083526, October 2017.

[200] John Skilling. Nested sampling for general bayesian computation. *Bayesian Anal.*, 1(4):833–859, 12 2006.

[201] V. Miranda, W. Hu, and C. Dvorkin. Polarization predictions for inflationary CMB power spectrum features. *Phys. Rev. D*, 91(6):063514, March 2015.

[202] W. Hu. Generalized slow roll for noncanonical kinetic terms. *Phys. Rev. D*, 84(2):027303, July 2011.

[203] J. Choe, J.-O. Gong, and E. D. Stewart. Second order general slow-roll power spectrum. *J. Cosmology Astropart. Phys.*, 7:012, July 2004.

[204] Antony Lewis, Anthony Challinor, and Anthony Lasenby. Efficient computation of CMB anisotropies in closed FRW models. *Astrophys. J.*, 538:473–476, 2000.

[205] J. W. Henning, J. T. Sayre, C. L. Reichardt, P. A. R. Ade, A. J. Anderson, J. E. Austermann, J. A. Beall, A. N. Bender, B. A. Benson, L. E. Bleem, et al. Measurements of the Temperature and E-mode Polarization of the CMB from 500 Square Degrees of SPTpol Data. *ApJ*, 852:97, January 2018.

[206] Planck Collaboration, N. Aghanim, M. Arnaud, M. Ashdown, J. Aumont, C. Baccigalupi, A. J. Banday, R. B. Barreiro, J. G. Bartlett, N. Bartolo, et al. Planck 2015 results. XI. CMB power spectra, likelihoods, and robustness of parameters. *A&A*, 594:A11, September 2016.

[207] A. Manzotti, W. Hu, and A. Benoit-Lévy. Super-sample CMB lensing. *Phys. Rev. D*,

90(2):023003, July 2014.

[208] Max A. Woodbury. *Inverting modified matrices*. Statistical Research Group, Memo. Rep. no. 42. Princeton University, Princeton, N. J., 1950.

[209] D. Jeong, J. Chluba, L. Dai, M. Kamionkowski, and X. Wang. Effect of aberration on partial-sky measurements of the cosmic microwave background temperature power spectrum. *Phys. Rev. D*, 89(2):023003, January 2014.

[210] T. Louis, E. Grace, M. Hasselfield, M. Lungu, L. Maurin, G. E. Addison, P. A. R. Ade, S. Aiola, R. Allison, M. Amiri, et al. The Atacama Cosmology Telescope: two-season ACTPol spectra and parameters. *J. Cosmology Astropart. Phys.*, 6:031, June 2017.

[211] Planck Collaboration, N. Aghanim, C. Armitage-Caplan, M. Arnaud, M. Ashdown, F. Atrio-Barandela, J. Aumont, C. Baccigalupi, A. J. Banday, R. B. Barreiro, et al. Planck 2013 results. XXVII. Doppler boosting of the CMB: Eppur si muove. *A&A*, 571:A27, November 2014.

[212] A. T. Crites, J. W. Henning, P. A. R. Ade, K. A. Aird, J. E. Austermann, J. A. Beall, A. N. Bender, B. A. Benson, L. E. Bleem, J. E. Carlstrom, et al. Measurements of E-Mode Polarization and Temperature-E-Mode Correlation in the Cosmic Microwave Background from 100 Square Degrees of SPTpol Data. *ApJ*, 805:36, May 2015.

[213] C. Heymans, L. Van Waerbeke, L. Miller, T. Erben, H. Hildebrandt, H. Hoekstra, T. D. Kitching, Y. Mellier, P. Simon, C. Bonnett, et al. CFHTLenS: the Canada-France-Hawaii Telescope Lensing Survey. *MNRAS*, 427:146–166, November 2012.

[214] C. Heymans, E. Grocutt, A. Heavens, M. Kilbinger, T. D. Kitching, F. Simpson, J. Benjamin, T. Erben, H. Hildebrandt, H. Hoekstra, et al. CFHTLenS tomographic weak lensing cosmological parameter constraints: Mitigating the impact of intrinsic galaxy alignments. *MNRAS*, 432:2433–2453, July 2013.

[215] S. Joudaki, C. Blake, C. Heymans, A. Choi, J. Harnois-Deraps, H. Hildebrandt, B. Joachimi, A. Johnson, A. Mead, D. Parkinson, et al. CFHTLenS revisited: assessing concordance with Planck including astrophysical systematics. *MNRAS*, 465:2033–2052, February 2017.

[216] T. Abbott, F. B. Abdalla, S. Allam, A. Amara, J. Annis, R. Armstrong, D. Bacon, M. Banerji, A. H. Bauer, E. Baxter, et al. Cosmology from cosmic shear with Dark Energy Survey Science Verification data. *Phys. Rev. D*, 94(2):022001, July 2016.

[217] T. D. Kitching, J. Alsing, A. F. Heavens, R. Jimenez, J. D. McEwen, and L. Verde. The Limits of Cosmic Shear. *ArXiv e-prints*, November 2016.

[218] D. N. Limber. The Analysis of Counts of the Extragalactic Nebulae in Terms of a Fluctuating Density Field. *ApJ*, 117:134, January 1953.

[219] M. Loverde and N. Afshordi. Extended Limber approximation. *Phys. Rev. D*,

78(12):123506, December 2008.

[220] P. Simon. How accurate is Limber's equation? *A&A*, 473:711–714, October 2007.

[221] T. D. Kitching and A. F. Heavens. Unequal-Time Correlators for Cosmology. *ArXiv e-prints*, December 2016.

[222] M. Kilbinger, C. Heymans, M. Asgari, S. Joudaki, P. Schneider, P. Simon, L. Van Waerbeke, J. Harnois-Déraps, H. Hildebrandt, F. Köhlinger, et al. Precision calculations of the cosmic shear power spectrum projection. *ArXiv e-prints*, February 2017.

[223] D. A. Varshalovich, A. N. Moskalev, and V. K. Khersonskii. *Quantum Theory of Angular Momentum*. World Scientific Publishing Co, 1988.

[224] W. Hu. Power Spectrum Tomography with Weak Lensing. *ApJ*, 522:L21–L24, September 1999.

[225] M. J. Jee, J. A. Tyson, S. Hilbert, M. D. Schneider, S. Schmidt, and D. Wittman. Cosmic Shear Results from the Deep Lens Survey. II. Full Cosmological Parameter Constraints from Tomography. *ApJ*, 824:77, June 2016.

[226] M. A. Troxel, N. MacCrann, J. Zuntz, T. F. Eifler, E. Krause, S. Dodelson, D. Gruen, J. Blazek, O. Friedrich, S. Samuroff, et al. Dark Energy Survey Year 1 Results: Cosmological Constraints from Cosmic Shear. *ArXiv e-prints*, August 2017.

[227] E. van Uitert, B. Joachimi, S. Joudaki, C. Heymans, F. Köhlinger, M. Asgari, C. Blake, A. Choi, T. Erben, D. J. Farrow, et al. KiDS+GAMA: Cosmology constraints from a joint analysis of cosmic shear, galaxy-galaxy lensing and angular clustering. *ArXiv e-prints*, June 2017.

[228] J. Blazek, N. MacCrann, M. A. Troxel, and X. Fang. Beyond linear galaxy alignments. *ArXiv e-prints*, August 2017.

[229] D. Kirk, A. Rassat, O. Host, and S. Bridle. The cosmological impact of intrinsic alignment model choice for cosmic shear. *MNRAS*, 424:1647–1657, August 2012.

[230] A. G. Riess, L. M. Macri, S. L. Hoffmann, D. Scolnic, S. Casertano, A. V. Filippenko, B. E. Tucker, M. J. Reid, D. O. Jones, J. M. Silverman, et al. A 2.4% Determination of the Local Value of the Hubble Constant. *ApJ*, 826:56, July 2016.

[231] S. M. Feeney, H. V. Peiris, A. R. Williamson, S. M. Nissanke, D. J. Mortlock, J. Alsing, and D. Scolnic. Prospects for resolving the Hubble constant tension with standard sirens. *ArXiv e-prints*, February 2018.

[232] N. Kaiser. Clustering in real space and in redshift space. *MNRAS*, 227:1–21, July 1987.

[233] D. Huterer, D. L. Shafer, D. M. Scolnic, and F. Schmidt. Testing ΛCDM at the lowest redshifts with SN Ia and galaxy velocities. *J. Cosmology Astropart. Phys.*, 5:015, May 2017.

[234] D. Scolnic, S. Casertano, A. Riess, A. Rest, E. Schlafly, R. J. Foley, D. Finkbeiner,

C. Tang, W. S. Burgett, K. C. Chambers, et al. Supercal: Cross-calibration of Multiple Photometric Systems to Improve Cosmological Measurements with Type Ia Supernovae. *ApJ*, 815:117, December 2015.

[235] C. M. Springob, C. Magoulas, M. Colless, J. Mould, P. Erdoğdu, D. H. Jones, J. R. Lucey, L. Campbell, and C. J. Fluke. The 6dF Galaxy Survey: peculiar velocity field and cosmography. *MNRAS*, 445:2677–2697, December 2014.

[236] A. Vikhlinin, A. V. Kravtsov, R. A. Burenin, H. Ebeling, W. R. Forman, A. Hornstrup, C. Jones, S. S. Murray, D. Nagai, H. Quintana, et al. Chandra Cluster Cosmology Project III: Cosmological Parameter Constraints. *ApJ*, 692:1060–1074, February 2009.

[237] E. Rozo, R. H. Wechsler, E. S. Rykoff, J. T. Annis, M. R. Becker, A. E. Evrard, J. A. Frieman, S. M. Hansen, J. Hao, D. E. Johnston, et al. Cosmological Constraints from the Sloan Digital Sky Survey maxBCG Cluster Catalog. *ApJ*, 708:645–660, January 2010.

[238] M. Hasselfield, M. Hilton, T. A. Marriage, G. E. Addison, L. F. Barrientos, N. Battaglia, E. S. Battistelli, J. R. Bond, D. Crichton, S. Das, et al. The Atacama Cosmology Telescope: Sunyaev-Zel'dovich selected galaxy clusters at 148 GHz from three seasons of data. *J. Cosmology Astropart. Phys.*, 7:008, July 2013.

[239] Planck Collaboration, P. A. R. Ade, N. Aghanim, C. Armitage-Caplan, M. Arnaud, M. Ashdown, F. Atrio-Barandela, J. Aumont, C. Baccigalupi, A. J. Banday, et al. Planck 2013 results. XX. Cosmology from Sunyaev-Zeldovich cluster counts. *A&A*, 571:A20, November 2014.

[240] A. B. Mantz, A. von der Linden, S. W. Allen, D. E. Applegate, P. L. Kelly, R. G. Morris, D. A. Rapetti, R. W. Schmidt, S. Adhikari, M. T. Allen, et al. Weighing the giants - IV. Cosmology and neutrino mass. *MNRAS*, 446:2205–2225, January 2015.

[241] Planck Collaboration, P. A. R. Ade, N. Aghanim, M. Arnaud, M. Ashdown, J. Aumont, C. Baccigalupi, A. J. Banday, R. B. Barreiro, J. G. Bartlett, et al. Planck 2015 results. XXIV. Cosmology from Sunyaev-Zeldovich cluster counts. *A&A*, 594:A24, September 2016.

[242] T. de Haan, B. A. Benson, L. E. Bleem, S. W. Allen, D. E. Applegate, M. L. N. Ashby, M. Bautz, M. Bayliss, S. Bocquet, M. Brodwin, et al. Cosmological Constraints from Galaxy Clusters in the 2500 Square-degree SPT-SZ Survey. *ApJ*, 832:95, November 2016.

[243] A. von der Linden, M. T. Allen, D. E. Applegate, P. L. Kelly, S. W. Allen, H. Ebeling, P. R. Burchat, D. L. Burke, D. Donovan, R. G. Morris, et al. Weighing the Giants - I. Weak-lensing masses for 51 massive galaxy clusters: project overview, data analysis methods and cluster images. *MNRAS*, 439:2–27, March 2014.

[244] P. L. Kelly, A. von der Linden, D. E. Applegate, M. T. Allen, S. W. Allen, P. R.

Burchat, D. L. Burke, H. Ebeling, P. Capak, O. Czoske, et al. Weighing the Giants - II. Improved calibration of photometry from stellar colours and accurate photometric redshifts. *MNRAS*, 439:28–47, March 2014.

[245] D. E. Applegate, A. von der Linden, P. L. Kelly, M. T. Allen, S. W. Allen, P. R. Burchat, D. L. Burke, H. Ebeling, A. Mantz, and R. G. Morris. Weighing the Giants - III. Methods and measurements of accurate galaxy cluster weak-lensing masses. *MNRAS*, 439:48–72, March 2014.

[246] M. A. Troxel and M. Ishak. The intrinsic alignment of galaxies and its impact on weak gravitational lensing in an era of precision cosmology. *Phys. Rep.*, 558:1–59, February 2015.

[247] B. Joachimi, M. Cacciato, T. D. Kitching, A. Leonard, R. Mandelbaum, B. M. Schäfer, C. Sifón, H. Hoekstra, A. Kiessling, D. Kirk, et al. Galaxy Alignments: An Overview. *Space Sci. Rev.*, 193:1–65, November 2015.

[248] B. Joachimi, R. Mandelbaum, F. B. Abdalla, and S. L. Bridle. Constraints on intrinsic alignment contamination of weak lensing surveys using the MegaZ-LRG sample. *A&A*, 527:A26, March 2011.

[249] S. P. Driver, D. T. Hill, L. S. Kelvin, A. S. G. Robotham, J. Liske, P. Norberg, I. K. Baldry, S. P. Bamford, A. M. Hopkins, J. Loveday, et al. Galaxy and Mass Assembly (GAMA): survey diagnostics and core data release. *MNRAS*, 413:971–995, May 2011.

[250] J. Liske, I. K. Baldry, S. P. Driver, R. J. Tuffs, M. Alpaslan, E. Andrae, S. Brough, M. E. Cluver, M. W. Grootes, M. L. P. Gunawardhana, et al. Galaxy And Mass Assembly (GAMA): end of survey report and data release 2. *MNRAS*, 452:2087–2126, September 2015.

[251] F. Köhlinger, B. Joachimi, M. Asgari, M. Viola, S. Joudaki, and T. Tröster. A Bayesian quantification of consistency in correlated datasets. *ArXiv e-prints*, September 2018.

[252] A. G. Riess, L. Macri, S. Casertano, M. Sosey, H. Lampeitl, H. C. Ferguson, A. V. Filippenko, S. W. Jha, W. Li, R. Chornock, et al. A Redetermination of the Hubble Constant with the Hubble Space Telescope from a Differential Distance Ladder. *ApJ*, 699:539–563, July 2009.

[253] A. G. Riess, L. Macri, S. Casertano, H. Lampeitl, H. C. Ferguson, A. V. Filippenko, S. W. Jha, W. Li, and R. Chornock. A 3% Solution: Determination of the Hubble Constant with the Hubble Space Telescope and Wide Field Camera 3. *ApJ*, 730:119, April 2011.

[254] A. G. Riess, S. Casertano, W. Yuan, L. Macri, B. Bucciarelli, M. G. Lattanzi, J. W. MacKenty, J. B. Bowers, W. Zheng, A. V. Filippenko, et al. Milky Way Cepheid Standards for Measuring Cosmic Distances and Application to Gaia DR2: Implications for the Hubble Constant. *ArXiv e-prints*, April 2018.

[255] Gaia Collaboration, A. G. A. Brown, A. Vallenari, T. Prusti, J. H. J. de Bruijne, C. Babusiaux, and C. A. L. Bailer-Jones. Gaia Data Release 2. Summary of the contents and survey properties. *ArXiv e-prints*, April 2018.

[256] W. L. Freedman, B. F. Madore, B. K. Gibson, L. Ferrarese, D. D. Kelson, S. Sakai, J. R. Mould, R. C. Kennicutt, Jr., H. C. Ford, J. A. Graham, et al. Final Results from the Hubble Space Telescope Key Project to Measure the Hubble Constant. *ApJ*, 553:47–72, May 2001.

[257] G. Efstathiou. H_0 revisited. *MNRAS*, 440:1138–1152, May 2014.

[258] W. Cardona, M. Kunz, and V. Pettorino. Determining H_0 with Bayesian hyperparameters. *J. Cosmology Astropart. Phys.*, 3:056, March 2017.

[259] B. R. Zhang, M. J. Childress, T. M. Davis, N. V. Karpenka, C. Lidman, B. P. Schmidt, and M. Smith. A blinded determination of H_0 from low-redshift Type Ia supernovae, calibrated by Cepheid variables. *MNRAS*, 471:2254–2285, October 2017.

[260] B. Follin and L. Knox. Insensitivity of The Distance Ladder Hubble Constant Determination to Cepheid Calibration Modeling Choices. *MNRAS*, March 2018.

[261] S. M. Feeney, D. J. Mortlock, and N. Dalmasso. Clarifying the Hubble constant tension with a Bayesian hierarchical model of the local distance ladder. *MNRAS*, 476:3861–3882, May 2018.

[262] A. Heavens, R. Jimenez, and L. Verde. Standard Rulers, Candles, and Clocks from the Low-Redshift Universe. *Physical Review Letters*, 113(24):241302, December 2014.

[263] J. L. Bernal, L. Verde, and A. G. Riess. The trouble with H_0. *J. Cosmology Astropart. Phys.*, 10:019, October 2016.

[264] L. Verde, J. L. Bernal, A. F. Heavens, and R. Jimenez. The length of the low-redshift standard ruler. *MNRAS*, 467:731–736, May 2017.

[265] D. M. Scolnic, D. O. Jones, A. Rest, Y. C. Pan, R. Chornock, R. J. Foley, M. E. Huber, R. Kessler, G. Narayan, A. G. Riess, et al. The Complete Light-curve Sample of Spectroscopically Confirmed Type Ia Supernovae from Pan-STARRS1 and Cosmological Constraints from The Combined Pantheon Sample. *ArXiv e-prints*, October 2017.

[266] F. Beutler, C. Blake, M. Colless, D. H. Jones, L. Staveley-Smith, L. Campbell, Q. Parker, W. Saunders, and F. Watson. The 6dF Galaxy Survey: baryon acoustic oscillations and the local Hubble constant. *MNRAS*, 416:3017–3032, October 2011.

[267] S. Joudaki, M. Kaplinghat, R. Keeley, and D. Kirkby. Model independent inference of the expansion history and implications for the growth of structure. *ArXiv e-prints*, October 2017.

[268] D. J. Eisenstein and W. Hu. Baryonic Features in the Matter Transfer Function. *ApJ*, 496:605–614, March 1998.

[269] G. E. Addison, D. J. Watts, C. L. Bennett, M. Halpern, G. Hinshaw, and J. L. Weiland. Elucidating ΛCDM: Impact of Baryon Acoustic Oscillation Measurements on the Hubble Constant Discrepancy. *ApJ*, 853:119, February 2018.

[270] J. Hamann, S. Hannestad, J. Lesgourgues, C. Rampf, and Y. Y. Y. Wong. Cosmological parameters from large scale structure - geometric versus shape information. *J. Cosmology Astropart. Phys.*, 7:022, July 2010.

[271] A. Rest, D. Scolnic, R. J. Foley, M. E. Huber, R. Chornock, G. Narayan, J. L. Tonry, E. Berger, A. M. Soderberg, C. W. Stubbs, et al. Cosmological Constraints from Measurements of Type Ia Supernovae Discovered during the First 1.5 yr of the Pan-STARRS1 Survey. *ApJ*, 795:44, November 2014.

[272] D. Scolnic, A. Rest, A. Riess, M. E. Huber, R. J. Foley, D. Brout, R. Chornock, G. Narayan, J. L. Tonry, E. Berger, et al. Systematic Uncertainties Associated with the Cosmological Analysis of the First Pan-STARRS1 Type Ia Supernova Sample. *ApJ*, 795:45, November 2014.

[273] S. Jha, R. P. Kirshner, P. Challis, P. M. Garnavich, T. Matheson, A. M. Soderberg, G. J. M. Graves, M. Hicken, J. F. Alves, H. G. Arce, et al. UBVRI Light Curves of 44 Type Ia Supernovae. *AJ*, 131:527–554, January 2006.

[274] M. Hicken, P. Challis, S. Jha, R. P. Kirshner, T. Matheson, M. Modjaz, A. Rest, W. M. Wood-Vasey, G. Bakos, E. J. Barton, et al. CfA3: 185 Type Ia Supernova Light Curves from the CfA. *ApJ*, 700:331–357, July 2009.

[275] M. Hicken, P. Challis, R. P. Kirshner, A. Rest, C. E. Cramer, W. M. Wood-Vasey, G. Bakos, P. Berlind, W. R. Brown, N. Caldwell, et al. CfA4: Light Curves for 94 Type Ia Supernovae. *ApJS*, 200:12, June 2012.

[276] C. Contreras, M. Hamuy, M. M. Phillips, G. Folatelli, N. B. Suntzeff, S. E. Persson, M. Stritzinger, L. Boldt, S. González, W. Krzeminski, et al. The Carnegie Supernova Project: First Photometry Data Release of Low-Redshift Type Ia Supernovae. *AJ*, 139:519–539, February 2010.

[277] G. Folatelli, M. M. Phillips, C. R. Burns, C. Contreras, M. Hamuy, W. L. Freedman, S. E. Persson, M. Stritzinger, N. B. Suntzeff, K. Krisciunas, et al. The Carnegie Supernova Project: Analysis of the First Sample of Low-Redshift Type-Ia Supernovae. *AJ*, 139:120–144, January 2010.

[278] M. D. Stritzinger, M. M. Phillips, L. N. Boldt, C. Burns, A. Campillay, C. Contreras, S. Gonzalez, G. Folatelli, N. Morrell, W. Krzeminski, et al. The Carnegie Supernova Project: Second Photometry Data Release of Low-redshift Type Ia Supernovae. *AJ*, 142:156, November 2011.

[279] A. Conley, J. Guy, M. Sullivan, N. Regnault, P. Astier, C. Balland, S. Basa, R. G. Carl-

berg, D. Fouchez, D. Hardin, et al. Supernova Constraints and Systematic Uncertainties from the First Three Years of the Supernova Legacy Survey. *ApJS*, 192:1, January 2011.

[280] M. Sullivan, J. Guy, A. Conley, N. Regnault, P. Astier, C. Balland, S. Basa, R. G. Carlberg, D. Fouchez, D. Hardin, et al. SNLS3: Constraints on Dark Energy Combining the Supernova Legacy Survey Three-year Data with Other Probes. *ApJ*, 737:102, August 2011.

[281] J. A. Frieman, B. Bassett, A. Becker, C. Choi, D. Cinabro, F. DeJongh, D. L. Depoy, B. Dilday, M. Doi, P. M. Garnavich, et al. The Sloan Digital Sky Survey-II Supernova Survey: Technical Summary. *AJ*, 135:338–347, January 2008.

[282] R. Kessler, A. C. Becker, D. Cinabro, J. Vanderplas, J. A. Frieman, J. Marriner, T. M. Davis, B. Dilday, J. Holtzman, S. W. Jha, et al. First-Year Sloan Digital Sky Survey-II Supernova Results: Hubble Diagram and Cosmological Parameters. *ApJS*, 185:32–84, November 2009.

[283] N. Suzuki, D. Rubin, C. Lidman, G. Aldering, R. Amanullah, K. Barbary, L. F. Barrientos, J. Botyanszki, M. Brodwin, N. Connolly, et al. The Hubble Space Telescope Cluster Supernova Survey. V. Improving the Dark-energy Constraints above z > 1 and Building an Early-type-hosted Supernova Sample. *ApJ*, 746:85, February 2012.

[284] A. G. Riess, L.-G. Strolger, S. Casertano, H. C. Ferguson, B. Mobasher, B. Gold, P. J. Challis, A. V. Filippenko, S. Jha, W. Li, et al. New Hubble Space Telescope Discoveries of Type Ia Supernovae at z >= 1: Narrowing Constraints on the Early Behavior of Dark Energy. *ApJ*, 659:98–121, April 2007.

[285] S. A. Rodney, A. G. Riess, L.-G. Strolger, T. Dahlen, O. Graur, S. Casertano, M. E. Dickinson, H. C. Ferguson, P. Garnavich, B. Hayden, et al. Type Ia Supernova Rate Measurements to Redshift 2.5 from CANDELS: Searching for Prompt Explosions in the Early Universe. *AJ*, 148:13, July 2014.

[286] O. Graur, S. A. Rodney, D. Maoz, A. G. Riess, S. W. Jha, M. Postman, T. Dahlen, T. W.-S. Holoien, C. McCully, B. Patel, et al. Type-Ia Supernova Rates to Redshift 2.4 from CLASH: The Cluster Lensing And Supernova Survey with Hubble. *ApJ*, 783:28, March 2014.

[287] A. G. Riess, S. A. Rodney, D. M. Scolnic, D. L. Shafer, L.-G. Strolger, H. C. Ferguson, M. Postman, O. Graur, D. Maoz, S. W. Jha, et al. Type Ia Supernova Distances at Redshift >1.5 from the Hubble Space Telescope Multi-cycle Treasury Programs: The Early Expansion Rate. *ApJ*, 853:126, February 2018.

[288] M. Betoule, R. Kessler, J. Guy, J. Mosher, D. Hardin, R. Biswas, P. Astier, P. El-Hage, M. Konig, S. Kuhlmann, et al. Improved cosmological constraints from a joint analysis of the SDSS-II and SNLS supernova samples. *A&A*, 568:A22, August 2014.

[289] L. E. Marcucci, G. Mangano, A. Kievsky, and M. Viviani. Implication of the Proton-Deuteron Radiative Capture for Big Bang Nucleosynthesis. *Physical Review Letters*, 116(10):102501, March 2016.

[290] E. G. Adelberger, A. García, R. G. H. Robertson, K. A. Snover, A. B. Balantekin, K. Heeger, M. J. Ramsey-Musolf, D. Bemmerer, A. Junghans, C. A. Bertulani, et al. Solar fusion cross sections. II. The pp chain and CNO cycles. *Reviews of Modern Physics*, 83:195–246, January 2011.

[291] G. Chon, A. Challinor, S. Prunet, E. Hivon, and I. Szapudi. Fast estimation of polarization power spectra using correlation functions. *MNRAS*, 350:914–926, May 2004.

[292] K.-W. Ng and G.-C. Liu. Correlation Functions of CMB Anisotropy and Polarization. *International Journal of Modern Physics D*, 8:61–83, 1999.

[293] J. Zuntz, M. Paterno, E. Jennings, D. Rudd, A. Manzotti, S. Dodelson, S. Bridle, S. Sehrish, and J. Kowalkowski. CosmoSIS: Modular cosmological parameter estimation. *Astronomy and Computing*, 12:45–59, September 2015.